Title

Fundamentals and emerging optical applications of hexagonal boron nitride: a tutorial

Journal

Advances in Optics and Photonics, 16(2)

ISSN

1943-8206

Authors

Su, Cong

Janzen, Eli

He, Mingze

et al.

Publication Date

2024-06-30

DOI

10.1364/aop.502922

Advances in Optics and Photonics

Fundamentals and emerging optical applications of hexagonal boron nitride: a tutorial

Cong Su,[1,†] Eli Janzen,[2,†] Mingze He,[3,†] Chi Li,[4,†] Alex Zettl,[5,6,7] Joshua D. Caldwell,[3] James H. Edgar,[2] and Igor Aharonovich[4,8,*]

[1]Mechanical Engineering and Materials Science, Yale University, New Haven, Connecticut 06520, USA
[2]Tim Taylor Department of Chemical Engineering, Kansas State University, Manhattan, Kansas 66506, USA
[3]Department of Mechanical Engineering, Vanderbilt University, Nashville, Tennessee 37212, USA
[4]School of Mathematical and Physical Sciences, Faculty of Science, University of Technology Sydney, Ultimo, New South Wales 2007, Australia
[5]Depart. of Physics, University of California at Berkeley, Berkeley, California 94720, USA
[6]Materials Science Division, Lawrence Berkeley National Laboratory, Berkeley, California 94720, USA
[7]Kavli Energy NanoSciences Institute at the University of California, Berkeley, California 94720, USA
[8]ARC Centre of Excellence for Transformative Meta-Optical Systems (TMOS), University of Technology Sydney, Ultimo, New South Wales 2007, Australia
[†]These authors contributed equally.
*igor.aharonovich@uts.edu.au

Received August 9, 2023; revised December 29, 2023; accepted January 3, 2024; published 13 May 2024

Hexagonal boron nitride (hBN), also known as white graphite, is a transparent layered crystal with a wide bandgap. Its crystal structure resembles graphite, featuring layers composed of honeycomb lattices held together through van der Waals forces. The layered crystal structure of hBN facilitates exfoliation into thinner flakes and makes it highly anisotropic in in-plane and out-of-plane directions. Unlike graphite, hBN is both insulating and transparent, making it an ideal material for isolating devices from the environment and acting as a waveguide. As a result, hBN has found extensive applications in optical devices, electronic devices, and quantum photonic devices. This comprehensive tutorial aims to provide readers with a thorough understanding of hBN, covering its synthesis, lattice and spectroscopic characterization, and various applications in optoelectronic and quantum photonic devices. This tutorial is designed for both readers without prior experience in hBN and those with expertise in specific fields seeking to understand its relevance and connections to others.

https://doi.org/10.1364/AOP.502922

Fundamentals and emerging optical applications of hexagonal boron nitride: a tutorial

Cong Su, Eli Janzen, Mingze He, Chi Li, Alex Zettl, Joshua D. Caldwell, James H. Edgar, and Igor Aharonovich

1. INTRODUCTION

Hexagonal boron nitride (hBN) is a layered material similar to the crystal structure of graphite, with hexagonal honeycomb layers held by van der Waals force. In industry, hBN has been widely applied in many products and fields, such as automobiles, metallurgy, fireproof materials, and cosmetics [1]. In research labs, the physical properties of hBN make it widely used in electronics and photonics. This tutorial serves as an introduction to the following basic questions: where does hBN come from (synthesis), how do we judge the quality of hBN (characterization), and how can hBN be used in the optical devices (optical applications)?

One of the most important properties of hBN is its crystal structure. It has strong sp^2 chemical bonds within its two-dimensional (2D) layers, and weak van der Waals interaction between the layers (Fig. 1). This structure is analogous to graphite, such that hBN is often called "white graphite," but hBN's in-plane lattice constant is 1.8% larger than that of graphite.

For hBN, the basal plane (0001) layers are stacked with boron atoms sandwiched between nitrogen atoms in the two adjacent layers and the hexagonal rings aligned, thus forming a sequence denoted as AA' (Fig. 2). Less common, metastable polytypes of sp^2 chemical bonding boron nitride are realized in nonequilibrium conditions such as with high impurity concentrations or under conditions of high stress [3]. For example, in Bernal stacking, the hexagonal rings in each layer are no longer aligned, but are instead shifted (Fig. 2). In rhombohedral sp^2 boron nitride (BN), the stacking sequence is ABC, which is similar to the AB stacking sequence but requires three shifts to recover the original orientation of atoms instead of the two shifts required in the AB sequence. In turbostratic BN, the layers lay parallel, but are randomly rotated relative to each other like a disordered stack of papers. Cubic boron nitride (cBN) has a different structure entirely, with alternating boron and nitrogen atoms arranged in a structure similar to diamond. Each of these structures have different physical properties, but this tutorial will focus on the most stable AA' hBN structure except in the discussion of twisted hBN in Section 5 where the stacking structure varies throughout the material due to intentional misalignment of adjacent layers.

Another key property of hBN is that it is a wide-gap insulator (with an optical bandgap around 6 eV). This is due to the effect of the different electronegativities between nitrogen and boron. A simple nearest-neighbor tight binding model yields two electronic bands around the Fermi level (i.e., valence and conduction bands) with the dispersion relationship $E = E_0 \pm \frac{1}{2}\sqrt{E_g^2 + 4|f|^2}$, where E_0 is the average potential of the site A and B (Fig. 3), E_g is the potential difference between site A and B, and f is a function of wave vector $\boldsymbol{k}$ (see [4]). This E–$\boldsymbol{k}$ relationship, with plus and minus signs representing the conduction and valence bands, respectively, has a reflection symmetry

Figure 1

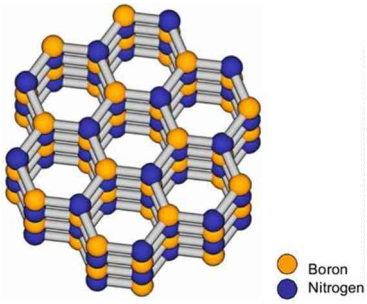

Crystal structure of hexagonal boron nitride. Figure 1 reprinted with permission from Alem *et al*., Phys. Rev. B: Condens. Matter Mater. Phys. **80**, 155425 (2009) [2]. Copyright 2009 by the American Physical Society.

Figure 2

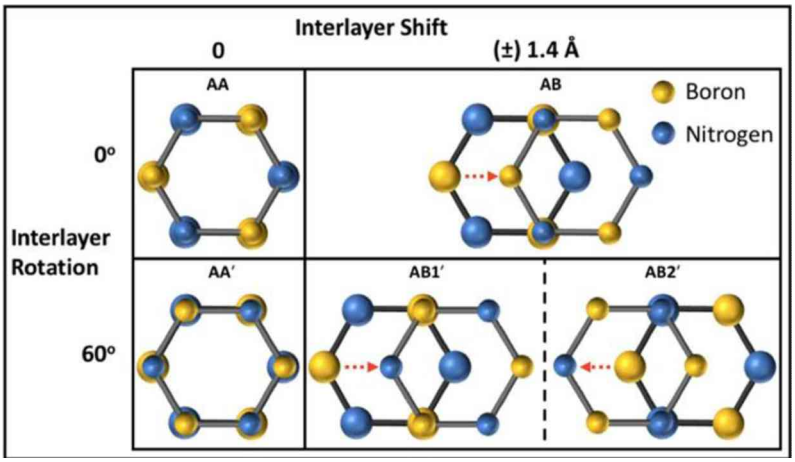

Different stacking structures in hBN. AA'' is the most thermodynamically stable stacking structure while the others are metastable. The AB stacking structure is also known as Bernal stacking and was successfully produced in [3]. Gilbert *et al*., "Alternative stacking sequences in hexagonal boron nitride," 2D Mater. **6**, 021006 (2019). https://doi.org/10.1088/2053-1583/ab0e24, © IOP Publishing. Repoduced with permission. All rights reserved.

with respect to $E = E_0$. Thus, it is apparent that valence band maximum (VBM) and conduction band minimum (CBM) are located where $f = 0$, corresponding to the K points. From this model, the VBM is equal to $E_0 - ½*E_g$ and CBM equals to $E_0 + ½*E_g$, resulting in a bandgap of exactly E_g. We therefore get an approximate result where the potential difference between the two atoms located at lattice A and B equals the bandgap of the hexagonal crystal, under the picture of this simple tight binding model. When the atoms on two sites are the same, as in the case of graphene, E_g becomes 0, and the valence and conduction bands meet with each other at K points, forming the Dirac cones with linear dispersions. In hBN, since sites A and B are occupied by B and N, respectively, E_g becomes nonzero, resulting in a bandgap. We can use the first ionization energies of elements to estimate the potential differences of elements in crystal lattices. The first ionization energies of nitrogen atom (1402.3 kJ/mol or 14.5 eV/atom) and boron atom (800.6 kJ/mol or 8.3 eV/atom) results in a gap of 6.2 eV at K points, which is very close to the measured optical bandgap of hBN (around 6 eV), discussed in Section 3. Note that a tight binding model could

Figure 3

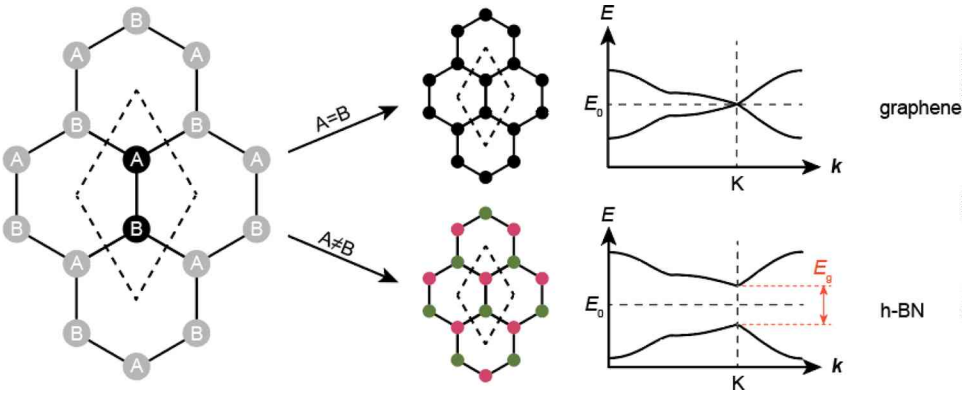

Effect of the symmetry of sites A and B. Graphene is an example with the same atomic species, and hBN is an example of different atomic species. The band structures shown here are from the tight binding model, which are only approximations of the real band structures.

only serve as the leading-order description of the band structure of hBN, where only the interaction of (1) two *p* electrons in unit cells and (2) nearest-neighbor atoms are considered. Many higher-order interactions will change the shape of bands, which could, in turn, change the positions of VBM and CBM. Self-energy is also important to properly describe the electronic band structure of hBN due to weak screening (more details are given in Section 3). We show that the insulating property of hBN makes it a very unique material in optical applications, as described in Section 4 and 5.

Thanks to the strong in-plane binding energy between boron and nitrogen, hBN is thermodynamically stable. This makes it an ideal fire-retardant material, and one of the best structural materials in high-temperature settings. Combined with its weakly bonded interlayer force, hBN outperforms graphite in many ways when used as a lubricant, where its thermal stability yields a cleaner interface, compared with graphite which can produce carbon-based by-products that contaminate the systems. In fact, the combined strong insulating and good thermal conductivity has made hBN one of the best materials for thermal management components in electronics. Monolayer hBN is even found to have the second largest thermal conductivity per unit weight among all semiconductors and insulators [5].

Because of the similarity of its crystal lattice to graphite, hBN is sometimes called "white graphite" (and likewise monolayer hBN is called "white graphene"). However, hBN is, in fact, transparent in its pristine form due to its insulating character, and the white color is usually the light scattered from its domain boundaries. With a layered structure, hBN can be exfoliated to produce an atomically flat surface, free from dangling bonds. The combined *insulating character* and *ultra-flat surface* makes hBN a wonderful dielectric material separating devices from the environment, causing minimum doping effect. hBN is especially important when the intrinsic properties of the devices need to be retained, where other commonly used dielectric substrates such SiO_2 cause the intrinsic properties of electronic devices to deteriorate [6].

Our tutorial is organized in the following logical order: Section 2 introduces the hBN growth methods, whose final product can be assessed by the characterization methods introduced in Section 3. Sections 4 and 5 cover the applications of hBN in optics, which utilize the structural and electronic properties introduced in Section 2 and 3. Some synopses of each section are introduced in the following.

It is hard to find hBN in nature, so the hBN used in industry and research laboratories is all artificially synthesized. Different synthesis methods include solution-based precipitation, chemical vapor deposition (CVD), and molecular beam epitaxy (MBE). To serve different purposes, various properties of hBN are considered when adopting these synthesis methods. Usually, the quality of hBN is determined by two factors: the concentration of defects and the average domain size. But for some purposes, the thickness, the type of defects, and the continuity of the hBN film also matter. In Section 2, we cover different synthesis methods with an emphasis on solution-based methods due to its wide applicability and consistency in sample quality. We discuss different factors that could influence the final product and how to optimize these factors for better quality. Like in cooking where sauces need to be balanced to produce a gourmet meal, many tunable parameters need to be optimized for the best-quality hBN. Temperature, pressure, composition of the source, alloy solutions, and cooling rate are all important "sauces" to make a better hBN. There are several targets of hBN growth. Crystallinity is ideally in a single domain, the size of hBN should be as big as possible, and the best color is transparent indicating a low concentration of defects. These visual appearances serve as the first quality inspection after growth, but how can we *quantify* the properties of hBN?

To do that, we can implement various spectroscopy and imaging methods. Raman spectroscopy, thermal conductivity, and defect sensitive etching are all viable methods for assessing hBN quality. In particular, the emission spectra is realized by stimulating the system with laser [photoluminescence (PL)] or electron beams [cathodoluminescence (CL)]. This is used for measuring the intrinsic bandgap or the defect states, where the energy of the radiative decay marks the distance between two states. In reality, even with highest-quality crystals synthesized, hBN flakes are always full of defects generating a huge number of localized states within the bandgap, emitting a broad spectrum of light ranging from ultraviolet (UV) to infrared (IR). The emission spectra of hBN thus become an important method to measure the quality of the hBN crystal, similar to the widely applied method in diamond appraisal, where the intensity of the red color indicates the concentration of defects. We want to emphasize that the precise band structure of hBN is still controversial at this moment. Its optical bandgap (which is measured by the photon energy emitted from a pristine crystal which is the bandgap minus the binding energy of exciton) is around 5.95 eV in the deep UV range. Theory and experiment still have not reached an agreement in the direct/indirect band structure of hBN: in theoretical calculations, the uncertainty of relative band positions of the conduction band is very sensitive to self-energy, a difficult parameter to include in calculations; in experiment, the highest-energy emission peak is too weak to probe systematically. In parallel to spectroscopy, the lattice of hBN can be characterized by transmission electron microscopy (TEM) or scanning tunneling microscopy (STM): TEM can clearly see the atoms with elements resolved, but the high-energy electron beam ($\sim$100 keV) can damage the crystal lattices; whereas STM, being a technique in the low-energy ($\sim$1 eV) regime, does not create defects during imaging, but it can only indirectly measure the crystal structure by guessing from the measured local density of states. All of these topics are covered in Section 3.

One notable application of hBN is its usage in optical devices. Due to its layered structure, hBN has a strong anisotropy of lattice vibration (phonon) behavior in-plane and out-of-plane. In some frequency ranges, the optical properties of hBN can be simultaneously metallic and dielectric along different directions, referred to as hyperbolicity. This allows momentum ($\boldsymbol{k}$) vectors of light to go to infinity within the material, compared with a limited allowable light mode in a dielectric (more "normal") material. For a finitely thick hBN, the hyperbolicity of hBN leads to extremely high wave vectors of propagating polaritons (light–matter hybrid quasiparticles). In

Table 1. Key Parameters of hBN

Properties	Values (with Notes)
Crystal symmetry (space group)	$P6_3/mmc$
Interlayer spacing	3.3 Å [7]
Bandgap (bulk)	5.95 eV (indirect gap) [8]
Bandgap (monolayer)	6.1 eV (direct gap*) [9] *calculation shows indirect gap [10]
Raman peaks	Around 52 cm^{-1} (shear mode) Around 1366 cm^{-1} (intralayer mode, thickness and isotope dependent) [11]
Displacement threshold in electron microscope	79.5 keV (boron atom), 118.6 keV (nitrogen atom) [12]
High-frequency dielectric constant (ε_{inf})	4.9 for the in-plane directions 2.95 for the out-of-plane directions [13]
Transverse and longitudinal optical phonon frequencies	1360 cm^{-1} (transverse) and 1614 cm^{-1} (longitudinal) for the in-plane directions 760 cm^{-1} (transverse) and 825 cm^{-1} (longitudinal) for the out-of-plane direction [13]
Optical phonon lifetime	~1.7 ps for isotopically enriched hBN ~0.8 ps for naturally abundant hBN [13]
Zero-phonon line (ZPL; mean excited-state lifetime) of different groups of quantum emitters	UV emitter: 4.1 eV (~1.1 ns) [14] Blue emitter: ~436 nm (~2 ns) [15–17]. Visible emitters: 580–700 nm (2–7 ns) [18,19] Boron vacancies: missing (~1.7 ns) [20–22]
Average ZPL linewidth of the quantum emitters	Nonresonant excitation: ~9 nm at room temperature [23]; spectrometer limited (<0.1 nm) at cryogenic temperature [24]. Resonant excitation: Fourier-transform limited at cryogenic temperature [25,26]

other words, the wavelength (inversely proportional to momentum vector) of polariton can be "squeezed" infinitely, which leads to an increased sensitivity as a light sensor, or a finer design of hBN device. The propagation of highly squeezed light can also be manipulated by controlling the substrate and/or geometries, realizing a deep subdiffractional lens or waveguide. They can also be excited in resonator designs for ultrasensitive chemical detections. This is discussed in detail in Section 4.

Another emerging application of hBN is in the field of quantum optics, where single-photon emitters (SPEs), as an important light source that support many photonics-based quantum techniques, could be generated from the defects in hBN. In Section 5, we discuss statistical optics where quantum optics are built upon, the signatures of defect emission, and the figures of merit that quantify the quality of quantum emitters in hBN. As an important part of quantum optics, the control of emitters via mechanical and electrical means is also briefly covered. To enhance the efficiency of quantum emission, the optical resonator is an important tool that confines the field to a specific location where higher brightness of emitters are needed. We hope that this section gives the reader an overview of the application of hBN in quantum optics and how to optimize it for applications.

This tutorial serves as an introduction to the fundamentals of hBN including synthesis, characterization, and its applications in plasmonics and quantum optics. Our intention is to provide readers, particularly young readers and early career researchers, with a concise and efficient means of acquiring essential knowledge in these fields, and facilitate a rapid and solid understanding of the subject matter. Some key parameters of hBN are listed in Table 1.

2. CRYSTAL SYNTHESIS

2.1. Introduction

Current research interest in hBN stems from its potential electronic, optoelectronic, and photonic device applications [27–29]. For these applications, single crystals with low

residual impurity concentrations and no unintentional defects such as grain boundaries are best. Thus, processes to produce hBN single crystals must be developed that meet these specifications.

Recent hBN synthesis studies have focused on precipitating bulk crystals from solution and depositing thin and thick films via CVD, MBE, and sputter deposition. Bulk crystal growth techniques generally produce higher-quality crystals than deposition methods, as demonstrated by narrow Raman $E_{2g}{}^{high}$ peak widths (7.6 cm^{-1}) [30], high-energy (>5.75 eV) PL or CL peaks [31], low residual impurity concentrations, and low surface roughness. On the other hand, deposition techniques offer fine control of the layer thickness, down to a single monolayer, and can produce crystals over much larger areas (on substrates 50 mm in diameter or larger) than bulk crystal growth (typically a few square millimeters). The following sections describe each of these techniques in detail, provide information on how they are optimized, and offer comparisons of their properties.

2.2. Solution Crystal Growth

In solution crystal growth of hBN, boron and nitrogen are dissolved in a metal or salt solvent, and crystals are grown by precipitation. It is one of the most effective methods to grow hBN crystals. Other methods are sometimes used to grow bulk single crystals of other materials, but they do not work well for hBN. For example, careful freezing of a melt is the standard way to grow single crystals of silicon and many metal alloys. hBN melts incongruently at a very high temperature (2501°C) [32], making crystal growth from melts (i.e., without a solvent) impractical. Similarly, the vapor pressure of boron above hBN is much lower than the nitrogen vapor pressure making crystal growth by sublimation also impractical.

The addition of a solvent enables crystal growth at much lower temperatures, but adds a layer of complexity as the identity of the solvent and composition of the solution become critical factors in the process. For instance, the solvent must be able to adequately dissolve both boron and nitrogen. Many molten metals are able to dissolve boron easily, which is why they are typically used for hBN solution growth. However, only a few molten metals have an appreciable nitrogen solubility. Thus, solvents are often a mixture of a high boron solubility metal and a high nitrogen solubility metal: nickel plus chromium for example. In addition to metals, molten salts [33] and silicon [34] have been demonstrated as solvents for hBN crystal growth. This section provides a guide on the basics of the solution growth process, provides details of the reported effects of process parameters, and highlights the values for the parameters that yielded the best results.

The best quality hBN single crystals are currently produced by Taniguchi and Watanabe, at the National Institute for Materials in Japan. Their crystals have been widely used in many fundamental studies of the properties of hBN and in its application in combination with other 2D materials such as graphene, MoS_2, and WSe_2. Zastrow [35] reported that Taniguchi and Watanabe co-authored 180 papers in which their material was used in 2018. A similar citation index search revealed they were co-authors of 294 papers in 2020. Their process uses an extremely high pressure, 4 GPa, which requires specialized equipment. Thus, few research groups have the ability to duplicate their process. The crystal quality is high, as indicated by their bright luminescence at short wavelengths (5.82 eV) and narrow Raman peak full width at half maximum (FWHM; 7.3 cm^{-1}) [31]. The bright luminescence from their hBN crystals (almost three orders of magnitude greater than diamond) led Watanabe *et al.* [36] to suggest that hBN is a direct bandgap material. Detailed theoretical predictions by Sponza *et al.* [37] and measurements by Cassabois *et al.* [8] later demonstrated that hBN is

Figure 4

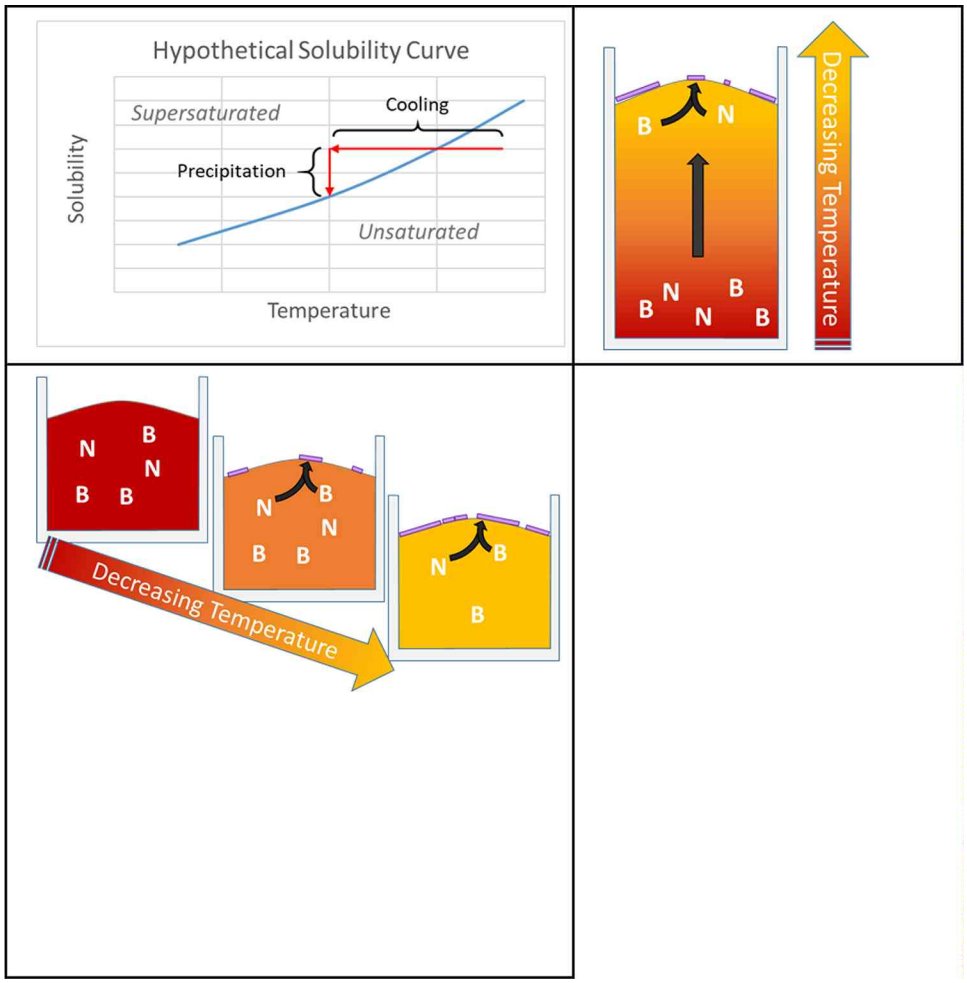

(Top left) Hypothetical solubility curve. As the temperature drops, the solution goes from unsaturated to supersaturated, causing hBN to precipitate. (Top right) Schematic of the temperature gradient method. Concentration gradient causes B and N to diffuse to the cold side, where hBN precipitates due to lower solubility. (Bottom left) Schematic of the slow cooling method. As temperature decreases, solubility decreases and any excess B and N precipitates as hBN. Reproduced with permission from [38].

actually an indirect bandgap material, but with an unusually high internal quantum efficiency.

2.2a. Basic Process of Bulk hBN Crystal Growth from Solutions

To grow hBN crystals from solution, the solvent must first be saturated with boron and nitrogen, then supersaturated to precipitate the solid hBN, i.e., the crystals. Saturation is spontaneous whenever the solution is subsaturated and exposed to boron and nitrogen sources, but the kinetics of the process and the temperature at which it occurs are important factors. To cause supersaturation, two methods are commonly used: slow cooling and temperature gradient. Both methods rely on the fact that BN solubility decreases with decreasing temperature (Fig. 4, top left). In the slow cooling method, the entire system is cooled uniformly, which decreases the solubility and causes any B and N in excess of the saturation limit to precipitate as hBN (Fig. 4, bottom left). In the temperature gradient method, a concentration gradient in the solution causes B and N to diffuse from the hot side to the cold side, where hBN precipitates due to the lower solubility (Fig. 4, top right).

Figure 5

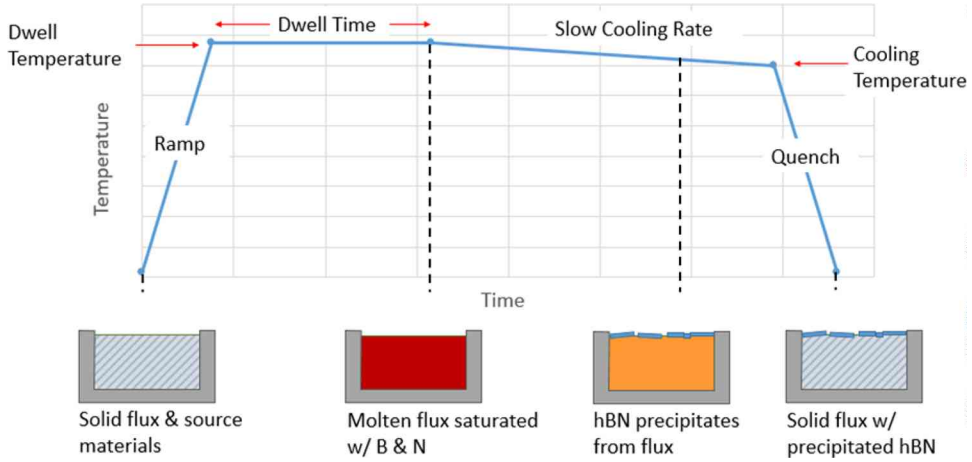

Slow cooling crystal growth process. This process consists of four stages: ramp, dwell, slow cool, and quench.

Each step in the solution growth process has its own parameters that require optimization, which depend on the system thermodynamics, and the kinetics of mass transport, nucleation, and crystal growth. This section breaks down each step and provides insights into how they can be optimized.

Saturation Every hBN solution growth experiment starts by saturating the solvent with boron and nitrogen. To saturate the solution, the system is typically held at a high temperature in the presence of boron and nitrogen sources until saturation is reached. This provides a consistent starting point for precipitating hBN, ideally resulting in a solution with no concentration or temperature gradients.

Most hBN solution growth researchers use a dwell time of 12 or 24 hours [39–46]. However, Ishii and Sato [34] reported 2 mm hBN crystals despite using a dwell time of only 2 hours, though they used a higher temperature than most others (1850°C compared with the more common temperature of 1600°C), which would increase the rate of nitrogen solvation and shorten the time necessary to saturate the solution. Clubine [41] tested dwell times up to 72 hours, but ultimately concluded that 24 hours was the optimum dwell time based on the consistent success of those experiments.

However, some researchers forgo an explicit saturation step, as is frequently the case with high-pressure–high-temperature (HPHT) crystal growth researchers utilizing a temperature gradient [36,47,48]. In these cases, the mechanisms that drive saturation and the mechanisms that drive supersaturation occur simultaneously until the solution becomes saturated and hBN begins precipitating from the solution.

Slow Cooling Method In the slow cooling method, the entire solution is heated and cooled uniformly throughout the crystal growth process, as illustrated in Fig. 5. Since boron and nitrogen solubility decreases with decreasing temperature, this causes the entire solution to become supersaturated, precipitating hBN. This precipitation can occur either by nucleating new crystals or by growing on existing crystals. Ideally, only one crystal would nucleate, then grow throughout the cooling process, so inhibiting nucleation while promoting crystal growth is critical for obtaining large single crystals. In general, the nucleation rate of new crystals increases with increasing supersaturation, which, in turn, increases with faster cooling rate. Thus, the system is usually cooled as slowly as is practical to inhibit the nucleation of crystals.

Reliable hBN crystal growth typically uses slow cooling rates of 1–4°C/h [39–46]. Faster cooling rates, up to 10°C/h, have also been tested, but typically produced relatively poor results in terms of both crystal size and defect density [41,42,49]. Tests with a slower cooling rate (0.5°C/h) [44] produced crystals with a similar size and quality to those grown using cooling rates of 1–4°C/h while significantly increasing the total time for crystal growth, suggesting that this extremely slow cooling rate is unnecessary.

Hoffman [42] concluded that extremely slow cooling also inhibits the nucleation of new layers on an established crystal, resulting in thinner, yet wider, hBN crystals than those formed with higher cooling rates. To grow both wide *and* thick crystals, he suggested a two-stage cooling process where the solution is first cooled slowly to promote the formation of wide single crystals, then cooled faster to promote nucleation of new layers on the established crystals. Sperber [43] found evidence to support this prediction, though the crystal width and thickness produced in these experiments were smaller than those produced by Hoffman with the typical single-stage cooling process. However, that could be attributed to the lower temperatures used in these experiments (1410°C compared with Hoffman's 1500°C).

The temperature at which slow cooling is stopped (the cooling temperature) could also have a significant impact on the crystal size. Stopping slow cooling prematurely might prevent the crystals from growing as large as they might have if the slow cooling step was continued to a lower temperature. One way to avoid this problem is to continue slow cooling until the solvent solidifies, at which point crystal growth will slow to a negligible rate. However, this drastically increases the time required for each experiment.

Furthermore, the crystal growth rate is faster and crystal quality is better at higher temperatures. Therefore, extending growth to lower temperatures may produce crystals with gradients in crystal quality depending on the temperature at which they precipitated. Thus, much higher cooling temperatures (within 100°C of the maximum temperature) are recommended, though the exact value depends heavily on the system being studied. Most hBN solution growth researchers using the slow cooling method specify cooling temperatures between 1200°C and 1525°C with Ni- or Fe-based solvents and maximum temperatures between 1410°C and 1550°C [39–46,50].

Temperature Gradient Method Another approach to hBN solution growth is to impose a temperature gradient along the length of the solution to drive crystal growth, as illustrated in Fig. 6. In this setup, supersaturation is maintained through a balance between diffusion and crystal growth. The temperature gradient produces a gradient in the solubility of hBN, which increases with increasing temperature. More boron and nitrogen will dissolve on the hot side than the cold side, which introduces a concentration gradient in the same direction as the temperature gradient. This, in turn, provides a driving force for boron and nitrogen mass transfer from the hot to the cold side, producing a supersaturated solution in the cooler region that causes hBN crystals to precipitate. This process persists because the concentration gradient is maintained through the continuous removal of boron and nitrogen on the cold side (due to crystal growth) and addition of these components on the hot side (due to solvation of the source material).

The important parameters in this process are the dwell temperature (in this case, the maximum temperature in the solution) and the temperature gradient. The dwell temperature is kept high to increase the boron and nitrogen solubility, improve the crystal quality, and produce a faster growth rate. The magnitude of the temperature gradient impacts the rate of nucleation and crystal growth. The higher the temperature gradient,

Figure 6

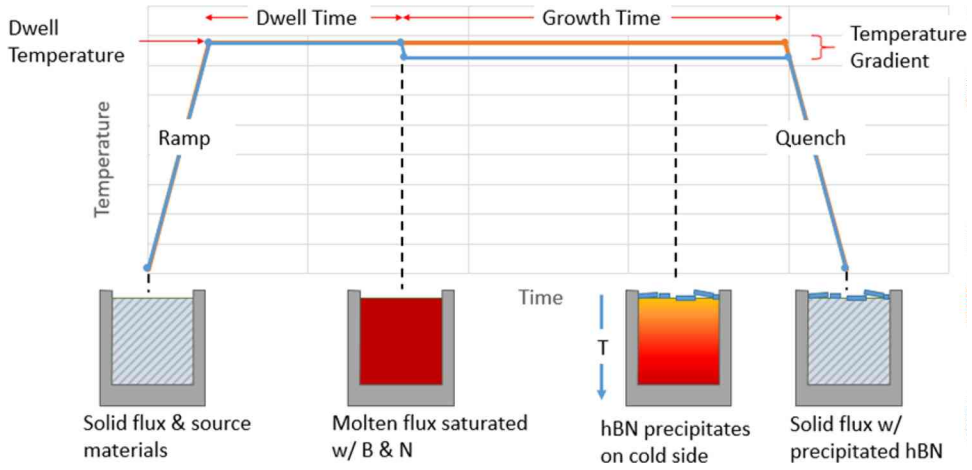

Temperature gradient crystal growth process.

the larger the solubility gradient, which, in turn, leads to a larger driving force for mass transfer. If the rate of boron and nitrogen diffusion outpaces the rate of hBN crystal growth, these components will "pile up" at the cold end of the solution, increasing the driving force for nucleation which results in smaller crystals. If the crystal growth outpaces diffusion, the degree of supersaturation will be smaller, decreasing the driving force and nucleation rate and resulting in larger crystals. The latter situation is generally desirable, but decreasing the temperature gradient too much will result in impractically long experiments. Typical temperature gradients are on the order of 100°C/cm.

One benefit of the temperature gradient method over the slow cooling method is that all crystal growth occurs at a constant, high temperature. Since crystal quality improves with temperature, this ensures that all crystals will form at the optimal temperature. In contrast, crystals grown with the slow cooling method will form across a range of temperatures, so crystal quality is expected to worsen somewhat over the course of the experiment.

2.2b. Development of Solution Growth Method

Solution growth of hBN can be split into three categories: HPHT, atmospheric-pressure–high-temperature (APHT), and monoisotopic hBN. HPHT hBN synthesis is widely considered the gold standard for growth of large, high-quality hBN. However, APHT synthesis can frequently produce hBN on par or better than that grown at HPHT. Monoisotopic hBN is synthesized so that both boron and nitrogen have only one isotope and has only been grown with APHT synthesis to date. The natural isotope distribution of boron is 20% ^{10}B and 80% ^{11}B while the natural isotope distribution of nitrogen is 99.6% ^{14}N and 0.4% ^{15}N (i.e., nearly isotopically pure ^{14}N). Thus, by using a monoisotopic boron source material, monoisotopic hBN can be grown. This section details the advances each hBN solution growth researcher has made in developing these processes.

High-Pressure Synthesis Taniguchi, Watanabi *et al.* [28,36] began research into HPHT synthesis of hBN when it formed as a by-product of cBN synthesis and they observed that it exhibited UV luminescent properties. They grew these crystals via the temperature gradient method with a barium solvent at high temperature (1500–1750°C) and high pressure (4.0–5.5 GPa). The crystals grown in these works were 1–6 mm^2 and were colorless, which indicates low carbon impurities. In later work [47] with the barium solvent, they used SIMS to analyze the carbon and oxygen

Figure 7

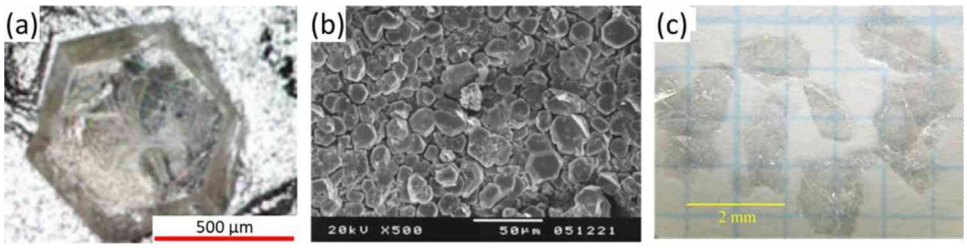

Examples of hBN crystals grown at high pressure and temperature. (a) Optical micrograph of a hBN single crystal grown from a Ba solvent at high temperature (1500–1650°C) and high pressure (4–5 GPa). Adapted from [47]. (b) SEM image of hBN crystals grown from a nickel solvent at 6 GPa and 1600°C. Kubota *et al*., "Synthesis of cubic and hexagonal boron nitrides by using Ni solvent under high pressure," Jpn. J. Appl. Phys. **46**, 311 (2007), https://doi.org/10.1143/JJAP.46.311, © IOP Publishing. Reproduced with permission. All rights reserved. (c) Photograph of hBN flakes produced using a magnesium solvent at 3 GPa and 1900–2100°C. Reprinted from J. Cryst. Growth **402**, Zhigadlo, "Crystal growth of hexagonal boron nitride (hBN) from Mg–B–N solvent system under high pressure," 308–311 Copyright 2014, with permission from Elsevier.

impurity concentrations in their hBN crystals; both were less than 10^{18} atoms/cm^3. An example of an hBN single crystal grown under these conditions is shown in Fig. 7(a). Kubota *et al*. [51] also tested a pure nickel solvent at high temperature (1300–1900°C) and high pressure (4.5–6 GPa). The crystals produced were relatively small (10–25 µm across) and were irregularly shaped, as shown in Fig. 7(b). The small size may be due to the extremely low solubility of nitrogen in pure nickel, which may inhibit the rate of crystal growth.

Zhigadlo [48] followed up on this work with a magnesium solvent at 1700–2100°C and 1–3 GPa using the temperature gradient method. A drawback of the barium solvent is that it is hygroscopic and oxidizes quickly in air, so it must always be handled in a dry nitrogen atmosphere. Magnesium is more stable and does not require such stringent care to be taken in handling it, so the author proposes it as a more practical solvent. The best results with this solvent were obtained at 1900–2100°C and 3 GPa, the maximum temperatures and pressure they tested. An image of hBN crystals produced with this solvent are shown in Fig. 7(c). The success of these parameters could be attributed to the improving kinetics with higher temperatures and increasing nitrogen solubility with higher pressure. These crystals have a similar size to those reported by Watanabe *et al.* [36] and produced a Raman $E_{2g}{}^{high}$ peak FWHM of 8 cm^{-1}, which indicates good quality, suggesting this is a viable substitute for barium.

Onodera *et al.* [52] discovered that hBN crystals grown with a Ba solvent as described in [47] consistently contained a carbon-rich domain. These domains are invisible in optical and electron microscope images, but visible in CL and PL images. They are also significantly detrimental to carrier mobility as determined by electrical measurements on a hBN–graphene heterostructure. No advice was given on how to eliminate the domain from forming, but their method of detecting them with CL or PL allows carbon-free crystals to be selected before device fabrication.

Atmospheric Pressure Synthesis The first demonstration of hBN solution growth for bulk single crystals was in 1983 by Ishii and Sato [34], who used a silicon solvent at atmospheric pressure. They were able to produce flakes up to 2 mm across and 20 µm

Figure 8

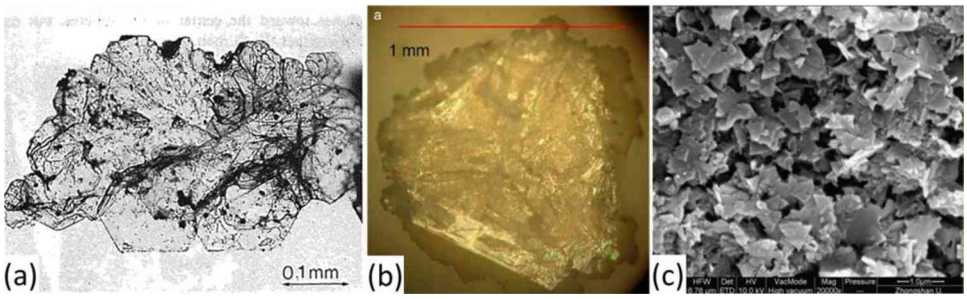

(a) Large hBN flake produced in a Si solvent at 1850°C. Reprinted from J. Cryst. Growth **61**, Ishii and Sato, "Growth of single crystals of hexagonal boron nitride," 689–690, Copyright 1983, with permission from Elsevier. (b) Large single crystal grown from molten BaF_2–Li_3N salt at 820°C. Reprinted from J. Cryst. Growth **305**, Feigelson *et al*., "III-Nitride crystal growth from nitride-salt solution," 399–402, Copyright 2007, with permission from Elsevier. (c) Crystals grown from a mixture of $NaBF_4$, $NaNH_2$, and LiBr at 650°C. Reprinted from J. Am. Ceram. Soc. **90**, Gu *et al*., "Low-temperature synthesis and growth of hexagonal boron-nitride in a lithium bromide melt," 1589–1591, Copyright 2007, with permission from Elsevier.

thick as shown in Fig. 8(a). The mechanism for hBN supersaturation and precipitation in their work is unclear, but the authors suggest that evaporation of the solvent could have been the driving force. The extreme temperature (1830°C) and low pressure makes this explanation plausible, but the driving force may also have been the cooling period from 1830°C to 1800°C. Unfortunately, the cooling rate was not specified. It is also unclear whether these flakes were single crystals or polycrystalline, but their Raman $E_{2g}{}^{high}$ peak FWHM was 8 cm^{-1}, indicating their quality was relatively good, even by today's standards. However, these crystals had a pale yellow color, which is indicative of carbon contamination, likely caused by the use of a graphite susceptor in their induction furnace.

A few different researchers tested hBN solution growth at low temperatures (<1000°C) and pressures using a variety of solvents and experimental setups. Ostrovskaya *et al*. [49] grew hBN at 650–1450°C from a lithium borate solvent, which was supersaturated by evaporating the solvent. Feigelson, Frazier, and Twigg [33] grew hBN [Fig. 8(b)] with a molten salt (BaF_2–Li_3N) as a solvent at 760–900°C under a temperature gradient, following procedures that were successful for growth of other III-nitrides such as GaN. Gu *et al*. [53] grew hBN [Fig. 8(c)] with a mixture of $NaBF_4$, $NaNH_2$, and LiBr at 600–700°C, though they did not specify how their solution was supersaturated. In all of these works, the width of hBN single crystals were very small (<10 μm) or their crystal quality was poor (Raman $E_{2g}{}^{high}$ peak FWHM >10 cm^{-1}).

Kubota *et al*. [39], following their success with high-pressure synthesis of hBN and the success of Ishii and Sato [34] at atmospheric pressure, developed the slow cooling method for hBN solution growth at atmospheric pressure. To grow crystals, they cooled the system from 1350–1500°C to 1200°C at 4°C/h and tested two different solvents: pure Ni and Ni–Mo. A major conclusion in their work was the importance of the nitrogen solubility of the solvent. Pure nickel has a very low nitrogen solubility and produced crystals that were 300 μm across or less with a thickness of a few micrometers. The addition of Mo significantly increased the nitrogen solubility of the solvent and crystals grown from Ni–Mo solvents [Fig. 9(a)] were significantly thicker (10 μm) and had a Raman $E_{2g}{}^{high}$ peak FWHM of 9.0 cm^{-1}, which indicates good quality.

Figure 9

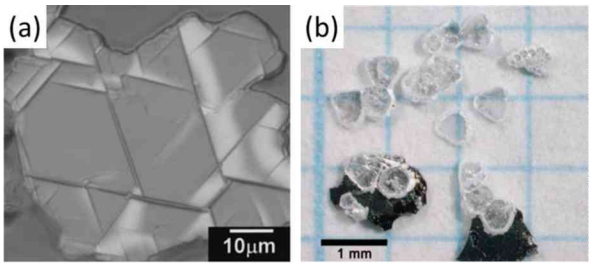

(a) Differential interference microscope image of hBN grown from Ni–Mo solvent at 1400°C. From Kubota *et al*., Science **317**, 932–934 (2007). Reprinted with permission from AAAS. (b) Photograph of hBN crystals grown from a Ni–Cr solvent at 1430°C. Reprinted with permission from Kubota *et al*., Chem. Mater. **20**, 1661–1663 (2008) [40]. Copyright 2008 American Chemical Society, https://doi.org/10.1021/cm7028382.

In a follow-up to this work, Kubota *et al*. [40] tested a Ni–Cr solvent. The addition of Cr enabled crystals [Fig. 9(b)] up to 500 μm across and 60 μm thick to be formed, which they attributed to its much higher nitrogen solubility than Ni–Mo. They also suggested that the optimal starting temperature of the process is near 1430°C due to obtaining their largest single crystals at that temperature [Fig. 9(b)].

The success of the APHT slow cooling method for hBN solution growth developed by Kubota *et al*. [39,40] led many others to build off of this process and improve it. Clubine [41] and Hoffman *et al*. [54] studied the effect of the cooling rate and dwell temperature with a Ni–Cr solvent and concluded that the slowest cooling rate (2°C/h) and highest dwell temperature (1700°C) they tested produced the largest crystals. This was attributed to a reduction in the nucleation rate with decreasing cooling rate and increasing atomic mobility with increasing growth temperature. However, the highest temperature in both works required use of a furnace with a graphite heating element, which may have contaminated the crystals with carbon. The largest crystal produced in these works [Fig. 10(a)] was 5 mm wide with a Raman $E_{2g}{}^{high}$ peak of 8 cm^{-1}, indicating they were high quality. Clubine [41] also tested pure Ni and pure Cu as solvents, but did not precipitate hBN from them.

Sperber [43] tested a stepped growth process with a Ni–Cr solvent intended to increase the thickness of hBN single crystals without affecting their domain area. In the first step, the solution was slowly cooled from 1410°C to 1394°C at 4°C/h to grow wide crystals as done in prior work. Then the system was dwelled at that temperature for 24 hours to allow the established crystals to grow thicker. The crystals were relatively small compared with prior work (~170 μm wide), but their thickness (~17 μm) was large relative to their width, suggesting that this process could be used to grow wide and thick crystals if it were further optimized. Notably, the crystals grown in this way also grew oriented so their a/b direction was perpendicular to the surface of the solvent as shown in Fig. 10(b).

Liu *et al.* [55] compared Ni–Cr with Fe–Cr as a solvent for hBN solution growth because Fe is significantly cheaper than Ni and would make the process more economical. They obtained hBN single crystals that were up to 2 mm wide [Fig. 10(c)] and had a Raman $E_{2g}{}^{high}$ peak of 7.8 cm^{-1}, indicating that both solvents produce similarly large and high-quality crystals and demonstrating that Fe–Cr will work as a low-cost alternative to Ni–Cr.

Figure 10

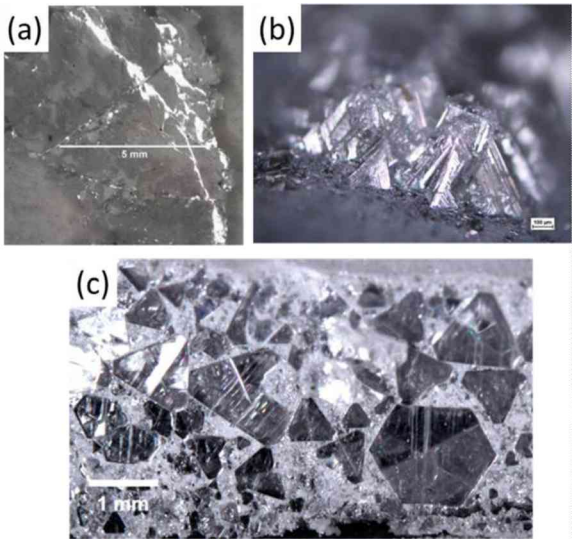

(a) Optical micrograph of a 5-mm-wide hBN single crystal grown from a Ni–Cr with a dwell temperature of 1700°C and a cooling rate of 2°C/h. Reprinted from J. Cryst. Growth **393**, Hoffman *et al*., "Optimization of Ni–Cr flux growth for hexagonal boron nitride single crystals," 114–118, Copyright 2014, with permission from Elsevier. (b) Optical micrograph of hBN crystals grown from Ni–Cr using a stepped growth process to encourage growth in both the *a/b* and *c* directions. Crystals tended to form the shape of pyramids with their *a/b* direction roughly perpendicular to the solvent surface. Reprinted with permission from [43]. (c) Photograph of large hBN single crystals on the surface of the solidified Fe–Cr flux they were grown from. Reprinted with permission from Liu *et al*., Cryst. Growth Des. **17**, 4932–4935 (2017) [55]. Copyright 2017 American Chemical Society, https://doi.org/10.1021/acs.cgd.7b00871.

Zhang *et al.* [45] demonstrated that intentionally adding carbon to their Ni–Cr solvent increased the size and yield of hBN crystals, claiming that carbon reduces any residual oxygen in the system that would have otherwise inhibited crystal formation. Their results showed a tenfold increase in domain size while using carbon concentrations between 1.8 and 6.8 mass % compared with their own results without any added carbon. No carbon was detected in the hBN crystals with electron energy loss spectroscopy (EELS), but their largest crystals [Fig. 11(a)] were 200 μm wide while all other researchers that tried Ni–Cr were able to grow crystals larger than 500 μm. Subsequent analysis by Cao *et al.* [56] of hBN crystal growth with a Ni/Cr solvent, hBN as the source material, and with the addition of 1.8 mass % carbon, demonstrate that graphite was precipitating where cracks appeared in the hBN crystals. This graphite precipitation was suppressed by adding 0.25 to 4.76 mass % gold, which suppressed the carbon aggregation and produced larger crystals [Fig. 11(b)]. The time-resolved PL properties were also improved with the addition of gold.

Li *et al.* [57] grew hBN from an Fe–Cr solvent with a process that combined features of the slow cooling and temperature gradient methods. One zone in their horizontal tube furnace was held at 1600°C throughout crystal growth while the temperature of the neighboring zone was steadily dropped from 1600°C to 1400°C at 4°C/h, creating a temperature gradient across the solution that gradually increased over the course of the experiment. These crystals were up to 3–4 mm wide [Fig. 12(a)] and had a Raman $E_{2g}{}^{high}$ peak FWHM of only 7.6 cm^{-1}, the narrowest peak width reported to date using natural isotope distribution boron.

Figure 11

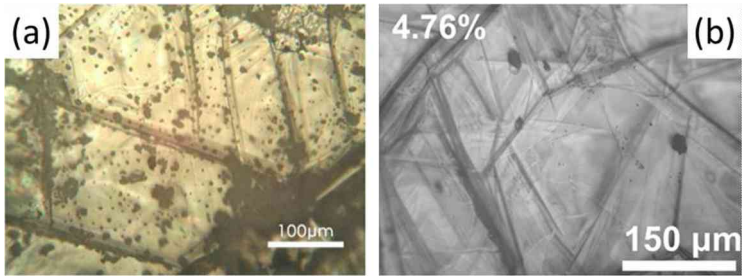

(a) Optical micrograph of hBN grown from a Ni–Cr solvent containing 1.8 mass % carbon. Reprinted with permission from Zhang *et al.*, Cryst. Growth Des. **19**, 6252–6257 (2019) [45]. Copyright 2019 American Chemical Society, https://doi.org/10.1021/acs.cgd.9b00712. (b) Optical micrograph of hBN grown from a Ni–Cr solvent containing 1.8 mass % carbon and 4.76 mass % gold to suppress precipitation of graphite. Reprinted by permission from Springer Nature: Cao *et al.*, J. Mater. Sci. **57**, 14668–14680, Copyright 2022.

Figure 12

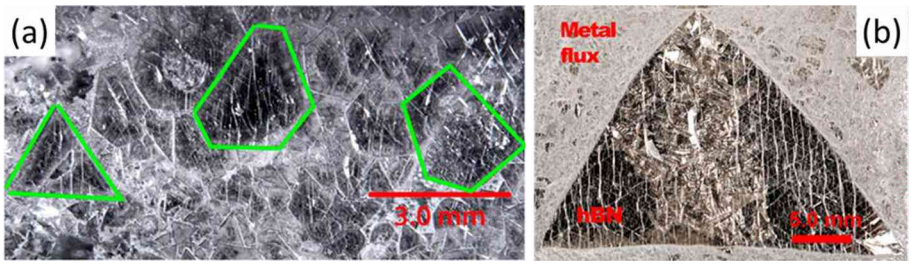

(a) Micrograph of hBN on the surface of an Fe–Cr ingot. Green lines outline grain boundaries of three crystals. Reprinted with permission from Li *et al.*, Chem. Mater. **32**, 5066–5072 (2020) [57]. Copyright 2021 American Chemical Society, https://doi.org/10.1021/acs.chemmater.0c00830. (b) Photograph of hBN single crystal grown from a pure iron solvent on solidified ingot. Triangular hBN sheet is ~4 cm^2 in area. Reprinted with permission from Li *et al.*, ACS Nano **15**, 7032–7039 (2021) [58]. Copyright 2021 American Chemical Society, https://doi.org/10.1021/acsnano.1c00115.

In another work, Li *et al.* [58] grew hBN from a pure Fe solvent by slowly cooling from 1550°C to 1450°C at 4°C/h. Pure Fe has a very low nitrogen solubility compared with other solvents that have been tested for hBN solution growth, but it still produced large, high-quality hBN (Raman $E_{2g}{}^{high}$ peak FWHM of 7.6 cm^{-1}). As shown in Fig. 12(b), this process also produced a highly ordered hBN flake ~4 cm^2 in area, one of the largest continuous hBN sheets reported.

Onodera *et al.* [50] tested Ni–Cr alongside Ni–Mo and Co–Cr. They concluded that Co–Cr was the best of these solvents because it produced crystals with the lowest impurity concentrations. The largest of these flakes were >180 μm^2 after exfoliation from the solidified ingot [Fig. 13(a)]. These are smaller than those produced from Ni–Cr, but the reason for this is unclear based on the information provided in the article. However, a major conclusion from this work is that the crystals they produced from Co–Cr with an APHT process were free of carbon-rich domains frequently found in crystals grown from Ba in a HPHT process, which were initially discovered in a

Figure 13

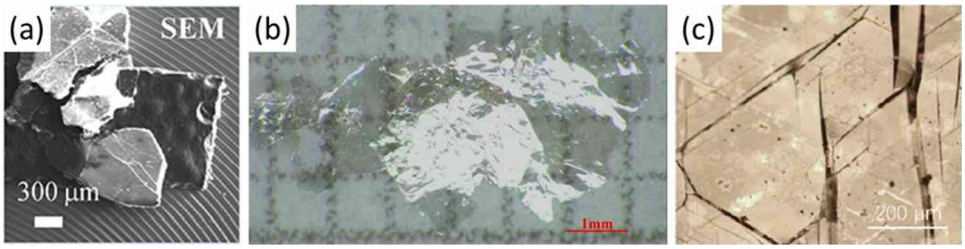

(a) SEM image of free-standing hBN crystal flakes grown from a Co–Cr solvent. Reprinted with permission from Onodera *et al.*, Nano Lett. **20**, 735–740 (2020) [50]. Copyright 2020 American Chemical Society, https://doi.org/10.1021/acs.nanolett.9b04641. (b) Photograph of hBN flake grown from a Cu–Cr solvent. Reprinted from J. Cryst. Growth **562**, Zhang *et al.*, "Growth of hexagonal boron nitride crystals at atmospheric pressure from Cu–Cr flux," 126074, Copyright 2021, with permission from Elsevier. (c) Optical micrograph of hBN grown with 16.2 at% B in a pure Fe solvent. Reproduced from [60] with permission from the Royal Society of Chemistry.

prior work [52]. These carbon domains were shown to degrade the carrier mobility of the material, so finding ways to avoid them is important.

Zhang *et al.* [59] grew hBN from a Cu–Cr solvent by slow cooling from 1700°C to 1500°C at a rate between 2.5 and 10°C/h. Copper was chosen as a replacement for Ni because it is much cheaper than Ni and has a very low carbon solubility, potentially reducing the concentration of carbon impurities in hBN grown from it. As in other works testing the effect of the cooling rate, the slowest rate they tested (2.5°C/h) produced the largest, clearest hBN flakes. These flakes were up to 6 mm wide [Fig. 13(b)] with a Raman $E_{2g}{}^{high}$ peak FWHM of 9.3 cm^{-1}, which is significantly higher than in other works, indicating that they have worse quality.

Li *et al.* [60], following the success of Li *et al.* [58], also studied hBN solution growth in pure Fe by slowly cooling the system from 1550°C to 1450°C at 4°C/h. They specifically studied how the concentration of boron in the melt (1.5–25.3 at%) affected the size of hBN grown, determining that a boron concentration of 16.2 at% produced the largest crystals [up to 400 μm wide; Fig. 13(c)]. These crystals had a Raman $E_{2g}{}^{high}$ peak FWHM of 7.9 cm^{-1}, which indicates that they have a high crystal quality.

Synthesis of Monoisotopic hBN To grow monoisotopic hBN, a hot-pressed boron nitride (HPBN) boat cannot be used as is often done for hBN solution growth because HPBN is only commercially available with the natural isotope distributions. Since HPBN dissolves into the solution during crystal growth, any hBN grown with it will have an unpredictable mixture of isotopes. Therefore, an inert crucible such as alumina is usually used and monoisotopic boron powder is used as the boron source material. However, this comes with the additional challenge of needing to decide what concentration of boron to add to the solution instead of relying on the solvent's boron solubility and the solvation kinetics of HPBN to control the concentration of boron. Several works have been published that detail how to grow high-quality hBN.

Hoffman *et al.* [61] were the first to describe how monoisotopic hBN can be grown via the solution growth method. They used a 46.76/ 41.47/11.78 mass % Ni/Cr/B solution with isotopically enriched ^{10}B (92.64 at%) or ^{11}B (99.99 at%) as the boron source material, cooling from 1500°C to 1200°C at 2°C/h. However, they performed

Figure 14

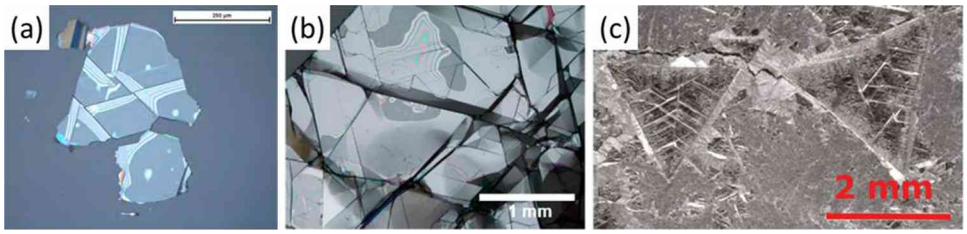

(a) Optical micrograph of $h^{10}BN$ grown from Ni–Cr with 11.78 mass % ^{10}B by slowly cooling at 4°C/h. Reprinted with permission from [42]. (b) Optical micrograph of $h^{10}BN$ grown from Ni–Cr with 4 mass % ^{10}B by slowly cooling at 0.5°C/h. Reprinted with permission from Liu *et al.*, Chem. Mater. **30**, 6222–6225 (2018) [62]. Copyright 2018 American Chemical Society, https://doi.org/10.1021/acs.chemmater.8b02589. (c) Optical micrograph of $h^{11}BN$ grown from Fe–Cr with 3.2 mass % ^{11}B by slowly cooling at 4°C/h. Reproduced from [63] with permission from the Royal Society of Chemistry.

the experiment in a HPBN crucible, which diluted the isotopically enriched boron with natural isotope distribution boron. Furthermore, the crystals grown in their work were small (20–30 μm) with wide Raman $E_{2g}{}^{high}$ peak FWHM (14.1 and 9.4 cm^{-1} for $h^{10}BN$ and $h^{11}BN$, respectively), indicating that they had relatively poor quality. In later attempts, Hoffman [42] replaced the HPBN crucible with an alumina one, leaving all else the same, to much greater success. These crystals were much larger [~300 μm; Fig. 14(a)] with Raman $E_{2g}{}^{high}$ peak FWHMs of 3.5 and 3.6 cm^{-1} for $h^{10}BN$ and $h^{11}BN$, respectively.

Liu *et al.* [62] achieved even better results using a process with a few key differences. The starting composition was 48/48/4 mass % Ni/Cr/B, hydrogen was added to the furnace atmosphere to remove carbon and oxygen impurities from the solution, and the cooling rate was lowered from 4°C/h to 0.5°C/h. Crystals grown with this process were up to 1 mm wide [Fig. 14(b)] and had Raman $E_{2g}{}^{high}$ peak FWHMs of 3.1 and 3.3 cm^{-1} for $h^{10}BN$ and $h^{11}BN$, respectively. As with the results of Hoffman [42], these peak widths are dramatically narrower than those produced by any hBN single crystal with a natural boron isotope distribution, which is attributed to eliminating isotopic disorder in the material.

Following this work, Li *et al.* [63] grew monoisotopic $h^{10}BN$ and $h^{11}BN$ from a Fe–Cr solvent. They used a faster cooling rate, cooling from 1550°C to 1450°C at 4°C/h, but the basic process was otherwise the same. The largest crystals grown were 1–5 mm across [Fig. 14(c)] and had Raman $E_{2g}{}^{high}$ peak FWHMs of 3.1 and 2.7 cm^{-1} for $h^{10}BN$ and $h^{11}BN$, respectively, indicating that they are larger and slightly higher quality than those produced by Liu *et al.* [62] with a Ni–Cr solvent.

Li *et al.* [60] grew monoisotopic $h^{10}BN$ and $h^{11}BN$ from a pure Fe solvent using the optimal boron concentration they determined in the same work (see previous section). They did not specify the domain size of monoisotopic hBN they grew, but it is likely close to the size of natural isotope distribution hBN they grew (~400 μm). Furthermore, the Raman $E_{2g}{}^{high}$ peak FWHMs for these crystals were 3.3 and 2.9 cm^{-1} for $h^{10}BN$ and $h^{11}BN$, respectively, indicating that they have crystal quality similar to those of Liu *et al.* [62] and Li *et al.* [63].

2.2c. Temperature

The temperature of the solution during crystal growth is an instrumental factor in both the kinetic and equilibrium mechanisms occurring during the process. Most researchers that have tested a range of temperatures demonstrated that the highest temperature they tested produced the best results in terms of crystal size and defect density [33,41–43,49,53,64,65]. This is as expected, since the solubility of boron and nitrogen and the kinetics of all the mechanisms involved in crystal growth typically increase with temperature.

However, Kubota *et al.* [40] concluded otherwise, claiming an optimal temperature at 1430°C in their Ni–Cr solvent. They claimed that at higher temperatures, the nucleation rate was too high, resulting in many small crystals; at lower temperatures, crystal growth was too slow, severely limiting the amount of hBN precipitated. Furthermore, Feigelson *et al*. [33] was able to grow an hBN single crystal about 1 mm across using a temperature of only 820°C with their BaF_2–Li_3N solvent, though the quality of their crystals were relatively poor (based on a Raman $E_{2g}{}^{high}$ FWHM of ~12 cm^{-1}) compared with bulk hBN crystals from other works. Most hBN solution growth researchers use temperatures between 1300°C and 2000°C with a rough average of about 1600°C, so the comparatively low temperature used by Feigelson *et al*. [33] is remarkable. These counterexamples demonstrate that the effect of temperature is not always intuitive.

The temperature of the system can affect hBN crystal growth in three primary ways: (1) the boron and nitrogen solubility, (2) the kinetics of the crystal growth process, including nucleation, crystal growth, nitrogen solvation, and diffusion, and (3) phase equilibria. Furthermore, considering the extreme temperatures used, the practical limitations of the equipment used in this work are a common factor.

Temperature and Solubility of Boron and Nitrogen Boron and nitrogen solubilities typically increase with temperature, which is why both the slow cooling and temperature gradient methods work for hBN solution growth. This is inherently at least a three-component system (boron, nitrogen, and a single- or multicomponent solvent), but some insights can be gained by considering the binaries within this multicomponent system.

Boron solubility in boron–solvent systems generally increases with increasing temperature regardless of the solvent used. Consider phase diagrams of boron and metals, which typically have a eutectic shape as shown in Fig. 15. The boron solubility in this situation can be defined as the maximum boron concentration in the single-phase liquid region, which is highlighted in red in the figure. Real metal–boron phase diagrams are full of compounds, which make this trend of increasing solubility with increasing temperature less straightforward, but the general trend holds true. In situations where an alloy is used as a solvent, the phase behavior becomes more complex than in a binary system, but the general trend still holds true.

In nitrogen–solvent systems, the trend of solubility versus temperature can be either positive or negative, depending on the solvent being used and its composition. For example, Fig. 16 shows how nitrogen solubility increases with temperature in pure iron, but decreases with temperature when the solvent is at least 6.5 wt% chromium [66]. Molten Ni–Cr alloys have similar trends [67]. Both Fe–Cr and Ni–Cr alloys have been used successfully for hBN crystal growth [40–46,50], so this trend clearly does not prevent a solvent from functioning well for hBN solution growth. However, it does make the trend expected for the multicomponent B–N–solvent system more uncertain.

Figure 15

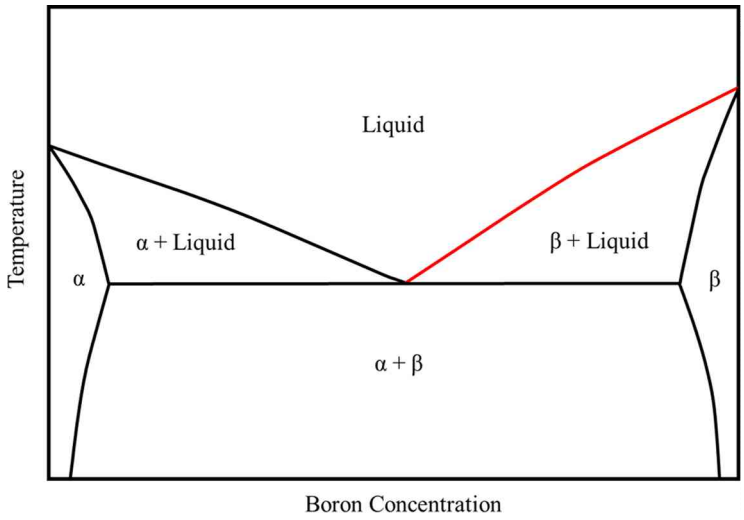

Hypothetical metal–boron phase diagram. Liquid-phase boron solubility (red line) increases with increasing temperature.

Figure 16

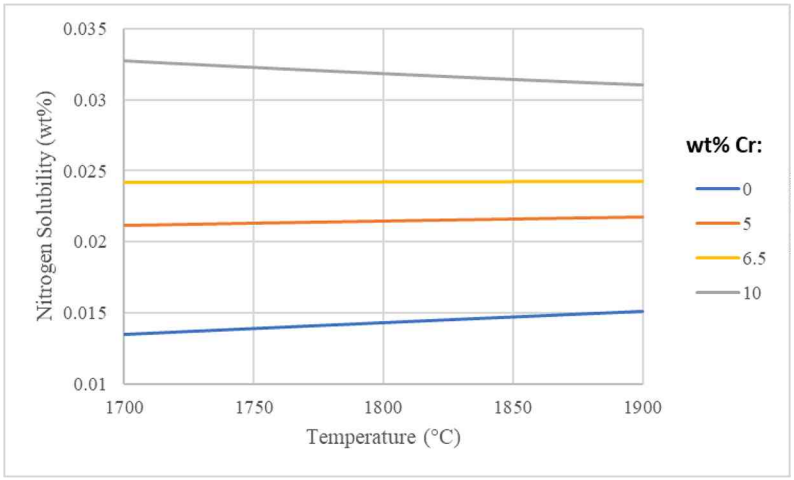

Solubility of nitrogen versus temperature in molten Fe–Cr alloys at varying chromium concentrations. Curves based on model parameters given in [66]. Concentration of chromium changes the slope and magnitude of the nitrogen solubility curve.

Without additional information, it is reasonable to assume that if both the B–solvent and N–solvent systems have a positive trend in solubility versus temperature, the multicomponent B–N–solvent system will as well. Since multicomponent phase equilibria data are often unavailable, this provides a decent starting point for understanding a given system. However, if the N–solvent system has a negative trend in solubility versus temperature, this may not be the case.

Studying the equilibrium reaction between boron and nitrogen can provide further insights:

$$\mathrm{BN}_{(\mathrm{solid})} \leftrightarrow \mathrm{B}_{(\mathrm{dissolved})} + \frac{1}{2}\mathrm{N}_{2\ (\mathrm{gas})}. \tag{2.1}$$

Figure 17

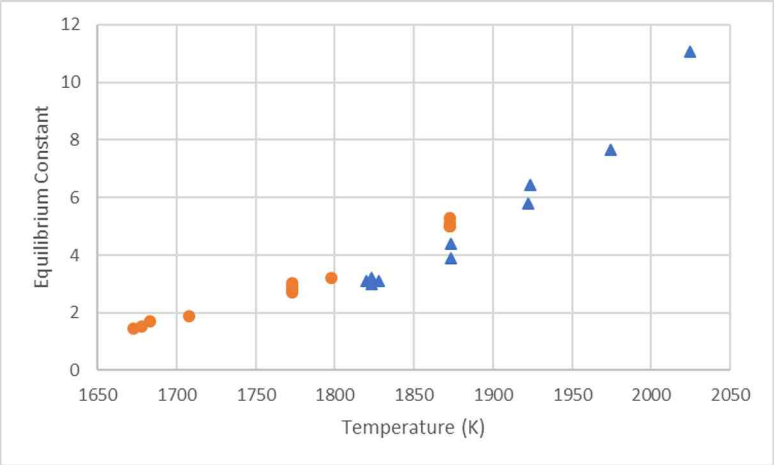

Equilibrium constant for hBN dissolution in molten iron. Increasing equilibrium constant with increasing temperature shows that hBN solubility increases with increasing temperature. Data from Evans and Pehlke [68] (blue triangles) and Ball [69] (orange circles).

This reaction can be quantified with its equilibrium constant, assuming the gas phase is ideal and the solid phase is pure hBN:

$$K = f_B m_B P_{N_2}^{1/2}, \tag{2.2}$$

where f_B is the activity coefficient of boron in the solution, m_B is the mass fraction of boron in the solution, and P_{N_2} is the partial pressure of nitrogen in the gas phase. As shown in Fig. 17, this equilibrium constant increases with increasing temperature in molten iron, which indicates that hBN solubility increases with increasing temperature.

The equilibrium constant is a more convenient parameter for understanding hBN solubility than concentration because the concentrations of boron and nitrogen in solution are nonstoichiometric in an atmospheric pressure process. If the partial pressure of nitrogen is held constant, the equilibrium constant could be replaced by the concentration of boron since it would be the last remaining dependent variable in Eq. (2.2). However, note that these equations will not represent high-pressure (>1 GPa) systems where a gas phase does not exist.

Practical Considerations Even though the size and quality of hBN single crystals grown via the solution growth process typically improves with increasing temperature, the maximum temperature is limited by the specific furnace. For example, the tube furnaces used for atmospheric pressure hBN solution growth at Kansas State University [54,55,58] are limited to 1600°C by both their $MoSi_2$ heating elements and alumina tubes. The limiting factor in each of these cases is what materials the furnaces are made of. Furnaces with graphite and tungsten heating elements and containment vessels can reach higher temperatures (up to 2000°C), but graphite furnaces are known to contribute carbon impurities into hBN crystals grown in them and tungsten reacts unfavorably to boron vapor.

Other furnaces, such as those used for high-pressure hBN solution growth [28,48,51], are able to reach temperatures up to 1900°C or higher by using graphite heating elements. The solution is protected from carbon contamination by placing it in a sealed sample chamber capable of being compressed to their extreme pressures (>1 GPa).

Figure 18

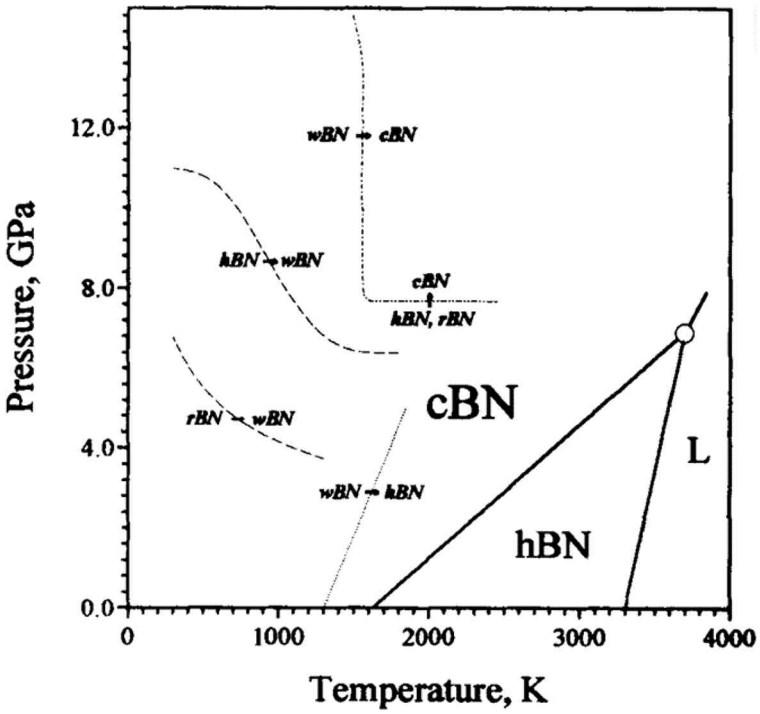

Phase diagram of boron nitride, including rough estimations of the boundary lines for kinetic transformations. Copyright 1995 from "Boron nitride phase diagram. State of the art" by [70] Solozhenko. Reproduced by permission of Taylor and Francis Group, LLC, a division of Informa pic.

2.2d. Pressure

Solution growth of hBN can be divided into two groups: APHT solution growth, which occurs at or slightly above 1 bar, and HPHT solution growth, which occurs at 1–6 GPa. Both of these pressure regimes have their own benefits and drawbacks. At high pressure, the concentration of dissolved nitrogen is increased and solvent evaporation is suppressed, but any impurities present in the source material are trapped there and the process becomes difficult to scale up. Regardless, the current industry standard for bulk hBN is grown at high pressures [36,47,51], so a discussion of this parameter is necessary.

At extremely high pressures (>1 GPa), such as those used by HPHT researchers, cBN is the thermodynamically stable structure as shown in Fig. 18. However, the addition of a solvent changes the phase behavior as shown in Fig. 19 for a Ni solvent. Both hBN and cBN can form simultaneously [51], but beyond 1800°C and 6 GPa, only cBN will form. This puts an upper limit on what conditions can be used when hBN is the desired crystal structure.

Pressure and Nitrogen Solubility The clearest effect of pressure on the crystal growth system is how it impacts the concentration of nitrogen in the solvent. Nitrogen solubility is one of the most important factors for hBN solution growth because nitrogen accounts for half of the atoms in hBN but it has a substantially lower solubility (typically <0.1 mass %) than boron (typically >1 mass %) in molten metals at the common crystal growth temperature of ~1600°C. Thus, nitrogen will be the limiting reagent in hBN solution growth, so increasing the nitrogen solubility is expected to increase the rate of crystal growth and the size of crystals produced.

Figure 19

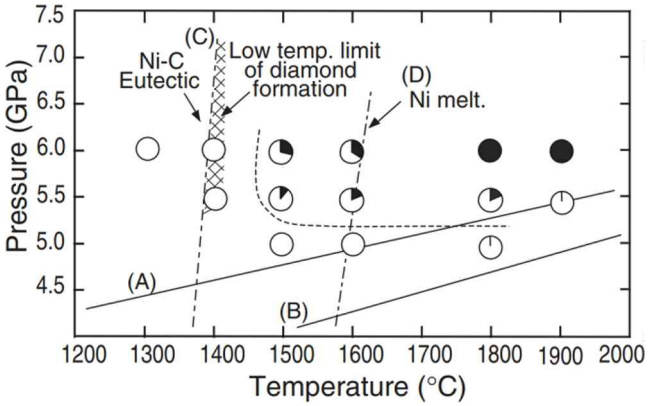

P–T phase diagram of BN formation in a Ni solvent. The darkened fraction of each circle represents the ratio of cBN:hBN and the dotted line indicates the conditions where the shift from hBN to cBN begins. Kubota *et al.*, "Synthesis of cubic and hexagonal boron nitrides by using Ni solvent under high pressure," Jpn. J. Appl. Phys. **46**, 311 (2007), https://doi.org/10.1143/JJAP.46.311,

Nitrogen solubility in molten metals typically follows Sievert's law, which shows that nitrogen concentration increases with increasing nitrogen partial pressure:

$$K_s = \frac{x_N}{P_{N_2}^{1/2}}. \tag{2.3}$$

This provides a conceptually simple way to increase the amount of nitrogen in the solvent by increasing the pressure. Depending on the solvent and the pressure, the increased nitrogen concentration may exceed the valid range of Sievert's law, requiring a more complex model, but the general trend will still hold true.

If the total amount of nitrogen in the system is limited and the pressure is sufficiently high, as is the case in Taniguchi and Watanabe's [47,51] high-pressure experiments, all the nitrogen in the system will be dissolved or bound in hBN. This sets an upper bound on what pressure will be useful to increase the amount of dissolved nitrogen for a given total amount of nitrogen in the system.

Pressure and Solvent Evaporation Some solvents used in hBN solution growth, such as barium as used by Taniguchi and Watanabe [36,47] or magnesium as used by Zhigadlo [48], have a relatively high vapor pressure at crystal growth temperatures. In an open system, the continuous loss of these solvents through evaporation would significantly increase the concentration of boron and nitrogen over the course of an experiment, which would then increase the rate of nucleation and crystal growth. If this effect is not accounted for, a measure of control over the experiment is lost and the re-condensation of the solvent inside the vacuum system could cause damage. Taniguchi and Watanabe avoided these issues by using a closed system with molybdenum crucibles wielded shut operating at extremely high pressure. In a closed system, the evaporating solvent will eventually saturate the gas phase, stopping any further loss of the solvent.

However, one potential benefit of using a solvent that readily evaporates is for the release of hBN crystals from the solidified solvent, which they are typically adhered to after crystal growth. By heating it at low pressure under a continuous gas flow,

Figure 20

Photograph of a horizontal tube furnace used in [42].

Figure 21

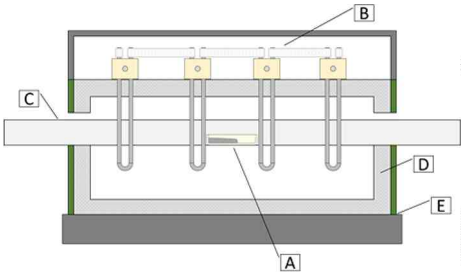

Schematic of tube furnace used at Kansas State University. (A) Alumina boat holding molten metal solution. (B) $MoSi_2$ heating elements. (C) Alumina tube (connected to vacuum system at ends; not shown). (D) Alumina foam insulation. (E) Furnace body.

the solvent evaporates, leaving free-standing hBN single crystals behind. This has been done successfully by Zhigadlo [48] with his magnesium solvent by heating the sample in a vacuum at 750°C for 30 minutes. Other methods for releasing crystals either require mechanical force, which can damage the crystals, or the solvent must be dissolved in acid or some other solvent, which produces hazardous waste.

Practical Considerations The equipment used in APHT solution growth and HPHT solution growth is dramatically different. For APHT solution growth, a standard tube furnace (as shown in Figs. 20 and 21) is usually used. These furnaces provide good control over the atmosphere and volatile impurities and evaporated solvent are swept out of the system with a continuous gas flow However, these furnaces are not designed for high pressure and are usually only run at slight positive pressure to prevent atmospheric oxygen from leaking into the tube.

For HPHT solution growth, a large hydraulic press (pictured in Fig. 22) is required to reach the extreme process pressures. In this case, the furnace is a closed system with no gas phase, so the composition of the solution is expected to be more precisely controlled, though any impurities present at the start will be trapped there. This furnace is loaded with a small cylindrical growth cell that contains the solvent and hBN powder. A schematic of one of these cells is shown in Fig. 23, which are 1–2 cm in each dimension. Clearly, the volume of the solution that can be used in this HPHT process is much more limited compared with APHT, which highlights one of the main drawbacks of HPHT solution growth: the scalability of the process.

The scalability of the hBN solution growth process is important for commercializing hBN single crystals. APHT solution growth has the upper hand here, despite historically producing slightly lower-quality crystals than HPHT. In the APHT process, the

Figure 22

Photograph of the hydraulic press used at the National Institute of Materials Science in Tsukuba, Japan. A small cylindrical capsule (1–2 cm in diameter) that contains the solution is placed in the center of the press. Reprinted by permission from Springer Nature: Zastrow, Nature **572**, 429–432, Copyright 2019.

Figure 23

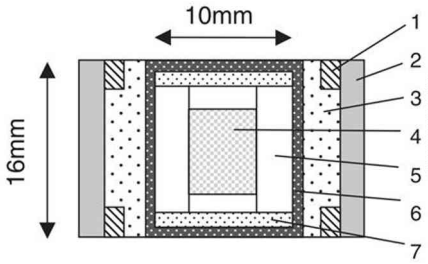

Schematic of crystal growth cell used in the hydraulic press at the National Institute of Materials Science in Tsukuba, Japan: 1, steel ring; 2, pyrophyllite sleeve; 3, pressure medium; 4, hBN and solvent; 5, MgO chamber; 6, graphite heater; 7, pressure medium. The temperature gradient that the cell experiences can be adjusted by adjusting its vertical position in the furnace. Kubota *et al.*, "Synthesis of cubic and hexagonal boron nitrides by using Ni solvent under high pressure," Jpn. J. Appl. Phys. **46**, 311 (2007), https://doi.org/10.1143/JJAP.46.311,

size of a batch can be increased simply by using a larger furnace with larger crucibles or multiple crucibles simultaneously. In contrast, the HPHT process is limited by the practical limitations of how to reach ultrahigher pressures for a given volume. Even state-of-the-art high-pressure furnaces are limited to container volumes of a few cubic centimeters.

2.3. CVD/MOVPE/MBE for Wafer-Scale Monolayers

Research into the heteroepitaxy of hBN is motivated by the availability of large-area single-crystal substrates (greater than 200 mm in diameter) such as sapphire and silicon. Heteroepitaxy is promoted as essential for scaling the fabrication of devices based on 2D materials and enabling the integration of multiple devices on a single substrate. Furthermore, the ability to deposit high-crystal-quality thin layers of different 2D materials (such as graphene on hBN) could be much faster and produce cleaner interfaces than mechanically stacking small thin flakes of material.

In general, heteroepitaxy of any material has many challenges. These include lattice constant and lattice symmetry mismatches, the stability of the substrate under deposition conditions, and control of the layer's nucleation on a substrate. Additional

Figure 24

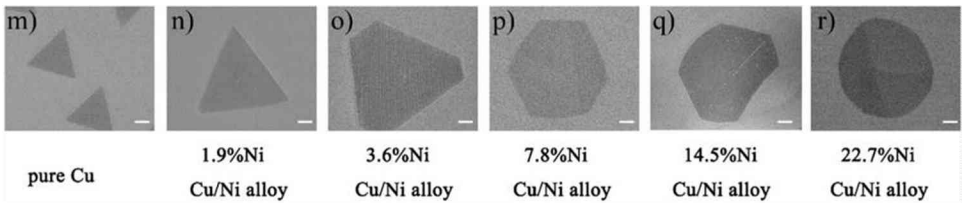

Example of the common practice among hBN deposition studies illustrating the evolution of the nuclei as a function of process parameters. In this case, SEM images of hBN as a function of the substrate composition. Yang *et al*., "Shape evolution of two dimensional hexagonal boron nitride single domains on Cu/Ni alloy and its applications in ultraviolet detection," Nanotechnology **30**, 245706 (2019), https://doi.org/10.1088/1361-6528/ab0d3d, © IOP Publishing. Reproduced with permission. All rights reserved.

challenges arise with hBN heteroepitaxy due to its unique properties. Since hBN only has weak van der Waal chemical bonds out of its (0001) plane, the interaction between the hBN film and the substrate is weak, making nucleation difficult. Because hBN has a negative coefficient of thermal expansion (CTE) [71] while most common substrates have a positive CTE, the hBN layers are almost certain to be strained as they are cooled from the deposition temperature. This can cause wrinkles to form in the hBN layer.

Many studies of hBN heteroepitaxy have been reported, as summarized in recent reviews [72–80]. The analysis of the processes and measured outcomes tends to be similar throughout these studies. Optical microscopy and scanning electron microscopy are employed to characterize the shapes and nucleation densities of the hBN deposits. hBN deposits of equilateral triangles and hexagons are common during the initial stage of epitaxy [81] (Fig. 24). X ray photoelectron spectroscopy (XPS) is frequently applied to confirm the hBN film's stoichiometry and purity. Almost inevitably, the 1:1 boron to nitrogen stoichiometry of the deposited film is confirmed. Oxygen and carbon are frequently detected by XPS, although their sources, whether advantageous or from the precursors is often unclear, especially if the hBN is very thin. Raman spectroscopy is a common method of assessing the hBN crystal quality. For heteroepitaxial deposited hBN thin films, the position of its E_{2g} peak is frequently shifted from its bulk position of 1366 cm^{-1} due to strain and broadened due to crystal defects. For example, Tian *et al.* [82] reported a peak position of 1368 cm^{-1} indicating compressive strain with a FWHM of 16 cm^{-1}, due to a combination of its thinness and to its fine grain size. Interpretation of the Raman spectra to characterize the crystal quality of very thin hBN layers (less than 10 nm) is difficult, since the $E_{2g}{}^{high}$ peak position and FWHM are different from those of bulk hBN [83].

2.3a. CVD and MOVPE

Researchers on hBN synthesis by CVD have explored a wide range of precursors, substrate materials, and deposition conditions (temperature, nitrogen-to-boron ratios). Precursors studied including ammonia borane (H_3NBH_3) [84], borazine ($B_3H_6N_3$) [85], triethylboron (TEB, $(CH_3CH_2)_3B$) [86,87], and diborane (B_2H_6). Ammonia (NH_3) is typically the nitrogen source of choice, since diatomic nitrogen (N_2) is thermally stable and unreactive. hBN films have been deposited on a wide variety of metal substrates, with nickel and copper being the most common choices. Many of these studies focus on controlling nucleation to maximize the hBN crystal grain size. Sapphire is the most commonly studied dielectric substrate for these studies. Challenges include maintaining the hBN crystal structure (rBN or tBN sometimes

forms), avoiding residual impurity incorporation such as carbon when TEB is the boron source, or oxygen due to decomposition of the sapphire substrate, especially when depositing at temperatures above 1500°C, which generally is necessary to produce the highest-quality hBN.

2.3b. MBE

MBE has certain advantages over other thin film deposition techniques including *in situ* characterization and a very slow deposition rate, enabling exquisite control of hBN layer thickness, down to a single monolayer. Source materials for MBE can include high-purity boron and nitrogen, the latter made more reactive by plasma decomposition. This is in contrast to CVD, which employs sources of boron containing other elements such as triethylboron, $(CH_3CH_2)_3B$, which has the potential to inadvertently incorporate carbon into the film. Lastly, while hydrogen is generally present in CVD from either a H_2 carrier gas or from NH_3, MBE can deposit hBN in a hydrogen-free atmosphere. This is particularly advantageous for the deposition of hBN layers on graphite, which could react with, and be etched by, hydrogen.

hBN has been deposited by MBE on many different substrates including sapphire, and nickel and cobalt foils. For example, the deposition of high-quality hBN on nickel at low temperatures has been demonstrated by many researchers. The nickel may act as a catalyst that helps to make this possible. Typical of these studies is that of Nakhaie *et al.* [88], who reported on MBE growth of hBN over a temperature range of 600°C to 835°C on Ni/MgO(111) substrates. The hBN films were polycrystalline due to the polycrystalline nature of the supporting nickel film. hBN associates nucleates at grain boundaries and pits in the nickel film. The quality was dependent on the surface roughness of the Ni. The authors reported a Raman peak width of 9.3 cm^{-1} centered at 1365 cm^{-1} for a three-atomic-layer-thick film. X ray diffraction indicates the hBN was under compressive strain.

The MBE deposition of hBN on highly oriented pyrolytic graphite (HOPG) is particularly notable, because these materials have similar crystal structures and a small in-plane lattice constant mismatch of 1.8%. Graphite is thermally and chemically stable at very high temperatures in oxygen- and hydrogen-free ambients. Its high thermal stability makes deposition at high temperatures, greater than 1350°C, possible. Wrigley *et al.* [89] demonstrated by atomic force microscopy (AFM) that the growth of hBN on HOPG is highly faceted with much larger grain sizes than growth on sapphire (Fig. 25). For multilayer hBN films, the deep-UV PL was dominated by a peak with maximum between 5.4 and 5.5 eV, but for the optimal deposition temperature (1390°C) had luminescence above 5.7 eV (Fig. 26).

A unique capability of hBN on HOPG is its ability to deposit monolayers. Studying such monolayers, Elias *et al.* [9] determined that, unlike bulk hBN which has an indirect energy bandgap, its monolayer has a direct bandgap transition. Furthermore, the energy bandgap magnitude increases from 5.95 eV for bulk hBN to 6.08 eV for the monolayer. In addition, the exciton binding energy also increases, from 0.7 eV for the bulk to 1.7 eV for the monolayer. This study was made possible due to the weak interaction between the hBN and the graphite substrate.

2.3c. Deposition of hBN by CVD on Molten Liquid Metals

To avoid the negative impact on the crystal quality caused by the mismatch of the hBN film and crystalline substrate properties that are inherent in heteroepitaxy, several studies have examined the deposition of hBN on molten metals. The molten metal surface lacks order and is compliant, thus the hBN layer adopts its natural, lowest-energy structure. Furthermore, the molten metal surface is very smooth, unlike solid surfaces

Figure 25

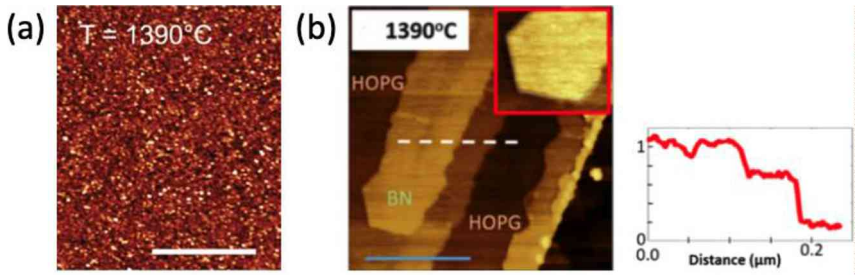

(a) AFM of hBN deposited on sapphire by MBE at 1390°C showing the structure is very fine grain (scale bar is 2 μm). Vuong *et al.*, "Deep ultraviolet emission in hexagonal boron nitride grown by high-temperature molecular beam epitaxy," 2D Mater. **4**, 021023 (2017), https://doi.org/10.1088/2053-1583/aa604a, © IOP Publishing. Reproduced with permission. All rights reserved. (b) In contrast, hBN deposited on HOPG was much more ordered and exhibited hexagonal faceting. hBN proceeds laterally from graphite step edges (scale bar is 200 nm). Wrigley *et al.*, "Epitaxy of boron nitride monolayers for graphene-based lateral heterostructures," 2D Mater. **8**, 034001 (2021), https://doi.org/10.1088/2053-1583/abea66, © IOP Publishing. Reproduced with permission. All rights reserved.

Figure 26

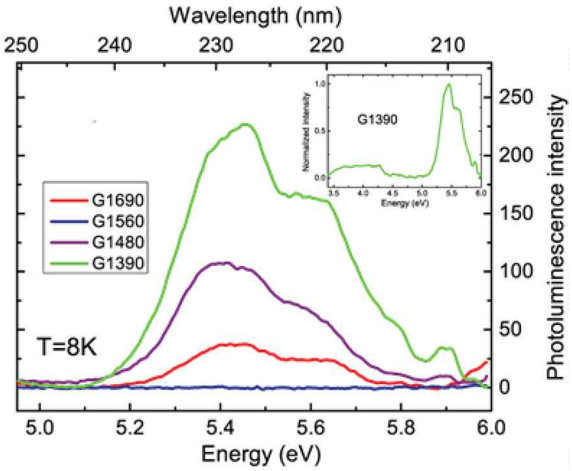

Low-temperature PL spectra from hBN deposited on HOPG at different substrate temperatures. The optimal deposition temperature was 1390°C, as this produced luminescence about 5.7 eV. Vuong *et al.*, "Deep ultraviolet emission in hexagonal boron nitride grown by high-temperature molecular beam epitaxy," 2D Mater. **4**, 021023 (2017), https://doi.org/10.1088/2053-1583/aa604a, © IOP Publishing. Reproduced with permission. All rights reserved.

which have atomic steps that become preferred points for nucleation. In contrast, there is no preferred place for hBN nucleation on the molten metal liquids. Instead nucleation occurs uniformly over the metal surface. Finally, metal surfaces, molten or solid, catalyze the chemical reactions, making deposition possible at relatively low temperatures, ~1000°C to 1100°C.

Lee *et al.* [91] demonstrated the deposition of large-area (at least several square millimeters) hBN monolayers on molten gold supported by a tungsten foil. The reactant was borazine with an argon/hydrogen carrier gas mixture at a temperature of 1100°C,

Figure 27

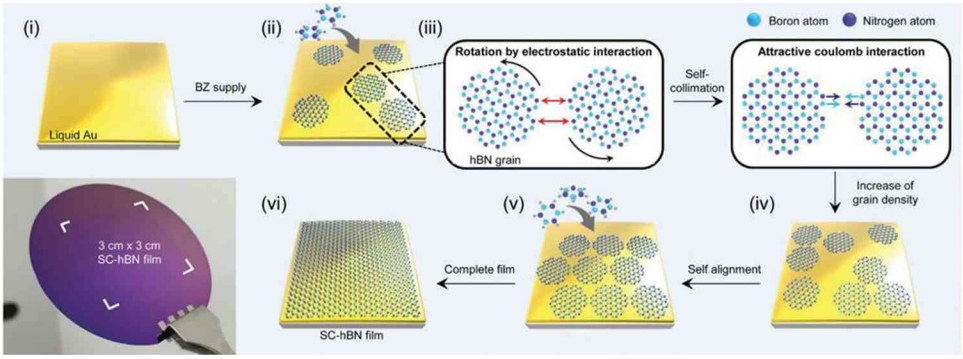

Schematic of self-collimated growth of hBN films on a molten gold substrate. When separate hBN nuclei collide, they self-align with each other due to Coulomb interactions between the B and N atoms at their edges, resulting in a much larger single crystalline film (i to vi). From Lee *et al*., Science **362**, 817–821 (2018). Reprinted with permission from AAAS.

i.e., above the melting temperature of gold (1064°C). The authors claimed the surface diffusion of the elements was promoted because of the limited solubility of boron and nitrogen in the gold. With optimized process parameters, the hBN nuclei were uniformly thick and equal in area. With continued growth, these nuclei rearrange to eliminate grain boundaries as they merge to form a continuous hBN layer, a process the authors called self-collimation, as shown in Fig. 27. The patches of hBN were assumed to rotate to match the bonding order of adjacent patches to form a continuous layer. The circular patches were approximately 15 μm in diameter when they merged. TEM and LEED (low energy electron diffraction) suggested a large area of the hBN was highly aligned in a single direction, however the type of defects that form at the point of merging would be difficult to detect. For this film the Raman $E_{2g}{}^{high}$ peak positions were shifted to higher wavenumbers (1370.1 cm^{-1}) than that of a monolayer exfoliated from a bulk crystal (1367 to 1368 cm^{-1}). The Raman peak width was approximately 18 cm^{-1}, which was also broader than an exfoliated monolayer (11–14 cm^{-1}) [83].

Liu *et al.* [92] examined hBN growth on molten copper instead of gold, characterizing the impact of reactant flow rate on the hBN island size and shape. Using the reactant ammonia–borane at a source temperature of 80°C produced the maximum grain size of 225 ± 50 μm^2 at a substrate temperature of 1085°C. Applying selective area electron diffraction in TEM, the authors concluded that the hBN islands did not self-collimate to form a single crystalline film. They suggest that this may be due to differences in the interaction strengths between hBN islands and hBN and the metals (Cu or Au) [92].

More recently, Zhang *et al.* [93] also studied copper ($T_{melting}$ = 1085°C) as the molten metal substrate for hBN deposition, promoting its lower cost than gold. Tungsten foil was the supporting substrate. Using ammonia–borane with a hydrogen carrier gas, these authors examined the effects of H_2 content and substrate temperature on the deposit properties of Cu substrate (1105°C). Carrier gas consisting of 500-sccm Ar and 40-sccm H_2 was flowed through the furnace. Raman E_{2g} peak position and width for the hBN monoatomic layer transferred to a SiO_2/Si substrate were 1370 cm^{-1} and 15 cm^{-1}, respectively. Selective area electron diffraction of two different regions of the monolayer showed a rotation angle deviation between grains of 0.7° over a distance of approximately 120 μm of 0.7°. The average lateral length of the nuclei at the point when they began to merge was 40 μm. Since the TEM selected area electron diffraction (SAED) spot size diameter was only 800 nm, the absence of grain boundaries was

Figure 28

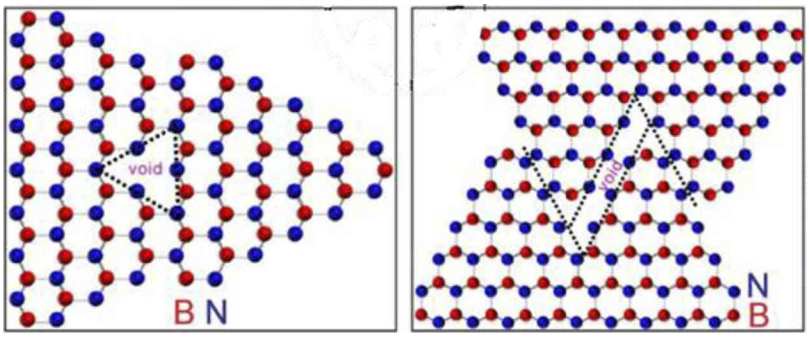

Illustration of two types of defects that may form as areas of hBN deposited on molten metals merge together. Reproduced from [93] with permission from the Royal Society of Chemistry.

confirmed only over small regions, hence the authors refer to the deposit as quasi-single-crystal. The authors note that the 60° in-plane rotation of grains would produce little to no change in contrast in their dark-field TEM images, making them difficult to defect. The types of defects that could form at the grain boundaries are shown in Fig. 28.

To further characterize the crystalline quality of the hBN films, they were etched in hydrogen at 1000°C which delineates the grain boundaries of the merged hBN grains and forms triangular holes at vacancies. Etching preferentially takes place at boundaries where incorrect bonds form such as between atoms of the same element, i.e., as B–B and N–N. These are weaker than the defect-free B–N bonds. All the triangular holes forming within individual grains were aligned in the same direction, indicating nearly single-crystal layers were formed.

3. SPECTROSCOPIES AND ATOMIC IMAGING

3.1. Spectroscopies

Spectroscopy uses the absorption and emission of light to distinguish the phases, the crystal quality, and defect types of boron nitride.

3.1a. Raman and Photoemission Spectroscopies

Raman spectroscopy is one of the simplest characterization tools to distinguish the different crystalline forms of BN. Different from bulk cBN which has Raman peaks at 1057 and 1309 cm^{-1}, corresponding to the transversal optical (TO) and longitudinal optical (LO) modes, respectively [94], hBN has a single Raman peak at around 52 cm^{-1} and 1366 cm^{-1}, corresponding to the shear mode perpendicular to the plane [Fig. 29(a)], and the intralayer mode corresponding to the B–N bond stretching [Fig. 29(b)] [62]. Due to its layered structure, hBN can be exfoliated to produce flakes with different thickness. When thickness increases, the Raman peak of hBN becomes lower in energy but higher in intensity [Fig. 29(c)] [11]. It is important to note that the Raman signal of BN can be very weak if a laser at visible range is used for excitation, and monolayer hBN on Cu foil may not be detectable by Raman spectroscopy. This is due to the low absorption rate of hBN to visible light.

Optical emission spectroscopy, which is commonly used to determine the optical bandgap, also shows differences between hBN and cBN [47]. To initiate an emission, an excitation source has to be applied on the target material. Two kinds of excitation sources are commonly used: laser beam which induces PL or electron beam which

induces CL. A detailed comparison between the two techniques is shown in the following section. In Fig. 30, CL measurements of bulk hBN show an emission peak at 215 nm, trailed by many lower-energy peaks. In contrast, cBN has the highest peak at 203 nm, followed by a very broad band centered at 280 nm. This broad band is attributed to defect emissions. The fine structure of the hBN edge emission will be discussed in detail later in this section.

3.1b. Note on PL and CL

Emission spectroscopies of materials are essential tools for probing the bandgap of semiconductors or insulators. PL uses photons (from laser, LED, lamps, etc.) as the source to excite electrons and create exciton, which later recombines and emits photons. CL, on the other hand, uses high-energy electron beams (usually inside electron microscopes) as the excitation source for the same purpose [95]. There are several major differences between PL and CL.

Figure 29

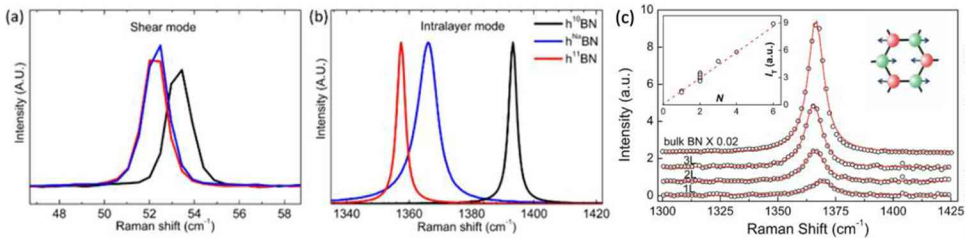

Raman spectra of (a) shear mode, (b) intralayer modes from $h^{10}BN$, $h^{11}BN$, and $h^{Na}BN$ crystals [62], and (c) intralayer modes from different thicknesses of hBN [11]. $h^{10}BN$ and $h^{11}BN$ are isotopically purified hBN with ^{10}B and ^{11}B. $h^{Na}BN$ and hBN represent hBN crystals with natural abundance. Reprinted with permission from Liu *et al.*, Chem. Mater. **30**, 6222–6225 (2018) [62]. Copyright 2018 American Chemical Society, https://doi.org/10.1021/acs.chemmater.8b02589. Gorbachev *et al.*, Small **7**, 465–468 (2011) [11]. Copyright Wiley-VCH Verlag GmbH & Co. KGaA. Reproduced with permission.

Figure 30

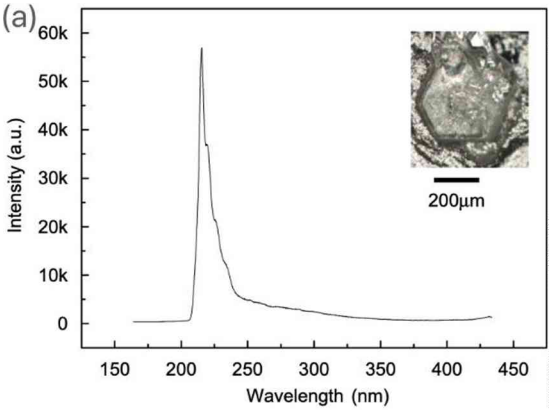

CL spectra of hBN. Reprinted from J. Cryst. Growth **303**, Taniguchi and Watanabe, "Synthesis of high-purity boron nitride single crystals under high pressure by using Ba–BN solvent," 525–529, Copyright 2007, with permission from Elsevier.

- First is on *spatial resolution*. PL is limited by the diffraction limit of light so the spatial resolution is of the order of hundreds of nanometers. CL usually has a much better spatial resolution than PL since the electron beam can be focused to a probe on the order of 0.1–1 nm. The real resolution limit on CL comes from the interaction volume between the electron beam and the materials, which is on the order of tens of nanometers.
- Second is *damage*. PL is usually regarded as a nondestructive method due to the low energy of incident photons. However, it is worth noting that some of the PL measurement could also damage the sample if the light has higher energy leading to ionization of the electrons in the sample. CL, on the other hand, could be destructive and change the lattice structure depending on the beam condition and the measured samples. Electron beam changes the local charging environment and could deposit contamination on top of the sample attracted by the charge.
- Third is the *detectable energy range*. The energy of the excitation source dictates the maximum energy in the emission spectrum. Since electron energies are usually around 1–30 keV, CL can usually be used for probing higher-energy emissions. In comparison, PL is hard for detecting high-energy (>3 eV) range when considering the fact that: (1) easily accessible lasers are normally operated around the visible range (around 2–3 eV); (2) the deep UV lasers are very expensive and usually require a new set of optical components to guide and focus. The high-energy photon sources are commonly from synchrotrons.
- Fourth is on the *momentum transfer* and the allowed transitions. Photons usually have a momentum on the order of 10^{-27} m kg/s. A high-energy electron in an electron microscope can reach 10^{-22} m kg/s. In comparison, the boundary of the first Brillouin zone of a honeycomb-lattice-like graphene or hBN is of the order of 10^{-24} m kg/s, which is three orders of magnitude larger than the momentum of photons but two orders of magnitude smaller than electrons. Therefore, electron beams can induce much more transitions due to the large momentum transfer than photons whose induced transition is usually confined around the Gamma point.
- Fifth is the *number of excitons* generated. An incident photon in PL can generate only one exciton, but a high-energy electron in CL can generate hundreds of excitons at a time [96]. The number of excitons, N, generated by an electron beam with energy E_0, on a semiconductor with a bandgap of E_g, can be estimated by the equation: $N = E_0/3E_g$, assuming that the sample is thick enough to absorb all the incident electrons, and the electron back scattering is neglected [97,98].

Some of the above conclusions are illustrated in Fig. 31. The defect of hBN can be probed by both methods and the emission spectra from PL and CL are usually different due to the different scattering process, where a side-by-side comparison can be found in the work by Hayee *et al*. [99].

3.1c. Bandgap Debate of hBN

The exact band structure of hBN has been a myth to the field for a long time, and there are still ongoing debates on the bandgap and the electronic band structure of hBN.

The controversy comes largely from two factors: the difficulty of calculating the bandgap of insulators from theory, and the everlasting defect emissions and phonon duplicates which look like band-edge emission in experiments.

In theory, the simulation of materials largely relies on density functional theory (DFT) for its reconciliation between accuracy and efficiency. However, DFT does not include

Figure 31

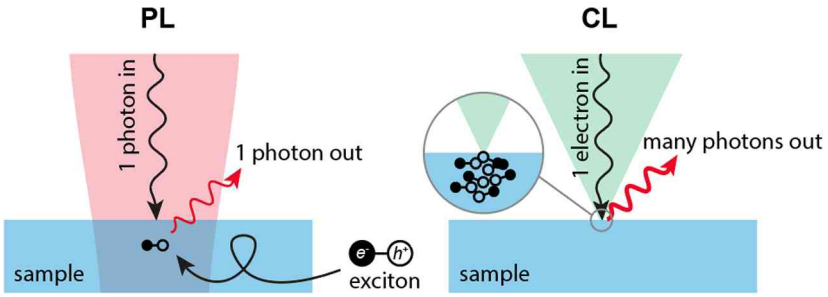

Differences between PL and CL, in spatial resolution, interaction volume, and the generated excitons. Here, we assume the incident electron energy is on the order of kiloelectronvolts. In the case of PL, "1 photon out" captures only the most likely scenario. If there is a downconversion process, there could be multiple photons emitted in PL. In the case of CL, if an electron has an energy on the order of kiloelectronvolts, there are usually more than 100 excitons being excited.

self-energy in the calculation, resulting in an underestimated the bandgap of semiconductors and insulators such as hBN. One way to solve this is to include empirical parameters to manually incorporate the effect of self-energy into the calculation. Many hybrid functional methods such as HSE06 are found to be effective in predicting the bandgap in hBN but it might not be accurate for estimating the energy levels of defects [100]. Alternatively, one can include self-energy by implementing the *GW* calculation that brings the bandgap up to 6.6 eV for a vacuum slab at 10 Å. This method is deemed to be the most accurate in predicting the relative energy levels [101], but the calculation is not without any problems. As can be seen from Fig. 32, the bandgap of hBN is highly dependent upon the thickness of the vacuum slab in between the hBN layers [102]. Unlike PBE and hybrid functional methods which reach a stable bandgap when the vacuum slab is thicker than a threshold, the bandgap of *GW* calculations converges with respect to $1/d$, so to completely rule out the interlayer coupling, the intercept E_{gap} ($1/d = 0$) should be used to represent the bandgap. An alternative is to add truncation in the calculation where the dipole interactions between the layers are forced to zero. For more detail-seeking readers, it should be noted that these *GW*-method-predicted bandgap values are calculated by Kohn–Sham quasiparticles under the single-electron approximation, so no binding energies between an electron–hole pair is included. The exciton energy that accounts for the emission spectra should have exciton binding energy subtracted from the *GW* calculated value. To account for that binding energy between electrons and holes, Bethe–Salpeter equation (BSE) formalism is commonly adopted [103] but the details are beyond the scope of this tutorial.

We will divert a little bit from the value of bandgap and look at the band structure in this part. Apart from the value of bandgap, the band configurations of hBN with various thicknesses are also controversial: one notable debate is among the direct and indirect bandgaps of hBN. We discussed the hardness of determining the bandgap which only deals with the energy degree of freedom, but the band structure, which needs to consider both energy and momentum, is even harder to determine experimentally. For bulk hBN, theory predicts that the electronic band structure has an indirect nature either at Perdew–Burke–Ernzerhof functional local density approximation (PBE-LDA) level [104] or at the *GW* level [105], as shown in Fig. 33. This has been at odds with experimental evidence for decades.

In 2004, Watanabe *et al*. showed that bulk hBN has a strong emission peak at 5.76 eV using CL [28], and hBN was deemed to have a direct bandgap, based on two pieces

Figure 32

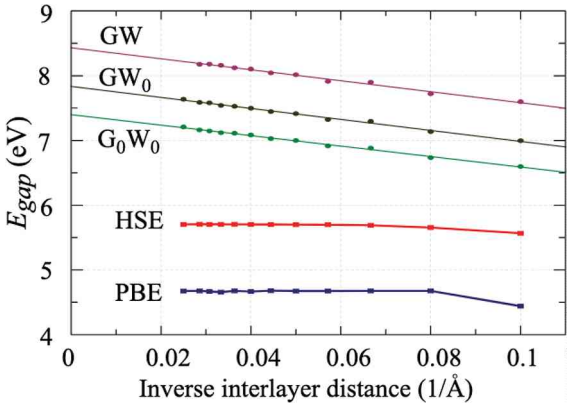

Bandgap value as a function of the inverse interlayer distance. The DFT-PBE and hybrid functional (HSE) are saturated when the distance is above a threshold, while *GW* does not converge should no truncation be applied to annihilate the long-range interaction between the neighbor layers. Figure 4 reprinted with permission from Berseneva *et al.*, Phys. Rev. B: Condens. Matter Mater. Phys. **87**, 035404 (2013) [102]. Copyright 2013 by the American Physical Society.

Figure 33

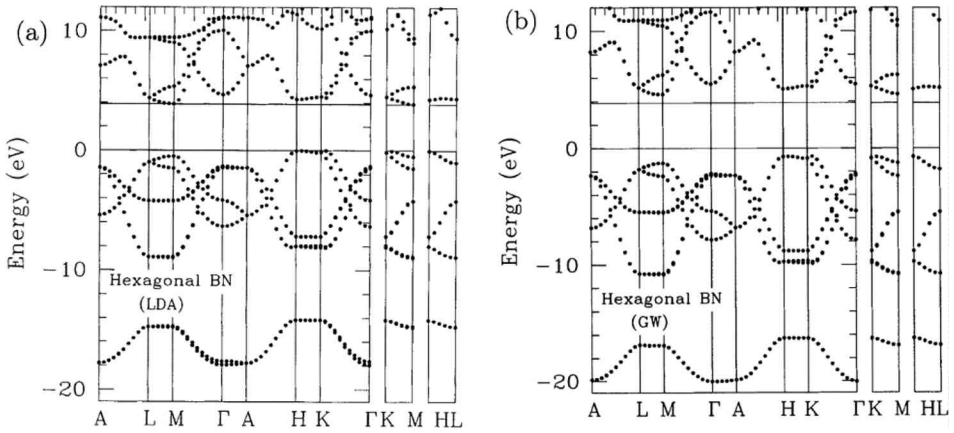

Electronic band structure of bulk hBN under the frame of (a) DFT-LDA and (b) *GW*. Both calculations predict an indirect bandgap for bulk hBN. Figure 2 reprinted with permission from Blasé *et al.*, Phys. Rev. B: Condens. Matter Mater. Phys. **51**, 6868–6875 (1995) [105]. Copyright 1995 by the American Physical Society.

of evidence: (1) the intensity of the emission peak at 5.76 eV is very strong; and (2) the absorption peaks match the signature of the Rydberg energies of an s-orbital-like exciton. Time-resolved PL experiments show that the lifetime of the 5.76 eV peak is 0.75 ns [106], compared with the lifetime of the defect emission in 3.3–4 eV which is around 1–2 ns, longer than the 5.76 eV peak [107]. However, higher-energy peaks with low intensity were discovered later. Cassabois *et al*. found that bulk hBN has an indirect bandgap in a PL experiment: the exciton energy is determined by the highest observable peak at 5.955 eV (Fig. 34), and the peaks at 5.76 and 5.86 eV are assigned to be phonon replicas of this indirect exciton, determined from the temperature-dependent PL measurement [8]. The success of observing the indirect exciton peak in this work is credited to the use of two-photon excitation to get rid of the background emission from the scattering of light.

Figure 34

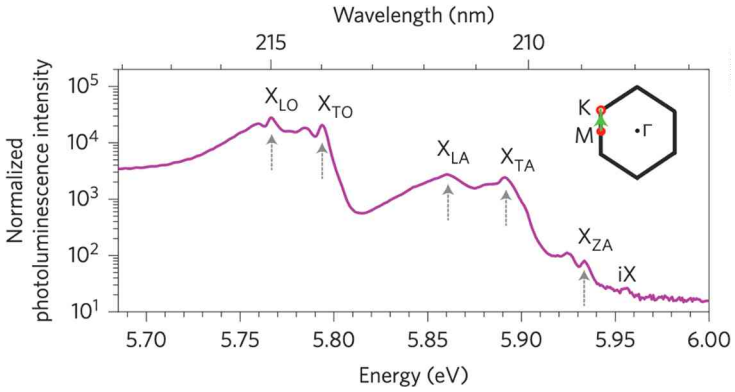

PL spectrum of a bulk hBN excited by two photons at an energy of 3.03 eV. iX indicates the energy position of the indirect exciton, and other peaks marked by arrows (X_{LO}, X_{TO}, X_{LA}, X_{TA}, and X_{ZA}) are the phonon replicas of the iX. Reprinted by permission from Springer Nature: Cassabois *et al.*, Nat. Photonics **10**, 262–266, Copyright 2016.

Figure 35

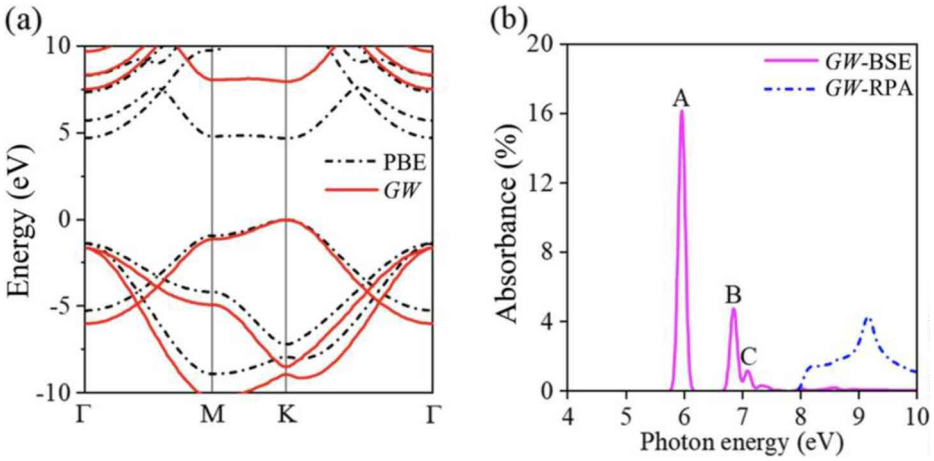

(a) DFT-PBE (dash black) and full-frequency eigenvalue self-consistent GW (solid red) band structures. The top of the valence band is set at 0 eV. (b) Calculated absorption spectrum with (GW-BSE, solid pink) and without (GW-RPA, dashed blue) electron–hole interactions for linear-polarized light. The first three peaks are labeled as A, B, and C, respectively. A Gaussian broadening factor of 100 meV is included. Figure 1 reprinted with permission from Zhang *et al.*, Phys. Rev. Lett. **128**, 047402 (2022) [10]. Copyright 2022 by the American Physical Society.

For monolayer hBN, at DFT-PBE level, the bandgap is predicted to be direct with both the VBM and CBM both located at the *K* point at the reciprocal space. However, the conduction band at the *K* point is shifted up more than that at the gamma point after including the self-energy in the *GW* method, (Fig. 35), turning the direct bandgap into an indirect bandgap with VBM at the *K* point and CBM at the Gamma point [10]. Therefore, GW calculation predicts that all hBN flakes, regardless of its thickness, have indirect bandgaps.

This also contradicts with previous experiment, where Elias *et al.* [9] showed the reflectance and PL spectra of monolayer hBN directly grown above graphite. Their

Figure 36

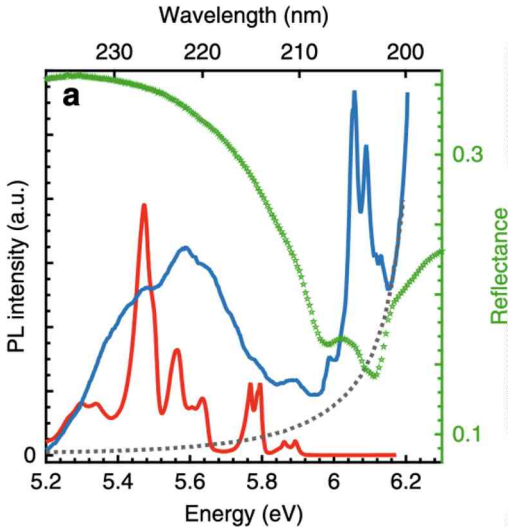

Reflectance and PL spectrum of various types of hBN. The curves are reflectance spectrum of monolayer hBN (green curve), PL spectrum of monolayer hBN (blue curve), PL spectrum of bulk hBN (red curve), and PL spectrum of bare graphite (gray dotted curve). Reprinted by permission from Springer Nature: Elias *et al.*, Nat. Commun. **10**, 2639, Copyright 2019.

data show a coincidence of the highest-energy peaks of PL and reflectance, which, according to the authors, indicates that there is no Stokes shift involved, a signature of direct bandgap (Fig. 36) [9]. One possible origin of the difference might be coming from the substrate effect of graphite, where the lattice mismatch between graphite and hBN creates a Moiré potential on monolayer hBN, modulating the original band structure in reciprocal space. It has been experimentally proven that the electronic properties of a monolayer hBN will be dramatically influenced by the substrate [108]. There is still no experimental data showing the PL spectra of freestanding monolayer hBN because of the difficulty in sample preparation and the low absorption rate of photons by hBN. A freestanding monolayer hBN might be the best sample for proving the intrinsic band structure of the theoretical predictions.

3.2. Atomic Imaging

3.2a. Atomic Imaging and Electron Beam Damaging

Understanding the atomic structure of hBN had been a pivotal task due to the request to understand many structure-related light emission phenomena [109,110]. Early studies of hBN crystal structure utilized x ray diffraction [111], but to resolve the atomic structure of defects, one needs real-space atomic imaging techniques, which falls into the realm of TEM and STM. Imaging the atomic structure of hBN attracts significant interest in quantum optics and nanophotonics since a full understanding of the quantum emitters is based upon a precise understanding of their atomic structures. This turns out to be one of the biggest challenges in the field since: (1) TEM has electron-irradiation damage and creates new defects on-the-fly during imaging; and (2) STM only detects the crystal structure on the surface but defects close to the surface are affected very badly by surface charging.

To understand these challenges, we need to briefly introduce the background of how atomic imaging works in both TEM and STM. TEM is a direct analogy to optical microscopy where the light source is replaced by high-energy electron beams. This

is to overcome the fundamental resolving power of light due to the Abbe diffraction limit: electrons with higher energy have much shorter wavelength (e.g., de Broglie wavelength) than visible photons, usually on the order of picometers, making atom imaging possible. The image signal (or contrast to be more precise) is generated by the Coulomb interaction between the negative-charged electrons and the positive-charged nuclei of atoms, which is usually called "elastic scattering" in particle physics. STM, on the other hand, uses a biased metal probe to scan the tunneling current across the sample surface, whose contrast depends on the distance between the atom at the tip front and the atoms on the target materials (an alternative STM contrast is measure the height of the tip while maintaining the tunneling current constant). However, there are significant differences between TEM and STM characterizations. Since STM relies on the tunneling current between probe and the surface of material, where the current decreases exponentially with respect to larger distance, the probe needs to be close to the conducting layer. The STM contrast will be brighter where there are higher electron densities. Therefore, the lattices that appear on STM images do not represent atoms but, instead, the electron distribution on the surface. In comparison, TEM directly visualizes atomic layout, but the image is a projection of atomic lattices to the screen parallel to the electron path (with very thin samples).

To image semiconductors and insulators, both STM and TEM face some problems. STM cannot generate a tunneling current on an insulator or semiconductor (like hBN), so an extra "auxiliary" thin conducting layer needs to be placed in contact. Usually, a monolayer of graphene is used for such purposes [112]. In TEM, the electron-irradiation damage comes from two parts: knock-on damage and the effect of radiolysis. Knock-on damage comes from an electron–nucleus scattering process where the direct energy and momentum transfer from high-energy electrons to the atoms. Radiolysis (chemical bond breaking after ionization) comes from electron–electron scattering processes, where high-energy electrons excite the electrons in crystals and ionize the atoms. Since the atoms are bonded through the electrons, a transition from bond to antibond or the loss of electrons through ionization may decouple the atoms. A higher electron energy usually leads to a more severe knock-on damage, but to mitigate the effect of radiolysis, a higher electron energy is actually preferred, especially when the sample is a semiconductor or insulator [113]. Another parameter that can mitigate the electron-beam damage is the electron flux density.

During imaging using high-energy electron beams inside TEM, the damage caused by the electrons is mainly due to two parts: knock-on damage and the effect of radiolysis.

Knock-on damage comes from the direct momentum and energy injection of high-energy electron beams, which is usually noted as "elastic scattering." When high-energy electrons from TEM come close to the atoms, momentum and energy can be transferred by the Coulomb interaction from the *negatively charged* high-energy electrons to the *positively charged* nuclei of atoms. When the electron trajectory is close enough to the nuclei, the energy transferred to the nuclei passes the minimum energy of knocking out an atom inside the crystal lattice where the chemical bonds are not strong enough to hold the atom at its original place. This minimum energy of high-energy electrons needed for knocking out an atom is called "displacement threshold." The energy that is transferable from the high-energy electron to an atom, E, is described as follows:

$$E = \frac{\tilde{E}_e(\tilde{E}_e + 1.02)}{496A}\sin^2\frac{\psi}{2},$$

where $\tilde{E}_e$ is the incident electron energy, A is the atomic mass number of the atom (e.g., $A = 12$ for carbon atoms), and ψ is the scattering angle of the electron ($\psi = 0$

Figure 37

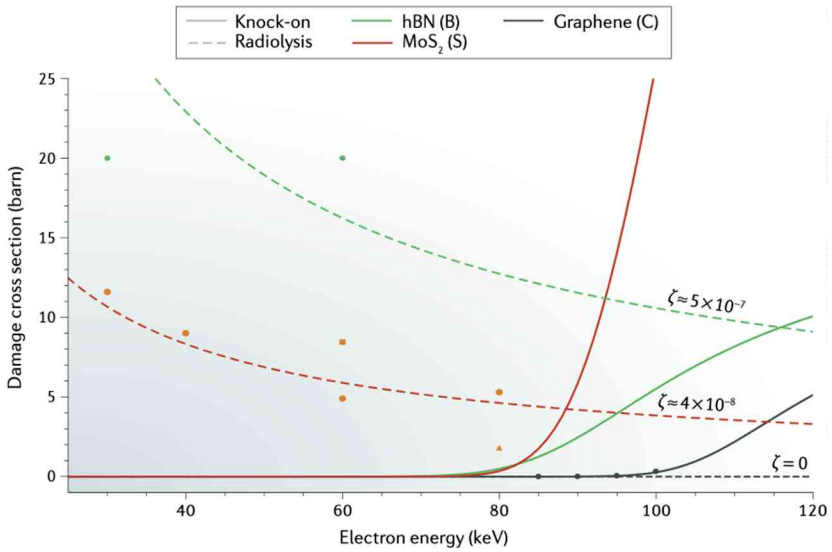

Electron-beam damage cross section of three representative monolayer materials in metal (graphene), semiconductor (MoS_2), and insulator (hBN). The knock-on damage (solid lines) has a clear reversed trend with radiolysis (dashed lines). The more insulating the material is, the more prominent the radiolysis effect is. Reprinted by permission from Springer Nature: Susi *et al.*, Nat. Rev. Phys. **1**, 397–405, Copyright 2019.

for no interaction and $\psi = 180°$ for complete back scattering). For an electron with certain energy $\tilde{E}_e$, the smaller the atom (the less A is), the higher E is.

Radiolysis comes from the ionization caused by the high-energy electrons. Different from the knock-on damage which is the interaction between TEM electrons and nuclei of atoms, radiolysis comes from the interaction between the TEM electrons and crystal electrons. When a high-energy electron of TEM traverses through the material, it creates an electromagnetic field acting as a perturbation to the crystal system. This perturbation may cause an excitation of an electron, that is, a resonance of electron hopping between two energy levels. This effect leads to a less stable atomic configuration which could result in damage.

A comparison between the effect of knock-on damage and radiolysis effect can be seen in Fig. 37.

In 2009, three research groups published results on using TEM and scanning transmission electron microscopy (STEM) to image the atomic structure of hBN [2,114,115]. They observed that B vacancies are always the defects created prior to N vacancies due to electron-beam damage. This result, as expected from theory, comes from the fact that B atom has a lighter mass than N atom, so more energy is transferred from high-energy electrons to B than N.

As seen from Fig. 38, when the electron beam is parked on the sample for a certain period, defects start to grow on the hBN sample. The defects are found to be starting from a B atom, and gradually extend into a triangle pointing in the same direction [Fig. 38(a) and (b)]. For a multilayer hBN sample, the layer at the bottom side is being peeled off first, and the atoms at the upper layer then start to disappear. This layer-by-layer peeling provides a method for creating a monolayer hBN inside TEM. A closer investigation of the boron vacancies shows that there is a lattice distortion around the boron vacancies [Fig. 38(c) and (d)]. When the temperature

Figure 38

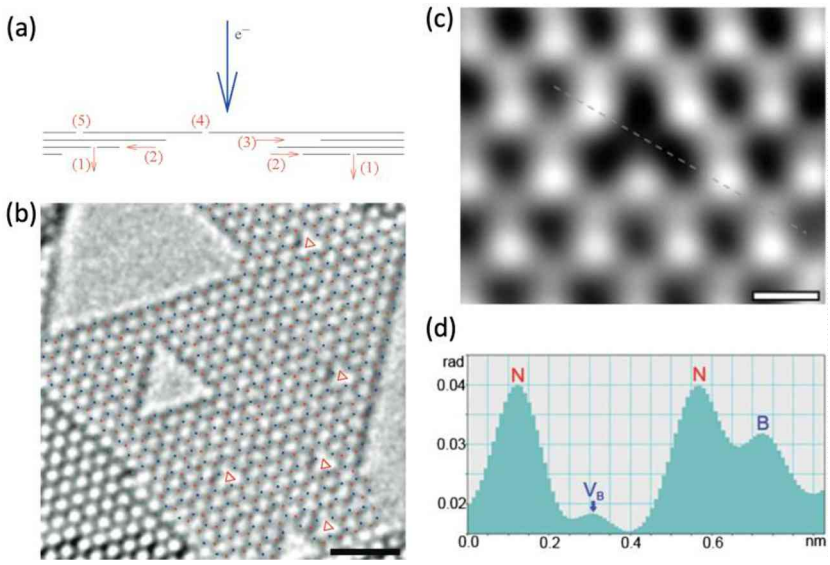

Electron-irradiation damage on hBN. (a) Schematic process of the electron-beam irradiation process used for layer-by-layer etching. (b) High-resolution TEM image of boron vacancies, and the expanded voids from those vacancies. The red triangles represent the locations of voids. Scale bar: 1 nm. (c) Enlarged exit-wave reconstructed image of a single boron vacancy (scale bar: 2 Å), with (d) the intensity profile showing the species of each atom. Figures 3(a) and 3(b) reprinted with permission from Jin *et al.*, Phys. Rev. Lett. **102**, 195505 (2009) [114]. Copyright 2009 by the American Physical Society. Reprinted with permission from Meyer *et al.*, Nano Lett. **9**, 2683–2689 (2009) [115]. Copyright 2009 American Chemical Society, https://doi.org/10.1021/nl9011497.

is raised, the dynamics of defect formation of hBN changes [116]. As can be seen from Fig. 39, when heated up to 900°C, the electron-irradiation-created void becomes a hexagon or parallelogram, instead of the triangles created at room temperature. Their DFT calculation shows that hexagonal defects are more stable than the triangular defects for small sizes ($n < 10$, where n is the number of atoms on all edges of the defect). Compared with graphene which usually has irregular shape voids under electron-beam irradiation, this controllable void formation in hBN leads to hopes that these nanopores could be used for various applications such as DNA sequencing or nanopower generators [117]. However, many of these applications are based upon the assumption that these nanopore systems are stable and do not change in shapes in ambient or ion-rich liquid conditions, which is found to be not entirely true [118]. The nanopores are merged or split, even exposed to air for only 1 hour, and the edges of nanopores change shape and get oxidized (Fig. 40). Therefore, more techniques to preserve the shape of nanopores are required when utilizing the nanopores of hBN.

The first atom-by-atom chemical analysis of hBN was completed in 2010 by Krivanek *et al.*, using an annular dark-field (ADF) technique inside STEM (Fig. 41) [119]. Since the intensity of the atoms are proportional to the atomic number (Z) of elements, the category of each atom can be distinguished simply by the intensity of each atom in ADF images. For low-Z elements (which applies to B and N), the ADF intensity is proportional to $Z^{1.64}$ [119]. The mapping of electric fields of hBN at atomic level was also made possible by measuring the deflection of the electron beam due to the electric

Figure 39

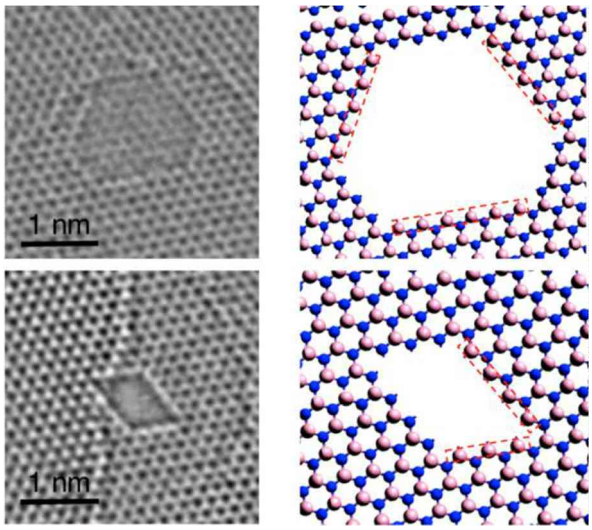

Different shapes of electron-irradiation-induced defects in hBN at 900°C (left column) and their corresponding atomic structure (right column). Reprinted with permission from Pham *et al.*, Nano Lett. **16**, 7142–7147 (2016) [116]. Copyright 2016 American Chemical Society, https://doi.org/10.1021/acs.nanolett.6b03442.

Figure 40

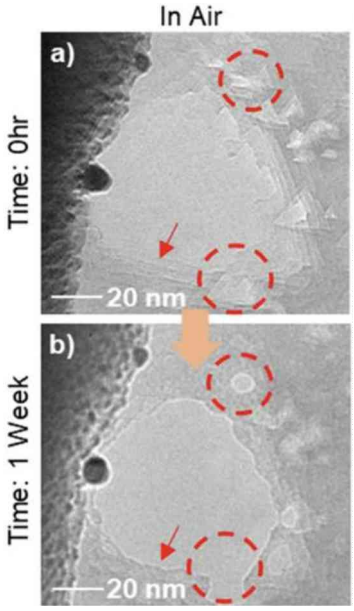

Evolution of hBN defects and nanopores in air, with TEM images taken on the defective area before air exposure (top), and another image taken after air exposure for a week (bottom). Reprinted with permission from Springer Nature: Dai *et al.*, Commun. Chem. **6**, 108, Copyright 2023.

dipoles inside STEM [120]. These dopants and defects are of particular interest due to their possible application in quantum information science which is discussed in detail in Section 5. Understanding the charge distribution and possible local doping of a defect is very critical as it changes the emission behavior of the defect. By measuring the center of mass of the electron beam, STEM is capable of measuring the local

Figure 41

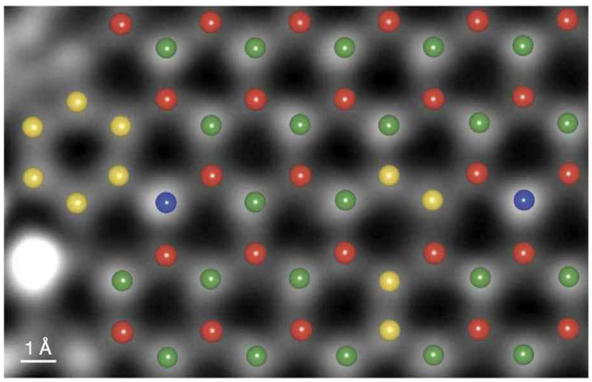

Atomic structure of hBN overlaid by the species of atoms labeled in different colors. The ball model is from DFT simulation of a single BN layer containing the experimentally observed substitutional impurities. Color coding: red, B; yellow, C; green, N; blue, O. Reprinted with permission from Springer Nature: Krivanek *et al*., Nature **464**, 571–574, Copyright 2010.

Figure 42

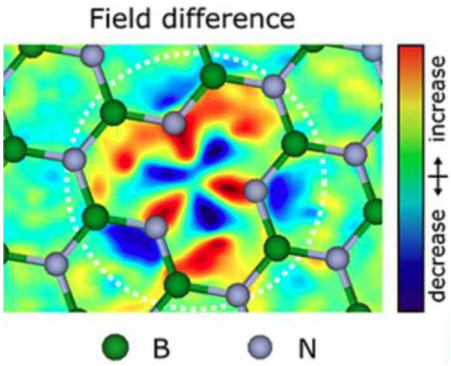

Electric field difference of a boron vacancy in hBN when compared with a pristine hBN. Reprinted with permission from Cretu *et al*., ACS Nano **15**, 5316–5321 (2021) [120]. Copyright 2021 American Chemical Society, https://doi.org/10.1021/acsnano.0c10849.

electric field in atomic resolution. From Fig. 42, we can see that the electric field change of a B vacancy in hBN is mostly confined around the defect. The precise measurement of the charge transfer can be done using holography inside TEM [121], but it requires a special biprism installed in the microscope.

As a comparison, STM is a nondestructive atomic imaging method. However, the image contrast of STM relies on the tunneling current so a conducting surface is required for the target materials, and it has been hard to image hBN due to its insulating state. Wong *et al*. showed that by capping hBN with a monolayer graphene, the STM signal can reveal the electronic distribution changes of graphene due to the influence of hBN underneath (Fig. 43) [112]. The charge states of the defects can be manipulated by applying a pulse through the STM tip to inject or extract electrons locally. The disadvantage of the STM contrast is that the precise atomic structure cannot be resolved, due to the fundamental mechanism of how an STM image is generated, which is discussed in the next section.

Figure 43

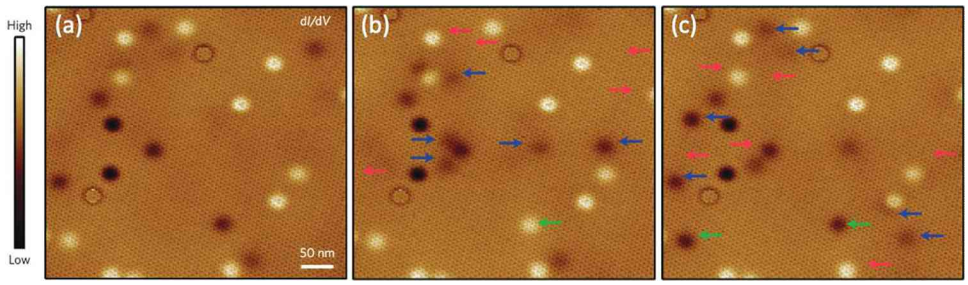

STM imaging and manipulation of the defect in hBN. The dI/dV map of the graphene/hBN system with (a) the original STM contrast of the system, (b) the STM contrast after a tip pulse is applied to the center of the defect to change the charge states of the defects, and (c) the STM contrast of the same region with a second tip pulse applied. Reprinted with permission from Springer Nature: Wong *et al.*, Nat. Nanotechnol. **10**, 949–953, Copyright 2015.

3.2b. Comparison between TEM/STEM and STM

As discussed above, both TEM/STEM and STM can be used for resolving and controlling the atomic features in hBN. However, there are many differences and complementary capabilities between these techniques.

- *The energy regime of spectroscopy*. The scanning tunneling spectroscopy (STS) in STM covers a lower energy range than TEM/STEM. The biasing voltage that is normally applied on an STM tip is on the order of 1–10 eV, which can form a dI/dV plot reflecting the local density of states. The energy resolution of STM can be better than 10 μeV at low temperature [122] so it can measure the defect states inside the bandgap at very high precision. EELS in TEM/STEM, on the other hand, covers a higher energy regime of the order of several electronvolts to hundreds of electronvolts. EELS can usually be used for measuring the bandgap and the plasmon modes of the crystal, and the core electron signatures of atoms which can be used for atomic mapping. The fine structure of the core electron can also be used for distinguishing the chemical environment of the atom [123]. The best energy resolution in EELS is sub-10 meV achieved by the monochromatic electron source [124].
- *Sample damage*. STM is a nondestructive imaging method that does not change the atomic structure of crystal lattices, even though it can move the adsorbed atoms on the surface using its tip [125]. TEM/STEM can lead to electron-irradiation damage on the crystal as discussed above.
- *Sample requirements*. STM requires a conducting surface whereas TEM/STEM can accept both conducting and insulating samples. The sample for STM is usually placed on top of a conducting substrate, whereas the sample for TEM/STEM is required to be freestanding and as thin as possible (ideally thinner than 100 nm).

Sometimes, TEM and STEM are also used interchangeably by mistake. A summary of the difference between TEM, STEM, and STM is given in Fig. 44.

4. HYPERBOLIC PHONON POLARITON

4.1. Optical Properties of hBN

The application of hBN (both thin and bulk) has to be discussed in the context of frequency ranges, as it has dramatically different properties in different spectral regimes.

Figure 44

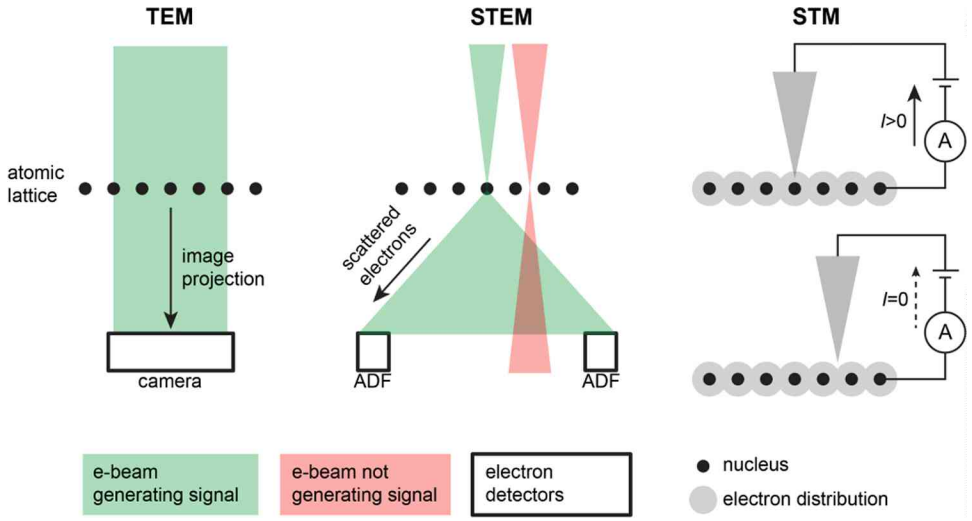

Operating schematics of TEM, STEM, and STM. ADF, annular dark field; e-beam, electron beam. (Left) Mechanism of TEM. The *parallel* electron beam projects the image of an atomic lattice to the camera. (Middle) Mechanism of STEM. The *focused* electron beam scanning across the atomic lattice gets deflected by nuclei when the beam aligns with an atom. The ADF detector captures the scattered electrons. (Right) Mechanism of STM. A metal probe is scanning across the surface of atomic lattice, and the current is generated by the tunneling current. Stronger signal means a stronger local density of states of electron. This is only one of the operation modes of STM (measuring current at fixed height).

The application of hBN in the visible and near-IR (~400–2000 nm) is mainly for encapsulation or serving as a host of SPEs, which is covered in Section 5. In the midwave to longwave IR (3–14 μm), the use of hBN is normally linked to the properties induced by the optical phonons, which is covered in this section. Importantly, regardless of the frequency range, in-plane and out-of-plane optical properties of hBN are distinct, resulting in a strong birefringence [29].

In the visible and near-IR range, hBN behaves as an optically dielectric material, due to the absence of free carriers and its wide bandgap. Therefore, in the near-UV and visible frequency range below the bandgap (5.95 eV [8]), the refractive index of hBN can be modeled with Sellmeier's equation like other transparent materials and semiconductors. The equation can be written as

$$\varepsilon = 1 + \frac{A\lambda^2}{\lambda^2 - \lambda_0^2}, \tag{4.1}$$

where λ is wavelength, and the parameters λ_0 and A are the energy and strength of the oscillator, respectively. Here λ_0 is 164 nm according to [126]. As a consequence, the optical permittivity of hBN in the near-IR (1–2 μm) is nominally nondispersive, i.e., optical property does not change with frequency, with dielectric permittivity values of ~6.95 in-plane and ~4.95 out-of-plane. Benefitting from the van der Waals structure of hBN, it can be stacked on and below different materials, and the chemical inertness makes hBN an excellent encapsulant material for other 2D materials, e.g., black phosphorus [127] and graphene [128], and hBN in this context mainly serves as a spacer that can be conveniently stacked with other materials. In the context of optical resonator design between 400 and 2000 nm free-space wavelength, many

design strategies developed on other dielectric materials can be used, giving rise to the potential for anisotropic so-called Mie resonators for metasurface designs [129].

In the midwave and longwave IR (3–14 μm), the optical properties of hBN become more complicated due to the IR active optical phonons and the anisotropic hexagonal crystal structure. Phonons are coherent atomic lattice vibrations in crystalline materials, and they can be classified into optical and acoustic phonons. Typically, acoustic phonons are critical to thermal transport properties while optical phonons in polar crystals, which have much higher vibrational frequencies, give rise to IR active modes. For optical phonons, the displacements of the two atoms are in opposite directions, and they exhibit longitudinal and transverse modes. While the TO phonon corresponds to lattice vibrations perpendicular to the propagation direction at the frequency ω_{TO}, the LO phonon corresponds to lattice vibrations along the propagation direction at frequency ω_{LO}. In polar materials such as hBN, the TO and LO phonon frequencies are split, with LO phonon frequency shifted to a higher range. The TO phonons possess a net polarizability that enables a strong interaction with light. This results in the real part of the dielectric permittivity becoming negative, indicative of a highly reflective spectral band between the TO and LO phonons, and this is referred to as the Reststrahlen band [129,130]. Mathematically, the permittivity of hBN in the mid-IR can be described by the TO–LO model [13]:

$$\varepsilon(\omega) = \varepsilon_{\infty}\frac{\omega_{LO}^2 - \omega^2 - i\gamma\omega}{\omega_{TO}^2 - \omega^2 - i\gamma\omega}, \tag{4.2}$$

where ω_{TO} and ω_{TO} are the phonon frequencies, and γ is the damping. Note that the TO and LO phonon frequencies of hBN in the in- and out-of-plane crystal axes are different. Thus, in the frequency range where the real part of the in-plane permittivity is negative (positive), the values for the out-of-plane direction are positive (negative). This inversion in the sign of the real part of the dielectric tensor is referred to as hyperbolicity [131]. For hBN, due to the off-set of phonon frequencies, there are two hyperbolic bands, as shown in Fig. 45. Note that the large permittivity amplitude also associatetes with the imaginary part of the permittivity, as indicated in Eq. (4.2). The imaginary part of the permittivity tensor contributes to the loss of the optical mode and/or polariton propagation length as discussed in the following subsections.

4.2. Light Propagation within Dielectric and Hyperbolic Materials

With the optical properties of hBN in mind, we now discuss hBN polariton-based nanophotonics in the mid-IR regime, which are mostly based on the phonon polaritons supported in hBN. The introduction and explanation of hyperbolic phonon polaritons (HPhPs) are organized in such an order. (1) We first review the light propagation behavior in "normal" dielectric materials, e.g., vacuum and silicon. (2) We then discuss the formation of polaritons, i.e., light propagation at the surface of isotropic materials with negative permittivity, e.g., metal. (3) With those foundations, we discuss the nature of HPhPs supported in hBN in a semi-infinite fashion. (4) We discuss the propagation of HPhPs in a finite-thickness hBN. (5) We summarize the meirts and disadvantages of HPhPs in hBN and related applications.

4.2a. Light Propagation in Dielectric Materials

Before diving into the complicated polaritonic behavior of hBN induced by the hyperbolicity, we first discuss the concept of an isofrequency contour (IFC) and light propagation in dielectric materials. For light propagating within a medium, we can

Figure 45

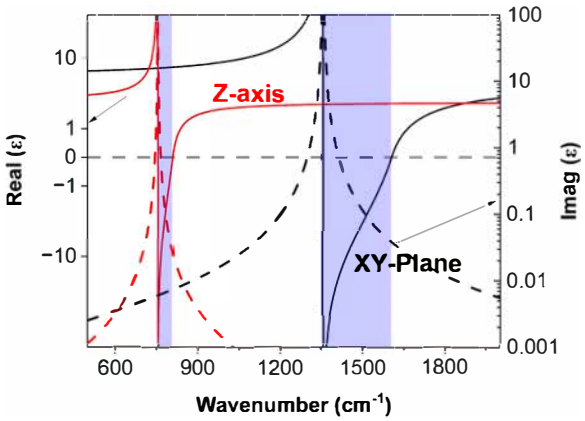

Dielectric functions of hBN. The real parts of the permittivity in the in- and out-of-plane directions are opposite in two frequency ranges: ~750–825 cm^{-1} and ~1360–1610 cm^{-1}. They are typically referred to as type I band (lower Reststrahlen band) and type II band (upper Restrahlen band) throughout the literature. The real and imaginary parts of the permittivity are plotted as solid and dashed curves, respectively. The permittivity model is based on [13].

use the wave equation to describe the electric field change with propagation distance:

$$E(r) = E_0\, e^{-ik\cdot r}, \tag{4.3}$$

where $\mathbf{r} = (x, y, z)$ is the position vector. Thus, when the propagation wave vector (k) is a real value, the electric field is an oscillating sinusoidal wave with no decay. The imaginary part of wave vector represents loss or gain based on the sign, and the electric field (light amplitude) will decrease or increase through propagation. If the wave vector does not contain a real part, then it is called an evanescent wave since it only decays instead of propagating.

For light in an isotropic dielectric (e.g., air), the wave vector follows the equation

$$k = k_0 \cdot \sqrt{\varepsilon} = k_0 \cdot n, \tag{4.4}$$

where k_0 is the wave vector (momentum) of light in free space, and the permittivity of material (ε) is identical in all directions.

4.2b. Note on Isofrequency Curve and Dispersions

For a given frequency of light, i.e., energy of the photons, the wavelength of light propagating within material can be different based on the refractive index. For instance, the wavelength of light in water is smaller than wavelength of light in air, even the photon energy is not changed. The definition of a couple of interchangeable concepts are listed here.

1. *Photon energy*: the energy of one single photon. It is an intrinsic property of light, and it is conserved in most cases, i.e., photon energy does not change. In some cases, e.g., nonlinear processes, it could be changed. In this section, it is always conserved and does not change. Terms 1–4 here are all interchangeable and they all represent the intrinsic properties of light.
2. *Frequency of light*: how many wavelengths pass by a fixed point in 1 second. It is an interchangeable unit with photon energy, and it is also conserved in most cases.

Figure 46

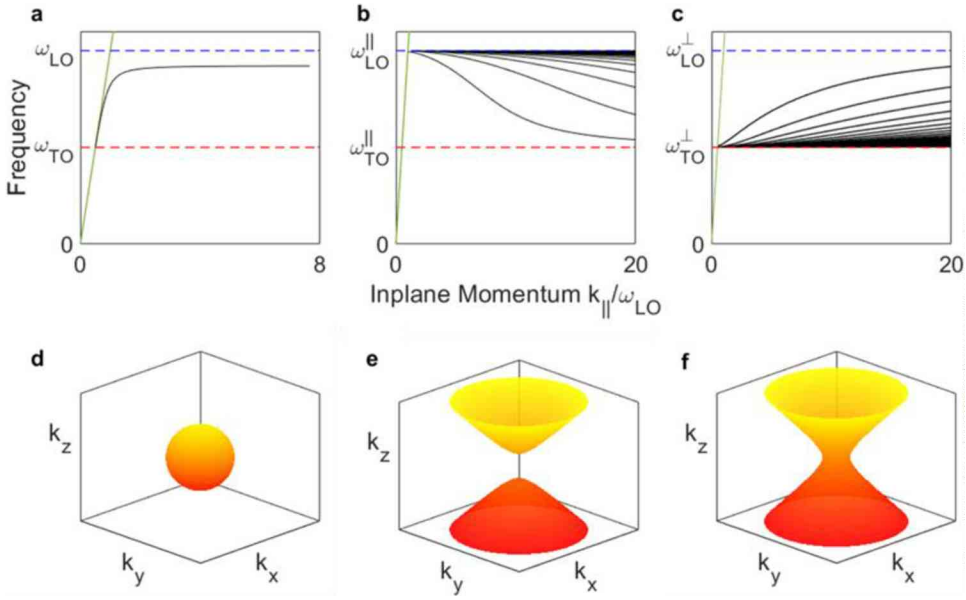

Isofrequency surfaces and dispersion plots of different materials. (a) Dispersion of an isotropic polar material, where surface phonon polaritons are supported with the TO and LO phonon frequencies. (b), (c) Dispersion of type I and II HPhPs, respectively. (d) Isofrequency surface of isotropic dielectric material. (e), (f) Isofrequency surfaces of type I and II hyperbolic materials, respectively. Reprinted with permission from He *et al.*, ACS Photonics **9**, 1078–1095 (2022) [132]. Copyright 2022 American Chemical Society, https://doi.org/10.1021/acsphotonics.1c01486.

3. *Free-space wavelength*: the periodicity of an electromagnetic wave when it is propagating within vacuum.
4. *Free-space wave vector* (k_0): the wave vector of light when it is propagating within vacuum. Term 4 is basically the inversion of term 3, and it can be conveniently be plugged into the wave equation (Eq. (4.3)) to describe the electric field change along the propagation distance.
5. *Wavelength and wave vector in material*: same as the definition of term 3 and 4, except that they describe the light behavior when it travels within a material. The wave vector can be calculated by

$$k = k_0 \cdot \sqrt{\varepsilon} = k_0 \cdot n.$$

For any material system, the wave vector of light traveling within it can be described by the above equation. Note that the refractive index (n) of a material is not necessarily a constant at all frequencies, and it actually varies with frequency as mentioned in the introduction. The frequency-dependent material optical permittivity (refractive index) is referred to as material dispersion. On the other hand, optical dispersion is to describe the relationship between wave vector and free-space wave vector at different frequencies (or free-space wave vectors).

At any given frequency, the free-space wave vector is a given constant. If the material is anisotropic, i.e., the refractive index (n) varies with directions, then the wave vectors also vary with directions. To describe this property, one can plot all wave vectors along all directions as a contour, which is referred to as an IFC. as shown in Fig. 46(d).

As such, while the wave vector is dependent on the frequency of light, it is also dependent on the propagation direction. For isotropic systems, the characteristics are identical along different directions so we only need to plot the wave vector versus frequency, which is called dispersion plot. One can also choose a frequency and plot a slice of an IFC at a specific plane instead of plotting a three-dimensional (3D) surface. For an isotropic medium, e.g., vacuum, the IFC is a sphere, and the light propagation along any direction exhibits identical properties. For birefringent materials, e.g., calcite, the IFC becomes elliptical, and the wave vectors along at least one of the directions is different.

4.2c. Polaritons Supported at Metal–Dielectric Interfaces

While materials with positive Re(ε) can support light propagation and refraction within the material, for materials exhibiting a negative Re(ε), light cannot penetrate or propagate within them. When Re(ε) is negative, the wave vectors becomes imaginary (Eq. (4.4)). Therefore, the waves are not propagating within the material (Eq. (4.3)), as the waves decay exponentially during propagation. Instead, optical modes can be supported provided part of the energy does not reside inside the material; that is, the mode exists as an evanescent field confined to the surface or interface with an adjacent dielectric. As this results from strong coupling between light and coherently oscillating charges, surface polaritons are mostly light-like at lower frequencies, as indicated by the coincidence of the light line with polaritonic dispersion (see Fig. 46(a), where the green and black curves converge near the red dashed line) transitioning to higher momenta (shorter wavelengths) associated with a more charge-like response as the frequency increases [black curve toward blue dashed line Fig. 46(a)]. While the negative permittivity of noble metals comes from the excess free carriers, similar effects arises in doped semiconductors, as well as in polar materials due to atomic vibrations, leading to negative permittivity between TO and LO phonon frequencies, resulting in the aforementioned Reststrahlen band.

4.2d. Note on Polaritons, Polariton Wave Vectors, and Polariton Wavelength

Polaritons are commonly described as light–matter hybrid quasiparticles. Therefore, they inherit their attributes from both their light and matter components. In the case of surface polaritons, the propagating surface waves are oscillating fields between the dielectric environment and the oscillators (e.g., phonons for surface phonon polaritons), as shown in Fig. 47. Those waves are exhibiting quasi-light and quasiparticle properties and are referred to as polaritons.

Note that the wave vectors within an isotropic material along different directions must satisfy the equation:

$$k_x^2 + k_y^2 + k_z^2 = k^2,$$

where k is the wave vector supported within the material, which is k_0 for vacuum. Since k_{x-y} in the SPPs are larger than k_0, k_z becomes imaginary, which is evanescently decaying, as shown in Fig. 47.

In the case of polaritons, the light frequency (or the free-space wavelength) is not changed, and what is changed is the wave vectors of the polaritons. The polariton wave vectors describe the spatial periodicity of electric field oscillation (Eq. (4.3)), and a larger wave vector implies smaller periodicity. The spatial periodicity of the polariton electric field is also referred to as the polaritonic wavelength, so that it may be differentiated from the free-space wavelength, which is determined by the energy of the photons.

Figure 47

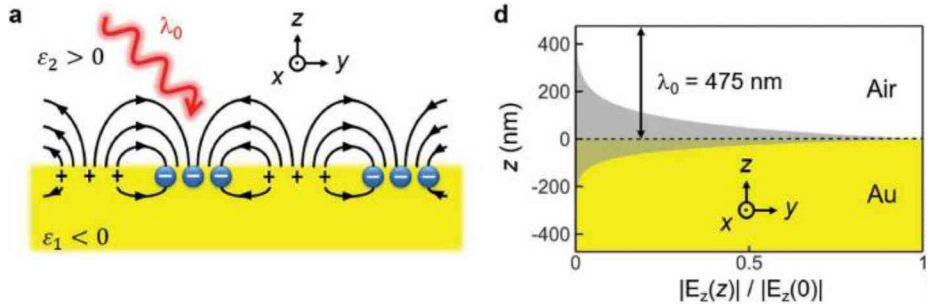

SPPs in noble metals. (a) Schematic of SPPs. The hybridization between incident photons (red arrow, wavelength λ_0) and electron collective oscillations results in propagating electromagnetic waves confined at the interface of metal ($\varepsilon_1 < 0$) and dielectric ($\varepsilon_2 > 0$). (b) Real (blue) and imaginary (red) part of the permittivity of Au. Hu *et al.*, Adv. Opt. Mater. **8**, 1901393 (2020) [133]. Copyright Wiley-VCH Verlag GmbH & Co. KGaA. Reproduced with permission.

4.2e. Propagation Characteristics of Polaritons in Hyperbolic Media

For hBN, the lattice structure (polar covalent bonds in-plane and van der Waal forces out-of-plane) determines that the phonon energies are different and within the two Reststrahlen bands opposite in sign (Fig. 45). Thus, we can mathematically define the IFC of hBN by the following equation:

$$\frac{k_x^2 + k_y^2}{\varepsilon_z} + \frac{k_z^2}{\varepsilon_{x,y}} = k_0^2, \tag{4.5}$$

where k_x, k_y, and k_z are wave vectors along the x, y, and z axes, respectively, and $\varepsilon_{x,y}$ and ε_z are permittivity along the xy plane and z axis, respectively. Dictated by this equation, the IFC of hBN within the two Reststrahlen bands feature hyperbolic shapes, as shown in Fig. 46(b) and (c). Since $\varepsilon_{x,y}$ and ε_z are opposite in sign, the isofrequency equation indicates that infinitely large wave vectors can be supported within hyperbolic media when loss is not taken into account.

The implication of such a hyperbolic IFC is that the polaritons within the material can only propagate at a defined angle at a given frequency when large wave vectors are considered. This frequency-dependent propagation angle is the basis for the hyperlens, whereby an object, e.g., a metal disk, can excite HPhPs via scattering incident light, which will then propagate through the hyperbolic medium at the frequency-defined angles calculated by Eq. (4.5). Therefore, when HPhPs are probed on the top of hBN, an enlarged image of the underlying object will be observed [Fig. 48(b, c)], as demonstrated by Li *et al.* [134] and Dai *et al.* [135]. However, the enlarged image is normally convoluted with overlapping rings together, especially when objects are closely spaced, as shown in Fig. 48(c), making it problematic to resolve the objects underneath hBN. He *et al.* demonstrated an algorithm to reconstruct the object image from under the hyperbolic medium, using only the dielectric function of the material and the collected hyperlense field profile [e.g., Fig. 48(b) and (c)] to overcome this challenge [136].

4.2f. Volume-Confined HPhPs

While the IFC helps understand the ray propagation behavior within hBN, it is under the assumption that hBN is infinitely thick. For a finite-thickness hBN material, HPhPs can be supported, and they are confined within the hyperbolic medium. Note that

Figure 48

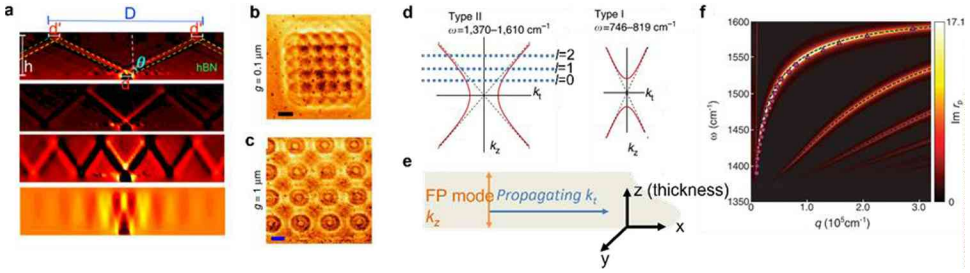

HPhPs supported in hBN. (a) Simulated field profiles of propagating HPhPs in a hBN slab. The working frequencies from top to bottom are 1433, 1500, 1560, and 1600 cm^{-1}, respectively. (b), (c) Near-field amplitude images of arrays at 1430 cm^{-1}, with array periods of 0.1 and 1 μm, respectively. (d) Isofrequency curve of hBN in the upper and lower Reststrahlen band. (e) Schematic of the volume-confined HPhPs. (f) Dispersion plot of HPhPs supported by hBN. Panel (a) is reprinted with permission from He *et al.*, Nano Lett. **21**, 7921–7928 (2021) [136]. Copyright 2021 American Chemical Society, https://doi.org/10.1021/acs.nanolett.1c01808. Panels (b) and (c) are reprinted with permsion from Springer Nature: Li *et al.*, Nat. Commun. **6**, 7507, Copyright 2015. Panels (d) and (e) are reprinted with permission from Springer Nature: Dai *et al.*, Nat. Commun. **6**, 6963 (2015). Panel (f) is from Dai *et al.*, Science **343**, 1125–1129 (2014). Reprinted with permission from AAAS.

the HPhPs do not propagate outside of hBN, leading to the vivid ray propagation picture shown in Fig. 48(a). This ray propagation is very similar to guided modes in dielectric slabs: they are both propagating within the slab with a defined angle, and they experience phase shifts when reflecting at the top and bottom boundaries, similar to Goos–Hänchen shift.

Dai *et al.* explained the similarity between HPhPs and waveguiding in [135]. For hBN, the IFC is a hyperbolic shape as shown in Fig. 48(d) and (e). When the thickness of hBN is finite, the k_z components of the guided modes are quantized to

$$k_{z,l} = (\pi/d)(l + \alpha), \tag{4.6}$$

where d is the thickness of hBN and l is modal order (nonnegative integers). Here α (in general, ω-dependent) quantifies the phase shift acquired at the total internal reflection (TIR) from the slab surfaces. Thus, for a given thickness of hBN, only a set of k_z can be supported in the system. Since the relationship between k_z and $k_{x,y}$ are already fixed by the IFC (Eq. (4.4)), only quantized $k_{x,y}$ values can be supported. Notably, due to the hyperbolic IFC, infinitely large k_z can be supported in the system in the absence of loss. As such, every allowed k_z would lead to a corresponding allowed $k_{x,y}$, and numerous HPhP modes can be supported simultaneously at each single frequency, as shown by the multiple branches of the dispersion relationship for hBN in the upper Reststrahlen [Fig. 48(f)]. Mathematically, the HPhP mode wave vector can be written as

$$k(\omega) = k' + k'' = -\frac{\psi}{d}\left[\operatorname{atan}\left(\frac{\varepsilon_0}{\varepsilon_{x,y}\psi}\right) + \operatorname{atan}\left(\frac{\varepsilon_s}{\varepsilon_{x,y}\psi}\right) + \pi l\right], \qquad \psi = -i\sqrt{\frac{\varepsilon_z}{\varepsilon_{x,y}}}, \tag{4.7}$$

where d represents the hBN thickness, ω is wavenumber, ε_o and ε_s are the complex dielectric functions of air and the substrate, respectively, whereas l represents the HPhP mode order. Typically, $l = 0$ is defined as the fundamental mode while larger l is defined as high-order modes.

It is important to note that the concept of hyperbolic materials and hyperbolic polaritons were originally pioneered in the field of plasmonics. In plasmonic systems, superlattices comprising multiple, alternating metal and dielectric layers can also result in hyperbolic material properties, with the effective dielectric function modeled via the effective media approach [131]. In those pioneering works on artificial hyperbolic metamaterials (HMMs), hyperlenses and negative refraction [138,139] were proposed and demonstrated. However, the negative permittivity arises from the Drude model of the integrated metal layers, which typically suffers from high optical loss. In addition, such HMMs cannot support truly infinitely large wave vectors even in the absence of loss, as the effective media theory will break down as the magnitude of wave vector becomes comparable to the individual layer thicknesses. Since the hyperbolic response of hBN arises from phonon vibrations instead of free carriers, the optical losses are significantly lower than HMMs, as shown in the literature [13,136,137], and much larger wave vectors can be supported for higher confinement. Furthermore, the optical loss in hBN can be further reduced via two approaches: (1) improving the material purity (less nitrogen or oxygen impurities for instance); and (2) decreasing the phonon scattering rates (increase phonon lifetimes [13,140]). On the second track, Liu *et al.* experimentally grew monoisotopic $h^{10}BN$ and $h^{11}BN$ crystals of millimeter lateral sizes [62,141], which resulted in substantial reductions in the phonon scattering. Giles *et al.* experimentally measured high-order HPhP modes with scattering-type scanning near-field optical microscopy (s-SNOM) with the isotopically enriched hBN flakes [13], while they further demonstrated that the phonon lifetimes of >99% $h^{10}BN$ and $h^{11}BN$ were ~3–4 times longer than those observed in naturally abundant hBN (~80% ^{11}B, ~20% ^{10}B), as a result of longer phonon lifetime, i.e., reduced imaginary part of the permittivity. This improvement of the material quality also contributes to the far-field resonance quality, and Lee *et al.* observed ~30–80% improvements of quality factor with isotopically enriched hBN [142].The origin of the improvement was thoroughly discussed through Raman spectroscopy, first-principles calculations, and temperature-dependent Raman studies [30,143].

4.2g. Applications of HPhPs

As discussed above, the wave vectors of HPhPs supported in hBN can be extremely large, i.e., the wavelength of light is compressed significantly. Therefore, it can carry information with high spatial resolutions and confine fields for strong light–matter interactions. We here list a few applications that can benefit from those properties of HPhPs.

1. Imaging through HPhPs

Since HPhPs propagating inside of the hBN can support infinitely large wave vectors without considering loss [131], HPhPs can carry information with high spatial resolution, e.g., "hyperlensing" [134–136,144]. The working principle of hyperlens is based on the ray-like propagation of HPhPs within hBN, and the angle is defined by the probing frequency (Eq. (4.5)). Therefore, the image of the object can be transferred (and magnified during this process) to the top surface of hBN, and the image can either be probed in the near-field [134] or couple to the far-field [145] with proper design. Although the wave vectors can be infinitely large for a lossless hyperbolic system, indicating no resolution limitations, the reaslitic resolution is heavily limited by the optical loss [146]. For instance, the reduced amplitude of polaritons during propagation determines the signal level in the system, and the noise equivalent power could lead to a finite resolution. Therefore, it is ideal to have a hyperlens system with minimum optical loss.

On the route of exploiting the high wave vectors of HPhPs in the imaging perspective, it has also been demonstrated that HPhPs could be used to diagnose defects in nanostructures. The defects, including structural defects [147,148] and wrinkles [149], could launch and/or reflect propagating HPhPs, and the location of those defects can be revealed, regardless of whether they can be measured in the topography.

2. Optical Sensing

Since the HPhPs have significantly larger wave vectors than the free space, the electric field is highly confined at the interface between hBN and the environment. Because of such confinement, the light–matter interaction between the IR probe beam and the material to be sensed is enhanced compared with plain silicon substrate. In [150], it has been demonstrated that 20-nm-thick organic semiconductor 4,4′-bis(N-carbazolyl)-1,1′-biphenyl (CBP) can be sensed with hBN nanostructure, and the same amount of signal change requires 100-nm-thick CBP if it is on plain substrate.

3. Optical Resonances in the IR

By coupling out the HPhP modes with grating or other simple resonance design, relatively high-quality-factor (~100–300) resonances can be realized [142,151–153]. Those optical resonators can be used as filters [154] and narrowband thermal emitters [155] by careful design.

It should be noted that the compression of wavelength, i.e., large wave vector, comes with a price of optical loss: the propagation of HPhPs in hBN is typically limited to 1–10 μm. Although the loss of HPhPs in hBN is several-fold lower than artificial HMMs formed by metal/dielectric alternating layers [136], this propagation length is still orders of magnitude shorter than guided mode in lossless dielectrics. The optical loss in hBN could potentially be suppressed by optimizing the growth procedure and reducing impuritis, but the improvements will be limited to onefold to twofold [30]. Therefore, for applications with long propagation length, the HPhPs might not be ideal candidates even if we take potential further material improvements into considerations.

4.3. Techniques and Principles of Probing HPhPs in the Near-Field

As mentioned above, HPhPs can be highly confined and deeply subdiffractional modes, meaning that the wave vector supported is much larger than the free-space wave vector and cannot be directly excited/probed from the free space due to the large momentum mismatch. This mismatch can be visualized as the large horizontal offset between the light line [green line in Fig. 46(a)–(c)] and polariton dispersions [curved lines in Fig. 46(a)–(c)]. To observe and engineer HPhPs, one must overcome this momentum mismatch and excite them directly [156]. The excitation and observation of HPhPs mainly fall into two strategies: near-field and far-field. In this subsection, we focus on the discussion on the probing and manipulation of HPhPs in the near-field.

In the near-field, HPhPs have been measured and directly imaged using s-SNOM. The working principle of s-SNOM is described thoroughly in a review article [157], and here we limit our discussion to the general concept regarding its use for probing HPhPs. In s-SNOM measurements, an incident laser is focused on a metalized AFM tip in tapping mode near the sample surface. The light is then scattered by the tip apex, generating high-wave-vector evanescent fields. Those evanescent fields can excite HPhPs at a broad range of wave vectors, with HPhPs excited at the tip apex and propagate from there, as shown in Fig. 49(c). Once the propagating HPhPs hit either a

Figure 49

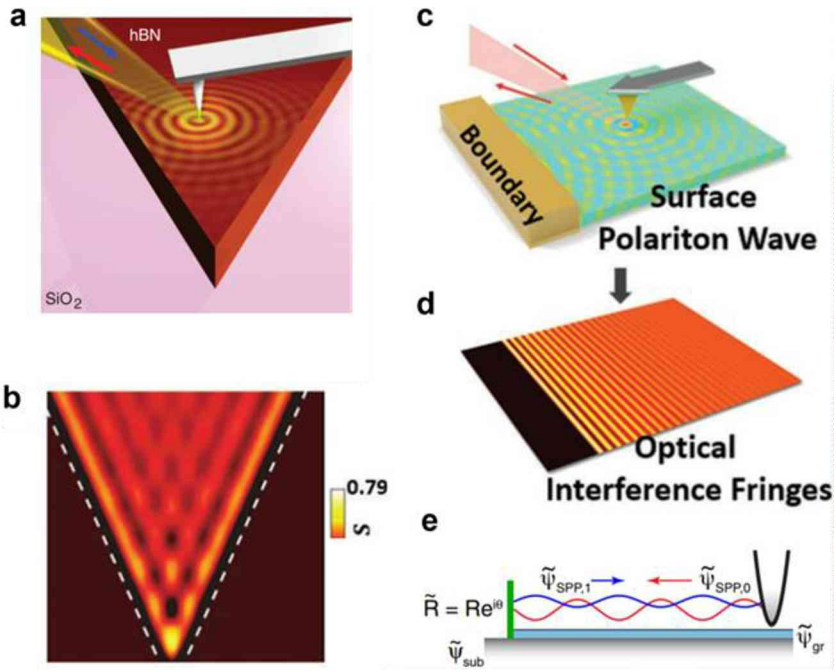

Propagating HPhPs measured by s-SNOM. (a) Schematic of s-SNOM measurement of HPhPs. (b) s-SNOM measured HPhPs supported by hBN flake. (c) HPhPs excited by tip before interference. (d) Interference fringes measured in s-SNOM, formed by the interference between tip-launched HPhPs and the reflected HPhPs from a boundary. (e) Schematic of the interference formation. Panels (a) and (b) are from Dai *et al*., Science **343**, 1125–1129 (2014). Reprinted with permission from AAAS. Panels (c) and (d) are from Chen *et al*., Adv. Mater. **34**, 1 (2019) [157]. Copyright Wiley-VCH Verlag GmbH & Co. KGaA. Reproduced with permission. Panel (e) is Figure 4 reprinted from Gerber *et al*., Phys. Rev. Lett. **113**, 055502 (2014) [158]. Copyright 2014 by the American Physical Society.

physical boundary of hBN (e.g., a flake edge) or a metal reflecting bar/pad, the HPhPs will be back-reflected and propagate back toward the tip. The tip-excited HPhPs and reflected HPhPs will interfere, resulting in constructively and destructively interference patterns, as shown in Fig. 49(d). This interference is shown schematically in Fig. 49(e), where the reflected wave Ψ_1 and the tip-excited wave Ψ_0 interfere to form the fringes observed in Fig. 49(b) [137]. In this case, the periodicity observed is half of the polariton wavelength, and detailed modeling was performed by Gerber *et al.* [158]. Notably, the metalized tip excites and probes HPhPs. Therefore, when other excitation sources exist in the system, s-SNOM will also pick up the excited HPhPs. For instance, HPhPs can also be directly excited by the scattering of incident light off of physical edges of hBN and/or metal disks, and they can be directly probed, referred to as "edge launched modes," and the observed periodicity is equivalent to the polariton wavelength. Dai *et al.* studied and summarized those different launching methods [159]. Moreover, Pons-Valencia *et al*. demonstrated that the launching efficiency can be enhanced with resonant metal plasmonic antennas compared with traditionally discussed metal disks [160]. Notably, HPhPs excited via different mechanisms will normally coexist in an s-SNOM image, typically with variable signal strengths and, thus, one needs to pay careful attention when analyzing the data.

With s-SNOM researchers now have the tools to directly image propagating HPhPs and study their exotic behaviors. The first experimental demonstration of propagating

Figure 50

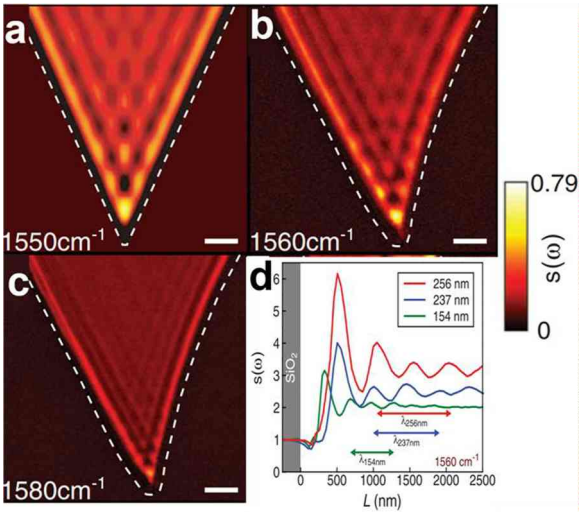

HPhPs probed with s-SNOM at different frequencies and thicknesses of hBN. (a)–(c) s-SNOM measured HPhPs supported by hBN flake at different frequencies. (d) Line profiles extracted from s-SNOM with different thicknesses of hBN. From Dai *et al*., Science **343**, 1125–1129 (2014). Reprinted with permission from AAAS.

HPhPs in the near-field is by Dai *et al.* [137] in 2014. In this seminal work, they showed that the HPhP modal wavelength varies with the incident frequency, and with the thickness of hBN (Eq. (4.6)). At the same time, Caldwell *et al.* [153] demonstrated that HPhP modes could be excited by patterning hBN into nanopillars where multiple resonances corresponding to the various HPhP higher-order modes are observed in the far-field. Importantly, those early demonstrations illustrate a couple of properties of HPhPs. (1) They are highly dispersive, i.e., the wave vectors rapidly change with excitation frequency, as shown in Fig. 50(a)–(c). (2) They can be tuned by changing the material thickness [Fig. 50(d)]. (3) There are, in principle, an infinite number of HPhP modes supported at any given frequency. The frequency-dependent property originates from the dispersion of the permittivity tensor, which determines the ψ term in Eq. (4.7). The thickness of hBN sets the quantized k_z as defined by Eq. (4.6), which, in turn, dictates k. Finally, the magnitude of the largest wave vectors supported are dictated by the HPhP wavelengths with respect to the unit cell of the structure and the absorptive losses associated with the materials.

4.4. Manipulation of HPhP Dispersion by the Local Environment

Although HPhP modes are volume confined, they remain highly sensitive to the local environment, i.e., the dielectric functions of substrate and superstrate, with this effect providing a potential methodology to control HPhP dispersion and propagation characteristics [149,161–165]. The mathematical relationship can be found in Eq. (4.6). This tuning is essentially through the optical phase change resulting from the TIR of HPhPs propagating within hBN at the top and bottom boundaries. Due to the van der Waals nature of hBN, it can be placed on top of arbitrary materials without considering lattice mismatch, making it a convenient approach to engineer HPhP wave vectors.

One of the initial demonstrations was by Duan *et al*. where hBN was placed over a gold nanoantenna encapsulated in SiO_2 [149,162] and over various substrates with varying dielectric functions, respectively. In both cases, the polariton wavelengths in regions over different dielectric constants were clearly different in the real-space image, as shown in Fig. 51(a) for hBN over SiO_2. They also extracted polariton dispersions at

Figure 51

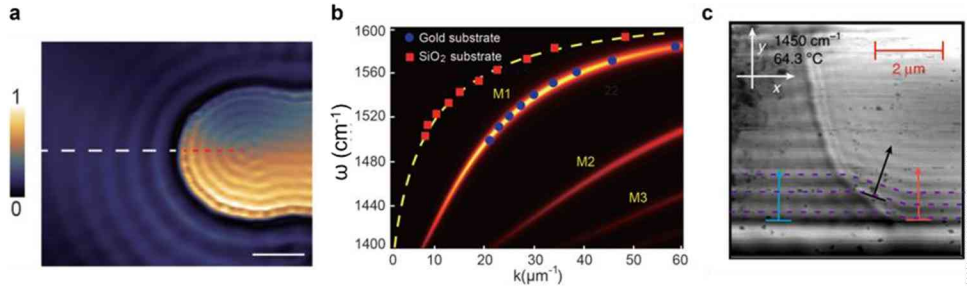

HPhPs tuned by substrate. (a) s-SNOM image of HPhPs supported by hBN over SiO_2 and gold, respectively. The imaging frequency is 1530 cm^{-1}. (b) HPhP dispersions of hBN over gold and SiO_2. (c) s-SNOM image of HPhPs supported by hBN over dielectric and metallic phases of VO_2. The imaging frequency is 1450 cm^{-1}. Panels (a) and (b) are reprinted from Duan *et al.*, Adv. Mater. **29**, 1 (2017) [149]. Copyright Wiley-VCH Verlag GmbH & Co. KGaA. Reproduced with permission. Panel (c) is reprinted with permission from Springer Nature: Folland *et al.*, Nat. Commun. **9**, 4371, Copyright 2018.

multiple frequencies [Fig. 51(b)] and confirmed that this wave vector contrast exists throughout the Reststrahlen band. Folland *et al.* further demonstrated that HPhPs can be actively tuned by using a phase change material substrate, i.e., VO_2 [162]. At around 65°C, VO_2 undergoes a phase transition from a dielectric-like monoclinic phase to metal-like rutile phase. At temperatures around the phase transition, various degrees of transitioned material can be nucleated, resulting in mixed domains of metal and dielectric phases coexisting. By adjusting the temperature of the heterostructure, they demonstrated HPhP refraction when the mode propagated within the hBN over a domain boundary, as shown in Fig. 51(c) black arrow. A list of demonstrations was also conducted to illustrate that HPhP properties are highly sensitive to local environment. For instance, Dai *et al.* demonstrated that HPhPs supported by suspended hBN have longer propagation lengths and lower damping coefficients than hBN over SiO_2 [164]. While Dai *et al.* also illustrated a case study of hBN/VO_2 heterostructure to dynamically tune HPhPs [165].

After those demonstrations of case studies of tuning HPhPs with varying dielectric substrates, Fali *et al.* generalized the trend and presented how the confinement and loss are related to the substrate properties [163]. Since hBN slabs are exfoliated mechanically, random thickness distributions result from this process and making it impractical to directly compare hBN samples over different substrates with the exact same thicknesses. To remove the influence of thickness, the HPhP wave vectors can be normalized by multiplying by the thickness of hBN, so that the wave vector is only dependent on hBN material properties and local environments:

$$k(\omega)d = (k' + k'')d = -\psi\left[\operatorname{atan}\left(\frac{\varepsilon_0}{\varepsilon_{x,y}\psi}\right) + \operatorname{atan}\left(\frac{\varepsilon_s}{\varepsilon_{x,y}\psi}\right) + \pi l\right], \qquad \psi = -i\sqrt{\frac{\varepsilon_z}{\varepsilon_{x,y}}}, \tag{4.8}$$

where d represents the hBN thickness, ω is wavenumber, ε_o and ε_s the complex dielectric functions of air and the substrate, respectively, whereas l represents the HPhP mode order. They reported that HPhPs can be tuned with substrate refractive index (ε_s) very effectively, especially in the small $|\varepsilon_s|$ range, with experimental data validating the calculations, as shown in Fig. 52(a). In other words, when the substrate has extremely large $|\varepsilon_s|$, e.g., over 100, the tuning capability provided by the substrate is negligible. Thus, if one can have a structure of hBN over gold in comparison

Figure 52

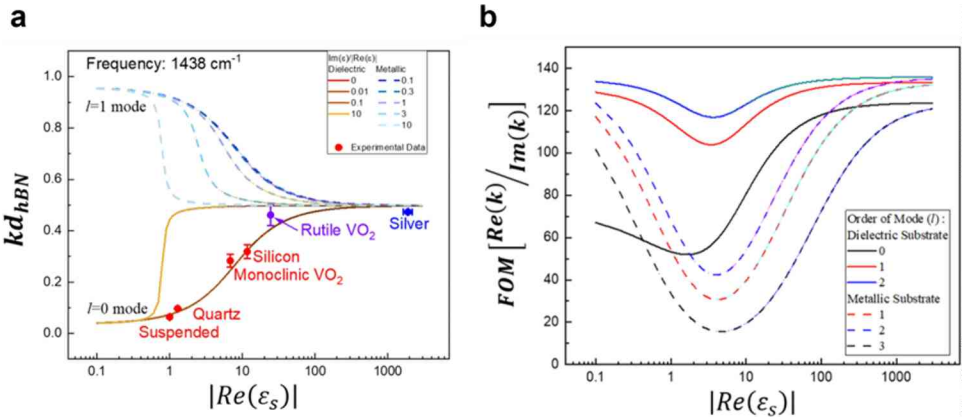

Dependence of HPhP over substrate permittivity. (a) Normalized HPhP wave vector dependence upon the real permittivity of the substrate dielectric function. (b) FOM of the first three orders of HPhPs in hBN as a function of the $|\mathrm{Re}(\varepsilon_s)|$. Reprinted with permission from Fali *et al.*, Nano Lett. **19**, 7725–7734 (2019) [163]. Copyright (2019) American Chemical Society, https://doi.org/10.1021/acs.nanolett.9b02651.

to a silver substrate, despite the differences in the magnitude in the corresponding permittivities, the polaritonic behaviors for the HPhPs over the two materials will be nominally the same. They also analyzed how the figure of merit (FOM) of HPhPs can be tuned by substrate properties. The FOM is defined as

$$\mathrm{FOM} = \frac{2\pi}{\lambda} \cdot 2L_{\mathrm{p}} = 4\pi Q, \tag{4.9}$$

where λ is the polariton wavelength, L_{p} is the propagation length, and Q is the quality factor that defines the number of cycles that the polariton wave oscillates before the amplitude decreases to $1/e$ of its initial value. The minimum value of the FOM occurs when $|\varepsilon_{\mathrm{s}}| = 3$, whereas extremely large or small $|\varepsilon_{\mathrm{s}}|$ result in nearly identical FOMs when substrate loss is not considered, as shown in Fig. 52(b). This effect is especially pronounced for the principal ($l = 0$) mode on dielectric substrates, as high-index substrates yield stronger confinement and higher Q. This calculation is in great agreement with Dai *et al.* [164] where suspended hBN shows improved FOM compared with SiO_2 substrate.

While HPhPs in hBN were demonstrated to be tuned by substrate permittivity in those aforementioned works, they are all based on the assumption of infinitely thick substrates. However, there may be multiple layers underneath hBN, and HPhP dispersions can be engineered by adjusting the various material layers under hBN instead. One of these concepts gives rise to subdiffractional optical modes called "image polaritons", which are supported in a hBN/dielectric gap/metal substrate geometry, as shown in Fig. 53(a, b). In the presence of a mirror plane within tens of nanometers from hBN, a polariton mode is mirrored, but with an inverted charge distribution [Fig. 53(a)]. This strategy has been utilized to enhance the confinement of SPPs in noble metals via gap plasmons [166,167] and acoustic plasmons in graphene [168]. In the case of hBN, HPhP modes supported in a slab are quantized with nonnegative integer mode number as discussed above. For very thin films, coupling efficiencies to modes with large mode number l become negligible due to the large momentum mismatch, thus we only discuss modes with relatively small mode number l (0–2). The existence of image charges significantly increases the confinement, with a normalized wave vector change of ~3–4 times reported. Notably, HPhP wave vectors can be continuously tuned

Figure 53

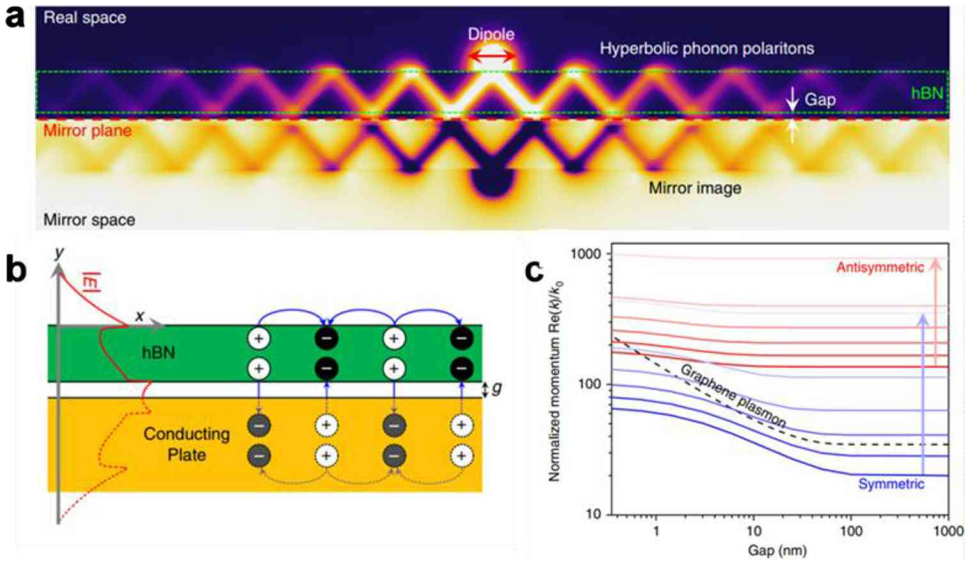

Image HPhPs. (a) Schematic illustrations of image polaritons. (b) Charge distributions for symmetric mode. In the presence of a mirror, image polaritons with out-of-phase charge oscillations are launched and confine radiation to the gap between the hBN layer and the mirror. (c) Normalized in-plane momentum and the FOM as a function of the gap size for the symmetric and antisymmetric polariton modes, and graphene plasmons at five different frequencies of 1522, 1545, 1569, 1592, 1616, and 1639 cm^{-1}. The arrows represent the direction of increasing frequency. Reprinted with permission from Springer Nature: Lee *et al.*, Nat. Commun. **11**, 3649, Copyright 2020.

by the gap size to be any value between the "nongap" and "infinite-gap" case, offering substantial freedom to engineer HPhPs. It is worth mentioning that the dielectric gap can be treated as infinite once it is larger than the depth of the extent of the evanescent field. Feres *et al.* also demonstrated this gap dependence, and they proposed an acceleration of HPhPs within a hBN/wedged dielectric gap/gold substrate geometry [169].

In addition to tuning image HPhP dispersion by the gap size, HPhPs can also be tuned by changing dielectric function of the gap (permittivity ε_1). Intuitively, the HPhP evanescent field in the dielectric material experiences an optical phase change, i.e., the term in Eq. (4.8), which modifies the HPhP dispersion. When the substrate thickness is finite with respect to this evanescent field distribution, or multiple dielectric layers are present within it, one can also expect fine-tuned HPhP dispersion by adjusting individual layer thicknesses and/or materials.

On the track of local-environment-tuned HPhPs, one specific method to engineer HPhP dispersion is modal hybridization, i.e., coupling with one or multiple different modes. It was first demonstrated by Dai *et al.* that the SPPs supported by graphene can be hybridized with the HPhPs supported by hBN, within a graphene/hBN heterostructure [170]. Importantly, the SPP supported by the graphene can be actively tuned by applying a gate voltage, leading to a dynamically tunable HPhP/SPP hybridized mode. Since this work, more related research has demonstrated that hybridized modes can be used to realize dynamic tuning for HPhPs supported within different materials, including α-phase molybdenum trioxide [171–174]. Moreover, HPhPs supported by hBN can be (strongly) coupled to molecular vibrations, leading to modified dispersions, as shown by Autore *et al.* [150,175].

HPhPs also offer the potential to provide substantial field confinement, i.e., polaritonic wavelengths that are tens to hundreds of times smaller than free-space wavelength, it typically comes at the cost of increased losses, because light–matter interactions are significantly stronger than purely refractive optics. Even though HPhPs possess reduced (~5–10 times) losses compared with noble metal counterparts [136], the loss is still a limiting factor for many applications, for instance, chip-scale communications. If we consider the HPhPs as a guided mode with a certain mode index, the FOM (real part of HPhP wave vector over the imaginary part) is normally ~80 for isotopically enriched hBN and ~30 for naturally abundant hBN, while it is typically around 10 for a-HMM (hyperbolic metamaterial) made of noble metals.

To summarize this section, there are essentially three approaches to tune HPhP wave vectors: (1) change the thickness of hBN [Fig. 50]; (2) change the working frequency [Fig. 51]; and (3) change the local environment [Fig. 53], including substrate and superstrate. Notably, in the third approach, the substrate and superstrate can be multilayer systems, adding more designability.

4.5. Manipulation of HPhP Propagation in the Near-Field

With all the concepts and approaches mentioned above, we now have the tools to manipulate HPhP dispersions and their behaviors. In this subsection, we discuss the HPhP propagation in the near-field, and how they can be manipulated for different applications. We first introduce the principles to engineer HPhP propagation, and then give examples of how they are realized.

In general, HPhPs can be manipulated in two approaches: (1) pattern hBN; and (2) pattern the substrate under hBN flakes/films to induce a HPhP wave vector difference. The second approach is preferred when both approaches can provide the same function, as the hBN is kept intact without any etching-induced material degradation. However, certain functions realized by approach (1) are not achievable with approach (2).

When hBN is patterned into strips, HPhPs are only supported within the hBN region, and alternating HPhP-supporting and HPhP-non-supporting regions can be used to engineer HPhP behavior [176–180]. For instance, Dolado *et al.* patterned hBN into nanobelts, so that Fabry–Perot (FP) modes can be formed that propagate along the confined direction [Fig. 54(a)] [176]. When k_{FP} is smaller than the HPhP wave vectors, a guided mode along the unconfined direction can be formed, as shown in [Fig. 54(b)]. In the case of similarly patterned hBN, we can also envision the edge of hBN as a hyperbolic medium with three boundaries being dielectrics. Along the edge, a surface-confined HPhP (s-HPhP) mode can be formed, which features stronger field confinement (i.e., higher momenta), smaller group velocities, and nearly identical lifetimes compared with volume-confined HPhPs discussed above [177], as shown in [Fig. 54(c) and (d)] . Those s-HPhPs are also known as "edge modes," since they are only supported along the edge of hBN. Such modes have also been directly probed via EELS in the aloof mode, that is the electron beam is transmitted just outside of the hBN slab along a flat edge. This allows the evanescent fields from the electron beam to stimulate s-HPhPs along the edges [178]. Due to the sidewall-confined nature of s-HPhPs, they can potentially be guided along non-straight hBN edges. Indeed, Dai *et al.* [179] demonstrated that reflection, transmission, scattering, and propagation of s-HPhPs can be controlled by tailoring the geometry of hBN nanostructures [Fig. 54(e)]. Moreover, Chen *et al.* showed that the reflection phase at the corner of hBN can be engineered by the angle of the corner [180], as shown in Fig. 54(f) and (g).

In addition to simplified structures such as ribbons as waveguides [176] and edges to guide s-HPhPs, hBN can be patterned into periodic structures to realize complicated functions. For instance, Alfaro-Mozaz *et al.* demonstrated a hBN polaritonic crystal

Figure 54

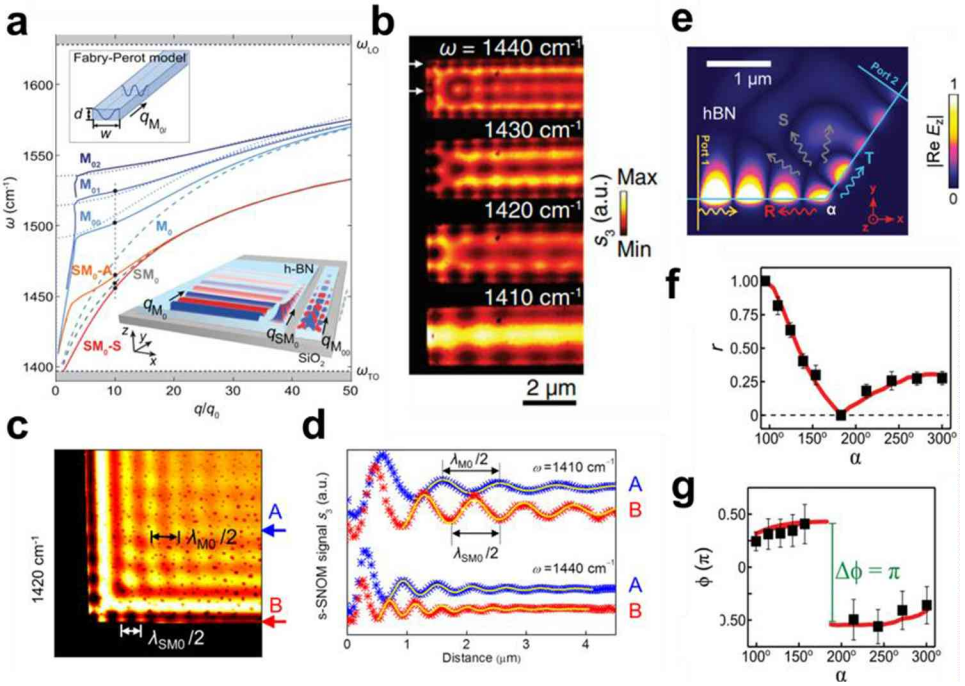

HPhP propagation within patterned hBN. (a) Mode dispersion of HPhP guiding behavior in hBN nanobelts. Gray dashed line: fundamental surface mode (SM0) at the edge of a semi-infinite slab. Blue dashed line: fundamental volume mode (M0) in an infinite slab. Orange and red solid lines: symmetric and antisymmetric hybridized surface modes ($SM_{0\text{-}S}$ and $SM_{0\text{-}A}$) in a ribbon, respectively. Blue solid lines: volume modes in a ribbon (M_{nl}, with n and l being the FP mode indices along the z and x axes). Gray shaded areas in the diagram indicate the frequency regions outside the Reststrahlen band. The upper inset shows a schematic of the FP model used for calculating the dispersion of the volume waveguide modes M_{nl} (dotted blue lines). The lower inset shows a schematic of an hBN slab and waveguide with a representation of the near-field distributions of the M_0, SM_0, and M_{00} modes. (b) s-SNOM amplitude images at different frequencies ω (bottom right) for a waveguide of thickness 38 nm and width w of 1 μm at different frequencies. (c) Experimental IR s-SNOM images (amplitude signal s3). The black and white arrows in the image at 1420 cm^{-1} indicate the periods of near-field oscillations on the hBN flake and its edge, corresponding to half the wavelengths of the M_0 and SM_0 modes, respectively. Small black dots on the hBN surface are due to sample contamination. (d) Horizontal line profiles extracted from panel (a) at the positions marked by blue and red arrows. The yellow curves display fittings to the experimental data. (e) s-HPhPs are guided along a nonstraight hBN waveguide. (f), (g) Reflection rate and reflection phase at the corner, with different corner angles. Panels (a) and (b) are reprinted from Dolado *et al.*, Adv. Mater. **32**, 1 (2020) [176]. Copyright Wiley-VCH Verlag GmbH & Co. KGaA. Reproduced with permission. Panels (c) and (d) are reprinted with permission from Li *et al.*, Nano Lett. **17**, 228–235 (2017) [177]. Copyright 2017 American Chemical Society, https://doi.org/10.48550/arXiv.1805.00662. Panel (e) is reprinted from Dai *et al.*, Adv. Mater. **30**, 1 (2018) [179]. Copyright Wiley-VCH Verlag GmbH & Co. KGaA. Reproduced with permission. Panels (f) and (g) are reprinted from Chen *et al.*, Adv. Opt. Mater. **10**, 1 (2022) [180]. 10.1002/adom.202102723.

[181], where the polaritons form Bloch modes, and the band structure is characterized through a near-field hyperspectral measurement. In this demonstration, the local density of photonic states (LDOS) is engineered in both frequency and spatial domains, as shown in Fig. 55(a) and (b). Although the length scales (nanobelt width or period of polaritonic crystal) of aforementioned demonstrations are significantly smaller than the free-space wavelength, they are actually comparable to the polaritonic wavelength. In other words, the deeply subdiffractional HPhPs can still experience boundary-induced variations. When the length scale of patterns is smaller than the polaritonic wavelength the periodically patterned hBN can be considered to behave as a new effective material. As demonstrated by Li *et al*., when hBN is patterned into gratings with 100 nm periodicity, the patterned hBN can be modeled using effective media theory [182]. With properly designed filling fraction the effective permittivity tensor parallel and perpendicular to the grating can be dictated to be opposite in sign, leading to in-plane HPhPs, as shown in Fig. 55(c) and (d). In the structured hBN, the wavefronts of a diverging polariton beam emitted by a point-like source can exhibit a concave curvature, in stark contrast to the circular wavefronts in pristine hBN. Further, the large wave vectors (limited only by the inverse of the structure size) yield a diverging, anomalously large photonic density of states. The same research group also studied the elliptical range in this structured hBN, i.e., where the real part of effective permittivity in both the x and y directions are positive, yet they are different values. They described the system more precisely with a modified effective medium model, taking polaritonic near-field coupling of hBN nanoribbons into account. In a specific frequency range, the HPhPs are only propagating along one direction, showing the canalization effect [Fig. 55(e) and (f)] [183].

Besides engineering HPhPs by patterning hBN into different geometries, it is also possible to manipulate HPhPs within pristine hBN. Recall that HPhPs supported by hBN over substrates with different permittivity values exhibit varying wave vectors. Folland *et al.* [162] first demonstrated that when a HPhP wave propagates across different substrate domains, hBN over dielectric and metallic VO_2 in their case, the HPhPs are refracted, of which the behavior can be described by the Snell's law, as shown in Fig. 56(a). The phenomenon is caused by the conservation of tangential component of wave vectors at the boundary, giving rise to the generalized Snell's law:

$$k_{\text{in}} \cdot \sin(\theta_{\text{in}}) = k_{\text{out}} \cdot \sin(\theta_{\text{out}}), \tag{4.10}$$

where θ_{in} and θ_{out} are the angles that k_{in} and k_{out} form with the normal to the boundary, respectively. They also proposed a structure with dielectric and metallic VO_2 to refract HPhPs and form an in-plane lens, as shown in Fig. 56(b). Chaudhary *et al.* [184] demonstrated more complicated functions with a nonvolatile phase-change material, i.e., Ge–Sb–Te (GST). GST exhibits large refractive index contrast in the mid-IR ($n_{\text{amorphous}} = 4.2$ and $n_{\text{crystalline}} = 6.1$), and the two states can be switched by laser writing or electrical pulses, and the states do not change without further perturbation. Therefore, this becomes a great platform to tune and manipulate HPhPs. They experimentally demonstrated various HPhP functions, including simple concave and convex lensing, prisms and waveguiding, as well as HPhP metalens [Fig. 56(c)]. Building on those work, He *et al.* demonstrated that HPhPs can be guided by an underlying silicon waveguide, while the silicon waveguide can still guide near-IR signals, thus realizing dual-band operation [185], as shown in Fig. 56(d) and (e).

While the polaritonic refraction concept is straightforward to model mathematically and induce experimentally, it provides a powerful platform to manipulate HPhPs. In fact, a couple of recent demonstrations with engineered substrates show that increasingly complicated functions can be realized. Yang *et al.* demonstrated that hBN over silicon dioxide periodic patterns could support polaritonic crystal modes, and the

Figure 55

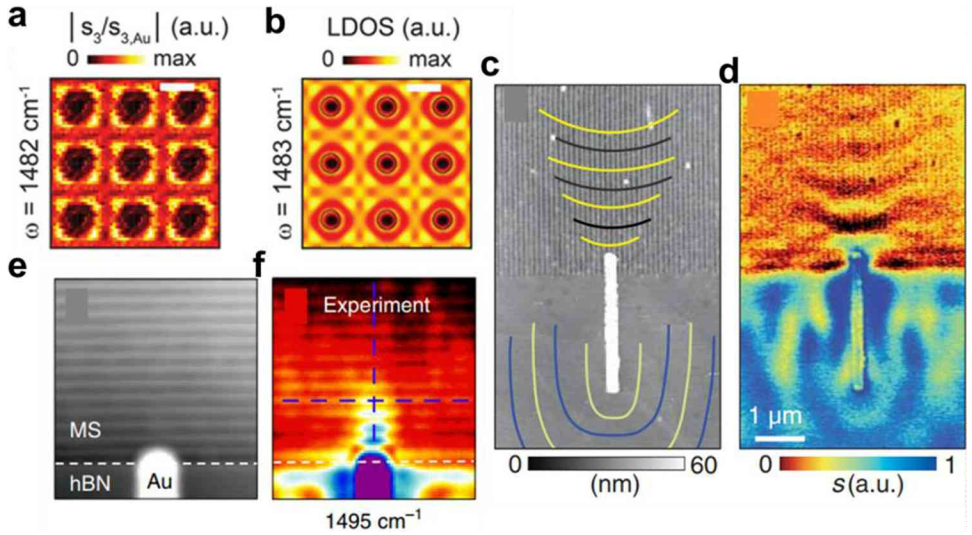

HPhPs supported by patterned hBN. (a) Nano-FTIR near-field images of hBN polaritonic crystal. The image of a single unit cell is shown 3×3 times. (b) LDOS images calculated for the same sample. The scale bar in panels (a) and (b) is 500 nm. (c) Topography image. The lines illustrate wavefronts of hyperbolic metasurface (HMS)-PhPs on the HMS (yellow and black) or phonon polaritons on the unpatterned flake (yellow and blue). (d) Near-field image recorded at $w = 1430\,\mathrm{cm}^{-1}$, revealing concave wavefronts of HMS-PhPs emerging from the rod's upper extremity. (e) Topography of the sample. (f) Experimental near-field distribution of antenna-launched elliptical polaritons on the metasurface at $1495\,\mathrm{cm}^{-1}$. White dashed lines mark the boundary of the metasurface. Panels (a) and (b) are reprinted with permission from Alfaro-Mozaz *et al*., Nano Lett. **21**, 7109–7115 (2021) [181]. Copyright (year) American Chemical Society, https://doi.org/10.1021/acs.nanolett.1c01452.s002. Panels (c) and (d) are from Li *et al*., Science **359**, 892–896 (2018). Reprinted with permission from AAAS. Panels (e) and (f) are reprinted with permission from Springer Nature: Li *et al*., Nat. Commun. **11**, 3663, Copyright 2020.

LDOS can be designed [186]. They observed archimedean-like tiling patterns in the near-field, including dipolar-like Bloch modes and the local phonon polariton interference patterns that evolve with the illumination frequency. The band structure of the polaritonic photonic crystal (PhC) can be tuned by changing the thickness of hBN, which effectively controls the polaritonic wave vector. Sheinfux *et al.* further demonstrated that the polaritonic band structure can be engineered, and experimentally illustrated the modified HPhP propagation behavior in such a system [187]. They demonstrated HPhP dispersion features such as negative group velocity, indicative of band zone-folding, and signatures of sharp peaks in the density of states, expected for polaritonic PhCs (and not for ordinary polaritonic modes).

Notably, when the polaritonic refraction is utilized to control HPhPs, the loss caused by defects is smaller compared with patterned hBN for no etching induced material degradation. For instance, the guided HPhPs in hBN nanobelts do not show monotonic exponential decays, and the loss cannot be extracted [176]. They attribute this finding to fabrication-induced defects and geometry variations along the waveguides, which can lead to some backreflection of the mode, and thus to the appearance of fringes far away from the waveguide terminus. In contrast, the guided HPhPs realized by fabricating structures into the underlying silicon led to significantly reduced scattering,

Figure 56

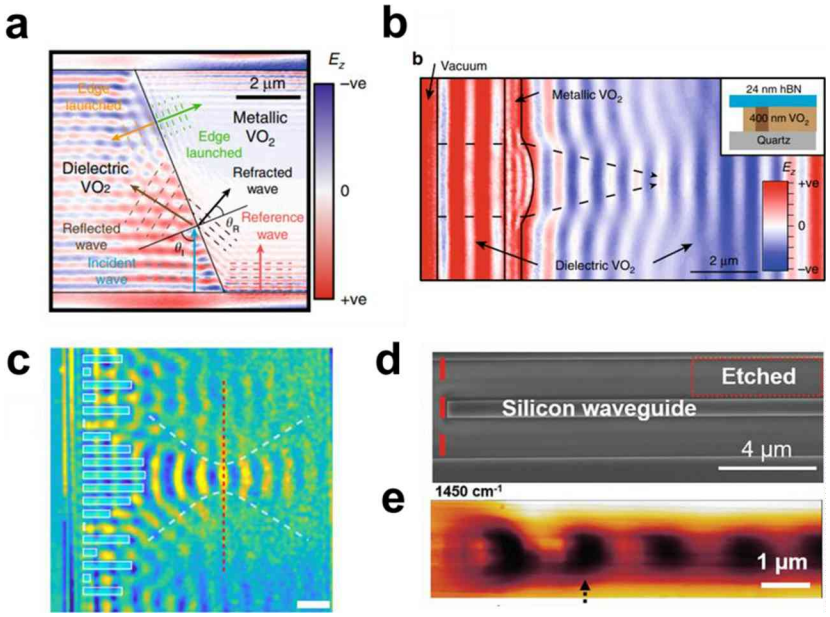

Controlled HPhP propagation by substrate engineering. (a) Electromagnetic-field simulation showing reflected, refracted, and edge-launched waves. Here, a uniform hBN covers over dielectric and metallic states of IO_2. The HPhPs propagating from the bottom (within the dielectric VO_2 domain) is refracted after entering the hBN/metallic VO_2 domain. (b) Simulation of a refractive polariton lens, which uses a semicircular domain of metallic VO_2 to launch polariton waves at 1418 cm^{-1}. (c) s-SNOM image of metalens showing focusing of polaritons at 1452 cm^{-1}. A uniform hBN is placed on nonvolatile phase change material Ge–Sb–Te (GST). The rectangle boxes indicate crystalline state GST, while the matrix of GST is amorphous state. The scale bar is 5 μm. (d) SEM image of the silicon waveguide component in the heterostructure. The dashed line shows the edge of the waveguide, which is designed to launch HPhPs into the hBN over the silicon waveguide. (e) Near-field optical amplitude image of the HPhP-waveguide modes in hBN over the silicon waveguide at 1450 cm^{-1}. Panels (a) and (b) are reprinted with permission from Springer Nature: Folland *et al.*, Nat. Commun. **9**, 4371, Copyright 2018. Panel (c) is reprinted with permission from Springer Nature: Chaudhary *et al.*, Nat. Commun. **10**, 4487, Copyright 2019. Panels (d) and (e) are reprinted from He *et al.*, Adv. Mater. **33**, e2004305 (2021) [185]. Copyright Wiley-VCH Verlag GmbH & Co. KGaA. Reproduced with permission.

and the lifetimes are extracted and compared with theoretical values [185]. However, certain functions realizable through patterned hBN are not accessible with substrate engineering. For instance, the s-HPhPs are only supported along the edge of hBN due to boundary conditions.

In summary, there are two approaches to manipulate HPhP propagation: (1) pattern hBN into different shapes, or (2) use intact hBN on a patterned substrate. For patterned hBN, when the scale is comparable to or larger than the HPhP wavelength, the system is similar to extruded 2D dielectric systems, except with much higher loss. However, when the pattern scale is significantly smaller than HPhP wavelength, the HPhPs can no longer experience the difference between regions, making the patterned hBN an effective composite material that can be described by (modified) effective medium theory.

Figure 57

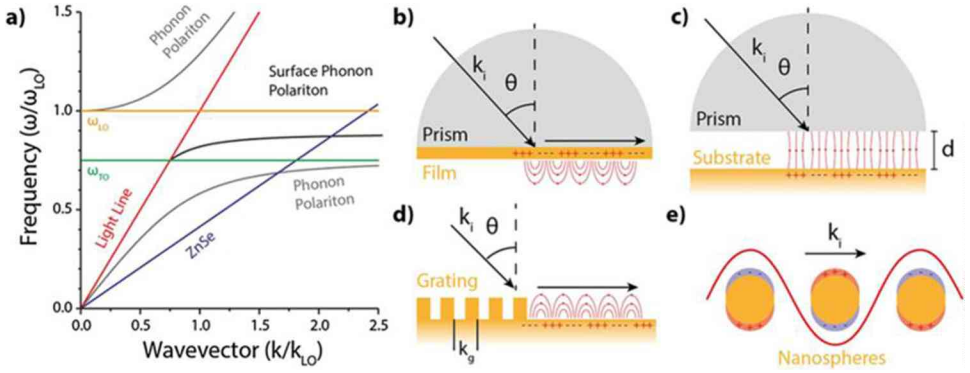

Surface polariton dispersion and coupling. (a) Dispersion relationship for electromagnetic waves in a polar semiconductor, highlighting the region between ω_{TO} and ω_{LO} which supports surface phonon polaritons. (b)–(e) Due to the momentum mismatch between free-space light and polaritons, methods to probe them require this mismatch to be overcome. This can be realized by coupling light to the polaritonic medium through a high-index prism in either the (b) Kretschmann or (c) Otto configurations, by (d) imparting higher momentum through grating coupling, or (e) through nanostructuring of the polaritonic medium, resulting in subdiffractional resonant cavities. Reprinted with permission from Folland *et al.*, J. Appl. Phys. **125**, 1 (2019) [156]. Copyright 2019, AIP Publishing LLC.

4.6. Engineering HPhPs in the Far-Field

Since HPhPs are subdiffractional modes, they cannot be directly excited from free space as mentioned above. In far-field excitation, the approach is to provide a sufficient wave vector to couple into HPhPs by fabrication of a (1) resonant structure or coupling with an external (2) evanescent field. In principle, all techniques that are used to excite surface plasmon polaritons (SPPs) can be used on HPhPs, including prism coupling, grating coupling, and resonators, as shown in Fig. 57 [156].

Prism coupling exploits the evanescent wave that results at the boundary of a high refractive index prism, either in contact with [Fig. 57(c)] or in close proximity to a polaritonic medium [Fig. 57(c)], with these two approaches referred to as the Kretschmann and Otto configurations, respectively. This allows coupling into polaritons with

$$k_{\text{polariton}} = n_{\text{prism}} \cdot \sin(\theta) k_0, \tag{4.11}$$

where θ is the incident angle. When excited $k_{\text{polariton}}$ is larger than k_0, the HPhPs supported by hBN can be excited [188]. Note that HPhPs excited in Kretschmann configuration are stimulated on the opposite side of a thin film with respect to the prism surface, e.g., within the substrate, meaning $k_{\text{polariton}}$ should be larger than $k_{\text{substrate}}$ instead of k_0, as thoroughly discussed in [188]. Meanwhile, when a prism is used, the contact should be optically flat within minimal to no air gaps, and index matching solutions are frequently used to ensure this condition is met. On the other hand, the Otto configuration utilizes the evanescent field between the prism and hBN, typically within an air gap between them, and they are not in direct contact, making this measurement scheme easier to realize compared with the Kretschmann configuration, albeit with the additional challenge of needing to ensure the prism and sample surfaces are parallel.

Since the prism coupling strategy relies on the evanescent field extending below the prism surface, the largest wave vector that can be stimulated via this approach is

dictated by the refractive index of the prism material at the frequency of interest. On the other hand, grating and nanoresonators enable the stimulation of polaritons with wave vectors dictated by the grating periodicity and/or nanoresonator size, and are not as limited in the range of accessible momenta. Since the design, fabrication, and characterization of polaritonic resonators represents an extremely broad topic, here we use gratings as an example to discuss the principle. For gratings, the momentum provide can be calculated by

$$k_{\text{polariton}} = k_0 \cdot \sin(\theta) + \frac{2m\pi}{d}, \tag{4.12}$$

where d is the grating period and m is an integer. This is essentially a form of Bragg scattering: light interacts with the grating, coupling into diffractive modes, which results in a slowing of the light propagation in the direction parallel to the surface. With a specific $k_{\text{polariton}}$, there is an intersection between $k_{\text{polariton}}$ and the HPhP dispersion plot, and the mode at the intersection can be coupled in or out. In the literature [142,168,189], researchers have used subdiffractional grating structures to excite HPhPs with designable momenta [Fig. 57(b)], as well as means to dictate the spatial coherence of thermal emission [190–192].

In addition to using prism coupling, optical structures, e.g., nanoresonators can be used to excitate polaritons in the far-field [142,150,153,175,193–196]. Nanoresonators could be based on the principle that a specific momentum is provided by the structure, with that momentum dictated by the material optical properties and structure size and shape, resulting in a resonant mode or modes (either with increased reflection or absorption) that can be observed in the far-field. In fact, one of the first publications studying HPhPs of hBN was using nanocones, where high-Q-factor and volume-confined resonances are observed by Caldwell *et al.* [153], as shown in Fig. 58(a).

The HPhPs excited in the far-field can be engineered and/or modulated with the same strategies described in previous sections, namely substrate tuning, where modal hybridization can be considered as a special case of local environment tuning. By Lee *et al.* [142], it was demonstrated that HPhPs stimulated by the same grating structures (thus, at the same wave vector) and similar thickness hBN exhibited different resonant frequencies due to the modified HPhP dispersion by grating gap size. The local environment change could also happen in the superstrate, which could be employed as a sensing approach. Autore *et al.* have demonstrated that the HPhP resonances observed in the far-field could be changed by the presence of molecules featuring spectrally overlapping vibrational modes [150]. Rather than simply shifting the HPhP dispersion and thus shifting the resonances, the molecular vibrational modes can be weakly and/or strongly coupled to the HPhPs, resulting in a spectral splitting of the resonances and enable improved molecular detection sensitivity and selectivity. Notably, this coupling has also been demonstrated in the near-field by Bylinkin *et al.* [175].

One can envision that other tuning mechanisms and demonstrations in the near-field can be migrated to far-field resonances. In simulations performed by Deng *et al.* [193], in a hBN/graphene heterostructure patterned into subdiffractional gratings, the resonances can be excited, and tuning graphene the Fermi energy by electrical or chemical doping can change the resonance response accordingly. Other strategies such as changing the VO_2 and GST phases demonstrated in the near-field are also applicable to far-field resonance and emission control.

Notably, phonon polaritons within the light cone can be supported in hBN, where the wave vector is still within the light line and HPhPs are not excited. One case is referred to as "Tamm phonon polaritons," where a polariton medium is in direct contact with a mirror, which could either be a metal mirror or dielectric mirror [Bragg reflector or

Figure 58

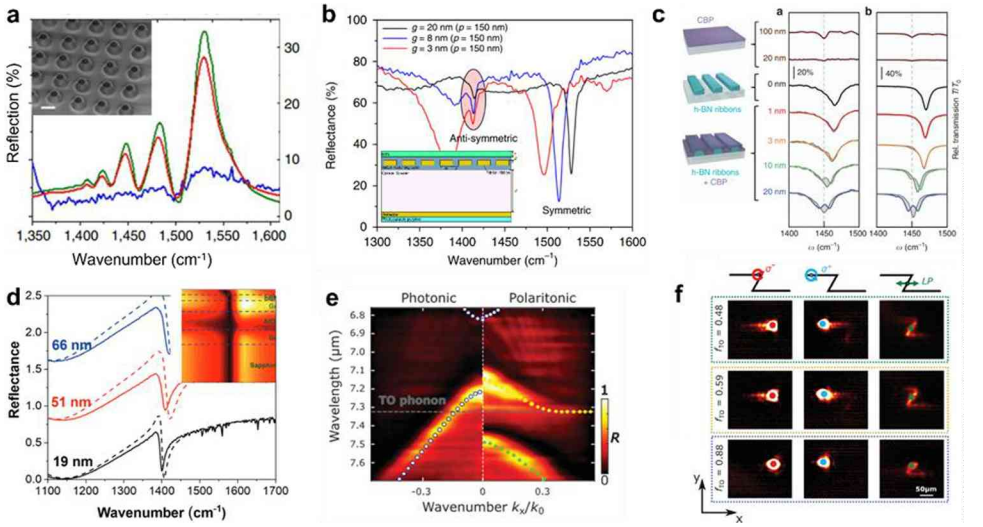

Far-field excited phonon polaritons supported in hBN. (a) HPhPs excited in the far-field by nanocone resonators. The reflection peaks are resonant modes. (b) Image HPhPs excited by subdiffractional gratings. The resonances (reflection dips) change with the dielectric gap size. (c) HPhPs excited by patterned subdiffractional hBN gratings show transmission dip (reflection peak) on the left panel. When CBP is coated on the sample, (strong) coupling between the HPhP mode and CBP molecule resonance causes Rabi splitting, separating the mode into two branches. (d) Tamm phonon polaritons can be supported in a hBN/DBR structure, forming reflection dips. (e) Modal hybridization between a trivial photonic mode and phonon polariton mode. (f) Hybridized polaritonic mode propagate unidirectional with circular excitation beam. Panel (a) is reprinted with permission from Springer Nature: Caldwell *et al.*, Nat. Commun. **5**, 5221, Copyright 2014. Panel (b) is reprinted with permission from Springer Nature: Lee *et al.*, Nat. Commun. **11**, 3649, Copyright 2020. Panel (c) is reprinted with permission from Springer Nature: Autore *et al.*, Light: Sci. Appl. **7**, 17172–17172, Copyright 2018. Panel (d) is reprinted from He et al., Adv. Mater. **35**, e2209909 (2023) [194]. Copyright Wiley-VCH Verlag GmbH & Co. KGaA. Reproduced with permission. Panels (e) and (f) are from Guddala *et al.*, Science **374**, 225–227 (2021). Reprinted with permission from AAAS.

distributed Bragg reflector (DBR)]. In fact, this Tamm mode is not dependent upon the hyperbolicity of hBN, and can still be supported even if hBN were an isotropic phonon polariton supporting material (such as cBN). He *et al.* have demonstrated that Tamm phonon modes can be coupled with Tamm plasmon polariton modes [194], whereas Barra-Burillo *et al.* demonstrated that a metal–hBN–metal structure can support a FP mode that can be strongly coupled to the optical phonon modes of hBN [195]. Moreover, Guddala *et al.* demonstrated that phonon polaritons can be coupled with topological edge states, thus the propagation becomes unidirectional [Fig. 58(e) and (f)] [196].

5. QUANTUM PHOTONICS AND OPTIMIZATION

5.1. Light and Photons

5.1a. Quantization of Light

Light, a form of electromagnetic radiation visible to the human eye, is also broadly associated with electromagnetic fields in various contexts. In 1900, Max Planck challenged the idea of continuous radiation, proposing instead that energy exists in distinct,

quantized units. This concept of energy quantization was pivotal in explaining blackbody radiation. Five years later, Albert Einstein revolutionized our understanding by describing the photoelectric effect through the notion that light is comprised of discrete, quantized energy packets known as photons. In this process, electrons within the inner shells of metal atoms absorb photons, surmounting the energy barrier (work function), and are subsequently liberated from the atom as free electrons carrying added kinetic energy. Notably, the energy needed for this liberation hinges solely on the frequency of light (a wave property) rather than its amplitude (the number of photons, a particle property). This revelation underscored the duality of light: simultaneously exhibiting characteristics of particles and waves. Einstein's breakthrough in this area earned him the Nobel Prize in 1921. This epochal discovery marked the genesis of the quantum era in physics, heralding a transformative shift in our comprehension of the fundamental nature of energy, particles, and their behaviors.

The photon, a fundamental boson, possesses no mass or charge, yet it engages with matter, particularly fermions. An illustrative instance of light-matter interaction is PL. Examining the photon (light)–electron (matter) interaction within PL unveils three primary phases: photon absorption, electron excitation and relaxation, and subsequent photon emission.

Figure 59 schematically depicts the PL process. Initially, an electron in the ground singlet state (S_0) absorbs a photon, taking $\sim 10^{-15}$ seconds, with an energy of $h\nu_1$, propelling it to a higher singlet state: S_1 or S_2. Subsequently, this electron quickly ($\sim 10^{-12}$ s) loses some energy through internal conversion, such as lattice vibration, reaching a relatively stable state. However, this electronic state is not entirely stable; the surplus energy tends to dissipate ($\sim 10^{-9}$–10^{-6} s) through either a radiative process (PL) or a nonradiative process (vibration or virtual photons). The PL follows two primary pathways: it typically relaxes to the S_0 state, releasing energy by emitting a photon ($h\nu_2$), a process termed fluorescence. Alternatively, in certain scenarios, an intersystem crossing may occur ($>10^{-5}$ s), where the electron transitions to a triplet T_1 state (with the electron spin flipped), then relaxing to S_1 by emitting ($>10^{-4}$ s) a lower-energy photon ($h\nu_3$). This process is known as phosphorescence. The distinction between these pathways lies in the excited state's lifetime: phosphorescence exhibits a far longer duration than fluorescence due to the involvement of a spin-flip step in the latter case. The timeframes in the above processes can be quantified/measured using photon number statistics. In addition, light classification can be categorized based on the observed characteristics.

5.1b. Photon Number Statistics

Probability reigns supreme in the quantum realm, largely due to the profound uncertainty principle, which asserts the impossibility of simultaneously and precisely measuring both position and momentum. Consequently, statistics become pivotal in high-speed scenarios, such as photon detection. Photon statistics have found widespread application in PL spectroscopy, notably in time-resolved PL decay used for measuring electron excited state lifetimes. Confirmation of these lifetimes involves mathematically fitting the intensity decay time from its maximum to the $1/e$ (where e is the Euler's number) level.

The essence lies in the spontaneous emission triggered by vacuum perturbation: a random process where photons are not emitted simultaneously. Hence, assessing the statistical behavior of photons becomes imperative. Similar to other bosons, photons adhere to the Bose–Einstein distribution, indicating their natural tendency to occupy the same quantum state. Figure 60(a)–c) schematically demonstrates three categories of light sources based on photon number statistics. In addition, Fig. 60(d) shows

Figure 59

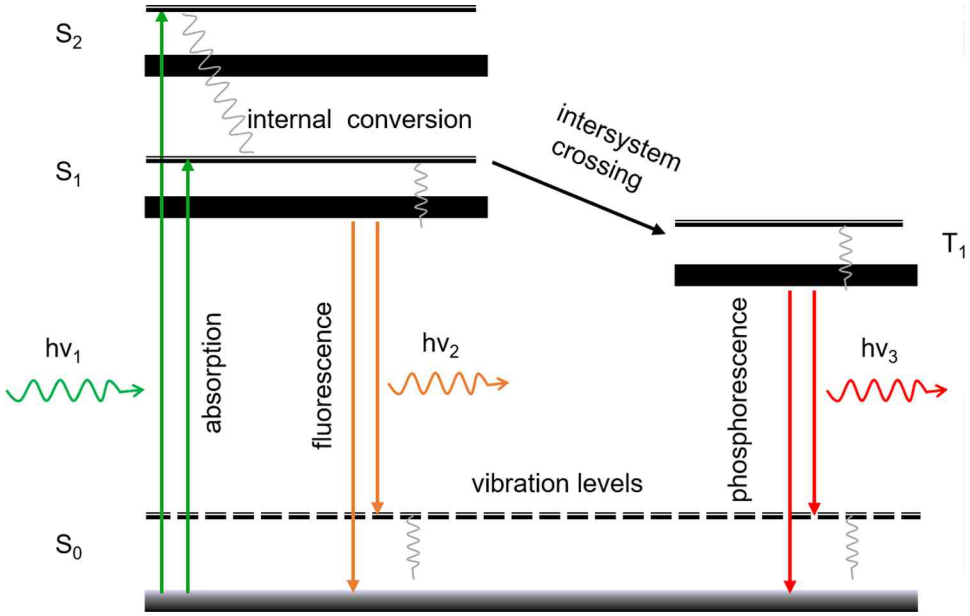

Schematics of the PL process. Thick lines are electronic energy levels, whereas the thin lines stand for sublevels such as vibrational and rotational energy levels.

Figure 60

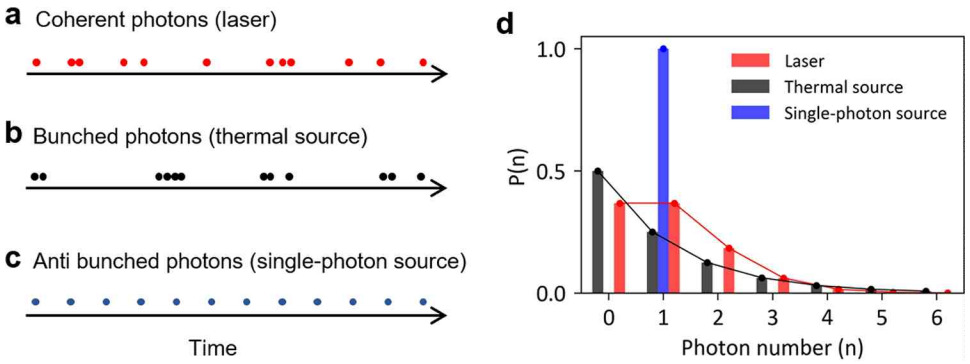

Schematics of bunching and antibunching light sources under the same intensity. (a) Randomly bunched photons in coherent light (laser). (b) Photon bunching in a classic thermal light source. (c) Photon antibunching in a single photon source. (d) Probability distribution of the number of photons for three sources when the average photon number $<n> = 1$, plotted based on equations from [197].

calculated probability values of detecting "n" photons at a given time. From top to bottom, they are coherent, bunched, and antibunched light sources, respectively.

The Poisson distribution elucidates the probability of a set number of occurrences within a specific time or space interval, assuming these events maintain a constant average rate and independence from each other. Hence, the probability distribution of photon numbers within a light beam is given by the following equation:

$$P(n) = \frac{\lambda^n e^{-\lambda}}{n!}, \tag{5.1}$$

where $P(n)$ signifies the probability of event "n" occurring, λ represents the mean value (average photon number), and n denotes the expected number of occurrences (expected

photon numbers). For comparative analysis, let us consider all three types of light sources with an average of one photon (i.e., $\lambda = 1$) over the same time span. In photon statistics adhering to the Poisson distribution, where all photons are independent, the red dots in Fig. 60(a) will tend to randomly cluster together. Accordingly, the red bar and line in Fig. 60(d) shows the histogram of this distribution. It is evident that most detection events would likely yield zero or one photon, whereas cases of two or more photons occurring in clusters remain possible. This inherent nature underscores the impossibility of attaining truly antibunched light solely by attenuating a laser source. A laser, being a coherent source, maintains a well-defined phase and amplitude across space and time. This coherence ensures that photons possess a fixed phase relationship with each other, implying a field devoid of intensity or frequency fluctuations.

Photons tend to cluster closely together in thermal light sources, such as sunlight and classical blackbody radiations [Fig. 60(b)]. Consequently, the majority of detection events from these sources typically yield zero photons [Fig. 60(d), represented by the black bar and line]. Conversely, in certain scenarios, photons can exhibit antibunching, forming the third category of light sources: referred to as single-photon sources [Fig. 60(c)]. In this case, photons adhere to a sub-Poissonian distribution, maintaining significant separation from each other. Here, the probability of detecting one photon in any detection event is nearly assured. An important consideration lies in the sampling time interval (detection), which significantly influences photon number statistics. Ideally, the time bin width for detection should be smaller than the photon interval to preserve the distinct features of the photon distribution. Otherwise, the information related to the distribution of photons might be obscured due to time averaging.

Given these nuances, how do we practically measure or validate the single-photon property experimentally?

Note on the Degree of Coherence and Correlation Function In quantum optics, correlation functions are used to characterize the statistical and coherence properties of an electromagnetic field. The first-order coherence is the amplitude–amplitude correlation of two fields. The correlation function can be described as $g^{(1)}(\tau) = \frac{\langle E^{\star}(t)E(t+\tau)\rangle}{\langle |E(t)|^2\rangle}$, where angled brackets represent the statistical averaging operator. Here $E(t)$ is the field at t moment and τ is the delay time. For instance, this applies to fringe patterns observed in Michelson interferometers or thin film interference patterns, which arise from the construction and destruction of the amplitudes of two fields. Second-order coherence, on the other hand, deals with intensity–intensity correlation. It is important to note that field intensity (or energy) relates to the square of the field amplitude. Consequently, fluctuations in the intensity of the electromagnetic field reflect variations in photon numbers within the stream. Considering the field intensity over a time scale (akin to our treatment for first-order coherence), the second-order coherence of the field pertains to the correlation between field intensities at moments t and $t + \tau$:

$$g^{(2)}(\tau) = \frac{\langle I(t)I(t+\tau)\rangle}{\langle I(t)\rangle^2}, \tag{5.2}$$

where $I(t)$ and $I(t+\tau)$ denote the field intensities at t and $t + \tau$ moments respectively, whereas τ represents the delay time.

The measurement of the second-order correlation can be done by a Hanbury Brown–Twiss (HBT) interferometer, a schematic of which is shown in Fig. 61.

Relating field intensity to photon numbers, considering their proportionality, if we assume an average photon number of 1, the intensity at two arms ($\tau = 0$) in Eq. (5.2)

Figure 61

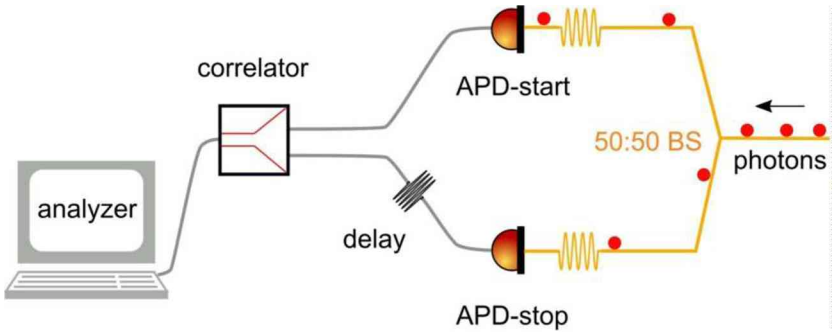

HBT interferometer and the schematics of photon antibunching measurement. Red dots stand for incident photons. Orange lines indicate the light paths, which can be fiber or free space.

can be expressed in term of photon numbers:

$$g^{(2)}(0) = \frac{\langle n(n-1)\rangle}{\langle n\rangle^2}. \tag{5.3}$$

Incoming photons are divided by a 50:50 fiber beam splitter before reaching two avalanche photodiodes (APDs) individually. Silicon-based APDs typically possess a dead time of approximately 50 ns, whereas for superconducting nanowire single-photon detectors, this time reduces to sub-1 ns. To validate the presence of single-photon sources, the capability to detect individual photons becomes crucial. Advanced photon detectors now enable the measurement of single photons within ultrashort time intervals. Time-correlated single-photon counting (TCSPC) is a precise and sensitive method with picosecond resolution to investigate the temporal dynamics of weak optical signals and is widely used for lifetime and time delay measurements. The common TCSPC is based on a "start–stop" technique, where a clock (counter or correlator) is triggered by the photon received from the "start" detector, then it is stopped by the subsequent photon received from the "stop" detector. The correlator carried out the intensity coincidence of two detectors as time delay. By iteratively performing these cycles, the relationship between coincidence and delay time is recorded as a $g^{(2)}$ histogram/curve. The characteristic light sources discussed earlier exhibit distinct $g^{(2)}$ curves, notably varying values at zero-delay time [Fig. 62]. This procedure mirrors time-resolved PL decay measurements, employing a pulsed laser to trigger the clock, and the detection of a single photon serves as the stop signal. Similar to lifetime measurements, the photon interval time in the HBT measurement can also be extracted.

5.2. SPEs in hBN

SPEs represent spontaneously emitting emitters operating within two-level systems. Zero-dimensional materials, inherently possessing discrete electron energy levels due to dimensionality confinement, exhibit the inherent potential to emit single photons. SPEs have long been documented in various entities, including single molecules [198,199], ions/atoms [200], and quantum dots [201]. Molecules, quantum dots and other complex objects in the condensed matter always possess higher excited levels, which can be reached by resonant absorption of a second photon by the first excited state. However, the swift relaxation back to the first excited state in most instances renders the emission from these higher levels undetectable. Consequently, only the emission between the lowest two levels becomes observable, effectively transforming the complex system into a two-level emitter [197].

Figure 62

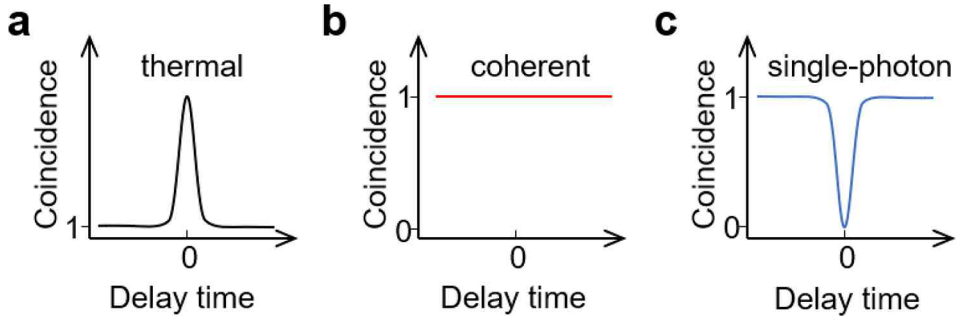

Schematics of normalized $g^{(2)}$ curves for three types of light sources: (a) thermal source; (b) coherent light; (c) single photon source.

Figure 63

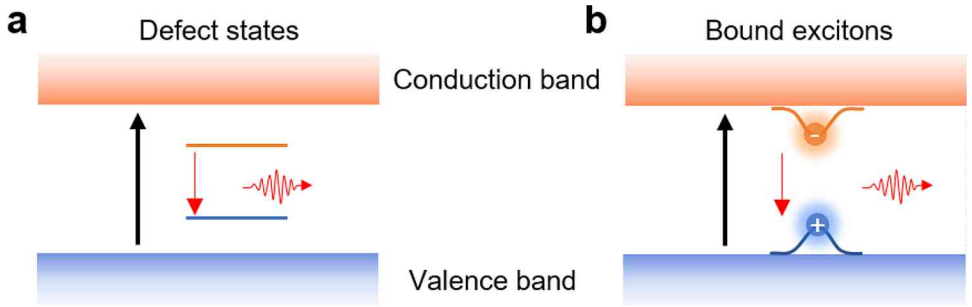

Two-level structure of SPEs in 2D materials: (a) deep defect levels in bandgap; (b) trapped bound excitons.

Another class of two-level systems comprises defect states within the bandgap [Fig. 63(a)]. These states are prevalent in solid-state matters, such as various color centers in diamond [202] and many others [203,204,205]. Nitrogen-vacancy (NV) center as an example, is the most well-studied defect, it consists of one lattice vacancy and an adjacent nitrogen atom which substitutes for a carbon atom. The nitrogen atom has five valence electrons, three of which form covalent bonds with the neighboring carbon atoms, whereas the other two form a lone pair. The vacancy has three unpaired electrons (from the nearest three carbon atoms), two of which form a quasi-covalent bond and one of which remains unpaired. The overall symmetry of the defect is axial (C_3 V). The NV center can exist in two charge states: neutral (NV^0) and negative (NV^-). The negative charge state is more stable and has a spin triplet ground state ($m_s = \pm 1$). The NV^- center can be optically excited and read out, making it a promising candidate for quantum information and sensing applications [206,207].

2D materials that host SPEs exhibit unique properties due to quantum confinement in the third dimension. Such as the bandgap transition from indirect to direct for monolayer transmission metal dichalcogenides (TMDCs) [208]. Over the past two decades, various techniques, such as stacking, twisting, and integration, based on 2D materials have been developed. The straightforward structure of these materials potentially simplifies the investigation of defect origins in comparison to their 3D counterparts. In addition, 2D materials showcase reduced losses in integrated photonics due to their high refractive index and ultraflat surface morphology. Furthermore, 2D materials offer a rich platform for exploring new quantum phenomena. An intriguing subset of sub-bandgap SPEs includes bound excitons [Fig. 63(b)], commonly observed in TMDCs, particularly in monolayer materials highly sensitive to localized strain confinement

[209,210]. However, the confining potential for electron–hole pairs is relatively limited (~0.5 eV [211]), and significant charge–phonon coupling restricts emissions primarily to lower temperatures. hBN stands prominently among 2D materials, often serving as a spacing layer in electronic devices for graphene and as a passivation layer for TMDCs [212,213]. Its layered nature and substantial bandgap largely position hBN as a flat and inert medium. However, since 2015, the photonic properties of hBN have gained substantial attention following the discovery of SPEs stemming from optically activated defects [108].

Figure 64 illustrates a distinctive emission pattern of hBN SPEs at room temperature under nonresonant excitation. In Fig. 64(a), the PL spectrum exhibits a prominent zero-phonon line (ZPL) accompanied by several satellite phonon sidebands (PSBs). In this instance, the ZPL is positioned at 567.1 nm, with a FWHM around 3.2 nm. The spectrum displays nonasymmetric shapes on the low-energy side, wherein additional peaks approximately at 570, 613, and 622 nm represent distinct PSBs contributing to the broadening of the ZPL. Specifically, these are linked to contributions from the out-of-plane acoustic and LO phonon modes, respectively [26,214]. Both emission and absorption processes are phonon-related phenomena. Previous reports on photoluminescence excitation (PLE) demonstrate phonon-assisted absorption processes [215]. Figure 64(b) depicts the corresponding second-order correlation curve, where the blue circles represent experimental data and the red line signifies the fitted curve. Typically, data are normalized to infinite delay time. Notably, the normalized data consistently surpass 1.0 in the flat region, indicating slight bunching, often attributed to the electron metastable state (discussed in the following). Hence, a fitting employing a three-level model is applied:

$$g^{(2)}(\tau) = a - (1+b)ee^{\frac{-|t|}{\tau_1}} + be^{\frac{-|t|}{\tau_2}}, \tag{5.4}$$

where t is the variant delay time and τ_1 and τ_2 in the negative and positive exponential decay components are the corresponding lifetime of the excited state and metastable state. The coincidence value at zero delay time can be extracted from the fitting. In this case, $g^{(2)}(0) = 0.10$ (without background emission correction) indicates the antibunching nature of the detected photons. hBN SPEs have very high brightness. As shown in Fig. 64(c), the saturated photon rate is over 4 million counts per second (cps). Although the atomic structure is unknown, for most situations, the dipole shows linear polarized emission [Fig. 64(d)].

5.2a. Note on ZPLs and PSBs

In solid-state emitters, the ZPL signifies emission originating from the intrinsic electronic transition: defined by the energy disparity between the ground and excited states. However, PL entails the absorption and subsequent emission of phonons, termed vibronic transitions, following the Franck–Condon principle (Fig. 65). Due to the huge mass difference, electronic transition takes place way faster than the nuclear movements. To realign with the new electronic configuration, the nucleus thus has to vibrate. Consequently, the emitted photon exhibits slightly reduced energy, manifesting as a tail in the spectrum [Fig. 64(a)].

This electron–phonon coupling-induced redshifted "tail" is called a PSB. ZPL together with PSB defines the line/spectral shape of the emission. Their intensity (energy) ratio is characterized by the Debye–Waller factor, a factor that describes thermal-motion-related scattering. It is also worth noting that the line shapes or the intensity ratio is not only temperature but also emitter species dependent. For example, the significant phonon coupling in NV color centers compared with group IV color centers (e.g., SiV) in diamond.

Figure 64

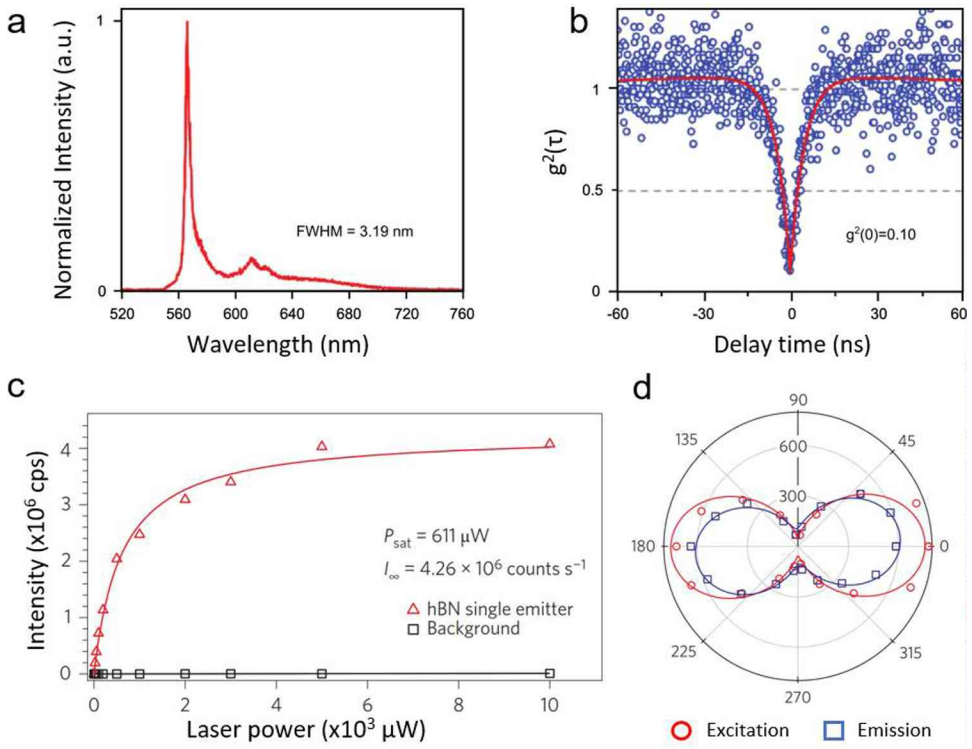

SPE from hBN: (a) one characteristic SPE PL spectrum at room temperature; (b) second-order autocorrelation curve of the emission; (c) saturated emission curve with increasing excitation power; (d) linear polarization of the excitation and emission. Panel (a) reprinted from Li *et al*., "Purification of single-photon emission from hBN using post-processing treatments," Nanophotonics **8**, 2049–2055 (2019). https://doi.org/10.1515/nanoph-2019-0099. © 2019 Li *et al*., published by De Gruyter, Berlin/Boston. Panel (b) reprinted with permission from Springer Nature: Tran *et al*., Nat. Nanotechnol. **11**, 37–41, Copyright 2016.

5.2b. Blinking and Metastable States

In an ideal scenario, a quantum emitter comprises a two-level electronic structure [Fig. 63(a)] exhibiting a distinct ZPL transition. However, in practical environments, the emitter is often influenced by its local surroundings, which can be significantly more complex. For instance, nearby defects, when optically pumped, may generate electric dipoles dynamically altering the emitter bandgap through the Stark effect. Consequently, the ZPL diffuses randomly within a small energy range, leading to spectrum broadening [216]. In the meantime, emission may be quenched via nonradiative transition such as charge and energy transfer to the environment [217,218]. A prevalent occurrence in such scenarios is the transition to intermediate metastable states or levels, resulting in emitter blinking.

Figure 66(a)–(d) illustrates characteristic variations in emission rates over time, with a histogram bin width of 10 ms [219]. As shown in Fig. 66(a), a stable emitter constantly emits photons, marked as an "on" state. Conversely, Fig. 66(b)–(d) portrays emitters randomly blinking, toggling between "on" and "off" states intermittently [220]. Here, the "off" states denote short-term absence or dim emission, distinct from bleaching, where the emitter undergoes permanent changes in a photoinduced reaction process, essentially "dying" [221]. The presence of metastable states is also evidenced in the autocorrelation curve, notably exhibiting bunching behavior, particularly in longer time

Figure 65

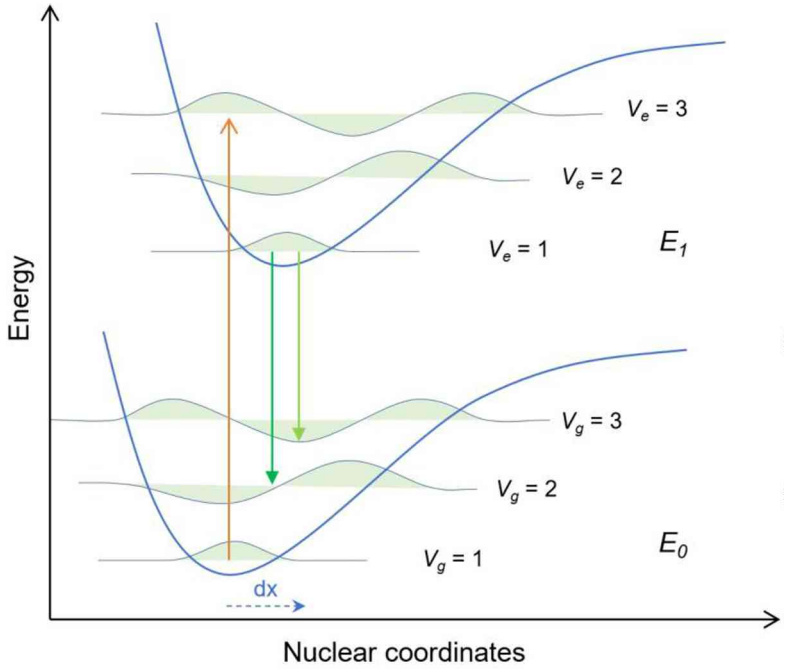

Franck–Condon diagram. Vertical transition stands for the electronic states, while the vibrational waves indicate the probability distribution of finding the nuclei in a given region of space. The nuclear movement is marked as dx. Here E_0 and E_1 are the ground state and excited state, respectively, and V_g and V_e are the vibration quantum numbers of the two states. The upward orange arrow represents absorption, and the green downward arrows indicate the corresponding emission.

scales [220]. When normalizing the coincidence data to infinite-long time, emitters without metastable states show a flat line shortly after its primary excited state lifetime decay region [Fig. 66(e)]. Contrastingly, the involvement of metastable states leads to prolonged decay, resulting in a bunching plateau [Fig. 66(f)]. For this specific emitter, a four-level model is applied to fit. The simulated $g^{(2)}$ curve and proposed level structures are demonstrated in Fig. 66(g) and (h), respectively. Although the number of metastable states can vary among emitters due to their complex and unknown local environments, this method enables the extraction or distinction of main components.

Given that the origin of blinking and spectrum diffusion is intricately linked to the local environment, engineering or suppressing blinking and spectrum diffusion is conceivable by employing thicker and higher-purity host materials [222]. In addition, studies have explored encapsulation, substrate effects, and repumping to investigate emitter stabilities [223–226]. On one hand, blinking diminishes the overall emission rate of SPEs and hinders their potential applications. On the other hand, this unique property can be leveraged to achieve optical superresolution, which is highly sought after in biosensing (discussed further in Section 5.2f).

5.2c. Resonant Excitation and Photon Dephasing

Photons, possessing identical quantum states akin to indistinguishable photons, wield significant influence across various quantum technologies such as quantum computing, communication, interference, and information processing [227,228]. Hence, characterizing the coherence of emitter photons holds paramount importance. Initially, one might expect the emission's ZPL energy to precisely match the electronic

Figure 66

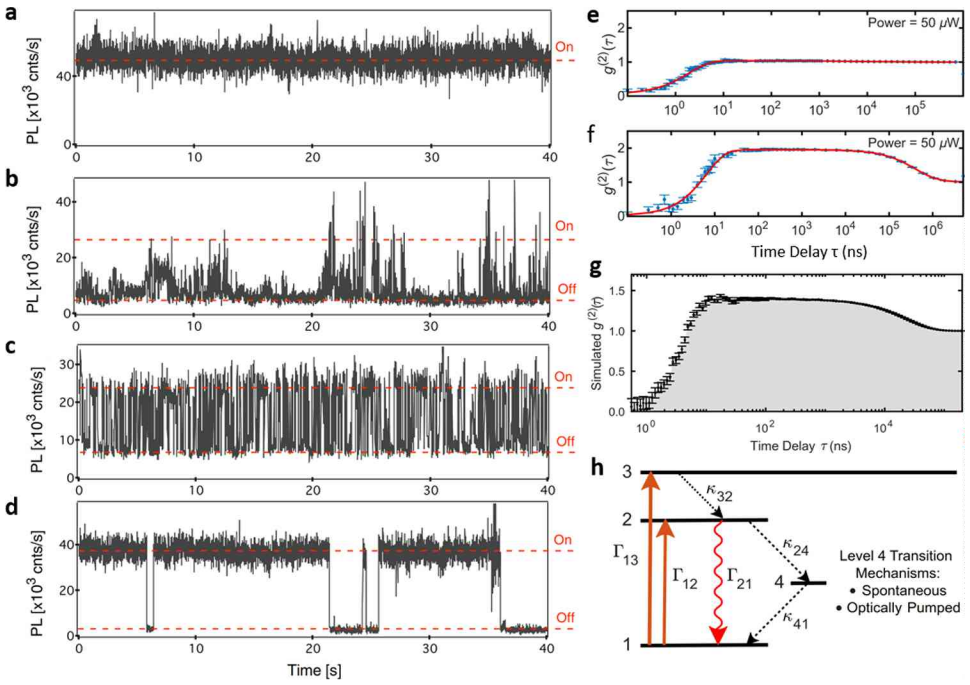

Blinking and metastable states of hBN SPEs. (a)–(d) Emission rate variation as time. Stable emission (a) and blinking emission shown in (b), (c), and (d). The bin width of histogram is 10 ms. (e) and (f) Characteristic autocorrelation curves of stable (e) and blinking (f) emitters. (g) Simulated $g^{(2)}$ curve with four-level schematics shown in (h). Panels (a)–(d) are Fig. 2 reprinted with permission from Martínez *et al.*, Phys. Rev. B: Condens. Matter Mater. Phys. **94**, 121405 (2016) [219]. Copyright 2016 by the American Physical Society. Panels (e)–(h) are Figs. 3 and 6(b) reprinted with permission from Patel *et al.*, PRX Quantum **3**, 030331 (2022) [220]. Copyright 2022 by the American Physical Society.

level's bandgap ($E_g = h\nu$), suggesting a monofrequency emission displayed as a delta function within the spectrum. However, in reality, the spectrum exhibits a natural linewidth, covering a range of frequencies caused by the uncertainty principle where we cannot measure the energy and lifetime of a particle simultaneously. Expressed as $\Delta E * \Delta t > \hbar/2$, here $\hbar$ is the reduced planck constant. Here ΔE and Δt are the uncertainty of the energy and lifetime, respectively. Therefore, the linewidth Γ (FWHM in frequency) is one half the broadening frequency ($\Delta\nu$):

$$\Gamma = \frac{\Delta\nu}{2} = \frac{\Delta E}{2h} > \frac{1}{2\pi\Delta t}.$$

As an example, a measured average lifetime of 4.4 ns corresponds to a linewidth of ~36 MHz [24]. This homogeneous broadening leads to a Lorentzian shape profile. The natural linewidth is temperature independent, as the lifetime does not change much with temperature. This linewidth, also termed the Fourier transfer limited (FTL) linewidth, is perceptible. Yet, in practical scenarios, the ZPL emission line substantially exceeds its natural linewidth due to other broadening mechanisms, primarily categorized into two types: Gaussian-shaped inhomogeneous broadening and Lorentzian-shaped homogeneous broadening [216]. Lattice phonons and charge fluctuations are identified as two principal pathways leading to dephasing. While phonon coupling contributes to homogeneous broadening, charge fluctuations induce spectral

diffusion, resulting in inhomogeneous broadening. Specifically, unlike an ideal two-level system where the ground and excited levels display singular, narrow lines, these levels extend when local charge fluctuates. Within the excitation beam spot (sub-1 μm^2 in lateral scale), numerous atomic impurities or optically active defects coexist. The excitation not only targets the intended emitter but also triggers these charges to create local fields that unpredictably shift the emitter's energy levels. Therefore, this inhomogeneous broadening yields the Gaussian-shaped line profile of the emitter.

Among these mechanisms, phonons emerge as the predominant dephasing pathway. Lattice phonons persist as long as the temperature remains above absolute zero (0 K), as per the temperature definition. A simple reduction in environmental temperature from room temperature to 5 K significantly reduces the linewidth from several nanometers to below 0.1 nm [24], as depicted in Fig. 67(a). In this illustration, a nonresonant laser excitation is employed, and the ZPL photons are filtered through a longpass filter. The observed emitter consistently demonstrates stable emission concerning both frequency and intensity within the recorded timescale. Notably, the displayed linewidth aligns with the spectrometer's resolution limit. To surpass this limitation, a proposed solution involves a resonant excitation scheme to directly/indirectly measure the ultra-narrow linewidth. The experimental approach includes PLE, where the excitation laser wavelength is meticulously swept, and emitted phonons are detected using photon detectors. This method prioritizes intensity information, leveraging the excitation laser to carry spectral frequency information, conveniently synchronized with detection events. Given the similar if not identical frequencies of the excitation laser and emitted phonons, collection can be accomplished through either a cross-polarization scheme [229] or PSB collection [230], effectively isolating the phonons from the laser.

Figure 67(b) portrays the PLE spectrum within a cryostat at 5 K with an excitation power that is well below the saturation power of the emitter. Owing to the low emission rate under the low-power excitation, usually multiple laser scans are applied, and the registered photons at each laser detuning frequency are integrated. The overall spectrum demonstrates an approximate FWHM of ~1.1 GHz. To discern the active broadening mechanism, researchers fit the spectrum using different functions, namely Lorenzian and Gaussian. Both models align well with experimental results; however, the Lorenzian function exhibits marginally lower residual levels, as indicated in the bottom panel of Fig. 67(b). This suggests that while both phonons and spectral diffusion contribute to the line shape, phonons exert a dominant influence even at 5 K and low excitation power. Mitigating spectral diffusion by low-power excitation and dynamic spectral tuning is crucial [24,231]. Individual scan suppresses the diffusion effect resulting in a narrower spectrum or even achieving FTL emission when the low frequency diffusion is resolved. The right-hand panel of Fig. 67(b) shows a single-scan spectral that reaches the FTL linewidth when the low-frequency diffusion is resolved by the fast laser detuning (<30 ms per scan) [26,231].

hBN's phonons have been studied extensively [26,214]. Figure 67(c) compares one-phonon band features (red curve in the left panel) with the intrinsic phonon modes in hBN crystal, elucidating the electron–phonon process. Here, the red curve one-phonon band is extracted from the experimental emission spectrum after carefully subtracting the Lorentzian-shaped ZPL [26]. Its main band features, particularly the out-of-plane acoustic (ZA) modes and in-plane LO modes (shaded in green), align well with theoretical phonon modes. Resent preprint results reveal that it's the gap between ZPL and the first ZA mode that likely limits the coherent optical control of the hBN quantum emitters [232]. Importantly, the local environment varies among emitters. For example, in another cryogenic study, a gradual yet uniform broadening occurs when the local temperature increases from 4 to 40 K [24]. However, as the pump

Figure 67

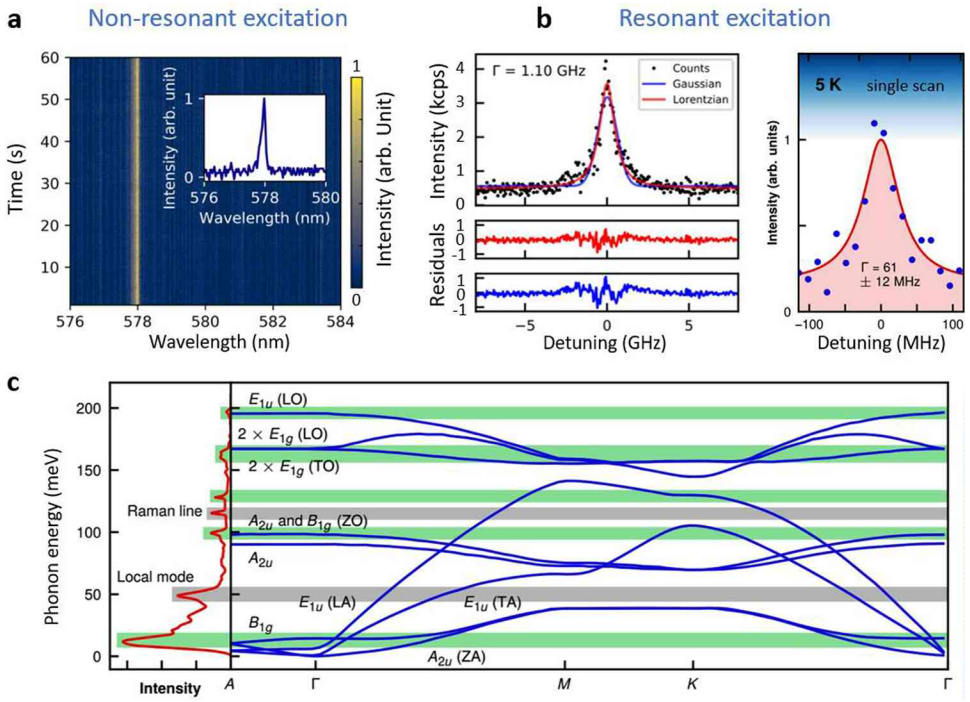

hBN SPE spectral dynamics in cryogenic temperature. (a) Spectrometer limited emission linewidth under nonresonant excitation. (b) Ultranarrow linewidth under resonant excitation of integrated scans (left) and single scan (right). (c) Comparison of the one-phonon band (red plot at the left) and the calculated intrinsic phonon band structure (blue plot at the right). Each band is labeled by its symmetry at the Γ-point. The green highlighted peaks in the one-phonon band are coincident with bands leveling off at high-symmetry points in the band structure. The gray bars indicate peaks that are not coincident with any features in the band structure. The phonon mode marks label L as in-plane longitudinal, T as in-plane transverse, and Z as out-of-plane combined with A for acoustic or O for optical. Panel (a) and left part of panel (b) reprinted with permission from [24] © The Optical Society. Right part of panel (b) and panel (c) from Hoese *et al.*, Sci. Adv. **6** (2020). Reprinted with permission from AAAS.

power increases from 3 to 210 nW, the inhomogeneous spectra diffusion becomes increasingly evident [24].

The broadening of the spectrum originates from variations in the electronic structure due to phonon–electron coupling and charge fluctuations. Moreover, the broadened line shape of the emitter is predominantly shaped by the spectral diffusion at high temperatures [232]. Despite being infrequent, reports indicate achieving FTL emission down to ~55 MHz (corresponding to ~2.88 ns excited state lifetime) from hBN SPEs even at room temperature by Dietrich *et al.* [25,231].

Recent findings by Horder *et al.* unveil the observation of Rabi oscillations from a group of blue emitters, where the emitter is driven to a coherent superposition of ground and excited states. Coherent time extend up to 0.9 ns through HBT experiments [17]. In addition, Fournier *et al.* have exhibited two-photon interference from the same group of emitters, demonstrating partial indistinguishability of approximately 0.44 within a 3-ns time window. Their simulations depict over 90% visibility when considering the Purcell effect [233]. These significant findings firmly position emitters sourced from

hBN as exceptionally promising candidates for a wide array of future quantum technologies. Their capabilities for achieving near-ideal characteristics—such as Fourier transform-limited emissions, coherent behavior, and the potential for high visibility in photon interference—underscore their potential contributions to the advancement of quantum applications.

5.2d. Spin Defects in hBN

Optically addressable spins serve as valuable platforms for quantum applications, as demonstrated in systems such as color centers in diamond and silicon carbide [220,234]. Reports suggest that hBN hosts several spin transitions, including ensembles of negatively charged boron vacancies (denoted as $V\mathrm{B}^-$) [235–239] and visible single-photon defects [221]. The technique employed to manipulate and measure the spin states of these defects is known as optically detected magnetic resonance (ODMR), utilizing laser and microwave.

The structure of $V\mathrm{B}^-$ comprises the hBN lattice with one missed boron atom as illustrated in Fig. 68(a) [235]. Its energy level structure includes a triplet ground state, a triplet excited state, and a singlet metastable state. The two electrons (negatively charged) on the ground state are antispin ($m_s = 0$). Under an optical pump (green arrow line) the electron is pumped to the excited state and then relaxes either directly to the ground state and emits a photon [red arrow line, spectrum shown in Fig. 68(b)] or alternatively to a singlet state by intersystem crossing and then return to the ground state (purple arrow lines). As shown in Fig. 68(b), the broad emission spectrum centered at around 850 nm, with a decay lifetime of about 1.2 ns [235]. However, the emission is found to be an ensemble of $V\mathrm{B}^-$ as no single emission has been verified so far. The alternative transition route results in the reduction of total PL intensity. Both transitions are allowed without external stimuli. Applying a resonant microwave frequency places the defect in a degenerate state ($m_s = \pm 1$). In this scenario, the second route is favored as the direct transition is spin-forbidden. A noticeable ODMR contrast, indicating differences in PL intensity, emerges [Fig. 68(c)] at about 3.5 GHz (ν_0). The energy splitting at zero magnetic field is attributed to the unpaired electron spins in the system [235]. Additional magnetic fields would further split the energy level through Zeeman effect, leading to two asymmetric resonances (ν_1 and ν_2) relative to the zero-field splitting frequency. However, $V\mathrm{B}^-$ suffers from a weak PL intensity due to its low quantum yield [20,240]. Various techniques have been implemented to significantly enhance its PL, such as coupling with plasmonic nanostructures [22,241,242], dielectric cavities [243,244], and metasurfaces [245]. Despite the enhanced emission, their ODMR contrasts remain similar. It has been shown that a coplanar microwave waveguide configuration is beneficial as it enables the microwave field to drive the spin defect more efficiently through improved field alignment [241,246]. In addition, thermal treatment above 500°C is reported to enhance the ODMR sensitivity of $V\mathrm{B}^-$, regardless of whether it occurs during or after the ion implantation process that generates the $V\mathrm{B}$ defects [247].

Figure 68(d)–(f) shows ODMR in a specific group of single emitters that operate in the visible range [221]. Figure 68(d) presents one SPE with multiple transitions in carbon incorporated hBN thin film grown using the metal organic vapor phase epitaxy (MOVPE) method [248,249]. Researchers have correlated the observation of ODMR with two distinct bunching timescales. Notably, the ODMR phenomenon is observed only in bunching curves that fit well with a tri-exponential function. Moreover, the ODMR contrast varies in sign among different emitters: some display positive contrast while others exhibit negative contrast. Consequently, the contrast from single defects is considerably stronger than that from ensembles [Fig. 68(e) and (f)]. Table 2 summarizes the primary hBN emitter properties to date.

Figure 68

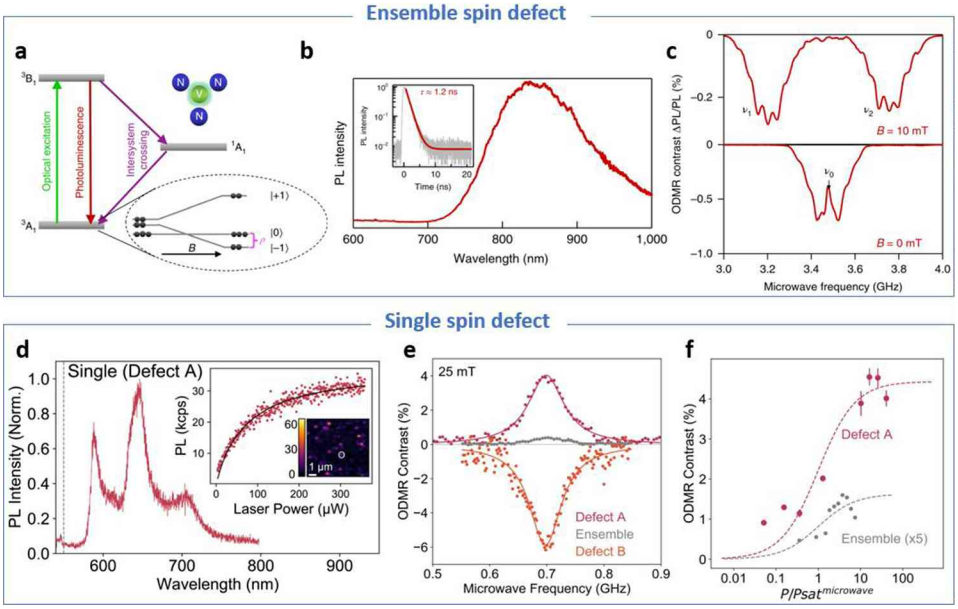

Single and ensemble spin defects in hBN. (a) Level structure of negatively charged boron vacancy defect and its PL spectrum (b). (c) ODMR and splitting under an external magnetic field. (d) Single spin emitter. (e) Positive and negative ODMR contrast. (f) Power-dependent ODMR contrast. Panels (a)–(c) reprinted with permission from Springer Nature: Springer Nature: Gottscholl *et al.*, Nat. Mater. **19**, 540–545, Copyright 2020. Panels (d)–(f) reprinted with permission from Springer Nature: Stern *et al.*, Nat. Commun. **13**, 618 (2022).

Table 2. hBN SPE Features

Properties	Values
Emission range	300–800 nm [14,15,18]
Single photon purity	<0.02 [250]
Brightness	>7 Mcps [251]
Operation temperature	Up to 800 K [252]
Peak width	<60 MHz at room temperature [231]
Emission lifetime	2–7 ns [19]
Polarization	Linear [108]
Stability	>8 months [250,253]
Spin defect	VB^- and some visible single emitters [221,236]
Cathodoluminescence	Yes [14,15,16]

5.2e. Note on Quantum Numbers

Quantum numbers play a pivotal role in describing the position and energy of the electron in an atom. There are four quantum numbers, the principal (n), azimuthal or orbital angular momentum (l), magnetic (m_l), and spin (m_s) quantum numbers, each with their respective permissible values as outlined in Table 3. The principal quantum number (n) designates the electron shell in an atom. Electrons can transition between different shells if they possess sufficient energy. For instance, when capturing a photon with enough energy, an electron can leap from an inner shell (lower energy) to an outer shell (higher energy, corresponding to a larger n value). Subsequent radiative relaxation emits a photon as the electron returns to a lower quantum number. In the PL process, electron transitions primarily occur between various principal quantum numbers, aside from vibrational levels. SPEs are part of such quantized systems,

Table 3. Four Quantum Numbers

Quantum Number	Symbol	Possible Values	Meaning
Principal quantum number	n	1,2,3,4. . .	Electron shell
Angular momentum quantum number	l	0,1,2,3,. . . ,(n – 1)	subshell
Magnetic quantum number	m_l	–l, . . . ,–1,0,1. . . l	Total orbital number and orientation
Spin quantum number	m_s	+½, –½	Electron spin direction

exhibiting different energy levels or bandgaps compared with classical many-body or ensemble systems.

The orbital angular momentum quantum number (l) is intimately tied to the principal quantum number, defining the subshells within each principal number and shaping specific electronic orbitals. The "s, p, d, f, g, h" orbitals are well known for people working in different fields, representing distinct orbital shapes. The magnetic quantum number (m_l) defines the total orbital number and the orientation of the orbitals. It considers the orbital projection of the angular momentum to a given axis. The last one is electron spin quantum number, m_i, it consists of only two possible values, either –½ or +½. It is worthwhile to know that maximally two electrons are allowed to occupy the same orbital only if they have different spin direction. It is also known as the Pauli exclusion principle, that interpreted as no two electrons can take the identical four-quantum numbers in an atom. Therefore, the microwave-induced electron spin flipping in the $V\mathrm{B}^-$ or $\mathrm{N}V^-$ defects must give rise to the energy level splitting (dashed circle in Fig. 68(a)).

5.2f. Optical Superresolution of hBN SPEs

hBN SPEs are instrumental in enabling optical superresolution imaging due to their stochastic and nonlinear emission properties. These characteristics encompass the spatial and spectral distribution alongside the induced blinking from metastable states. Notably, the nontoxicity and room-temperature operation of hBN emitters make them potentially valuable for superresolution imaging within biological environments [254]. Two approaches are reported to achieve optical superresolution imaging, namely the wide-field spectral single-molecule localization microscopy (spectral SMLM) and reversible saturable optical fluorescence transitions (RESOLFTs).

Spectral SMLM heavily relies on a highly sensitive detector, such as an electron-multiplying CCD. During operation, this detector captures both the spatial (x, y) information of the emitters within the field of view (excited area) and their spectral data (λ) over time (t). As distinct emitters exhibit independent blinking, even those closely positioned in space can be distinguished at different moments. This capability allows for the reconstruction of a superresolution map based on numerous snapshots, achieving resolutions as fine as 20 nm. As illustrated in Fig. 69(a), the continuous excitation of an hBN thin film on a transparent substrate is captured, while simultaneously recording spectral data. The resulting reconstructed map showcases colorful emitters upon stacking the spatial and spectral information [255,256]. This method, according to researchers, provides insights into the correlation between defect emission and strain, as well as the impact of substrate and encapsulation on defect formation and stability.

Ground state depletion (GSD) represents a RESOLFT microscopy technique that operates by employing a high-intensity laser beam to deplete the fluorescence emission of molecules in the excited state. This action effectively retains only a small fraction of molecules in the ground state, capable of emitting light. By systematically scanning the laser beam across the sample, a subdiffraction image can be reconstructed using the fluorescence signals emitted by the remaining ground state molecules [257]. When

Figure 69

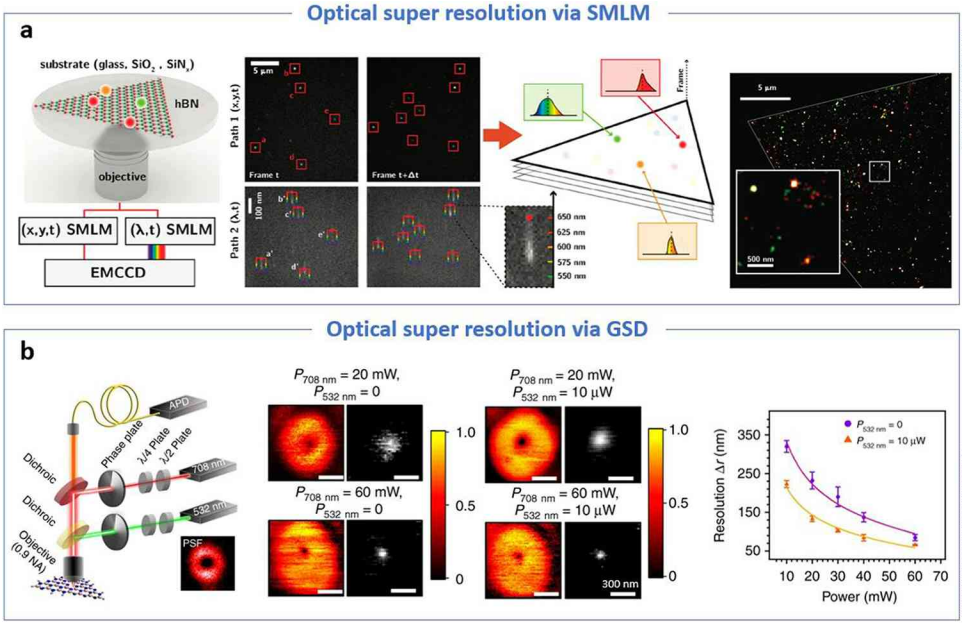

SPE optical superresolution: (a) wide-field spectral SMLM and (b) ground-state depletion microscopy. The scale bars in (b) are equal to 300 nm. Panel (a) reprinted with permission from Comtet *et al.*, Nano Lett. **19**, 2516–2523 (2019) [255]. Copyright 2019, American Chemical Society, https://doi.org/10.1021/acs.nanolett.9b00178. Panel (b) reprinted with permission from Springer Nature: Kianinia *et al.*, Nat. Commun. **9**, 874, Copyright 2018.

combined with structured light illumination, GSD can achieve high lateral resolution, approaching approximately 50 nm.

Mehran *et al.* have reported a category of hBN quantum emitters featuring a fast-decaying four-level intermediate state and a long-lived metastable state accessible from the first excited state. The emission intensity is greatly enhanced when repump the defect with a second laser that manipulates the transition of metastable state [226]. While this approach requires controllable emitter bright/dark transition and high-power resilience. In the imaging process, dual-doughnut-beam lasers at 532 and 708 nm are employed. The beam point spread function of two lasers is shown in the inset of Fig. 69(b) which shows near-zero intensity in the center. To deplete the ground state, the 708-nm laser with high power of 20 mW (70 mW) was applied to the emitter. And the repumping 532-nm laser power of 10 μW was used. Consequently, far-field superresolution imaging of individual emitters with ~60 nm resolution is then achieved.

5.2g. SPE Hosts and Generation Engineering

Crystals inherently contain defects, and SPEs have been discovered in various forms of hBN, including nanoflakes, bulk crystals, and thin films, as depicted in Fig. 70. Nanoflakes [Fig. 70(a)] tend to possess more defects due to their higher specific surface area compared with bulk crystals or films. In addition, a straightforward annealing process has been observed to activate or create emitters in hBN, a phenomenon reported in numerous studies [18,108,225,258–260]. One reason behind this is the reaction of hBN in air beyond 800°C [261]. Small hBN nanoflakes can be produced either through a top-down approach, such as sonication exfoliation [262] and cryomediated exfoliation [263], or by a bottom-up approach, such as hydrothermal synthesis [264].

Figure 70

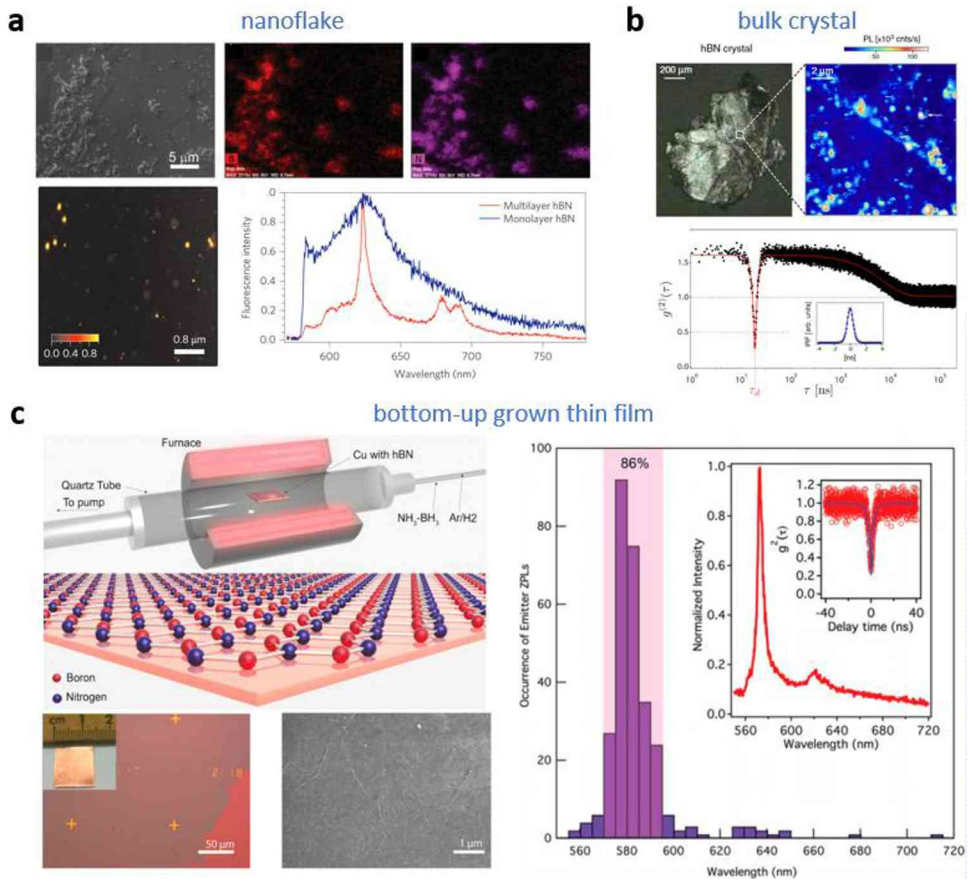

Main hBN SPE sources: (a) hBN nanoflake; (b) hBN bulk crystal; (c) hBN thin film by bottom-up growth. Panel (a) reprinted with permission from Springer Nature: Tran *et al*., Nat. Nanotechnol. **11**, 37–41, Copyright 2016. Panel (b) is Figure 1 reprinted with permission from Martínez *et al*., Phys. Rev. B: Condens. Matter Mater. Phys. **94**, 121405 (2016) [219]. Copyright 2016 by the American Physical Society. Panel (c) reprinted with permission from Mendelson *et al*., ACS Nano. **13**, 3132–3140 (2019) [267]. Copyright 2019 American Chemical Society, https://doi.org/10.1021/acsnano.8b08511.

The second source of hBN SPEs is bulk crystals. High-purity hBN bulk crystals naturally contain few SPEs [Fig. 70(b)] [219,265]. Although the bulk crystal is rarely used directly, the exfoliated flake is well known for its high-crystallinity and low-dimensional nature. Many efforts have been directed toward increasing the emitter density in these exfoliated flakes, a topic that we discuss later.

The third significant source is thin films grown through bottom-up techniques such as CVD. CVD encompasses various formats classified by vacuum levels, vapor types, precursors, deposit rates, plasma assistance, etc. Verified sources for hBN SPEs include methods such as low-pressure CVD (LPCVD) and MOVPE [248,266]. Epitaxy methods such as MBE, among others, have also been used [90]. Figure 70(c) is the LPCVD growth of hBN by Mendelson *et al.* [267]. The gown hBN film on copper foil shows a large film scale and high emitter density (~100 to 200 emitters per 10 μm^2). Over 80% of them are centered at 580 nm when pumped with a 532-nm laser. Given precise thickness control and a high density of emitters/defects, CVD-related methods are gaining increasing attention. Furthermore, by performing ion-implantation experiments, Mendelson *et al*. confirmed that carbon implantation creates SPEs in the

visible spectral range. Their computational analysis of the simplest carbon-containing defect species suggests the negatively charged $V_BC_N^{(-)}$ defect as a viable candidate and predicts that out-of-plane deformations make the defect environmentally sensitive [248].

Highly crystalline hBN crystals have lower defect density which makes SPEs rare. Therefore, researchers have developed methods to engineer the local defect density and manipulate the SPE generation. One such method involves using tape-exfoliated hBN flakes from bulk crystals for defect generation and emitter formation study as shown in Fig. 71. The effectiveness of plasma in emitter generation has been reported since 2018 [250,268]. Recent studies highlight that both oxygen plasma irradiation and high-temperature annealing (850°C) are crucial for generating hBN SPEs [Fig. 71(a)] [259]. Nitrogen ion and heavy-ion irradiation have also been reported to create SPEs in hBN. Previous studies have often employed annealing in an aragon atmosphere around 850°C for emitter activation [269,270,271]. A recent work from Lyu *et al*. demonstrated that carbon-rich atmosphere annealing is more effective for single-crystal hBN flakes [Fig. 71(b)] [258]. In this study, samples were annealed at 900, 1000, and 1100°C in a mixed atmosphere ($Ar:CH_4:H_2 = 15:5:1$) under a pressure of 1 Torr for 1 hour and then cooled to room temperature naturally in the tube furnace. Optimizing conditions at 1000°C resulted in the best performance, hosting SPEs with a density of 0.012 μm^{-2} [258]. This serves as supportive evidence indicating that carbon-related atomic structures are likely the origin of hBN emitters.

SPEs tend to form at the edges and ridges of the high-purity hBN flakes, and their occurrence probability can be manipulated by destructive irradiations [272,273]. Femtosecond laser ablation is a direct wring technique to create boron vacancy (VB) ensembles as shown in the left part of Fig. 71(c) [274]. However, to date the single-photon emission from VB has not yet been confirmed. Recent work indicates visible emitters can also be generated with laser ablation and annealing [right part of Fig. 71(c)] [275]. Figure 71(d)–(h) are three more different ways for generating SPEs in a controllable manner [15,276–279]. In Fig. 71(d), researchers use focused ion beam (FIB) to drill small holes (less than 1 μm diameter) on the hBN thin film [276]. They observed bright and localized PL that matched the geometry of the patterned structures. Moreover, second-order photon correlation measurements on these bright spots reveal single and multiple SPEs. By optimizing the FIB parameters and annealing (in oxygen at 850 °C), they create patterned single SPEs with a yield of 31% which is close to the Poissonian limit. They also used AFM to study the morphology near emission sites and discover that single SPE yield is maximized with smoothly milled holes on unwrinkled hBN. Notably, this work is processed on the CVD hBN film. Subsequently, Glushkov *et al*. apply FIB milling to exfoliated flakes. Although they do not observe SPEs in this work, they managed to create optically active defects by FIB and water [280]. Another straightforward concept is mechanical indentation. By scratching the hBN flakes with an AFM tip, researchers introduce defects to the lattice. After 1000°C annealing in argon, they managed to get SPEs. The achieved SPEs yields are above 30% by utilizing multiple indent sizes, and a maximum output of 36% is demonstrated for the indent size of around 400 nm [277].

An alternative approach showing promise in modifying the electronic structure of hBN involves electron beam irradiation [Fig. 71(f)]. This method is less destructive compared with using high-kinetic-energy ions, as electrons process less momentum and smaller interaction volume. Moreover, the high spatial resolution of the electron beam enables precise defect generation. Clarisse *et al*. demonstrated stable and bright single-photon emission from electron-beam-induced defects under nonresonant laser

Figure 71

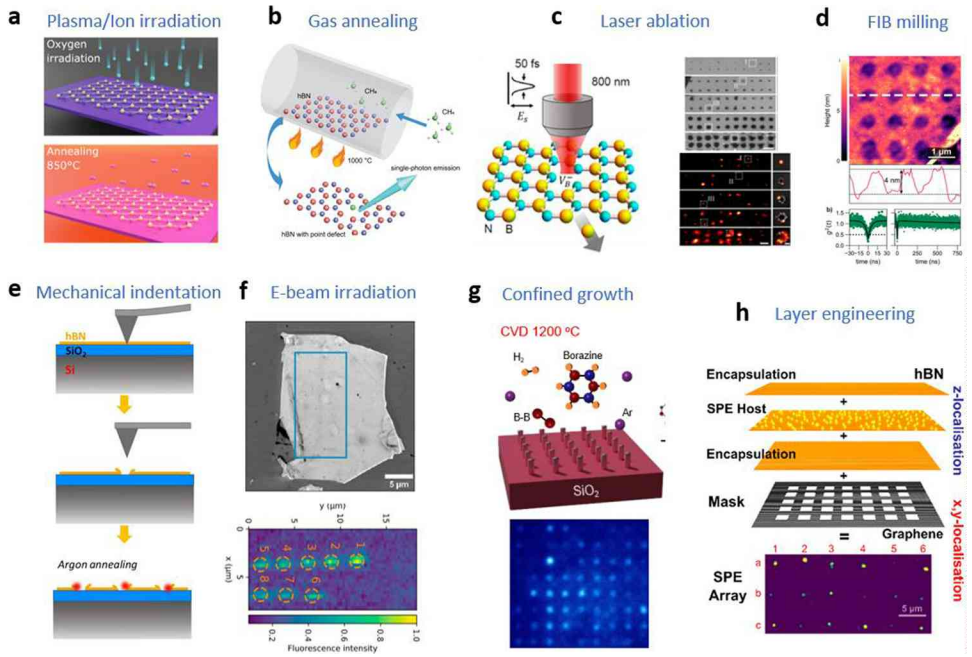

SPE generation thin hBN flakes/films: (a) plasma etching and annealing in exfoliated flakes; (b) carbon environment annealing in exfoliated flakes; (c) femtosecond laser irradiation of *V*B ensembles and visible emitters [275]; (d) FIB milling in exfoliated flakes; (e) mechanical indentation by the AFM tip in exfoliated flakes; (f) electron-beam irradiation in exfoliated flakes; (g) grown thin film on nanopillars; (h) thin film layer engineering. Panel (a) from Fischer *et al.*, Sci. Adv. **7**, eabe7138 (2021). Reprinted with permission from AAAS. Panel (b) reprinted with permission from Lyu *et al.*, Appl. Phys. Lett. **117** (2020) [258]. Copyright 2020, AIP Publishing LLC. Panel (c) reprinted with permission from Gao *et al.*, ACS Photonics **8**, 994–1000 (2021) [274]. Copyright 2021 American Chemical Society, https://doi.org/10.1021/acsphotonics.0c01847, and Gan *et al.*, ACS Nano **16**, 14254–14261 (2022) [275]. Copyright 2022 American Chemical Society, https://doi.org/10.1021/acsnano.2c04386. Panel (d) reprinted with permission from Ziegler *et al.*, Nano Lett. **19**, 2121–2127 (2019). Copyright 2019 American Chemical Society, https://doi.org/10.1021/acs.nanolett.9b00357. Panel (e) reprinted with permission from Xu *et al.*, Nano Lett. **21**, 8182–8189 (2021). Copyright 2021 American Chemical Society, https://doi.org/10.1021/acs.nanolett.1c02640. Panel (f) reprinted with permission from Springer Nature: Fournier *et al.*, Nat. Commun. **12**, 3779, Copyright 2021. Panel (g) reprinted with permission from Li *et al.*, Nano Lett. **21**, 3626–3632 (2021) [278]. Copyright 2021 American Chemical Society, https://doi.org/10.1021/acs.nanolett.1c00685. Panel (h) reprinted with permission from Stewart *et al.*, ACS Nano **15**, 13591–13603 (2021) [279]. Copyright 2021 American Chemical Society, https://doi.org/10.1021/acsnano.1c04467.

excitation [15]. They observed a group of blue color (~440 nm) SPEs in their work. Gale *et al.* later enhanced this approach and created an array of blue emitters [16]. Notably, the CL results indicate the atomic structure of this specific type of defect may be linked to a known group of existing UV defects [14]. This marks the first confirmed hBN SPE that can be deterministically fabricated in both space and spectrum simultaneously.

Table 4. hBN SPE Sources

Source Type	Synthesis	Process
Bulk crystal	HPHT	
Nanoflakes	Exfoliation Hydrothermal LPCVD	Annealing [18,108,215,219,265]
Thin film	MOVPE MBE	Annealing [23,248,267,281] /UV–ozone [23]/strain [281]
Thin flake	Exfoliation	FIB milling [276] Chemical etching [282] Gas annealing [18,258] e-beam irradiation [14–16] Laser irradiation [272,274,283] Mechanical indentation [277]

Several other endeavors aim to deterministically create or activate SPEs in CVD hBN films. By confining growth to specific scale, Chi *et al.* demonstrated a scalable and large-area hBN SPE array on SiO_2 nanopillars [278]. Similarly, strain activation involves transferring CVD films to pillar structures. Proscia *et al*. proposed that the large energy gap inherent to this van der Waals material stabilizes the emitters at room temperature within nanoscale regions defined by substrate-induced deformation of few-atomic-layer hBN. Their analytical and numerical modeling show that emitter activation is the result of carrier trapping in deformation potential wells localized near the points where the hBN film reaches the highest curvature [281]. Stewart *et al*. [279] explored the quenching and protection effect of SPE emission to achieve 3D control of hBN SPEs. While hBN emitters can be quenched by contact with graphene [218], sandwiching the emitter between two monolayer hBN layers can protect it from quenching. This layer stacking strategy allows atomic-level modulation of SPEs vertically (z axis) and control in the x–y plane by stacking hBN with a patterned graphene layer [279]. These methods for creating/activating the hBN emitters are summarized in Table 4.

5.2h. hBN SPE Emission Tuning (Strain, Stark Shift, and Electrical Gating)

hBN SPEs prove highly adaptable and versatile in practical applications, particularly for large-scale integration, owing to their facile emission tuning and engineering capabilities. However, there are instances where emitters are not perfectly coupled to their corresponding cavity due to slight wavelength mismatch. This issue can arise due to various real-life factors. Hence, dynamic tuning of the emission becomes necessary.

Primarily, the bandgap and energy levels are dictated by the periodic geometrical structure of crystal lattices. Any deformation in the lattice structure or a shift in the nuclei–electron location, caused by strain or external electric fields, can result in variations in energy levels. The advantageous aspect with 2D materials such as hBN is the ease with which local strain and external fields can be applied.

Grosso *et al*. reported strain-induced tuning of SPE emission at room temperature, achieving a shift of over 6 meV, approximately equivalent to a 15-nm shift in the visible range [251,284,285]. The experiment involved transferring hBN films hosting SPEs onto a 1.5 mm-thick polycarbonate (PC) beam, which is flexible and bendable. In the experimental setup depicted in Fig. 72(a), strain was applied to the hBN lattice by bending the far edge of the x direction of the PC beam downward (or upward) while fixing the other. This bending in the x direction also induced slight compression along the width direction due to the high Poisson's ratio of the PC material. While the observed shift was small, simulations indicated a much larger potential tuning range. The right-hand panel of Fig. 72(a) shows the simulated spectral distribution in response to strain, predicting significant tunability along specific directions AC2 and

Figure 72

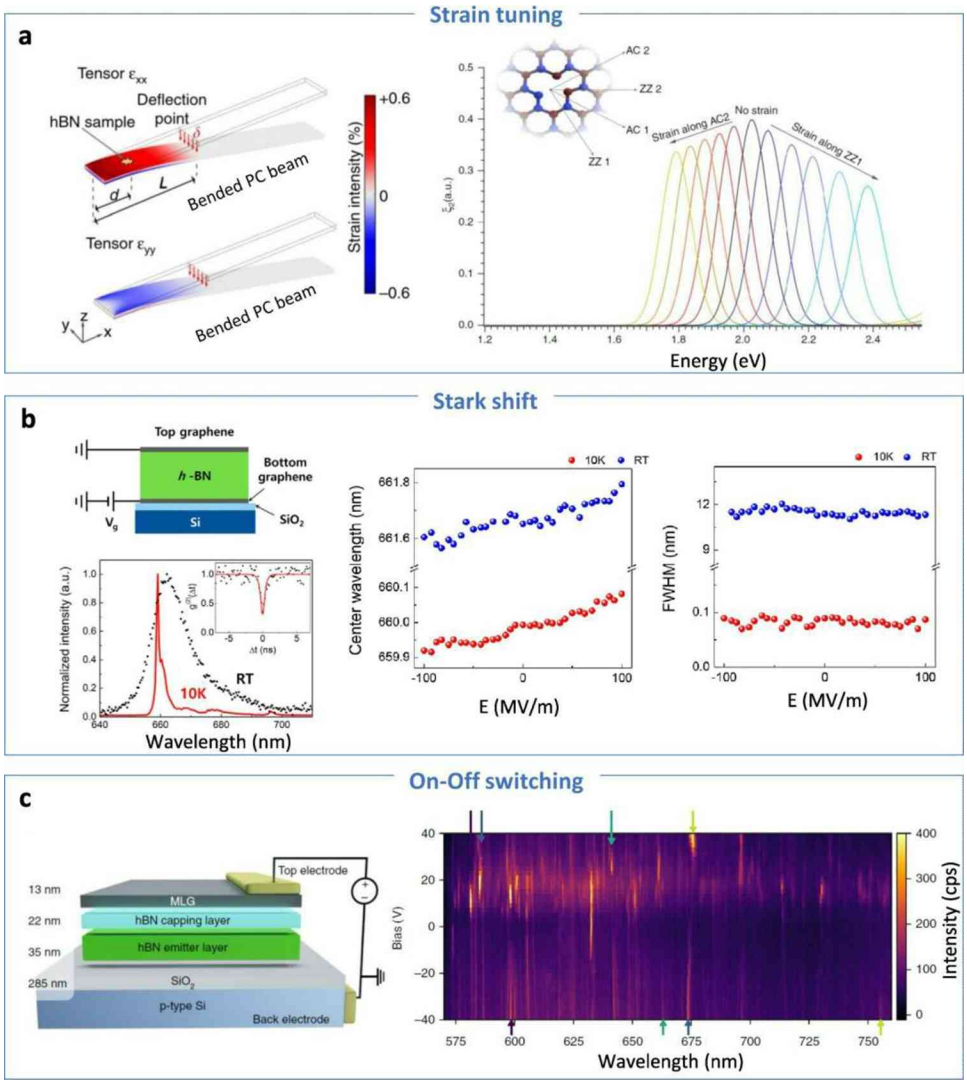

hBN SPE manipulation. (a) Energy level tuning with strain offered by a polycarbonate (PC) beam bending. (b) Energy level tuning with Stark shift effect. (c) Emission on-and-off switch with external bias. Panel (a) reprinted with permission from Springer Nature: Grosso *et al.*, Nat. Commun. **8**, 705, Copyright 2017. Panel (b) reprinted with permission from Noh *et al.*, Nano Lett. **18**, 4710–4715 (2018) [284]. Copyright (year) American Chemical Society, https://doi.org/10.1021/acs.nanolett.8b01030. Panel (c) reprinted with permission from Springer Nature: White *et al.*, Light Sci Appl **11**, 186, Copyright 2022.

ZZ1 (AC and ZZ stand for armchair and zigzag direction, respectively, as shown in the inset).

The Stark effect and Zeeman effect are two well-known methods to shift and split spectral lines using external electric and magnetic fields, respectively. The Zeeman effect introduces shifts based on electron spins (the spin quantum number, m_s), while the Stark effect impacts the electronic orbital levels (the principal quantum number, n). Zeeman splitting is sensitive to slight changes in the external magnetic field strength and is commonly used for magnetic field sensing. In contrast, the Stark effect offers a much larger tunable spectral range. Researchers have been working on tuning emission wavelength of emitters with the electric bias. In Fig. 72(b), a vertical gating device

using van der Waals heterostructures of hBN and graphene is demonstrated. An out-of-plane electric field was applied through graphene gates to tune the emission energy of individual defects. Investigations revealed Stark shifts of up to 5.4 nm per GV/m, suggesting the existence of out-of-plane dipole moments associated with atomic defect emitters. This Stark effect was observable not only at cryogenic temperatures but also at room temperature, which is crucial for applications operating under typical conditions. In addition, significant Stark effects with lateral bias have also been studied by Xia *et al.* [267,286].

A recent study showcased the achievement of optical ON–OFF switching of hBN emitters with bias voltage [285]. This device, similar in structure to the aforementioned Stark tuning setup, included an additional hBN layer to prevent direct contact with graphene, which could otherwise quench the emitter via charge transfer. When varying the voltage, certain emitters were observed to activate only at nonzero voltages. Furthermore, emission wavelength, intensity, and spectral linewidth could be tuned simultaneously. This behavior was attributed to the Stark effect, which shifts and splits the energy levels of the SPEs due to the electric field. The selective activation was linked to the emitter's electric structures, and the authors proposed a hot electron injection model to explain this phenomenon.

Overall, the capacity for mechanical and electric modulation of single emitters harnesses the advantages of electronics for scalable integration in photonics and introduces new avenues for studying light–matter interaction in van der Waals heterostructures. Moreover, hBN SPEs show great promise in emerging fields such as quantum cryptography, sensing, and imaging. Among these applications, quantum key distribution (QKD) stands out as a straightforward quantum cryptography application due to the high antibunching purity, elevated photon rate, and the advantage of operating at room temperature using hBN SPEs. Two recent studies have demonstrated successful implementation of QKD using different protocols. Zeng, Al-Juboori *et al*. demonstrated QKD using the BB84 protocol [287,288], whereas Samaner *et al*. implemented free-space QKD based on the B92 protocol [289]. In addition to quantum cryptography, a plethora of quantum sensing applications have been investigated intensively with either single or ensemble emitters. These applications span over temperature [290–292], magnetic field [292–294], strain [295], nuclear magnetic resonance [239], radiofrequency [296], and more. While hBN SPEs have demonstrated Fourier-transform-limited linewidth for resonant excitation, obstacles such as spectral diffusion have impeded the production of indistinguishable photons [297,298]. Recent experimental advancements have showcased the potential for achieving two-photon interference from a specific subset of hBN emitters, demonstrating the capability to generate identical photons from hBN defects [233]. However, the observed level of indistinguishability remains moderate, signaling the need for further advancements in future studies. A recent report has underscored the manipulation of single-phonon wavefronts, enabling the tailored creation of structured single photons from hBN SPEs [299]. These developments shed light on the potential of hBN SPEs for more intricate quantum information applications, such as quantum computing and communication.

5.3. Optical Resonators

Optical resonators generally represent an arrangement of optical components that allows a beam of light to circulate in a closed path, representing one of the most useful optical components employed extensively in tunable laser systems, interferometers, optical parametric oscillators, etc. [300–302]. The confinement of light in resonators primarily relies on the high level of reflection in a closed system. Distinguished with their implementation, it can be further divided into three subclasses: FP cavity,

whispering gallery (WG) cavity, and photonic crystal cavity (PCC). In addition, an emerging type of resonator is the bound state in the continuum in an open system.

hBN-based optical structures, including resonators, waveguides, metasurface etc., are attractive given their low absorption (own to a large bandgap), high chemical stability and relatively high refractive index. Specifically, its refractive indices reach values as high as 1.86 (out of plane) and 2.14 (in plane) at a wavelength of 600 nm, respectively [303,304]. Leveraging its layered structure and accessibility through mechanical exfoliation or bottom-up growth methods, large-scale and atomically flat hBN are readily obtainable, as discussed in previous sections. The demand for hBN optical components is propelled by the burgeoning quantum emission from hBN defects. Photons are deemed superior for conveying quantum information across considerable distances. However, in certain scenarios, more robust interaction is desired, such as photon information storage and processing within a quantum network. By coupling quantum emitters to cavities, brighter emission sources, indistinguishable photons, and enhanced photon–matter interaction can be achieved.

This section will delve into various types of hBN optical resonators and their applications. The focus primarily lies on resonators operating in the visible to near-IR range, where the spectrum aligns with relevant quantum emitters in hBN.

5.3a. WG Resonator

The wide bandgap of hBN results in low absorption and high transparency within the visible spectrum. This characteristic makes the FP cavity, formed by two parallel flat mirrors, less than ideal due to significant optical loss. However, the WG cavity, defined by unique geometries such as a ring shape, effectively utilizes TIR to overcome this limitation. TIR occurs when electromagnetic waves move from a high-index material to a low-index material, being reflected rather than refracted. Assume we have a dipole light source in a suspended hBN disk cavity (Fig. 73). Arrow lines stand for the emission rays. At small incident angles (blue lines), both reflection and refraction occur at the hBN/air interface, following Snell's law:

$$n_{\mathrm{air}}\sin\theta_{\mathrm{air}} = n_{\mathrm{hBN}}\sin\theta_{\mathrm{hBN}},$$

where n_{air} and n_{hBN} denotes refractive indices of the two different mediua and θ_{air} and θ_{hBN} are the refraction and reflection (equal to the incidence) angles relative to the normal, respectively.

In a suspended hBN disk cavity (as shown in Fig. 73), a dipole light source emits rays, and at small incident angles (blue lines), both reflection and refraction occur at the hBN/air interface, following Snell's law. As per Snell's law, the refractive angle θ_{air} is greater than the incident angle θ_{hBN} due to $n_{\mathrm{hBN}} > n_{\mathrm{air}}$. As the incident angle increases, θ_{air} approaches a maximum value of 90°, leading to significant suppression of refractive light and predominant reflection (Fresnel's equation). At the critical angle, light gets confined within the disk (red lines), facilitated by the refractive index difference between hBN and its substrate. For instance, at the spectral wavelength of 600 nm (wavelength in the vacuum, same as the rest if not stated otherwise), the critical angle $\theta_{\mathrm{critical}} = \arcsin(n_{\mathrm{air}}/n_{\mathrm{hBN}}) \sim 28^{\mathrm{o}}$. For the same reason, the emission from emitters embedded in the lattice has been partially confined, leading to a significant collection issue for all the solid-state emitters (e.g., hBN and diamond) [305,306].

TIR reduces optical loss within the resonator. For field enhancement, confined waves must meet specific conditions, including phase coherence for constructive interference. In a disk, the phase shift of one complete circle is given by $\Phi = 2\pi n L_{\mathrm{cavity}}/\lambda$, where n is the refractive index and λ is the emission wavelength, L_{cavity} is the circumference

Figure 73

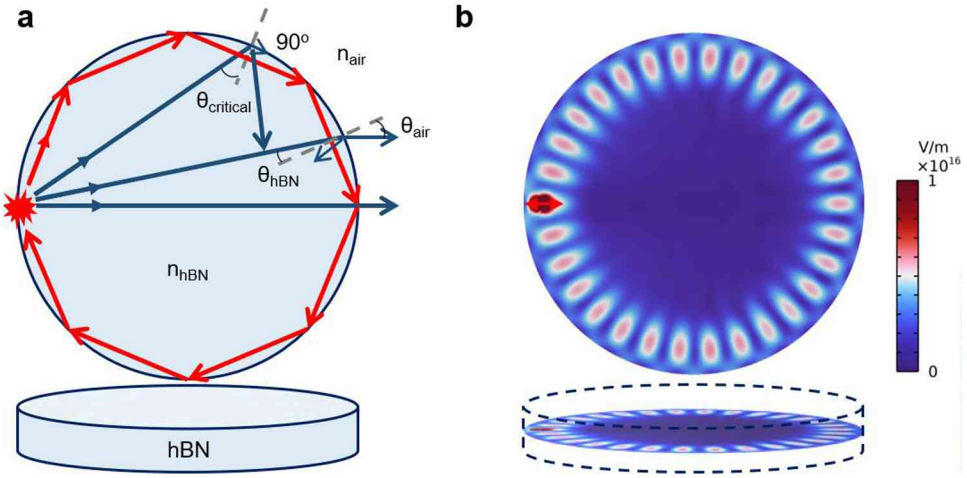

(a) Schematics of TIR in an hBN microdisk. (b) An example of numerically simulated electric field distribution of hBN emitter coupled in a suspending hBN mircodisk. A linearly polarized dipole at the wavelength of 607 nm, represented by a red arrow in the map, was placed at the edge of the microdisk. The simulation was conducted in COMSOL multiphysics.

of the disk. The cavity is said to be on-resonance if $\Phi = 2\pi m$, where m is an integer number indicating the resonance modes or the azimuthal indices. With the above two conditions, we also can get

$$nL_{\text{cavity}} = m\lambda.$$

These resonance modes are spatially distributed along the inner edge of the disk for a given resonance wavelength, such as the WG mode pattern illustrated in Fig. 73(b). The WG cavity supports multiple wavelength modes for a given cavity circumstance L_{cavity}. The spectral spacing of two successive modes is called free spectral range (FSR) which can be calculated by

$$\Delta\lambda_{\text{FSR}} = \frac{\lambda^2}{n_g L_{\text{cavity}}}.$$

Note that n_g here is the group index for a dispersive material. For instance, a 4-μm-diameter hBN disk hosts modes with FSR of about 13 nm at 600 nm ($n_g = 2.26$) wavelength. A question arises: since light is confined in a cavity, how can we describe the quality of confinement? We can evaluate it from two aspects: temporal and spatial confinements. Temporal confinement is defined as quality factor (Q). It is usually the ratio of resonance wavelength to its spectral width:

$$Q = \frac{\lambda}{\Delta\lambda}.$$

The higher the Q, the longer light will remain in the cavity and the sharper the related dome spectrum. In contrast, spatial confinement reflecting field localization, also known as mode volume (V), describes how small light can be confined in the cavity. It is worth noting that compared with the definition of Q, the mathematical equation of V is still ambiguous, different definitions exist to date [307–309]. One of the most broadly used definitions is [310]

$$V = \frac{\int \varepsilon |E(r)|^2 \int \mathrm{d}V}{\max[\varepsilon |E(r)|^2]},$$

Figure 74

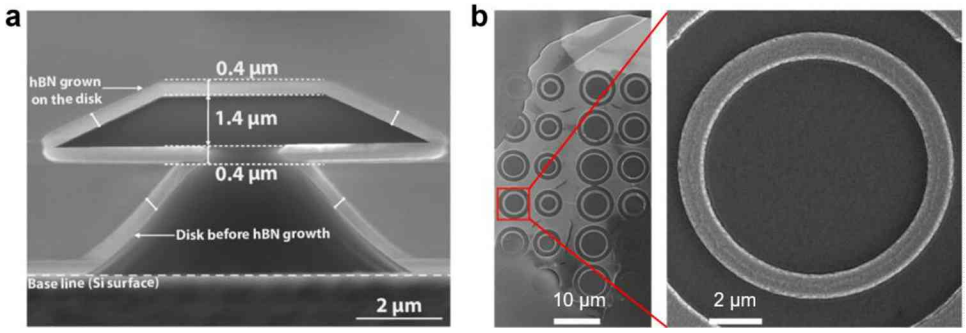

(a) SEM cross section view of hBN on wedged silica disk. (b) hBN microring resonator. Panel (a) reprinted with permission from Das *et al.*, ACS Photonics **8**, 3027–3033 (2021) [311]. Copyright 2021 American Chemical Society, https://doi.org/10.1021/acsphotonics.1c00973. Panel (b) reprinted from Fröch *et al.*, Adv. Opt. Mater. **7**, 1801344 (2019) [312]. Copyright Wiley-VCH Verlag GmbH & Co. KGaA. Reproduced with permission.

where ε is the dielectric constant and $E(r)$ is the electric field distribution through the cavity space.

Experimental work on hBN microresonators has been reported. Figure 74(a) showcases a cross section SEM image of 400-nm hBN film growing over a prefabricated wedged SiO_2 disk, achieving a remarkable Q of over 7×10^5 in the telecommunication spectral range [311]. In Fig. 74(b), hBN microring resonators fabricated on exfoliated hBN flakes on a silica substrate are depicted [312]. Wang *et al*. delved into numerical simulations exploring how the dimensions of hBN disk resonators impact Q and V. Their findings suggested that a well-designed microdisk resonator could potentially achieve a strong emitter–cavity coupling [313].

5.3b. PhC Cavity

In a semiconductor, the motion of an electron is confined by the geometry of the lattice and the strength of the potential. As a result, only electrons with specific energy and momentum are allowed to exist in the crystal. Overall, it forms allowed and forbidden bands for electrons. A PhC is an analog of the above, instead of atoms in the natural lattice structure, the dielectric "lattice" consists of periodic composite geometry to create periodic "potential" [314]. Usually, the periodicity of the electromagnetic wave (photons) is in the wavelength scale.

The above description may still be intricate and abstract, we now consider a one-dimensional (1D) PCC structured like a FP cavity. Unlike traditional mirrors, PCC employs dielectric mirrors such as DBRs. One DBR schematic is shown in Fig. 75(a), where hBN and air gaps are alternatively spaced, and the thickness of each layer satisfies one-quarter wavelength of its optical path:

$$n_1 d_1 = n_2 d_2 = \lambda_0/4,$$

where λ_0 is the target resonance wavelength. Red arrows are the optical paths of the light. To display multiple reflection hierarchies, the incident wave is plotted with a nonzero angle. For simplicity, we treat them as normal incidences.

By arranging layers to meet the above optical path conditions, incident waves reflect in phase. Reflection paths, such as r_1, exhibit a half-wavelength optical path difference (π phase shift) compared with r_0. Despite the π phase shift at low-to-high index

Figure 75

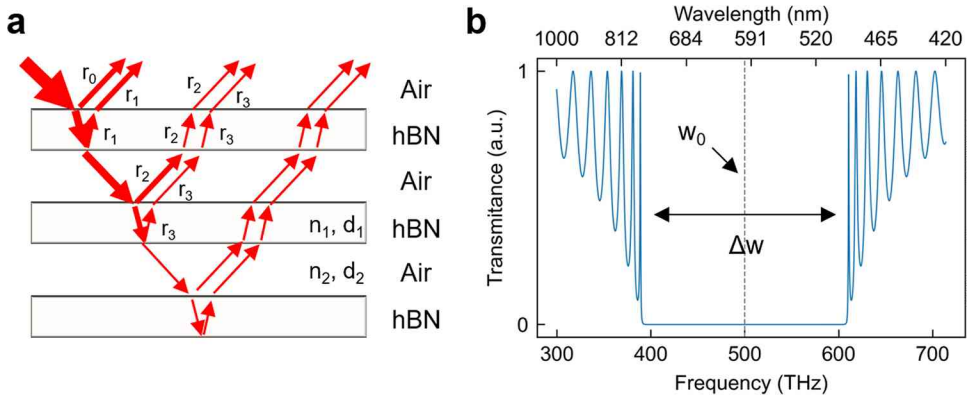

(a) Schematics of an hBN dielectric mirror. (b) Example of a PhC bandgap for hBN DBR mirror. The example is calculated by the transfer matrix method, where the designed central wavelength was set to 600 nm.

boundaries in r_0, the phases align at the interface, resulting in constructive interference among reflected waves. Same as the reflected path of r_2 and r_3 at the second air-hBN interface. As a result, all the reflected light constructively interferes with each other. It is worth noting that the reflectance of a dielectric mirror is proportional to the absolute refractive indices difference and total layer numbers. It means one can achieve ultrahigh reflectance to make a high-finesse cavity with dielectric mirrors. Thus, a DBR acting as a PCC or open cavity, in which on-resonance photons (w_0) are not allowed to transmit but partially pass for those off-resonance photons. A transmission spectrum of the DBR is shown in Fig. 75(b). An obvious bandgap appears with a bandwidth of Δw. As shown in the following equation below, Δw is determined solely by the material refractive indices:

$$\frac{\Delta w}{w_0} = \frac{4}{\pi}\arcsin\left(\frac{|n_1 - n_2|}{n_1 + n_2}\right),$$

where w_0 is the resonance frequency. For materials such as hBN and air, at a resonance of 600 nm ($w_0 = 500$ THz), the frequency bandgap $\Delta w \sim 0.47 w_0$ equates to a spectral window of ~300 nm in the visible range.

A PCC forms by adding a small local perturbation in the preriodic structure of the PhC lattice [as shown in Fig. 76(a)]. By creating a local defect in an otherwise periodic PhC structure, the periodicity of the structures and the PhC bandgap are broken. The structure defect can be a missing or varying size/shape/position of one or more holes [315]. For example, to remove one air gap at the center of the PhC. Two quarter-wave layers of hBN appear next to each other, thus forming a $\lambda_0/2$ layer which leads to a perfect destructive interference of reflectance and a perfect constructive interference of transmittance at w_0. As a result, a close-to-unity transmission channel is formed at the center of the photonic bandgap [Fig. 76(b)]. Note that the spectral sharpness is determined by the Q factor of the cavity. It is also essential to know that there is a dramatic increase in the density of state and, consequently, the suppression of group velocity at the microcavity resonance frequency [316].

The structure defect region may support one or a group of modes at frequencies which lie inside the bandgap. A similar equation can describe modes in the PCC as in WG cavity, where the round travel optical path satisfies integer wavelength $2nL_{\text{cavity}} = m\lambda$. The supported number of modes (m) can be engineered by modifying the defect (L_{cavity}) in the cavity. For instance, in a single-mode cavity, $m = 1$, corresponding to

Figure 76

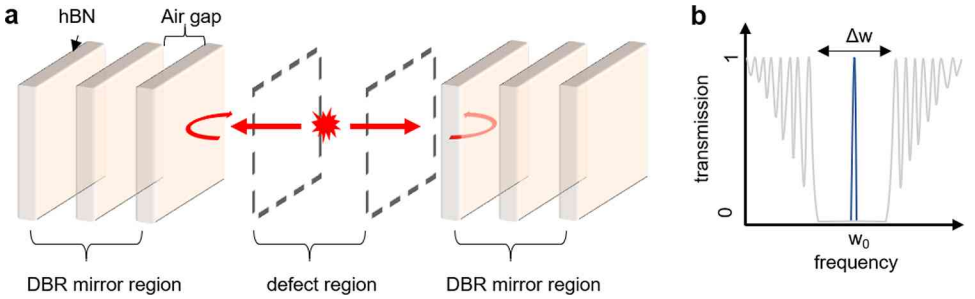

(a) Schematics of general PCC structures. (b) Schematic demonstration of the leaky mode spectrum in a PCC.

$L_{\text{cavity}} = \lambda/2n$. We know it is difficult to obtain high Q and small V simultaneously in a WG cavity, as TIR determines its optical loss at the disk boundary, and high Q comes from those high-order mode numbers formed in a large-size disk. In contrast, the spatial confinement in a PCC can easily approach the theoretical diffraction limit volume of $V = (\lambda/2n)^3$. Some recent work reports that the mode volume can be far below this limit via a special defect strategy [317–320]. The Q of a PCC, similar to other cavities, is limited by two main factors, loss caused by material absorption and scattering. It could occur through the intrinsic coupling of the PCC mode to the radiation modes and scattering through the defects due to the imperfect fabrication in nanoscale. So far, the highest Q achieved is about 10^5–10^6 in the literature [315].

Fröch *et al*. first reported 1D and 2D PCCs from hBN in 2018 [312,321]. Figure 77(a) and (b) are SEM images of two suspended 1D PCC from hBN with different airhole structures [312,322]. Figure 77(c) and (d) are tilted and top views of suspended 2D PCC. The authors also demonstrate the deterministic, iterative tuning of individual cavities by direct electron-beam-induced etching (EBIE) without significant degradation of the Q factor [321].

Similar to 2D PCCs, DBRs also prove advantageous for circular grating cavities. These microcavities prioritize collection enhancement rather than aiming for high Q, particularly benefiting emission from out-of-plane dipoles or within high-index materials [323]. Optical and SEM images in Fig. 78 show the fabricated bullseye grating designed for boron vacancy color centers in hBN [243]. With the optimized parameters, lattice defining parameter (475 nm), central disk diameter (950 nm), and air gap (180 nm), a maximum SPE PL enhancement by a factor of 6 is achieved. PL characterization reveals that the corresponding Q factor of the best performance cavity is around 100.

5.3c. Bound State in the Continuum

An intriguing and counterintuitive cavity type is the bound states in the continuum (BIC). While initially proposed by von Neuman and Wigner in the 1920s, its development only gained momentum in the 21st century. Figure 79 shows the frequency and spatial profile of propagating waves [324]. The conventional confinement (bound state) is manifested by discrete frequencies/levels shown as green lines, such as guided modes in a fiber and defect modes in a bandgap. Resonances depict normal cavity leaky modes (orange lines), namely the waves are not perfectly confined inside the cavity (Q factor is finite). The leaky waves in the space are the continuum state or the extended state as shown in blue lines in the figure. The BIC state confines light

Figure 77

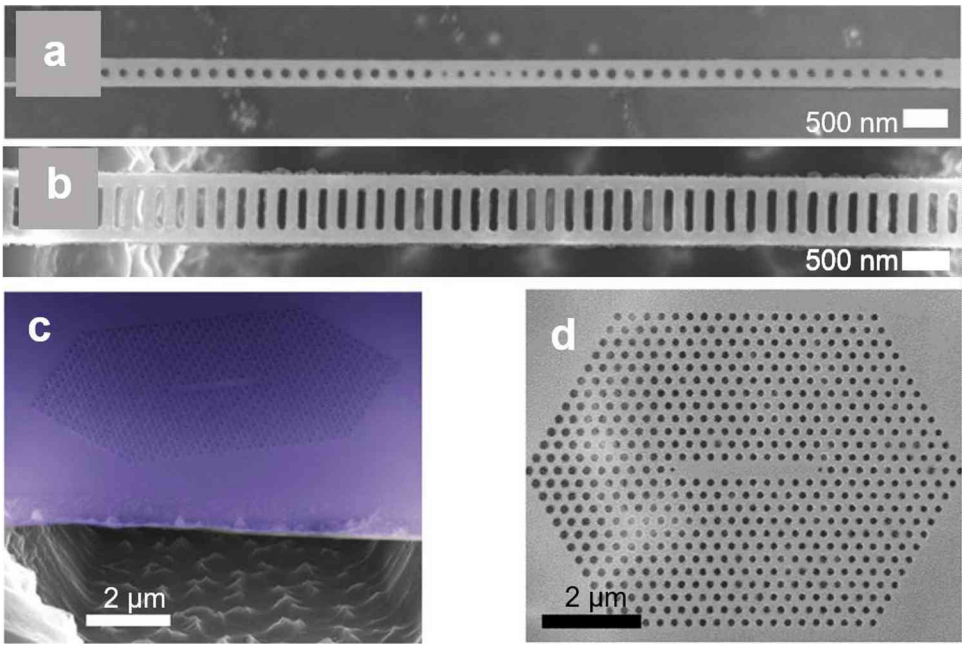

SEM images of suspended 1D (a, b) and 2D (c, d) PCC from hBN. Panel (a) reprinted from Fröch *et al*., Small **18**, 1 (2022) [322]. Copyright Wiley-VCH Verlag GmbH & Co. KGaA. Reproduced with permission. Panel (b) reprinted from Fröch *et al*., Adv. Opt. Mater. **7**, 1801344 (2019) [312]. Copyright Wiley-VCH Verlag GmbH & Co. KGaA. Reproduced with permission. Panels (c) and (d) reprinted with permission from Springer Nature: Kim *et al*., Nat. Commun. **9**, 2623, Copyright 2018.

Figure 78

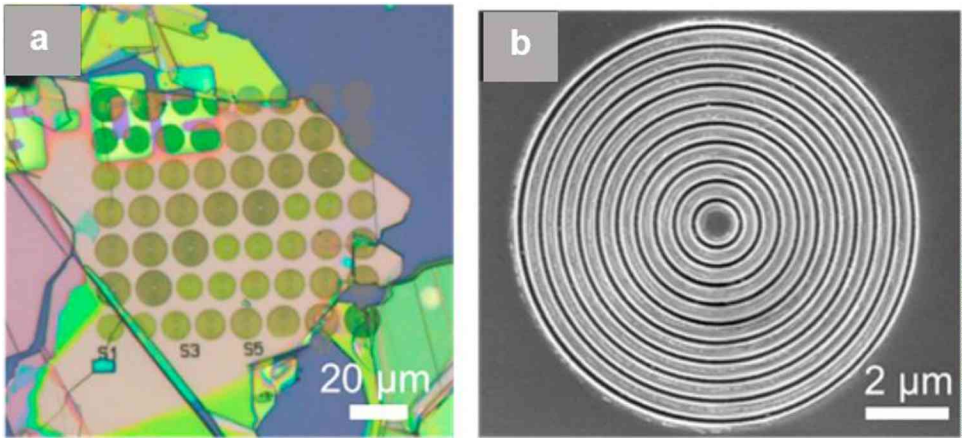

hBN circular grating (Bullseye) cavity. (a) Optical image of bull's eye cavities on 290-nm-thick hBN flakes on thermal oxide silicon substrate. (b) Enlarged SEM image the cavity in (a). Reprinted with permission from Fröch *et al*., Nano Lett. **21**, 6549–6555 (2021) [243]. Copyright 2021 American Chemical Society, https://doi.org/10.1021/acs.nanolett.1c01843.

Figure 79

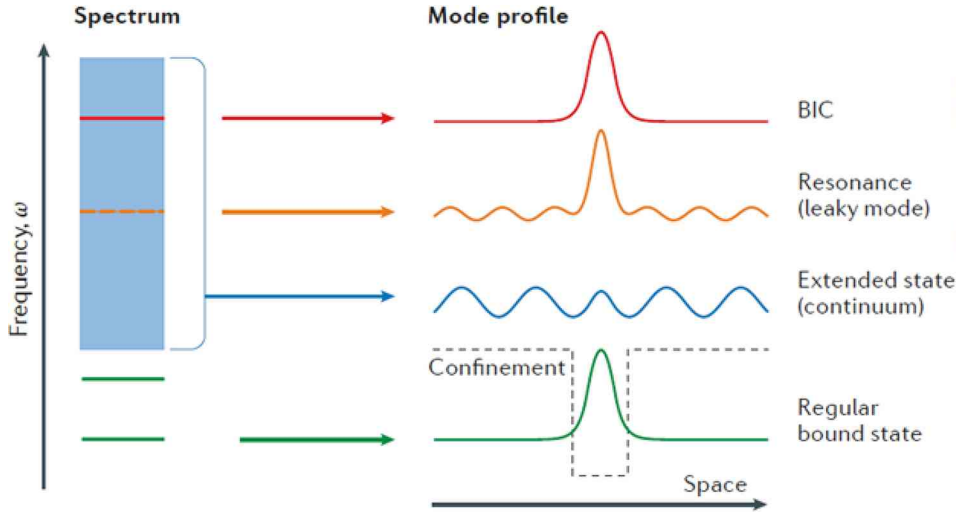

Spectrum and mode profile of waves. Green: discrete levels of bound state, confined in space usually by confining structures or potential. Blue: frequency continuum and spatially extended. Orange: frequency continuum coupled to the extended waves and radiate, became leaky resonances. Red: bound state in the continuum. Reprinted with permission from Springer Nature: Hsu *et al.*, Nat. Rev. Mater. **1**, 16048, Copyright 2016.

perfectly (Q factor is infinitely large) but with its frequency located inside the continuum range. In practice, the infinite Q factor in BIC collapses to a Fano resonance with limited Q or known as quasi-BIC, resulting from perturbation and other restrictions. BIC can be achieved via different approaches, such as far-field destructive interference [325], strong mode coupling [326], and symmetry breaking [327]. Such a novel cavity enables the use of low-index lossless materials for realizing high-Q resonances. Furthermore, BIC is closely linked with the emerging field of metasurface, the latter platform offering powerful ways for manipulating light filed at the subwavelength scale. Dedicated reviews on photonic BIC are available [324,328].

Indistinguishable photons, strong Purcell enhancement, and entangled photons necessitate the precise coupling and engineering of SPEs with ultrahigh-Q cavities. Despite hBN's relatively lower refractive index compared with silicon and other III–IV group materials, its low-loss properties and monolithic integration with hBN SPEs provide distinct advantages for optical components in hBN SPE-related applications. Recent progress in hBN-based cavities, waveguides, and other optical components presents a promising pathway toward constructing a quantum chip platform. This is primarily due to the streamlined processes of nanofabrication and coupling enabled by the monolithic approach [245,322,329–331]. A recent study by Kühner *et al.* presents experimental evidence showcasing symmetry-broken quasi-BIC from single-crystal hBN flakes [332]. As shown in Fig. 80, the cavity comprises a substantial metasurface area featuring asymmetric nanorods made of hBN. By carefully engineering the geometry and orientation of these hBN nanorods, Q factors exceeding 1000 have been achieved across the entire visible spectrum. In addition, the latest work demonstrates the coupling of hBN monolithic qBIC with later irradiated VB spin defects, resulting in a remarkable 25-fold increase in the PL intensity [245].

Figure 80

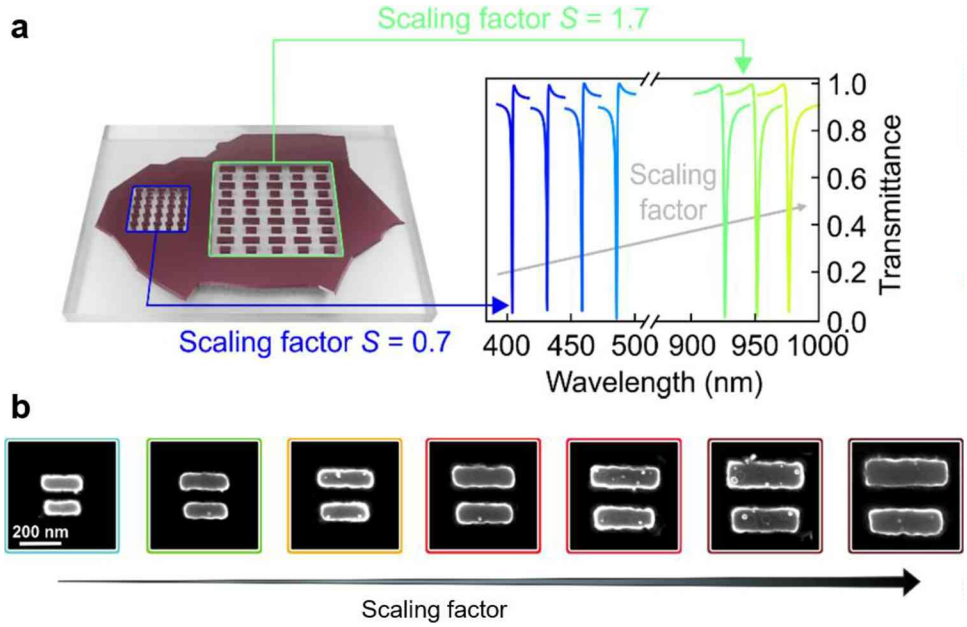

(a) Schematics of fabricated BIC structure in hBN flake and measured hBN quasi-BIC resonance. (b) SEM images of related BIC meta-atoms. Reprinted from Kühner *et al*., Adv. Mater. **35**, e2209688 (2023) [332]. Copyright Wiley-VCH Verlag GmbH & Co. KGaA. Reproduced with permission.

5.3d. Cavity Quantum Electrodynamics

Cavity quantum electrodynamics (QED) describes light–matter interaction between an emitter (e.g., fluorescent atoms and color centers) and a cavity. The term "QED" was coined by Paul Dirac in 1927. For cavity QED, it is thought to have been historically started by Edward Mills Purcell in the 1940s when he studied the spontaneous emission enhancement by a cavity [333]. Purcell's findings revealed that an atom's spontaneous emission is not an inherent property but rather reliant on its environment. This framework proves invaluable in understanding various light–matter interaction phenomena, encompassing modifications in spontaneous emission rates, shifts in energy levels, and energy exchanges. We now discern that the first two processes occur within the realm of weak coupling, whereas the third necessitates a condition of strong coupling. Atom–cavity QED has garnered detailed and exclusive reviews [126,304], providing comprehensive insights. Hence, here we briefly delve into the interaction between emitters and cavities.

Quantum emitters are like isolated atoms in that both can be simplified as a two-level system. The spontaneous transition of excited electrons from their excited state to the ground state arises due to vacuum field fluctuations, where the emission rate hinges on the electromagnetic field's mode density at the transition frequency. When a cavity is introduced, the emitter's spontaneous decay rate undergoes modification due to changes in the mode density [334]. This alteration aims to achieve brighter SPEs by enhancing the emission rate (Γ) within the cavity compared with the original resonant decay rate (γ_0) in free space, quantified by the Purcell factor (F_p), proportionate to Q/V:

$$F_\mathrm{p} = \frac{\Gamma}{\gamma_0} = \frac{3}{4\pi^2}\left(\frac{\lambda}{n}\right)^3 \frac{Q}{V}.$$

Figure 81

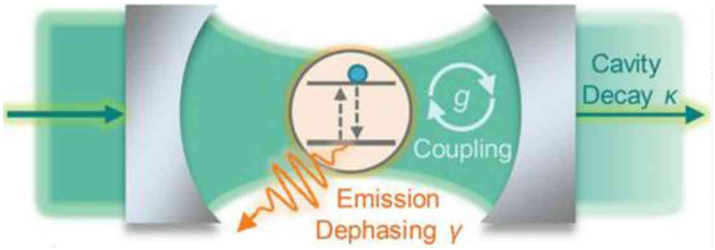

Schematics of the emitter–cavity coupling, where G is the coupling rate, r is the emitter dephasing rate, and k is the cavity decay rate. Reprinted with permission from Wang *et al.*, Appl. Phys. Lett. **118** (2021) [313]. Copyright 2021, AIP Publishing LLC.

Here, n is the refractive index of the inner media, which is 1 for free space. Essentially, the longer time light spends in the cavity (high Q), and the more confined the light is (small V), the stronger impact of the resonator to the emitter spontaneous emission (high F_p). For instance, we can simply estimate the emission enhancement of an emitter radiation at $\lambda = 0.6\,\mu m$, assuming V is sub-μm^3 (the same order of magnitude as λ^3), an emission rate enhancement ($F_p > 1$) is anticipated when Q surpasses 100. The emitter will effectively interact with photons in such a confined volume in the cavity.

Figure 81 shows the schematics of a two-level emitter interacting with a cavity. The interaction comprises three parts: emitter overall dephasing (γ), cavity overall decay (k), and coupling strength (g). The γ is determined by the emitter, so we can adopt the value from the Fourier-transform-limited linewidth (spontaneous emission lifetime τ_{sp}). The cavity decay rate k is quality factor Q dependent, $k/2\pi = w/4\pi Q$. The coherent coupling rate g is mode volume V dependent:

$$\frac{g}{2\pi} = \frac{1}{2\tau_{sp}}\sqrt{\frac{3c\lambda\tau_{sp}}{2\pi n^3 V}}.$$

The Purcell factor depicts the enhancement of resonant optical decay (γ_0, ZPL) instead of the total decay (γ) processes, the latter also includes nonradiative decay, radiative phonon broadening (γ_1) as well as pure dephasing (γ_d). Therefore, the above Purcell factor is ideal for an ideal case ($\gamma_0 = \gamma$), but not suitable for practical situations. Alternatively, taking all decoherence mechanisms into consideration, the absolute probability of coherent emitter–photon interaction can be described by a cooperativity parameter, C,

$$C = \frac{\Gamma}{\gamma} = \frac{4g^2}{k\gamma}.$$

(1) Weak coupling regime

This is a cavity field decay-rate-dominant regime: $C < 1$, $\kappa/2 >> g >> \gamma$ and emitter–cavity mode detuning $\delta = 0$.

Solid-state emitters are commonly broadened due to various dephasing mechanisms. At room temperature, γ_d is usually orders of magnitude higher than the optical decay paths [335]. In general, phonon related decay paths will be greatly suppressed at low temperature ($k >> \gamma$), the main optical dephasing is γ_d though the total dephase is still dominated by γ_d. In this scenario, the optical transition is enhanced by F_P. When cavity emission Γ is larger than free space $\gamma_0 + \gamma_1$, the excited state lifetime of the emitter will

drop significantly and increase the overall emission [336]. Light–matter interaction in this regime is extremely useful for applications such as ultralow-threshold lasers and bright single-photon sources.

(2) Strong coupling regime

This is a coupling rate dominant regime: $C > 1$, $g > \kappa/2 >> \gamma$, that emitter–cavity mode detuning $\delta = 0$.

The high cooperativity regime $C > 1$ corresponds to conditions of near-deterministic interactions, where the emitter has a high probability to interact with a cavity photon before it dephases. To reach this regime, one has to increase g relative to κ, which can be achieved by reducing cavity mode volume V (increase g) and by increasing cavity Q factor (decrease κ) [337]. This regime is vital for quantum state generation used in quantum technologies, such as quantum information processing and communication.

(3) Other regimes

(a) These regimes are pure dephasing rate dominant: $C < 1$, $\gamma >> g >> \kappa/2$, that emitter–cavity mode detuning $\delta \neq 0$.
(b) Ultrahigh strong coupling and deep strong coupling regimes. These regimes are defined in a different way where losses are not included, but directly compare g with bare energies in the system. It is thus possible for a system to be in the ultrastrong coupling regime without having strong coupling if losses are large [338]. Therefore, one needs to be careful when referring to the coupling regimes.

5.4. Twistronics

Twisting van der Waals materials has become a hot topic recently and we want to briefly cover it in this tutorial. A twist of one layer with respect to another creates Moiré patterns, which generates a new lattice with larger unit cells. There are several effects of Moiré pattern: (1) changes the periodicity of the crystal; (2) influences the Coulomb interaction of the two layers; (3) the larger unit cell affects the band structure of the twisted interface and could lead to many new quantum phenomena that do not exist in its pristine crystal form. In the systems consisting of transitional metal dichalcogenides and graphene, the Moiré potential could lead to many new phenomena, including Moiré exciton [339,340], strongly correlated phenomenon and superconductor [341,342]. In hBN, Moiré pattern results in ferroelectricity due to the inhomogeneous alignment of the B and N atoms which breaks the inversion symmetry at the interface, first predicted by theory in 2017 [343]. The experimental confirmation was completed in 2021 [344,345]. Yasuda *et al*. proved the ferroelectricity using a tunneling device and the polarization switching is observed when the vertical voltage is applied in opposite directions [Fig. 82(a)–(d)] [345], and Woods *et al*. used electrostatic force microscopy and obtained the Moiré pattern caused by the alternate switching of polarization directions due to Moiré patterns [Fig. 83(e) and (f)] [344].

The twisting between hBN flakes is also found to be able to influence the optical emission of hBN at deep UV range [346,347]. CL is used for characterizing this emission for the reasons discussed in Section 3. The simple twist of the hBN crystal could enhance the emission of a deep-UV emitter by nearly two orders of magnitude [Fig. 83(a) and (b)]. A vertical voltage is proved to be able to control the intensity of the defect emission. The intensity of the defect emission is anticorrelated to the electron-beam-induced current [EBIC; Fig. 83(c) and (d)], which shows that the electron/hole supply to the defect levels are redirected to the electrodes without recombination. *GW* calculation predicted that N vacancies are the most likely origin compared with other

Figure 82

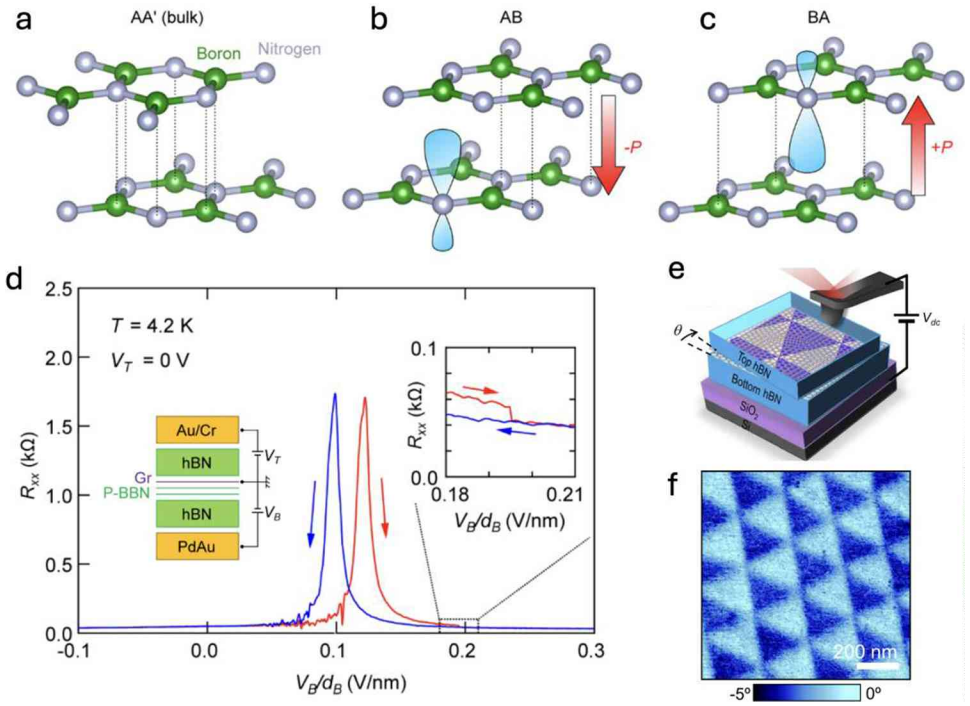

Stacking-engineered ferroelectricity in bilayer boron nitride. (a)–(c) AA', AB, and BA stacking orders of bilayer hBN. The AB and BA stackings manifest ferroelectric dipoles (marked by the arrow and P), originating from the asymmetry of the atoms of the adjacent layers. (d) Resistance as a function of electric field strength of the bottom gate (V_B/d_B), showcasing the ferroic character with the forward (red curve) and backward (blue curve) scanning. The insets are the structure of the device and a blow-up of the region where polarization starts to switch. (e) Schematic of an EFM setup for measuring the electric dipoles. (f) EFM contrast of the twisted bilayer hBN with alternating polarized domains. Panels (a)–(d) from Yasuda *et al*., Science **372**, 1458–1462 (2021). Reprinted with permission from AAAS.. Panels (e) and (f) reprinted with permission from Springer Nature: Woods *et al*., Nat. Commun. **12**, 347, Copyright 2021.

simple defects such as B vacancies or C substitutions. However, Li *et al*. recently showed that the likely origin of this emission is a 2-C defect (where a pair of B and N is replaced by two C atoms), and the defect has a strong Stark effect caused by the ferroelectricity at the interface [348]. It is still a challenge to correlate the atomic structure of these defect emitters with their emission spectra.

6. OUTLOOK

Boron nitride has garnered significant attention over the last decade, mostly due to the discoveries of unexpected phenomena. Spanning intriguing polariton physics, quantum photonics, and becoming a key enabler for graphene devices and van der Waals heterostructures, hBN became a vital component of many laboratories worldwide. It is hard to pinpoint which of the myriad applications will become dominant in years to come, but the following points should be considered for those who join the field.

1. Perhaps the biggest challenge in the hBN community is realizing large wafer-scale crystals with controllable thicknesses. So far, most hBN flakes for devices are achieved via exfoliation from bulk crystals that are often limited to a few square

Figure 83

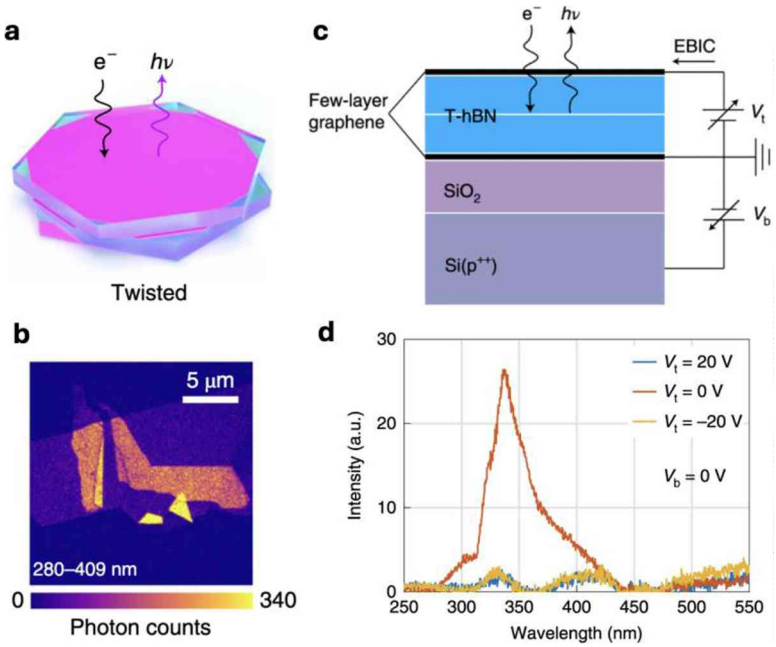

Tuning color centers at a twisted hBN interface. (a) Schematic of twist-induced defect emission enhancement. (b) CL mapping of the two hBN flakes where the bright region overlaps with the twisted interfaces. (c) Structure of the device for testing the voltage-dependent emission of the twisted hBN. Reprinted with permission from Springer Nature: Su *et al*., Nat. Mater. **21**, 896–902, Copyright 2022.

millimeters. On the other hand, large wafer-scale films are limited to a thickness of few monolayers, or rarely to a few tens of nanometers. Alternative growth approaches should be explored to achieve large single-crystal hBN materials. The synthesis of high-quality hBN with precise control over thickness, purity, and defects is still challenging. Likewise, achieving cost-effective production remains a goal for industrial applications.

2. Cubic boron nitride is a polytype that has been scarcely studied. Like its hexagonal counterpart, it is a wide-bandgap material, with excellent thermal properties and chemical stability, making it an ideal material for use in high-temperature and corrosive environments. It also possesses color centers, and can potentially be employed for a range of applications in photonics.
3. A long-standing question surrounding hBN is the nature of its bandgap, which is indirect but exhibits "direct-like" features. Consequently, its transparency in the UV to IR range should be appealing for the development of various optoelectronic devices such as photodetectors, LEDs, and lasers. Bandgap properties are also vital to better understanding the properties of excitons as well as to engineer new twistronics devices.
4. Mechanical properties of both hBN and cBN should also be studied in more detail. hBN can be exfoliated to a few-nanometer-thick layers, and hence are an attractive candidate for nanoelectromechanical systems and optomechanics. Of course, hBN nanotubes are widely available commercially, but their mechanical properties are not well investigated, as compared with their older sibling the carbon nanotubes.
5. hBN (and cBN) surfaces remain poorly understood both experimentally and theoretically. However, integration into existing device architectures and compatibility with other materials should accelerate these studies. Ensuring proper interfaces, and

bonding with other components while maintaining the desired properties requires careful engineering and optimization.

6. In terms of emerging technologies, quantum applications from the SPEs, and polariton propagation are the most well-studied topics in the last few years. Both can benefit from more effort and development of isotopically controlled crystals and purposely grown hBN. But new applications are constantly emerging, including twistronics, bio-imaging, and more.

These are just snapshots of looming directions that the boron nitride community is exploring. As new applications emerge, new challenges and opportunities follow. We are therefore optimistic that hBN, and its family member cBN, will become active wide bandgap materials in their own right and with their own suite of applications.

FUNDING

U.S. Department of Energy (DE-AC02-05-CH11231); Australian Research Council (CE200100010, FT220100053); Office of Naval Research (N00014-22-12035).

ACKNOWLEDGEMENTS

C.S. would like to acknowledge the generous support from Yale University. M.H. gratefully acknowledges support for this work by the Office of Naval Research. J.D.C. gratefully acknowledges support for this work by the Office of Naval Research under a MURI grant. A.Z. was supported by the U.S. Department of Energy, Office of Science, Office of Basic Energy Sciences, Materials Sciences and Engineering Division, within the van der Waals Heterostructure Program (KCWF16), which provided for materials synthesis, and within the Nanomachines Program, which provided for TEM sample preparation. I.A. acknowledges the Australian Research Council and the Office of Naval Research Global.

DISCLOSURES

The authors declare no conflicts of interest.

DATA AVAILABILITY

No data were generated or analyzed in the presented research.

REFERENCES

1. M. Engler, C. Lesniak, R. Damasch, *et al.*, "Hexagonal boron nitride (hBN) – applications from metallurgy to cosmetics," Ceram. Forum Int. **84**, E49 (2007).
2. N. Alem, R. Erni, C. Kisielowski, *et al.*, "Atomically thin hexagonal boron nitride probed by ultrahigh-resolution transmission electron microscopy," Phys. Rev. B: Condens. Matter Mater. Phys. **80**, 155425 (2009).
3. S. M. Gilbert, T. Pham, M. Dogan, *et al.*, "Alternative stacking sequences in hexagonal boron nitride," 2D Mater. **6**, 021006 (2019).
4. R. M. Ribeiro and N. M. R. Peres, "Stability of boron nitride bilayers: ground-state energies, interlayer distances, and tight-binding description," Phys. Rev. B: Condens. Matter Mater. Phys. **83**, 235312 (2011).
5. Q. Cai, D. Scullion, W. Gan, *et al.*, "High thermal conductivity of high-quality monolayer boron nitride and its thermal expansion," Sci. Adv. **5**, eaav0129 (2019).
6. C. R. Dean, A. F. Young, I. Meric, *et al.*, "Boron nitride substrates for high-quality graphene electronics," Nat. Nanotechnol. **5**, 722–726 (2010).

7. O. Hod, "Graphite and hexagonal boron-nitride have the same interlayer distance. Why?" J. Chem. Theory Comput. **8**, 1360–1369 (2012).
8. G. Cassabois, P. Valvin, and B. Gil, "Hexagonal boron nitride is an indirect bandgap semiconductor," Nat. Photonics **10**, 262–266 (2016).
9. C. Elias, P. Valvin, T. Pelini, *et al.*, "Direct band-gap crossover in epitaxial monolayer boron nitride," Nat. Commun. **10**, 2639 (2019).
10. F. Zhang, C. S. Ong, J. W. Ruan, *et al.*, "Intervalley excitonic hybridization, optical selection rules, and imperfect circular dichroism in monolayer *h*-BN," Phys. Rev. Lett. **128**, 047402 (2022).
11. R. V. Gorbachev, I. Riaz, R. R. Nair, *et al.*, "Hunting for monolayer boron nitride: optical and raman signatures," Small **7**, 465–468 (2011).
12. J. Kotakoski, C. H. Jin, O. Lehtinen, *et al.*, "Electron knock-on damage in hexagonal boron nitride monolayers," Phys. Rev. B: Condens. Matter Mater. Phys. **82**, 113404 (2010).
13. A. J. Giles, S. Dai, I. Vurgaftman, *et al.*, "Ultralow-loss polaritons in isotopically pure boron nitride," Nat. Mater. **17**, 134–139 (2018).
14. R. Bourrellier, S. Meuret, A. Tararan, *et al.*, "Bright UV single photon emission at point defects in *h*-BN," Nano Lett. **16**, 4317–4321 (2016).
15. C. Fournier, A. Plaud, S. Roux, *et al.*, "Position-controlled quantum emitters with reproducible emission wavelength in hexagonal boron nitride," Nat. Commun. **12**, 3779 (2021).
16. A. Gale, C. Li, Y. Chen, *et al.*, "Site-specific fabrication of blue quantum emitters in hexagonal boron nitride," ACS Photonics **9**, 2170–2177 (2022).
17. J. Horder, S. J. U. White, A. Gale, *et al.*, "Coherence properties of electron-beam-activated emitters in hexagonal boron nitride under resonant excitation," Phys. Rev. Appl. **18**, 064021 (2022).
18. T. T. Tran, C. Elbadawi, D. Totonjian, *et al.*, "Robust multicolor single photon emission from point defects in hexagonal boron nitride," ACS Nano **10**, 7331–7338 (2016).
19. N. R. Jungwirth and G. D. Fuchs, "Optical absorption and emission mechanisms of single defects in hexagonal boron nitride," Phys. Rev. Lett. **119**, 057401 (2017).
20. J. R. Reimers, J. Shen, M. Kianinia, *et al.*, "Photoluminescence, photophysics, and photochemistry of the V_B^- defect in hexagonal boron nitride," Phys. Rev. B: Condens. Matter Mater. Phys. **102**, 144105 (2020).
21. Z. Mu, H. Cai, D. Chen, *et al.*, "Excited-state optically detected magnetic resonance of spin defects in hexagonal boron nitride," Phys. Rev. Lett. **128**, 216402 (2022).
22. N. Mendelson, R. Ritika, M. Kianinia, *et al.*, "Coupling spin defects in a layered material to nanoscale plasmonic cavities," Adv. Mater. **34**, e2106046 (2022).
23. C. Li, Z.-Q. Xu, N. Mendelson, *et al.*, "Purification of single-photon emission from hBN using post-processing treatments," Nanophotonics **8**, 2049–2055 (2019).
24. S. White, C. Stewart, A. S. Solntsev, *et al.*, "Phonon dephasing and spectral diffusion of quantum emitters in hexagonal boron nitride," Optica **8**, 1153 (2021).
25. A. Dietrich, M. Bürk, E. S. Steiger, *et al.*, "Observation of Fourier transform limited lines in hexagonal boron nitride," Phys. Rev. B: Condens. Matter Mater. Phys. **98**, 081414 (2018).
26. M. Hoese, P. Reddy, A. Dietrich, *et al.*, "Mechanical decoupling of quantum emitters in hexagonal boron nitride from low-energy phonon modes," Sci. Adv. **6**, eaba6038 (2020).
27. P. Siddiqua, M. S. Shur, and S. K. O'Leary, "Electron transport within bulk cubic boron nitride: a Monte Carlo simulation analysis," J. Appl. Phys. **128**, 185704 (2020).

28. K. Watanabe, T. Taniguchi, and H. Kanda, "Direct-bandgap properties and evidence for ultraviolet lasing of hexagonal boron nitride single crystal," Nat. Mater. **3**, 404–409 (2004).
29. J. D. Caldwell, I. Aharonovich, G. Cassabois, *et al.*, "Photonics with hexagonal boron nitride," Nat. Rev. Mater. **4**, 552–567 (2019).
30. R. Cuscó, J. H. Edgar, S. Liu, *et al.*, "Isotopic disorder: the prevailing mechanism in limiting the phonon lifetime in hexagonal BN," Phys. Rev. Lett. **124**, 167402 (2020).
31. L. Schué, I. Stenger, F. Fossard, *et al.*, "Characterization methods dedicated to nanometer-thick hBN layers," 2D Mater. **4**, 015028 (2016).
32. S. Sridar, R. Kumar, and K. C. H. Kumar, "Thermodynamic modelling of Al-B-N system," CALPHAD: Comput. Coupling Phase Diagrams Thermochem. **65**, 291–298 (2019).
33. B. N. Feigelson, R. M. Frazier, and M. Twigg, "III-nitride crystal growth from nitride-salt solution," J. Cryst. Growth **305**, 399–402 (2007).
34. T. Ishii and T. Sato, "Growth of single crystals of hexagonal boron nitride," J. Cryst. Growth **61**, 689–690 (1983).
35. M. Zastrow, "Meet the crystal growers who sparked a revolution in graphene electronics," Nature **572**, 429–432 (2019).
36. K. Watanabe, T. Taniguchi, and H. Kanda, "Ultraviolet luminescence spectra of boron nitride single crystals grown under high pressure and high temperature," Physica Status Solidi A Appl. Res. **201**, 2561–2565 (2004).
37. L. Sponza, H. Amara, C. Attaccalite, *et al.*, "Direct and indirect excitons in boron nitride polymorphs: a story of atomic configuration and electronic correlation," Phys. Rev. B: Condens. Matter Mater. Phys. **98**, 125206 (2018).
38. E. Janzen, "Optimization of solution composition in hexagonal boron nitride crystal growth via the flux method," *Doctor of Philosophy* (Kansas State University, 2023).
39. Y. Kubota, K. Watanabe, O. Tsuda, *et al.*, "Deep ultraviolet light-emitting hexagonal boron nitride synthesized at atmospheric pressure," Science **317**, 932–934 (2007).
40. Y. Kubota, K. Watanabe, O. Tsuda, *et al.*, "Hexagonal boron nitride single crystal growth at atmospheric pressure using Ni−Cr solvent," Chem. Mater. **20**, 1661–1663 (2008).
41. B. Clubine, "Synthesis and characterization of bulk single crystal hexagonal boron nitride from metal solvents," Mast. Sci. (Kansas State University, 2012).
42. T. Hoffman, "Optimization and characterization of bulk hexagonal boron nitride single crystals grown by the nickel-chromium flux method," Doctor of Philosophy (Kansas State University, 2016).
43. J. L. Sperber, "Investigations of hexagonal boron nitride: bulk crystals and atomically-thin two dimensional layers," Master of Science (Kansas State University, 2016).
44. S. Liu, "Experimental and theoretical studies of hexagonal boron nitride single crystal growth," Ph.D. (Kansas State University, 2018).
45. S.-Y. Zhang, K. Xu, X.-K. Zhao, *et al.*, "Improved hBN single-crystal growth by adding carbon in the metal flux," Cryst. Growth Des. **19**, 6252–6257 (2019).
46. J. Li, "Growth and characterization of high-quality bulk hexagonal boron nitride crystals," Ph.D. (Kansas State University, 2019).
47. T. Taniguchi and K. Watanabe, "Synthesis of high-purity boron nitride single crystals under high pressure by using Ba–BN solvent," J. Cryst. Growth **303**, 525–529 (2007).
48. N. D. Zhigadlo, "Crystal growth of hexagonal boron nitride (hBN) from Mg–B–N solvent system under high pressure," J. Cryst. Growth **402**, 308–311 (2014).

49. N. F. Ostrovskaya, T. S. Bartnitskaya, V. I. Lyashenko, *et al.*, "Crystallization of boron nitride from solution in a lithium borate melt," Powder Metal. Metal Ceram. **35**, 636–639 (1996).
50. M. Onodera, T. Taniguchi, K. Watanabe, *et al.*, "Hexagonal boron nitride synthesized at atmospheric pressure using metal alloy solvents: evaluation as a substrate for 2D materials," Nano Lett. **20**, 735–740 (2020).
51. Y. Kubota, K. Watanabe, and T. Taniguchi, "Synthesis of cubic and hexagonal boron nitrides by using Ni solvent under high pressure," Jpn. J. Appl. Phys. **46**, 311 (2007).
52. M. Onodera, K. Watanabe, M. Isayama, *et al.*, "Carbon-rich domain in hexagonal boron nitride: carrier mobility degradation and anomalous bending of the landau fan diagram in adjacent graphene," Nano Lett. **19**, 7282–7286 (2019).
53. Y. Gu, M. Zheng, Y. Liu, *et al.*, "Low-temperature synthesis and growth of hexagonal boron-nitride in a lithium bromide melt," J. Am. Ceram. Soc. **90**, 1589–1591 (2007).
54. T. B. Hoffman, B. Clubine, Y. Zhang, *et al.*, "Optimization of Ni–Cr flux growth for hexagonal boron nitride single crystals," J. Cryst. Growth **393**, 114–118 (2014).
55. S. Liu, R. He, Z. Ye, *et al.*, "Large-scale growth of high-quality hexagonal boron nitride crystals at atmospheric pressure from an Fe–Cr flux," Cryst. Growth Des. **17**, 4932–4935 (2017).
56. J. Cao, M. Tian, S. Zhang, *et al.*, "Carbon-related defect control of bulk hBN single crystals growth by atmospheric-pressure metal-flux-based fusion synthesis," J. Mater. Sci. **57**, 14668–14680 (2022).
57. J. Li, C. Yuan, C. Elias, *et al.*, "Hexagonal boron nitride single crystal growth from solution with a temperature gradient," Chem. Mater. **32**, 5066–5072 (2020).
58. J. Li, J. Wang, X. Zhang, *et al.*, "Hexagonal boron nitride crystal growth from iron, a single component flux," ACS Nano **15**, 7032–7039 (2021).
59. N. Zhang, N. Yang, W. Wang, *et al.*, "Growth of hexagonal boron nitride crystals at atmospheric pressure from Cu–Cr flux," J. Cryst. Growth **562**, 126074 (2021).
60. Y. Li, X. Wen, C. Tan, *et al.*, "Synthesis of centimeter-scale high-quality polycrystalline hexagonal boron nitride films from Fe fluxes," Nanoscale **13**, 11223–11231 (2021).
61. T. B. Hoffman, Y. Zhang, J. H. Edgar, *et al.*, "Growth of hBN using metallic boron: isotopically enriched $h^{10}BN$ and $h^{11}BN$," Mater. Res. Soc. Symp. Proc. **1635**, 35–40 (2014).
62. S. Liu, R. He, L. Xue, *et al.*, "Single crystal growth of millimeter-sized monoisotopic hexagonal boron nitride," Chem. Mater. **30**, 6222–6225 (2018).
63. J. Li, C. Elias, G. Ye, *et al.*, "Single crystal growth of monoisotopic hexagonal boron nitride from a Fe–Cr flux," J. Mater. Chem. C **8**, 9931–9935 (2020).
64. M. Y. K. Yap, M. O. M. Okamoto, M. O. M. Onda, *et al.*, "Na: a new flux for growing hexagonal boron nitride crystals at low temperature," Jpn. J. Appl. Phys. **39**, L300 (2000).
65. T. Yamada, Y. Kamiya, N. Naruse, *et al.*, "Exclusive growth of low-aspect ratio, polyhedral h-BN crystals in molten Li_2CO_3 as the reactive flux," Cryst. Growth Des. **19**, 5720–5728 (2019).
66. J. Siwka, "Equilibrium constants and nitrogen activity in liquid metals and iron alloys," ISIJ Int. **48**, 385–394 (2008).
67. R. F. Abdulrahman and A. Hendry, "Solubility of nitrogen in liquid nickel-based alloys," Metall. Mater. Trans. B **32**, 1103–1112 (2001).
68. D. B. Evans and R. D. Pehlke, "The boron-nitrogen equilibrium in liquid iron," *Trans. Metall. Soc. AIME* **230**, 1657–1662 (1964).

69. D. L. Ball, "The precipitation of boron nitride from ferrous melts," Aime. Met. Soc. Trans. **239**, 31 (1967).
70. V. L. Solozhenko, "Boron nitride phase diagram. State of the art," High Pressure Res. **13**, 199–214 (1995).
71. Q. Cai, E. Janzen, J. H. Edgar, *et al.*, "Isotope effect on the thermal expansion coefficient of atomically thin boron nitride," 2D Mater. **8**, 034006 (2021).
72. K. K. Kim, S. M. Kim, and Y. H. Lee, "A new horizon for hexagonal boron nitride film," J. Korean Phys. Soc. **64**, 1605–1616 (2014).
73. M. H. Khan, H. K. Liu, X. Sun, *et al.*, "Few-atomic-layered hexagonal boron nitride: CVD growth, characterization, and applications," Mater. Today **20**, 611–628 (2017).
74. K. Zhang, Y. Feng, F. Wang, *et al.*, "Two dimensional hexagonal boron nitride (2D-hBN): synthesis, properties and applications," J. Mater. Chem. **5**, 11992–12022 (2017).
75. J. Meng, D. Wang, L. Cheng, *et al.*, "Recent progress in synthesis, properties, and applications of hexagonal boron nitride-based heterostructures," Nanotechnology **30**, 074003 (2019).
76. A. F. Rigosi, A. L. Levy, M. R. Snure, *et al.*, "Turn of the decade: versatility of 2d hexagonal boron nitride," JPhys Mater. **4**, 032003 (2021).
77. A. Maity, S. J. Grenadier, J. Li, *et al.*, "Hexagonal boron nitride: epitaxial growth and device applications," Prog. Quantum Electron. **76**, 100302 (2021).
78. J. Ren and P. Innocenzi, "2D boron nitride heterostructures: recent advances and future challenges," Small Struct. **2**, 2100068 (2021).
79. S. Roy, X. Zhang, A. B. Puthirath, *et al.*, "Structure, properties and applications of two-dimensional hexagonal boron nitride," Adv. Mater. **33**, e2101589 (2021).
80. C. Maestre, B. Toury, P. Steyer, *et al.*, "Hexagonal boron nitride: a review on selfstanding crystals synthesis towards 2D nanosheets," JPhys Mater. **4**, 044018 (2021).
81. H. Yang, L. Wang, F. Gao, *et al.*, "Shape evolution of two dimensional hexagonal boron nitride single domains on Cu/Ni alloy and its applications in ultraviolet detection," Nanotechnology **30**, 245706 (2019).
82. H. Tian, A. Khanaki, P. Das, *et al.*, "Role of carbon interstitials in transition metal substrates on controllable synthesis of high-quality large-area two-dimensional hexagonal boron nitride layers," Nano Lett. **18**, 3352–3361 (2018).
83. Q. Cai, D. Scullion, A. Falin, *et al.*, "Raman signature and phonon dispersion of atomically thin boron nitride," Nanoscale **9**, 3059–3067 (2017).
84. K. K. Kim, A. Hsu, X. Jia, *et al.*, "Synthesis and characterization of hexagonal boron nitride film as a dielectric layer for graphene devices," ACS Nano **6**, 8583–8590 (2012).
85. P. Bachmann, F. Düll, F. Späth, *et al.*, "A HR-XPS study of the formation of *h*-BN on Ni(111) from the two precursors, ammonia borane and borazine," J. Chem. Phys. **149**, 164709 (2018).
86. Q. S. Paduano, M. Snure, J. Bondy, *et al.*, "Self-terminating growth in hexagonal boron nitride by metal organic chemical vapor deposition," Appl. Phys. Express **7**, 071004 (2014).
87. A. Henry, M. Chubarov, Z. Czigány, *et al.*, "Early stages of growth and crystal structure evolution of boron nitride thin films," Jpn. J. Appl. Phys. **55**, 05FD06 (2016).
88. S. Nakhaie, M. Heilmann, T. Krause, *et al.*, "Nucleation and growth of atomically thin hexagonal boron nitride on Ni/MgO(111) by molecular beam epitaxy," J. Appl. Phys. **125**, 115301 (2019).
89. J. Wrigley, J. Bradford, T. James, *et al.*, "Epitaxy of boron nitride monolayers for graphene-based lateral heterostructures," 2D Mater. **8**, 034001 (2021).

90. T. Q. P. Vuong, G. Cassabois, P. Valvin, *et al.*, "Deep ultraviolet emission in hexagonal boron nitride grown by high-temperature molecular beam epitaxy," 2D Mater. **4**, 021023 (2017).
91. J. S. Lee, S. H. Choi, S. J. Yun, *et al.*, "Wafer-scale single-crystal hexagonal boron nitride film via self-collimated grain formation," Science **362**, 817–821 (2018).
92. H. Liu, W. He, Z. Liu, *et al.*, "Structure evolution of hBN grown on molten Cu by regulating precursor flux during chemical vapor deposition," 2D Mater. **9**, 015004 (2022).
93. Q. Zhang, H. Chen, S. Liu, *et al.*, "Self-aligned stitching growth of centimeter-scale quasi-single-crystalline hexagonal boron nitride monolayers on liquid copper," Nanoscale **14**, 3112–3122 (2022).
94. T. Werninghaus, J. Hahn, F. Richter, *et al.*, "Raman spectroscopy investigation of size effects in cubic boron nitride," Appl. Phys. Lett. **70**, 958–960 (1997).
95. B. G. Yacobi and D. B. Holt, *Cathodoluminescence Microscopy of Inorganic Solids* (Springer, 1990).
96. L. Schué, B. Berini, A. C. Betz, *et al.*, "Dimensionality effects on the luminescence properties of hBN," Nanoscale **8**, 6986–6993 (2016).
97. B. Shevitski, S. M. Gilbert, C. T. Chen, *et al.*, "Blue-light-emitting color centers in high-quality hexagonal boron nitride," Phys. Rev. B: Condens. Matter Mater. Phys. **100**, 155419 (2019).
98. C. A. Klein, "Bandgap dependence and related features of radiation ionization energies in semiconductors," J. Appl. Phys. **39**, 2029–2038 (1968).
99. F. Hayee, L. Yu, J. L. Zhang, *et al.*, "Revealing multiple classes of stable quantum emitters in hexagonal boron nitride with correlated optical and electron microscopy," Nat. Mater. **19**, 534–539 (2020).
100. S. A. Tawfik, S. Ali, M. Fronzi, *et al.*, "First-principles investigation of quantum emission from hBN defects," Nanoscale **9**, 13575–13582 (2017).
101. A. Kirchhoff, T. Deilmann, P. Krüger, *et al.*, "Electronic and optical properties of a hexagonal boron nitride monolayer in its pristine form and with point defects from first principles," Phys. Rev. B: Condens. Matter Mater. Phys. **106**, 045118 (2022).
102. N. Berseneva, A. Gulans, A. V. Krasheninnikov, *et al.*, "Electronic structure of boron nitride sheets doped with carbon from first-principles calculations," Phys. Rev. B: Condens. Matter Mater. Phys. **87**, 035404 (2013).
103. X. Blase, I. Duchemin, D. Jacquemin, *et al.*, "The Bethe-Salpeter equation formalism: from physics to chemistry," J. Phys. Chem. Lett. **11**, 7371–7382 (2020).
104. Y. N. Xu and W. Y. Ching, "Calculation of ground-state and optical properties of boron nitrides in the hexagonal, cubic, and wurtzite structures," Phys. Rev. B: Condens. Matter Mater. Phys. **44**, 7787–7798 (1991).
105. X. Blase, A. Rubio, S. G. Louie, *et al.*, "Quasiparticle band structure of bulk hexagonal boron nitride and related systems," Phys. Rev. B: Condens. Matter Mater. Phys. **51**, 6868–6875 (1995).
106. J. Li, X. K. Cao, T. B. Hoffman, *et al.*, "Nature of exciton transitions in hexagonal boron nitride," Appl. Phys. Lett. **108**, 122101 (2016).
107. J. Wu, W.-Q. Han, W. Walukiewicz, *et al.*, "Raman spectroscopy and time-resolved photoluminescence of BN and $B_xC_yN_z$ nanotubes," Nano Lett. **4**, 647–650 (2004).
108. T. T. Tran, K. Bray, M. J. Ford, *et al.*, "Quantum emission from hexagonal boron nitride monolayers," Nat. Nanotechnol. **11**, 37–41 (2016).

109. A. Katzir, J. T. Suss, A. Zunger, *et al.*, "Point defects in hexagonal boron nitride. I. EPR, thermoluminescence, and thermally-stimulated-current measurements," Phys. Rev. B: Condens. Matter Mater. Phys. **11**, 2370–2377 (1975).
110. A. Zunger and A. Katzir, "Point defects in hexagonal boron nitride. II. Theoretical studies," Phys. Rev. B: Condens. Matter Mater. Phys. **11**, 2378–2390 (1975).
111. R. S. Pease, "An X-ray study of boron nitride," Acta Crystallogr. **5**, 356–361 (1952).
112. D. Wong, J. Velasco, L. Ju, *et al.*, "Characterization and manipulation of individual defects in insulating hexagonal boron nitride using scanning tunnelling microscopy," Nat. Nanotechnol. **10**, 949–953 (2015).
113. T. Susi, J. C. Meyer, and J. Kotakoski, "Quantifying transmission electron microscopy irradiation effects using two-dimensional materials," Nat. Rev. Phys. **1**, 397–405 (2019).
114. C. Jin, F. Lin, K. Suenaga, *et al.*, "Fabrication of a freestanding boron nitride single layer and its defect assignments," Phys. Rev. Lett. **102**, 195505 (2009).
115. J. C. Meyer, A. Chuvilin, G. Algara-Siller, *et al.*, "Selective sputtering and atomic resolution imaging of atomically thin boron nitride membranes," Nano Lett. **9**, 2683–2689 (2009).
116. T. Pham, A. L. Gibb, Z. Li, *et al.*, "Formation and dynamics of electron-irradiation-induced defects in hexagonal boron nitride at elevated temperatures," Nano Lett. **16**, 7142–7147 (2016).
117. Y. He, M. Tsutsui, Y. Zhou, *et al.*, "Solid-state nanopore systems: from materials to applications," NPG Asia Mater. **13**, 48 (2021).
118. C. Dai, D. Popple, C. Su, *et al.*, "Evolution of nanopores in hexagonal boron nitride," Commun. Chem. **6**, 108 (2023).
119. O. L. Krivanek, M. F. Chisholm, V. Nicolosi, *et al.*, "Atom-by-atom structural and chemical analysis by annular dark-field electron microscopy," Nature **464**, 571–574 (2010).
120. O. Cretu, A. Ishizuka, K. Yanagisawa, *et al.*, "Atomic-scale electrical field mapping of hexagonal boron nitride defects," ACS Nano **15**, 5316–5321 (2021).
121. J. Cumings, A. Zettl, M. R. McCartney, *et al.*, "Electron holography of field-emitting carbon nanotubes," Phys. Rev. Lett. **88**, 056804 (2002).
122. M. Fernández-Lomana, B. Wu, F. Martín-Vega, *et al.*, "Millikelvin scanning tunneling microscope at 20/22 T with a graphite enabled stick-slip approach and an energy resolution below 8 μeV: application to conductance quantization at 20 T in single atom point contacts of Al and Au and to the charge density wave of 2H-$NbSe_2$," Rev. Sci. Instrum. **92**, 093701 (2021).
123. A. Gloter, V. Badjeck, L. Bocher, *et al.*, "Atomically resolved mapping of EELS fine structures," Mater. Sci. Semicond. Process. **65**, 2–17 (2017).
124. N. Dellby, O. L. Krivanek, N. J. Bacon, *et al.*, "Multi-sun EELS: ultra-high energy resolution combined with high spatial resolution and high beam current," Microsc. Microanal. **28**, 2640–2642 (2022).
125. R. S. Becker, J. A. Golovchenko, and B. S. Swartzentruber, "Atomic-scale surface modifications using a tunnelling microscope," Nature **325**, 419–421 (1987).
126. S.-Y. Lee, T.-Y. Jeong, S. Jung, *et al.*, "Refractive index dispersion of hexagonal boron nitride in the visible and near-infrared," Phys. Status Solidi B **256**, 1800417 (2019).
127. A. Avsar, I. J. Vera-Marun, J. Y. Tan, *et al.*, "Air-stable transport in graphene-contacted, fully encapsulated ultrathin black phosphorus-based field-effect transistors," ACS Nano **9**, 4138–4145 (2015).
128. A. Woessner, P. Alonso-González, M. B. Lundeberg, *et al.*, "Near-field photocurrent nanoscopy on bare and encapsulated graphene," Nat. Commun. **7**, 10783 (2016).

129. E. Semouchkina, *Dielectric Metamaterials and Metasurfaces in Transformation Optics and Photonics* (Woodhead Publishing, 2021).
130. S. Adachi, *Optical Properties of Crystalline and Amorphous Semiconductors: Materials and Fundamental Principles* (Springer Science & Business Media, 2012).
131. A. Poddubny, I. Iorsh, P. Belov, *et al.*, "Hyperbolic metamaterials," Nat. Photonics **7**, 948–957 (2013).
132. M. He, T. G. Folland, J. Duan, *et al.*, "Anisotropy and modal hybridization in infrared nanophotonics using low-symmetry materials," ACS Photonics **9**, 1078–1095 (2022).
133. G. Hu, J. Shen, C.-W. Qiu, *et al.*, "Phonon polaritons and hyperbolic response in van der Waals materials," Adv. Opt. Mater. **8**, 1901393 (2020).
134. P. Li, M. Lewin, A. V. Kretinin, *et al.*, "Hyperbolic phonon-polaritons in boron nitride for near-field optical imaging and focusing," Nat. Commun. **6**, 7507 (2015).
135. S. Dai, Q. Ma, T. Andersen, *et al.*, "Subdiffractional focusing and guiding of polaritonic rays in a natural hyperbolic material," Nat. Commun. **6**, 6963 (2015).
136. M. He, G. R. S. Iyer, S. Aarav, *et al.*, "Ultrahigh-resolution, label-free hyperlens imaging in the mid-IR," Nano Lett. **21**, 7921–7928 (2021).
137. S. Dai, Z. Fei, Q. Ma, *et al.*, "Tunable phonon polaritons in atomically thin van der Waals crystals of boron nitride," Science **343**, 1125–1129 (2014).
138. X. Fan, G. P. Wang, J. C. W. Lee, *et al.*, "All-angle broadband negative refraction of metal waveguide arrays in the visible range: theoretical analysis and numerical demonstration," Phys. Rev. Lett. **97**, 073901 (2006).
139. A. J. Hoffman, L. Alekseyev, S. S. Howard, *et al.*, "Negative refraction in semiconductor metamaterials," Nat. Mater. **6**, 946–950 (2007).
140. J. D. Caldwell, L. Lindsay, V. Giannini, *et al.*, "Low-loss, infrared and terahertz nanophotonics using surface phonon polaritons," Nanophotonics **4**, 44–68 (2015).
141. A. J. Giles, S. Dai, I. Vurgaftman, *et al.*, "Author correction: ultralow-loss polaritons in isotopically pure boron nitride," Nat. Mater. **18**, 1024 (2019).
142. I.-H. Lee, M. He, X. Zhang, *et al.*, "Image polaritons in boron nitride for extreme polariton confinement with low losses," Nat. Commun. **11**, 3649 (2020).
143. T. Q. P. Vuong, S. Liu, A. Van der Lee, *et al.*, "Isotope engineering of van der Waals interactions in hexagonal boron nitride," Nat. Mater. **17**, 152–158 (2018).
144. Z. Liu, H. Lee, Y. Xiong, *et al.*, "Far-field optical hyperlens magnifying sub-diffraction-limited objects," Science **315**, 1686 (2007).
145. Y. Xiong, Z. Liu, and X. Zhang, "A simple design of flat hyperlens for lithography and imaging with half-pitch resolution down to 20 Nm," Appl. Phys. Lett. **94**, 203108 (2009).
146. D. Lee, Y. D. Kim, M. Kim, *et al.*, "Realization of wafer-scale hyperlens device for sub-diffractional biomolecular imaging," ACS Photonics **5**, 2549–2554 (2018).
147. B. Lyu, H. Li, L. Jiang, *et al.*, "Phonon polariton-assisted infrared nanoimaging of local strain in hexagonal boron nitride," Nano Lett. **19**, 1982–1989 (2019).
148. S. Dai, M. Tymchenko, Z.-Q. Xu, *et al.*, "Internal nanostructure diagnosis with hyperbolic phonon polaritons in hexagonal boron nitride," Nano Lett. **18**, 5205–5210 (2018).
149. J. Duan, R. Chen, J. Li, *et al.*, "Launching phonon polaritons by natural boron nitride wrinkles with modifiable dispersion by dielectric environments," Adv. Mater. **29**, 1 (2017).
150. M. Autore, P. Li, I. Dolado, *et al.*, "Boron nitride nanoresonators for phonon-enhanced molecular vibrational spectroscopy at the strong coupling limit," Light: Sci. Appl. **7**, 17172 (2017).

151. B. Zhao and Z. M. Zhang, "Resonance perfect absorption by exciting hyperbolic phonon polaritons in 1D hBN gratings," Opt. Express **25**, 7791 (2017).
152. Q. Pan, G. Zhang, R. Pan, *et al.*, "Tunable absorption as multi-wavelength at infrared on graphene/hBN/Al grating structure," Opt. Express **26**, 18230 (2018).
153. J. D. Caldwell, A. V. Kretinin, Y. Chen, *et al.*, "Sub-diffractional volume-confined polaritons in the natural hyperbolic material hexagonal boron nitride," Nat. Commun. **5**, 5221 (2014).
154. W. Huang, T. G. Folland, F. Sun, *et al.*, "In-plane hyperbolic polariton tuners in terahertz and long-wave infrared regimes," Nat. Commun. **14**, 2716 (2023).
155. D. G. Baranov, Y. Xiao, I. A. Nechepurenko, *et al.*, "Nanophotonic engineering of far-field thermal emitters," Nat. Mater. **18**, 920–930 (2019).
156. T. G. Folland, L. Nordin, and D. Wasserman, "Probing polaritons in the mid-to far-infrared," J. Appl. Phys. **125**, 1 (2019).
157. X. Chen, D. Hu, R. Mescall, *et al.*, "Modern scattering-type scanning near-field optical microscopy for advanced material research," Adv. Mater. **34**, 1 (2022).
158. J. A. Gerber, S. Berweger, B. T. O'Callahan, *et al.*, "Phase-resolved surface plasmon interferometry of graphene," Phys. Rev. Lett. **113**, 055502 (2014).
159. S. Dai, Q. Ma, Y. Yang, *et al.*, "Efficiency of launching highly confined polaritons by infrared light incident on a hyperbolic material," Nano Lett. **17**, 5285–5290 (2017).
160. P. Pons-Valencia, F. J. Alfaro-Mozaz, M. M. Wiecha, *et al.*, "Launching of hyperbolic phonon-polaritons in h-BN slabs by resonant metal plasmonic antennas," Nat. Commun. **10**, 3242 (2019).
161. M. He, J. R. Matson, M. Yu, *et al.*, "Polariton design and modulation via van der Waals/doped semiconductor heterostructures," Nat. Commun. **14**, 7965 (2023).
162. T. G. Folland, A. Fali, S. T. White, *et al.*, "Reconfigurable infrared hyperbolic metasurfaces using phase change materials," Nat. Commun. **9**, 4371 (2018).
163. A. Fali, S. T. White, T. G. Folland, *et al.*, "Refractive index-based control of hyperbolic phonon-polariton propagation," Nano Lett. **19**, 7725–7734 (2019).
164. S. Dai, J. Quan, G. Hu, *et al.*, "Hyperbolic phonon polaritons in suspended hexagonal boron nitride," Nano Lett. **19**, 1009–1014 (2019).
165. S. Dai, J. Zhang, Q. Ma, *et al.*, "Phase-change hyperbolic heterostructures for nanopolaritonics: a case study of hBN/VO_2," Adv. Mater. **31**, 1 (2019).
166. C. Ciracì, R. T. Hill, J. J. Mock, *et al.*, "Probing the ultimate limits of plasmonic enhancement," Science **337**, 1072–1074 (2012).
167. J. J. Baumberg, J. Aizpurua, M. H. Mikkelsen, *et al.*, "Extreme nanophotonics from ultrathin metallic gaps," Nat. Mater. **18**, 668–678 (2019).
168. I.-H. Lee, D. Yoo, P. Avouris, *et al.*, "Graphene acoustic plasmon resonator for ultrasensitive infrared spectroscopy," Nat. Nanotechnol. **14**, 313–319 (2019).
169. F. H. Feres, R. A. Mayer, I. D. Barcelos, *et al.*, "Acceleration of subwavelength polaritons by engineering dielectric-metallic substrates," ACS Photonics **7**, 1396–1402 (2020).
170. S. Dai, Q. Ma, M. K. Liu, *et al.*, "Graphene on hexagonal boron nitride as a tunable hyperbolic metamaterial," Nat. Nanotechnol. **10**, 682–686 (2015).
171. F. L. Ruta, B. S. Y. Kim, Z. Sun, *et al.*, "Surface plasmons induce topological transition in graphene/α-MoO_3 heterostructures," Nat. Commun. **13**, 3719 (2022).
172. H. Hu, N. Chen, H. Teng, *et al.*, "Doping-driven topological polaritons in graphene/α-MoO_3 heterostructures," Nat. Nanotechnol. **17**, 940–946 (2022).
173. G. Álvarez-Pérez, A. González-Morán, N. Capote-Robayna, *et al.*, "Active tuning of highly anisotropic phonon polaritons in van der Waals crystal slabs by gated graphene," ACS Photonics **9**, 383–390 (2022).

174. A. J. Sternbach, S. L. Moore, A. Rikhter, *et al.*, "Negative refraction in hyperbolic hetero-bicrystals," Science **379**, 555–557 (2023).
175. A. Bylinkin, M. Schnell, M. Autore, *et al.*, "Real-space observation of vibrational strong coupling between propagating phonon polaritons and organic molecules," Nat. Photonics **15**, 197–202 (2021).
176. I. Dolado, F. J. Alfaro-Mozaz, P. Li, *et al.*, "Nanoscale guiding of infrared light with hyperbolic volume and surface polaritons in van der Waals material ribbons," Adv. Mater. **32**, 1 (2020).
177. P. Li, I. Dolado, F. J. Alfaro-Mozaz, *et al.*, "Optical nanoimaging of hyperbolic surface polaritons at the edges of van der Waals materials," Nano Lett. **17**, 228–235 (2017).
178. A. Konečná, J. Li, J. H. Edgar, *et al.*, "Revealing nanoscale confinement effects on hyperbolic phonon polaritons with an electron beam," Small **17**, e2103404 (2021).
179. S. Dai, M. Tymchenko, Y. Yang, *et al.*, "Manipulation and steering of hyperbolic surface polaritons in hexagonal boron nitride," Adv. Mater. **30**, 1 (2018).
180. M. Chen, S. Sanders, J. Shen, *et al.*, "Altering the reflection phase for nano-polaritons: a case study of hyperbolic surface polaritons in hexagonal boron nitride," Adv. Opt. Mater. **10**, 1 (2022).
181. F. J. Alfaro-Mozaz, S. G. Rodrigo, S. Vélez, *et al.*, "Hyperspectral nanoimaging of van der Waals polaritonic crystals," Nano Lett. **21**, 7109–7115 (2021).
182. P. Li, I. Dolado, F. J. Alfaro-Mozaz, *et al.*, "Infrared hyperbolic metasurface based on nanostructured van der Waals materials," Science **359**, 892–896 (2018).
183. P. Li, G. Hu, I. Dolado, *et al.*, "Collective near-field coupling and nonlocal phenomena in infrared-phononic metasurfaces for nano-light canalization," Nat. Commun. **11**, 3663 (2020).
184. K. Chaudhary, M. Tamagnone, X. Yin, *et al.*, "Polariton nanophotonics using phase-change materials," Nat. Commun. **10**, 4487 (2019).
185. M. He, S. I. Halimi, T. G. Folland, *et al.*, "Guided mid-IR and near-IR light within a hybrid hyperbolic-material/silicon waveguide heterostructure," Adv. Mater. **33**, e2004305 (2021).
186. J. Yang, Z. E. Krix, S. Kim, *et al.*, "Near-field excited Archimedean-like tiling patterns in phonon-polaritonic crystals," ACS Nano **15**, 9134–9142 (2021).
187. H. Herzig Sheinfux, M. Jung, L. Orsini, *et al.*, "Transverse hypercrystals formed by periodically modulated phonon polaritons," ACS Nano **17**, 7377–7383 (2023).
188. T. G. Folland, T. W. W. Maß, J. R. Matson, *et al.*, "Probing hyperbolic polaritons using infrared attenuated total reflectance micro-spectroscopy," MRS Commun. **8**, 1418–1425 (2018).
189. P. Sohr, D. Wei, Z. Wang, *et al.*, "Strong coupling in semiconductor hyperbolic metamaterials," Nano Lett. **21**, 9951–9957 (2021).
190. J.-J. Greffet, R. Carminati, K. Joulain, *et al.*, "Coherent emission of light by thermal sources," Nature **416**, 61–64 (2002).
191. G. Lu, C. R. Gubbin, J. R. Nolen, *et al.*, "Engineering the spectral and spatial dispersion of thermal emission via polariton–phonon strong coupling," Nano Lett. **21**, 1831–1838 (2021).
192. G. Lu, J. R. Nolen, T. G. Folland, *et al.*, "Narrowband polaritonic thermal emitters driven by waste heat," ACS Omega **5**, 10900–10908 (2020).
193. G. Deng, X. Song, S. A. Dereshgi, *et al.*, "Tunable multi-wavelength absorption in mid-IR region based on a hybrid patterned graphene-hBN structure," Opt. Express **27**, 23576 (2019).
194. M. He, J. R. Nolen, J. Nordlander, *et al.*, "Coupled Tamm phonon and plasmon polaritons for designer planar multiresonance absorbers," Adv. Mater. **35**, e2209909 (2023).

195. M. Barra-Burillo, U. Muniain, S. Catalano, *et al.*, "Microcavity phonon polaritons from the weak to the ultrastrong phonon–photon coupling regime," Nat. Commun. **12**, 6206 (2021).
196. S. Guddala, F. Komissarenko, S. Kiriushechkina, *et al.*, "Topological phonon-polariton funneling in midinfrared metasurfaces," Science **374**, 225–227 (2021).
197. B. Lounis and M. Orrit, "Single-photon sources," Rep. Prog. Phys. **68**, 1129–1179 (2005).
198. B. Lounis and W. E. Moerner, "Single photons on demand from a single molecule at room temperature," Nature **407**, 491–493 (2000).
199. X.-L. Chu, S. Götzinger, and V. Sandoghdar, "A single molecule as a high-fidelity photon gun for producing intensity-squeezed light," Nat. Photonics **11**, 58–62 (2017).
200. M. Hijlkema, B. Weber, H. P. Specht, *et al.*, "A single-photon server with just one atom," Nat. Phys. **3**, 253–255 (2007).
201. P. Senellart, G. Solomon, and A. White, "High-performance semiconductor quantum-dot single-photon sources," Nat. Nanotechnol. **12**, 1026–1039 (2017).
202. R. Brouri, A. Beveratos, J. P. Poizat, *et al.*, "Photon antibunching in the fluorescence of individual color centers in diamond," Opt. Lett. **25**, 1294 (2000).
203. A. Lohrmann, N. Iwamoto, Z. Bodrog, *et al.*, "Single-photon emitting diode in silicon carbide," Nat. Commun. **6**, 7783 (2015).
204. S. Tamariz, G. Callsen, J. Stachurski, *et al.*, "Toward bright and pure single photon emitters at 300 K based on GaN quantum dots on silicon," ACS Photonics **7**, 1515–1522 (2020).
205. P. Udvarhelyi, B. Somogyi, G. Thiering, *et al.*, "Identification of a telecom wavelength single photon emitter in silicon," Phys. Rev. Lett. **127**, 196402 (2021).
206. P. Maletinsky, S. Hong, M. S. Grinolds, *et al.*, "A robust scanning diamond sensor for nanoscale imaging with single nitrogen-vacancy centres," Nat. Nanotechnol. **7**, 320–324 (2012).
207. A. Sipahigil, M. L. Goldman, E. Togan, *et al.*, "Quantum interference of single photons from remote nitrogen-vacancy centers in diamond," Phys. Rev. Lett. **108**, 143601 (2012).
208. A. Splendiani, L. Sun, Y. Zhang, *et al.*, "Emerging photoluminescence in monolayer MoS_2," Nano Lett. **10**, 1271–1275 (2010).
209. M. Koperski, K. Nogajewski, A. Arora, *et al.*, "Single photon emitters in exfoliated WSe_2 structures," Nat. Nanotechnol. **10**, 503–506 (2015).
210. A. Branny, S. Kumar, R. Proux, *et al.*, "Deterministic strain-induced arrays of quantum emitters in a two-dimensional semiconductor," Nat. Commun. **8**, 15053 (2017).
211. T. Mueller and E. Malic, "Exciton physics and device application of two-dimensional transition metal dichalcogenide semiconductors," npj 2D Mater. Appl. **2**, 29 (2018).
212. Z. Sun, A. Martinez, and F. Wang, "Optical modulators with 2D layered materials," Nat. Photonics **10**, 227–238 (2016).
213. F. Withers, O. Del Pozo-Zamudio, S. Schwarz, *et al.*, "WSe_2 light-emitting tunneling transistors with enhanced brightness at room temperature," Nano Lett. **15**, 8223–8228 (2015).
214. D. Wigger, R. Schmidt, O. Del Pozo-Zamudio, *et al.*, "Phonon-assisted emission and absorption of individual color centers in hexagonal boron nitride," 2D Mater. **6**, 035006 (2019).
215. A. W. Schell, M. Svedendahl, and R. Quidant, "Quantum emitters in hexagonal boron nitride have spectrally tunable quantum efficiency," Adv. Mater. **30**, e1704237 (2018).

216. B. Sontheimer, M. Braun, N. Nikolay, *et al.*, "Photodynamics of quantum emitters in hexagonal boron nitride revealed by low-temperature spectroscopy," Phys. Rev. B: Condens. Matter Mater. Phys. **96**, 121202 (2017).
217. M. Krecmarova and R. Canet-Albiach, "Extrinsic effects on the optical properties of surface color defects generated in hexagonal boron nitride nanosheets," Appl. Material **13**, 46105 (2021).
218. Z. Q. Xu, N. Mendelson, J. A. Scott, *et al.*, "Charge and energy transfer of quantum emitters in 2D heterostructures," 2D Mater. **7**, 031001 (2020).
219. L. J. Martínez, T. Pelini, V. Waselowski, *et al.*, "Efficient single photon emission from a high-purity hexagonal boron nitride crystal," Phys. Rev. B: Condens. Matter Mater. Phys. **94**, 121405 (2016).
220. R. N. Patel, D. A. Hopper, J. A. Gusdorff, *et al.*, "Probing the optical dynamics of quantum emitters in hexagonal boron nitride," PRX Quantum **3**, 030331 (2022).
221. H. L. Stern, Q. Gu, J. Jarman, *et al.*, "Room-temperature optically detected magnetic resonance of single defects in hexagonal boron nitride," Nat. Commun. **13**, 618 (2022).
222. H. L. Stern, R. Wang, Y. Fan, *et al.*, "Spectrally resolved photodynamics of individual emitters in large-area monolayers of hexagonal boron nitride," ACS Nano **13**, 4538–4547 (2019).
223. X. Li, G. D. Shepard, A. Cupo, *et al.*, "Nonmagnetic quantum emitters in boron nitride with ultranarrow and sideband-free emission spectra," ACS Nano **11**, 6652–6660 (2017).
224. H. Akbari, W.-H. Lin, B. Vest, *et al.*, "Temperature-dependent spectral emission of hexagonal boron nitride quantum emitters on conductive and dielectric substrates," Phys. Rev. Appl. **15**, 014036 (2021).
225. S. X. Li, T. Ichihara, H. Park, *et al.*, "Prolonged photostability in hexagonal boron nitride quantum emitters," Commun. Mater. **4**, 19 (2023).
226. M. Kianinia, C. Bradac, B. Sontheimer, *et al.*, "All-optical control and super-resolution imaging of quantum emitters in layered materials," Nat. Commun. **9**, 874 (2018).
227. G. Wolfowicz, F. J. Heremans, C. P. Anderson, *et al.*, "Quantum guidelines for solid-state spin defects," Nat. Rev. Mater. **6**, 906–925 (2021).
228. C. Babin, R. Stöhr, N. Morioka, *et al.*, "Fabrication and nanophotonic waveguide integration of silicon carbide colour centres with preserved spin-optical coherence," Nat. Mater. **21**, 67–73 (2022).
229. N. H. Wan, T.-J. Lu, K. C. Chen, *et al.*, "Large-scale integration of artificial atoms in hybrid photonic circuits," Nature **583**, 226–231 (2020).
230. T. T. Tran, M. Kianinia, M. Nguyen, *et al.*, "Resonant excitation of quantum emitters in hexagonal boron nitride," ACS Photonics **5**, 295–300 (2018).
231. A. Dietrich, M. W. Doherty, I. Aharonovich, *et al.*, "Solid-state single photon source with Fourier transform limited lines at room temperature," Phys. Rev. B: Condens. Matter Mater. Phys. **101**, 081401 (2020).
232. M. K. Koch, V. Bharadwaj, and A. Kubanek, "Limits for coherent optical control of quantum emitters in layered materials," arXiv, arXiv:2312.11090 (2023).
233. C. Fournier, S. Roux, K. Watanabe, *et al.*, "Two-photon interference from a quantum emitter in hexagonal boron nitride," Phys. Rev. Appl. **19**, L041003 (2023).
234. S. Li, R. Yang, D. Zhang, *et al.*, "Room-temperature coherent manipulation of single-spin qubits in silicon carbide with a high readout contrast," Natl. Sci. Rev. **9**, nwab122 (2022).
235. A. Gottscholl, M. Kianinia, V. Soltamov, *et al.*, "Initialization and read-out of intrinsic spin defects in a van der Waals crystal at room temperature," Nat. Mater. **19**, 540–545 (2020).

236. A. Gottscholl, M. Diez, V. Soltamov, *et al.*, "Spin defects in hBN as promising temperature, pressure and magnetic field quantum sensors," Nat. Commun. **12**, 4480 (2021).
237. A. Haykal, R. Tanos, N. Minotto, *et al.*, "Decoherence of VB^- spin defects in monoisotopic hexagonal boron nitride," Nat. Commun. **13**, 4347 (2022).
238. N. Mathur, A. Mukherjee, X. Gao, *et al.*, "Excited-state spin-resonance spectroscopy of VB^- defect centers in hexagonal boron nitride," Nat. Commun. **13**, 3233 (2022).
239. X. Gao, S. Vaidya, K. Li, *et al.*, "Nuclear spin polarization and control in hexagonal boron nitride," Nat. Mater. **21**, 1024–1028 (2022).
240. V. Ivády, G. Barcza, G. Thiering, *et al.*, "*Ab initio* theory of the negatively charged boron vacancy qubit in hexagonal boron nitride," npj Comput. Mater. **6**, 41 (2020).
241. X. Xu, A. B. Solanki, D. Sychev, *et al.*, "Greatly enhanced emission from spin defects in hexagonal boron nitride enabled by a low-loss plasmonic nanocavity," Nano Lett. **23**, 25–33 (2023).
242. H. Cai, S. Ru, Z. Jiang, *et al.*, "Spin defects in hBN assisted by metallic nanotrenches for quantum sensing," Nano Lett. **23**, 4991–4996 (2023).
243. J. E. Fröch, L. P. Spencer, M. Kianinia, *et al.*, "Coupling spin defects in hexagonal boron nitride to monolithic bullseye cavities," Nano Lett. **21**, 6549–6555 (2021).
244. M. Nonahal, C. Li, F. Tjiptoharsono, *et al.*, "Coupling spin defects in hexagonal boron nitride to titanium dioxide ring resonators," Nanoscale **14**, 14950–14955 (2022).
245. L. Sortino, A. Gale, L. Kühner, *et al.*, "Optically addressable spin defects coupled to bound states in the continuum metasurfaces," Nat. Commun. **15**, 2008 (2024).
246. X. Gao, B. Jiang, A. E. Llacsahuanga Allcca, *et al.*, "High-contrast plasmonic-enhanced shallow spin defects in hexagonal boron nitride for quantum sensing," Nano Lett. **21**, 7708–7714 (2021).
247. T. Suzuki, Y. Yamazaki, T. Taniguchi, *et al.*, "Spin property improvement of boron vacancy defect in hexagonal boron nitride by thermal treatment," Appl. Phys. Express **16**, 032006 (2023).
248. N. Mendelson, D. Chugh, J. R. Reimers, *et al.*, "Identifying carbon as the source of visible single-photon emission from hexagonal boron nitride," Nat. Mater. **20**, 321–328 (2021).
249. D. Chugh, J. Wong-Leung, L. Li, *et al.*, "Flow modulation epitaxy of hexagonal boron nitride," 2D Mater. **5**, 045018 (2018).
250. T. Vogl, G. Campbell, B. C. Buchler, *et al.*, "Fabrication and deterministic transfer of high-quality quantum emitters in hexagonal boron nitride," ACS Photonics **5**, 2305–2312 (2018).
251. G. Grosso, H. Moon, B. Lienhard, *et al.*, "Tunable and high-purity room temperature single-photon emission from atomic defects in hexagonal boron nitride," Nat. Commun. **8**, 705 (2017).
252. M. Kianinia, S. A. Tawfik, B. Regan, *et al.*, "Robust solid state quantum system operating at 800 K," in *Conference on Lasers and Electro-Optics* (OSA, 2017), p. JTu5A.24.
253. W. Liu, Y.-T. Wang, Z.-P. Li, *et al.*, "An ultrastable and robust single-photon emitter in hexagonal boron nitride," Phys. E **124**, 114251 (2020).
254. C. Bradac, "High-resolution optical imaging and sensing using quantum emitters in hexagonal boron-nitride," Front. Phys. **9**, 117 (2021).
255. J. Comtet, E. Glushkov, V. Navikas, *et al.*, "Wide-field spectral super-resolution mapping of optically active defects in hexagonal boron nitride," Nano Lett. **19**, 2516–2523 (2019).

256. J. Feng, H. Deschout, S. Caneva, *et al.*, "Imaging of optically active defects with nanometer resolution," Nano Lett. **18**, 1739–1744 (2018).
257. S. W. Hell and M. Kroug, "Ground-state-depletion fluorscence microscopy: a concept for breaking the diffraction resolution limit," Appl. Phys. B **60**, 495–497 (1995).
258. C. Lyu, Y. Zhu, P. Gu, *et al.*, "Single-photon emission from two-dimensional hexagonal boron nitride annealed in a carbon-rich environment," Appl. Phys. Lett. **117**, 244002 (2020).
259. M. Fischer, J. M. Caridad, A. Sajid, *et al.*, "Controlled generation of luminescent centers in hexagonal boron nitride by irradiation engineering," Sci. Adv. **7**, eabe7138 (2021).
260. Y. Chen, C. Li, S. White, *et al.*, "Generation of high-density quantum emitters in high-quality, exfoliated hexagonal boron nitride," ACS Appl. Mater. Interfaces **13**, 47283–47292 (2021).
261. L. H. Li, J. Cervenka, K. Watanabe, *et al.*, "Strong oxidation resistance of atomically thin boron nitride nanosheets," ACS Nano **8**, 1457–1462 (2014).
262. B. Zhang, Q. Wu, H. Yu, *et al.*, "High-efficient liquid exfoliation of boron nitride nanosheets using aqueous solution of alkanolamine," Nanoscale Res. Lett. **12**, 596 (2017).
263. N. M. H. Duong, E. Glushkov, A. Chernev, *et al.*, "Facile production of hexagonal boron nitride nanoparticles by cryogenic exfoliation," Nano Lett. **19**, 5417–5422 (2019).
264. N. Wang, G. Yang, H. Wang, *et al.*, "A universal method for large-yield and high-concentration exfoliation of two-dimensional hexagonal boron nitride nanosheets," Mater. Today **27**, 33–42 (2019).
265. T. T. Tran, C. Zachreson, A. M. Berhane, *et al.*, "Quantum emission from defects in single-crystalline hexagonal boron nitride," Phys. Rev. Appl. **5**, 034005 (2016).
266. D. Chugh, C. Jagadish, and H. Tan, "Large-area hexagonal boron nitride for surface enhanced Raman spectroscopy," Adv. Mater. Technol. **4**, 1900220 (2019).
267. N. Mendelson, Z.-Q. Xu, T. T. Tran, *et al.*, "Engineering and tuning of quantum emitters in few-layer hexagonal boron nitride," ACS Nano **13**, 3132–3140 (2019).
268. Z.-Q. Xu, C. Elbadawi, T. T. Tran, *et al.*, "Single photon emission from plasma treated 2d hexagonal boron nitride," Nanoscale **10**, 7957–7965 (2018).
269. M. Kianinia, S. White, J. E. Fröch, *et al.*, "Generation of spin defects in hexagonal boron nitride," ACS Photonics **7**, 2147–2152 (2020).
270. R. Gu, L. Wang, H. Zhu, *et al.*, "Engineering and microscopic mechanism of quantum emitters induced by heavy ions in hBN," ACS Photonics **8**, 2912–2922 (2021).
271. N.-J. Guo, W. Liu, Z.-P. Li, *et al.*, "Generation of spin defects by ion implantation in hexagonal boron nitride," ACS Omega **7**, 1733–1739 (2022).
272. S. Choi, T. T. Tran, C. Elbadawi, *et al.*, "Engineering and localization of quantum emitters in large hexagonal boron nitride layers," ACS Appl. Mater. Interfaces **8**, 29642–29648 (2016).
273. H. Ngoc My Duong, M. A. P. Nguyen, M. Kianinia, *et al.*, "Effects of high-energy electron irradiation on quantum emitters in hexagonal boron nitride," ACS Appl. Mater. Interfaces **10**, 24886–24891 (2018).
274. X. Gao, S. Pandey, M. Kianinia, *et al.*, "Femtosecond laser writing of spin defects in hexagonal boron nitride," ACS Photonics **8**, 994–1000 (2021).
275. L. Gan, D. Zhang, R. Zhang, *et al.*, "Large-scale, high-yield laser fabrication of bright and pure single-photon emitters at room temperature in hexagonal boron nitride," ACS Nano **16**, 14254–14261 (2022).

276. J. Ziegler, R. Klaiss, A. Blaikie, *et al.*, "Deterministic quantum emitter formation in hexagonal boron nitride via controlled edge creation," Nano Lett. **19**, 2121–2127 (2019).
277. X. Xu, Z. O. Martin, D. Sychev, *et al.*, "Creating quantum emitters in hexagonal boron nitride deterministically on chip-compatible substrates," Nano Lett. **21**, 8182–8189 (2021).
278. C. Li, N. Mendelson, R. Ritika, *et al.*, "Scalable and deterministic fabrication of quantum emitter arrays from hexagonal boron nitride," Nano Lett. **21**, 3626–3632 (2021).
279. J. C. Stewart, Y. Fan, J. S. H. Danial, *et al.*, "Quantum emitter localization in layer-engineered hexagonal boron nitride," ACS Nano **15**, 13591–13603 (2021).
280. E. Glushkov, M. Macha, E. Räth, *et al.*, "Engineering optically active defects in hexagonal boron nitride using focused ion beam and water," ACS Nano **16**, 3695–3703 (2022).
281. N. V. Proscia, Z. Shotan, H. Jayakumar, *et al.*, "Near-deterministic activation of room-temperature quantum emitters in hexagonal boron nitride," Optica **5**, 1128 (2018).
282. N. Chejanovsky, M. Rezai, F. Paolucci, *et al.*, "Structural attributes and photodynamics of visible spectrum quantum emitters in hexagonal boron nitride," Nano Lett. **16**, 7037–7045 (2016).
283. S. Hou, M. D. Birowosuto, S. Umar, *et al.*, "Localized emission from laser-irradiated defects in 2D hexagonal boron nitride," 2D Mater. **5**, 015010 (2017).
284. G. Noh, D. Choi, J.-H. Kim, *et al.*, "Stark tuning of single-photon emitters in hexagonal boron nitride," Nano Lett. **18**, 4710–4715 (2018).
285. S. J. U. White, T. Yang, N. Dontschuk, *et al.*, "Electrical control of quantum emitters in a van der Waals heterostructure," Light: Sci. Appl. **11**, 186 (2022).
286. Y. Xia, Q. Li, J. Kim, *et al.*, "Room-temperature giant stark effect of single photon emitter in van der Waals material," Nano Lett. **19**, 7100–7105 (2019).
287. A. Al-Juboori, H. Z. J. Zeng, M. A. P. Nguyen, *et al.*, "Quantum key distribution using a quantum emitter in hexagonal boron nitride," Adv. Quantum Technol. **6**, 1 (2023).
288. H. Z. Zeng, M. A. P. Ngyuen, X. Ai, *et al.*, "Integrated room temperature single-photon source for quantum key distribution: publisher's note," Opt. Lett. **47**, 2161 (2022).
289. Ç Samaner, S. Paçal, G. Mutlu, *et al.*, "Free-space quantum key distribution with single photons from defects in hexagonal boron nitride," Adv. Quantum Technol. **5**, 2200059 (2022).
290. Y. Chen, T. N. Tran, N. M. H. Duong, *et al.*, "Optical thermometry with quantum emitters in hexagonal boron nitride," ACS Appl. Mater. Interfaces **12**, 25464–25470 (2020).
291. W. Liu, Z.-P. Li, Y.-Z. Yang, *et al.*, "Temperature-dependent energy-level shifts of spin defects in hexagonal boron nitride," ACS Photonics **8**, 1889–1895 (2021).
292. A. J. Healey, S. C. Scholten, T. Yang, *et al.*, "Quantum microscopy with van der Waals heterostructures," Nat. Phys. **19**, 87–91 (2023).
293. M. Huang, J. Zhou, D. Chen, *et al.*, "Wide field imaging of van der Waals ferromagnet Fe_3GeTe_2 by spin defects in hexagonal boron nitride," Nat. Commun. **13**, 5369 (2022).
294. P. Kumar, F. Fabre, A. Durand, *et al.*, "Magnetic imaging with spin defects in hexagonal boron nitride," Phys. Rev. Appl. **18**, L061002 (2022).
295. X. Lyu, Q. Tan, L. Wu, *et al.*, "Strain quantum sensing with spin defects in hexagonal boron nitride," Nano Lett. **22**, 6553–6559 (2022).

296. R. Rizzato, M. Schalk, S. Mohr, *et al.*, "Extending the coherence of spin defects in hBN enables advanced qubit control and quantum sensing," Nat. Commun. **14**, 5089 (2023).
297. A. Kubanek, "Coherent quantum emitters in hexagonal boron nitride," Adv. Quantum Technol. **5**, 2200009 (2022).
298. C. Fournier, K. Watanabe, T. Taniguchi, *et al.*, "Investigating the fast spectral diffusion of a quantum emitter in hBN using resonant excitation and photon correlations," Phys. Rev. B: Condens. Matter Mater. Phys. **107**, 195304 (2023).
299. C. Li, J. Jang, T. Badloe, *et al.*, "Arbitrarily structured quantum emission with a multifunctional metalens," eLight **3**, 19 (2023).
300. L. A. Coldren, G. A. Fish, Y. Akulova, *et al.*, "Tunable semiconductor lasers: a tutorial," J. Lightwave Technol. **22**, 193–202 (2004).
301. N. Ismail, C. C. Kores, D. Geskus, *et al.*, "Fabry-Pérot resonator: spectral line shapes, generic and related airy distributions, linewidths, finesses, and performance at low or frequency-dependent reflectivity," Opt. Express **24**, 16366 (2016).
302. G. Cerullo and S. De Silvestri, "Ultrafast optical parametric amplifiers," Rev. Sci. Instrum. **74**, 1–18 (2003).
303. D. V. Grudinin, G. A. Ermolaev, D. G. Baranov, *et al.*, "Hexagonal boron nitride nanophotonics: a record-breaking material for the ultraviolet and visible spectral ranges," Mater Horiz **10**, 2427–2435 (2023).
304. Y. Rah, Y. Jin, S. Kim, *et al.*, "Optical analysis of the refractive index and birefringence of hexagonal boron nitride from the visible to near-infrared," Opt. Lett. **44**, 3797 (2019).
305. T. M. Babinec, B. J. M. Hausmann, M. Khan, *et al.*, "A diamond nanowire single-photon source," Nat. Nanotechnol. **5**, 195–199 (2010).
306. W. L. Barnes, G. Björk, J. M. Gérard, *et al.*, "Solid-state single photon sources: light collection strategies," Eur. Phys. J. D **18**, 197–210 (2002).
307. C. Sauvan, J. P. Hugonin, I. S. Maksymov, *et al.*, "Theory of the spontaneous optical emission of nanosize photonic and plasmon resonators," Phys. Rev. Lett. **110**, 237401 (2013).
308. E. A. Muljarov and W. Langbein, "Exact mode volume and Purcell factor of open optical systems," Phys. Rev. B: Condens. Matter Mater. Phys. **94**, 235438 (2016).
309. P. T. Kristensen, C. Van Vlack, and S. Hughes, "Generalized effective mode volume for leaky optical cavities," Opt. Lett. **37**, 1649 (2012).
310. T. J. Kippenberg, S. M. Spillane, and K. J. Vahala, "Demonstration of ultra-high-Q small mode volume toroid microcavities on a chip," Appl. Phys. Lett. **85**, 6113–6115 (2004).
311. A. Das, D. J. Lee, P. K. Shandilya, *et al.*, "Demonstration of hybrid high-Q hexagonal boron nitride microresonators," ACS Photonics **8**, 3027–3033 (2021).
312. J. E. Fröch, Y. Hwang, S. Kim, *et al.*, "Photonic nanostructures from hexagonal boron nitride," Adv. Opt. Mater. **7**, 1801344 (2019).
313. Y. Wang, J. Lee, J. Berezovsky, *et al.*, "Cavity quantum electrodynamics design with single photon emitters in hexagonal boron nitride," Appl. Phys. Lett. **118**, 244003 (2021).
314. J. D. Joannopoulos, P. R. Villeneuve, and S. Fan, "Photonic crystals: putting a new twist on light," Nature **386**, 143–149 (1997).
315. E. Kuramochi, H. Taniyama, T. Tanabe, *et al.*, "Ultrahigh-Q one-dimensional photonic crystal nanocavities with modulated mode-gap barriers on SiO_2 claddings and on air claddings," Opt. Express **18**, 15859 (2010).
316. M. Ghulinyan and L. Pavesi, *Light Localisation and Lasing: Random and Quasi-Random Photonic Structures* (Cambridge University Press, 2014).

317. S. Hu and S. M. Weiss, "Design of photonic crystal cavities for extreme light concentration," ACS Photonics **3**, 1647–1653 (2016).
318. J. D. Joannopoulos, S. G. Johnson, J. N. Winn, *et al.*, *Photonic Crystals* (Princeton University Press, 2011).
319. J. D. Ryckman and S. M. Weiss, "Low mode volume slotted photonic crystal single nanobeam cavity," in *The 9th International Conference on Group IV Photonics (GFP)* (IEEE, 2012).
320. P. Seidler, K. Lister, U. Drechsler, *et al.*, "Slotted photonic crystal nanobeam cavity with an ultrahigh quality factor-to-mode volume ratio," Opt. Express **21**, 32468 (2013).
321. S. Kim, J. E. Fröch, J. Christian, *et al.*, "Photonic crystal cavities from hexagonal boron nitride," Nat. Commun. **9**, 2623 (2018).
322. J. E. Fröch, C. Li, Y. Chen, *et al.*, "Purcell enhancement of a cavity-coupled emitter in hexagonal boron nitride," Small **18**, 1 (2022).
323. N. H. Wan, B. J. Shields, D. Kim, *et al.*, "Efficient extraction of light from a nitrogen-vacancy center in a diamond parabolic reflector," Nano Lett. **18**, 2787–2793 (2018).
324. C. W. Hsu, B. Zhen, A. D. Stone, *et al.*, "Bound states in the continuum," Nat. Rev. Mater. **1**, 16048 (2016).
325. A. Kodigala, T. Lepetit, Q. Gu, *et al.*, "Lasing action from photonic bound states in continuum," Nature **541**, 196–199 (2017).
326. K. Koshelev, S. Kruk, E. Melik-Gaykazyan, *et al.*, "Subwavelength dielectric resonators for nonlinear nanophotonics," Science **367**, 288–292 (2020).
327. K. Koshelev, S. Lepeshov, M. Liu, *et al.*, "Asymmetric metasurfaces with high-Q resonances governed by bound states in the continuum," Phys. Rev. Lett. **121**, 193903 (2018).
328. S. I. Azzam and A. V. Kildishev, "Photonic bound states in the continuum: from basics to applications," Adv. Opt. Mater. **9**, 2001469 (2021).
329. C. Li, J. E. Fröch, M. Nonahal, *et al.*, "Integration of hBN quantum emitters in monolithically fabricated waveguides," ACS Photonics **8**, 2966–2972 (2021).
330. M. Nonahal, C. Li, H. Ren, *et al.*, "Engineering quantum nanophotonic components from hexagonal boron nitride," Laser Photonics Rev. **17**, 2300019 (2023).
331. M. Nonahal, J. Horder, A. Gale, *et al.*, "Deterministic fabrication of a coupled cavity–emitter system in hexagonal boron nitride," Nano Lett. **23**, 6645–6650 (2023).
332. L. Kühner, L. Sortino, B. Tilmann, *et al.*, "High-Q nanophotonics over the full visible spectrum enabled by hexagonal boron nitride metasurfaces," Adv. Mater. **35**, e2209688 (2023).
333. E. M. Purcell, H. C. Torrey, and R. V. Pound, "Resonance absorption by nuclear magnetic moments in a solid," Phys. Rev. **69**, 37–38 (1946).
334. E. A. Power, *Introductory Quantum Electrodynamics* (DA Information Services, 1964).
335. T. Grange, G. Hornecker, D. Hunger, *et al.*, "Cavity-funneled generation of indistinguishable single photons from strongly dissipative quantum emitters," Phys. Rev. Lett. **114**, 193601 (2015).
336. E. Janitz, M. K. Bhaskar, and L. Childress, "Cavity quantum electrodynamics with color centers in diamond," Optica **7**, 1232 (2020).
337. J. Vučković, "Quantum optics and cavity QED with quantum dots in photonic crystals," Quantum Optics and Nanophotonics **365**, 365–406 (2017).
338. A. Frisk Kockum, A. Miranowicz, S. De Liberato, *et al.*, "Ultrastrong coupling between light and matter," Nat. Rev. Phys. **1**, 19–40 (2019).

339. C. Jin, E. C. Regan, A. Yan, *et al.*, "Observation of moiré excitons in WSe_2/WS_2 heterostructure superlattices," Nature **567**, 76–80 (2019).
340. K. Tran, G. Moody, F. Wu, *et al.*, "Evidence for moiré excitons in van der Waals heterostructures," Nature **567**, 71–75 (2019).
341. Y. Cao, V. Fatemi, A. Demir, *et al.*, "Correlated insulator behaviour at half-filling in magic-angle graphene superlattices," Nature **556**, 80–84 (2018).
342. Y. Cao, V. Fatemi, S. Fang, *et al.*, "Unconventional superconductivity in magic-angle graphene superlattices," Nature **556**, 43–50 (2018).
343. L. Li and M. Wu, "Binary compound bilayer and multilayer with vertical polarizations: two-dimensional ferroelectrics, multiferroics, and nanogenerators," ACS Nano **11**, 6382–6388 (2017).
344. C. R. Woods, P. Ares, H. Nevison-Andrews, *et al.*, "Charge-polarized interfacial superlattices in marginally twisted hexagonal boron nitride," Nat. Commun. **12**, 347 (2021).
345. K. Yasuda, X. Wang, K. Watanabe, *et al.*, "Stacking-engineered ferroelectricity in bilayer boron nitride," Science **372**, 1458–1462 (2021).
346. H. Y. Lee, M. M. Al Ezzi, N. Raghuvanshi, *et al.*, "Tunable optical properties of thin films controlled by the interface twist angle," Nano Lett. **21**, 2832–2839 (2021).
347. C. Su, F. Zhang, S. Kahn, *et al.*, "Tuning colour centres at a twisted hexagonal boron nitride interface," Nat. Mater. **21**, 896–902 (2022).
348. S. Li, A. Pershin, P. Li, *et al.*, "Exceptionally strong coupling of defect emission in hexagonal boron nitride to stacking sequences," npj 2D Mater. Appl. **8**, 16 (2024).

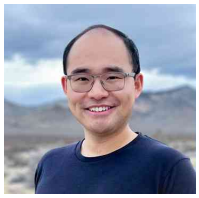

Cong Su is an assistant professor in the Department of Mechanical Engineering and Materials Science and the Department of Applied Physics at Yale University. His research focuses on developing methods to modify the crystal structure atom-by-atom at room temperature using electron beams. Prior to that, he was the Heising-Simons Junior Postdoc Fellow in the Department of Physics at the University of California at Berkeley and a postdoc fellow at Lawrence Berkeley National Laboratory. He got his Ph.D. from Massachusetts Institute of Technology and his bachelor's from Peking University.

Eli Janzen is a postdoc researcher at the University of California at Berkeley. He received his Ph.D. from Kansas State University. He has been awarded national laboratory residency at Lawrence Berkeley National Laboratory.

Mingze He is a research fellow at the Advanced Science Research Center at City University of New York. His research interests focus on engineering polaritonic devices for wave manipulation and infrared light sources. Currently, his research is focused on developing light sources in the mid-infrared with both spectral and spatial control. He received his Ph.D. from Vanderbilt University in 2023. Prior to that, he got both B.Eng. and M. Eng. from Huazhong University of Science and Technology.

Chi Li is a research fellow at the School of Physics and Astronomy at Monash University. His research interests focus on solid-state quantum emitters, low-dimensional materials, and integrated nanophotonics. Currently, his research is centered around developing integrated photonic chips that use structured photons for high-dimensional quantum applications. He received his Ph.D. from the University of Technology Sydney in 2022. Prior to that, he obtained a BSc from Anhui University and an MSc from Soochow University.

Alex Zettl is a professor in the Department of Physics at the University of California at Berkeley and a senior faculty scientist in the Materials Science Division at Lawrence Berkeley National Laboratory. His research interests are in experimental condensed matter physics, including synthesizing and characterizing novel materials with unusual electronic and magnetic ground states. He has received numerous awards, including Feynman Prize in Nanotechnology and APS James C. McGroddy Prize for New Materials. He is a member of American Academy of Arts and Sciences and Clarivate Citation Laureate.

Joshua D. Caldwell is a professor of mechanical engineering, electrical engineering, and chemistry at Vanderbilt University. He obtained his B.A. in Chemistry in 2000 from Virginia Tech and obtained his Ph.D. in Physical Chemistry in 2004 at the University of Florida. His research focuses on the confinement of electromagnetic energy to the nano- to atomic-scale and the interactions between light and matter within such confined systems.

James H. Edgar is University Distinguished Professor and Tom Barrett Faculty Chair in the Tim Taylor Department of Chemical Engineering at Kansas State University. He was formerly head of his department. He served as a National Science Foundation manager of the Electronic and Photonic Materials program (2019-2022).

Igor Aharonovich is a professor in the School of Mathematical and Physical Sciences at University of Technology Sydney (UTS) and the UTS node director of the ARC Centre of Excellence for Transformative Meta-Optical Materials (TMOS). Igor is an elected fellow of Optica and the Royal Society of NSW.